

**RESPONSIVE MICRO- AND NANO-STRUCTURES THROUGH  
INTERFACIAL ASSEMBLY OF STAR POLYMERS**

A Dissertation  
Presented to  
The Academic Faculty

by

Weinan Xu

In Partial Fulfillment  
of the Requirements for the Degree  
Doctor of Philosophy in the  
School of Materials Science and Engineering

Georgia Institute of Technology  
December 2015

Copyright © 2015 by Weinan Xu

**RESPONSIVE MICRO- AND NANO-STRUCTURES THROUGH  
INTERFACIAL ASSEMBLY OF STAR POLYMERS**

Approved by:

Dr. Vladimir V. Tsukruk, Advisor  
School of Materials Science and  
Engineering  
*Georgia Institute of Technology*

Dr. Valeria Milam  
School of Materials Science and  
Engineering  
*Georgia Institute of Technology*

Dr. Alexander Alexeev  
School of Mechanical Engineering  
*Georgia Institute of Technology*

Dr. Zhiqun Lin  
School of Materials Science and  
Engineering  
*Georgia Institute of Technology*

Dr. Paul Russo  
School of Materials Science and  
Engineering  
*Georgia Institute of Technology*

Date Approved: October 21, 2015

*Dedicated to my loving family*

## ACKNOWLEDGEMENTS

First of all, I would like to thank my advisor Prof. Vladimir Tsukruk for his constant guidance, motivation and support, not only in my research projects but also in many other aspects of being a responsible, independent and diligent researcher. He gives me valuable trust and freedom to explore challenging scientific problems, the lessons and experiences I obtained from this process are valuable preparation for my future career.

Secondly, I would also like to thank all PhD dissertation committee members, Prof. Zhiqun Lin, Prof. Valeria Milam, Prof. Alexander Alexeev, and Prof. Paul Russo for their helpful discussion, feedback, and suggestions. I would also like to give special thanks to our close collaborators in this project, which include Prof. Axel Müller (Johannes Gutenberg University Mainz, Germany), Dr. Felix Plamper (RWTH Aachen University, Germany), Dr. Christopher Synatschke (Universitat Bayreuth, Germany), Prof. Constantinos Tsitsilianis (University of Patras, Greece), Prof. V. Shevchenko (National Academy of Sciences of Ukraine, Ukraine), and Prof. Krzysztof Matyjaszewski (Carnegie Mellon University). They are excellent polymer chemists and leaders in their fields; it is a great honor to have the chance to work with them. I also want to thank our collaborators in ORNL: Dr. Yuri Melnichenko and Dr. William Heller for the assistance with neutron scattering.

Also I would like to thank Dr. Petr Ledin, Dr. Ikjun Choi, Dr. Dhaval Kulkarni, Dr. Zachary Combs, Kesong Hu, Sidney Malak, Andrew Erwin, and other SEMA lab

members for their helpful discussion and technical assistance. The neutron scattering measurements were done at Oak Ridge National Laboratory, and we would like to thank DOE Office of Basic Energy Sciences, the Neutron Scattering Directorate at ORNL for the beam time. Funding for this work has been provided by the National Science Foundation.

Finally, I am deeply grateful to my parents and my wife Jie Zhou for their unconditional support and love, without which none of my accomplishments was possible.

# TABLE OF CONTENTS

<b>ACKNOWLEDGEMENTS</b>	<b>iv</b>
<b>LIST OF TABLES</b>	<b>x</b>
<b>LIST OF FIGURES</b>	<b>xi</b>
<b>LIST OF SYMBOLS AND ABBREVIATIONS</b>	<b>xxii</b>
<b>SUMMARY</b>	<b>xxiv</b>
<b>CHAPTER 1. INTRODUCTION</b>	<b>1</b>
1.1 General Background	1
1.2 Branched Polyelectrolytes and Their Physical Properties	2
1.3 Assembly of Branched Polyelectrolytes	7
1.3.1 Assembly of Cylindrical Polyelectrolyte Brushes	8
1.3.2 Assembly of Star Polyelectrolytes	12
1.3.3 Assembly of Hyperbranched Polyelectrolytes	16
1.3.4 Assembly of Polyelectrolyte Dendrimers	20
1.4 Emerging Applications	25
<b>CHAPTER 2. RESEARCH GOALS AND OVERVIEW</b>	<b>29</b>
2.1 Research Goals	29
2.2 Organization and Composition of Dissertation	35
<b>CHAPTER 3. EXPERIMENTAL TECHNIQUES</b>	<b>38</b>
3.1. Materials: Composition and Chemistry	38
3.1.1 Star and Linear Polyelectrolytes	38
3.1.2 Amphiphilic Star Block Copolymers	39
3.1.3 Miktoarm Star Polymers	41
3.2 Fabrication of Microstructures	42
3.2.1 Preparation of LB Monolayer Film	42
3.2.2 Preparation of LbL Thin Films	43
3.2.3 Preparation of LbL Microcapsules	44
3.3 Characterization of Solution and Microstructures	45
3.3.1 Characterization of Star Polymer Solution by SANS	45
3.3.2 Characterization of Thin Films and Microcapsules	46
<b>CHAPTER 4. SOLUTION PHASE BEHAVIORS OF RESPONSIVE STAR POLYELECTROLYTES</b>	<b>49</b>
4.1 Introduction	49
4.2 Experimental Section	52

4.3 Results	53
4.3.1 SANS Data Analysis Notes	53
4.3.2 Structure Study of PDMAEMA Stars in Semi-Dilute Solution	55
4.3.3 Thermo-Responsiveness of PDMAEMA Star Polyelectrolytes	66
4.3.4 Comparison with Linear PDMAEMA Polyelectrolytes	70
4.3.5 General Discussion	72
4.4 Conclusions	77
Appendix: Supporting Information	78
<b>CHAPTER 5. INTERFACIAL RESPONSIVE PROPERTIES AND ASSEMBLY OF STAR-GRAFT QUARTERPOLYMERS</b>	<b>87</b>
5.1 Introduction	87
5.2 Experimental Section	90
5.3 Results and Discussion	92
5.3.1 Molecular Structure and Solution Properties	92
5.3.2 Langmuir Monolayers: pH-Responsive Behaviors at the Air/Water Interface	95
5.3.3 Thermo-Responsive Behavior of Stars at Interfaces.	105
5.3.4 Effect of Graft Density and Arm Number on the Thermo-Responsive Behaviors	108
5.3.5 Effect of Ionic Strength and pH on the Thermo-Responsive Behavior.	110
5.4 Conclusions	113
Appendix: Supporting Information	114
<b>CHAPTER 6. pH- AND THERMO- DUAL RESPONSIVE MICROCAPSULES BASED ON PDMAEMA STAR POLYMERS</b>	<b>121</b>
6.1 Introduction	121
6.2 Experimental Section	124
6.3 Results and Discussion	126
6.3.1 Fabrication of LbL Microcapsules	126
6.3.2 Morphology of (PSS/PDMAEMA) <sub>n</sub> LbL Microcapsules	128
6.3.3 The Effects of Ionic Strength and Polymer Architecture on Microcapsule Behavior	132
6.3.4 pH-Response of (PSS/PDMAEMA <sub>18</sub> ) LbL Microcapsules	138
6.3.5 Temperature Response of (PSS/PDMAEMA <sub>18</sub> ) Microcapsules	144
6.3.6 SANS Study on the Structural Changes of Microcapsules	149
6.4 Conclusions	151
Appendix: Supporting Information	153

<b>CHAPTER 7. ION AND UV RESPONSIVE MICROCAPSELS BASED ON QPDMAEMA STAR POLYMERS</b>	<b>159</b>
7.1 Introduction	159
7.2 Experimental Section	163
7.3 Results and Discussion	165
7.3.1 Properties of qPDMAEMA Star Polyelectrolytes and the LbL Thin Films	165
7.3.2 Morphology of (PSS/ qPDMAEMA) <sub>n</sub> LbL Microcapsules	170
7.3.3 Controlled Permeability of (PSS/ qPDMAEMA) <sub>n</sub> Microcapsules	176
7.3.4 UV Triggered Release of (PSS/ qPDMAEMA) <sub>n</sub> Microcapsules	185
7.3.5 SANS Study on the Structural Changes of Microcapsules	189
7.4 Conclusions	195
Appendix: Supporting Information	197
<b>CHAPTER 8. MULTI-COMPARTMENTAL MICROCAPSULES WITH DUALCARRIER AND PROGRAMMABLE RELEASE CAPABILITIES</b>	<b>206</b>
8.1 Introduction	206
8.2 Experimental section	207
8.3 Results and Discussion	209
8.3.1 Properties of SG Polymers and the LbL Films	209
8.3.2 Morphology of the (TA/SG3) LbL Microcapsules	213
8.3.3 pH Controlled Permeability of Microcapsules	216
8.3.4 Temperature Controlled Release of Nile Red from the Shell	220
8.3.5 Programmable Encapsulation and Release Induced by pH and Temperature	222
8.4 Conclusions	224
Appendix: Supporting Information	226
<b>CHAPTER 9. POLYMERSOME BASED MULTI-COMPARTMENTAL MICROCAPSULES</b>	<b>228</b>
9.1 Introduction	228
9.2 Experimental section	230
9.3 Results and Discussion	232
9.3.1 Polymersome Formation via Electrostatic Interaction	232
9.3.2 Encapsulation of Rhodamine B Inside the Polymersomes	235
9.3.3 LbL Assembly of Polymersomes and TA	236
9.3.4 (TA/polymersome) LbL Microcapsules	237
9.3.5 Response to External Conditions and Multicompartmental Capability	239
9.4 Conclusions	243
<b>CHAPTER 10. GENREAL CONCLUSIONS AND BROAD IMPACT</b>	<b>245</b>

10.1 Summary of Major Results	245
10.2 Proposed Future Work and Applications	254
<b>REFERENCES</b>	<b>258</b>
<b>VITA</b>	<b>274</b>

## LIST OF TABLES

Table 1.1. Property summary of linear and branched polyelectrolytes with various architectures.	3
Table 3.1. Molecular Weight Averages (in g/mol) of PDMAEMA Stars Determined by Different Methods	39
Table 3.2 Characterization data of the $PS_n[P2VP-b-(PAA-g-PNIPAM)]_n$ heteroarm star-graft quarterpolymers.	41
Table 4.1. Structural parameters for PDMAEMA star polyelectrolytes and their quaternized salts with different number of arms or arm length, all units are in nm.	57
Table 4.2. Theoretical dimensions estimated for PDMAEMA star polyelectrolytes under different model assumptions, the unit is nm.	61
Table S5.1. Molecular characteristics of the $PS_n(P2VP-b-PAA)_n$ star block terpolymers	
Table 6.1. Permeability of $(PSS/PDMAEMA_{18})_n$ and $(PSS/PDMAEMA_1)_n$ microcapsules to FITC at different pH conditions (“+”: permeable, “-” not permeable).	114
Table 6.1. Permeability of $(PSS/PDMAEMA_{18})_n$ and $(PSS/PDMAEMA_1)_n$ microcapsules to FITC at different pH conditions (“+”: permeable, “-” not permeable).	139
Table 7.1. Permeability of $(PSS/qPDMAEMA_{18})_n$ capsules to FITC-dextran with different molecular weight (“+”: permeable, “-” not permeable).	177
Table 7.2. SANS fitting results for from $(PSS/qPDMAEMA_{18})_n$ microcapsules using Power-law model and DAB model. The first index indicates the number of arms of the star and the second one the number of bilayers. The salt added is $K_3Co(CN)_6$ .	192
Table 8.1. Permeability of $(TA/SG3)_6$ microcapsules to FITC-dextran with various molecular weights at different pH conditions (“+”: permeable, “-” not permeable, “+/-” partially permeable).	217
Table 9.1. Permeability of $(TA/polymersome)_5$ microcapsules to FITC-dextran with various molecular weights at different pH conditions (“+”: permeable, “-” not permeable, “+/-” partially permeable).	241

## LIST OF FIGURES

- Figure 1.1. Top: structure of major types of branched polyelectrolytes: (from left to right) cylindrical brushes, dendrimers, hyperbranched and star polyelectrolytes. Bottom: representative examples of assembled structures discussed in this chapter. 4
- Figure 1.2. Chemical structures of common types of (a) cationic and (b) anionic arms of branched polyelectrolytes. 5
- Figure 1.3. (a) Preparation of ion incorporated silica hybrid nanoparticles via template-directed assembly. (b) AFM images of the precursor CPB macromolecules. (c) TEM image of the  $\text{Ln}^{3+}$ -incorporated silica hybrid nanoparticles. 10
- Figure 1.4. (a) Schematic of morphology changes of cationic CPBs and corresponding AFM images (b, c, d) of the worm-like, pearl-necklace and spherical morphologies. 11
- Figure 1.5. (a) Schematics of the vesicles prepared from miktoarm stars with pH-responsive nanochannels. (b) AFM images of cross-linked vesicles. TEM images of the (c) unimolecular micelle, (d) multicore micelle, and (e) worm-like micelle from PS-(P2VP-*b*-PAA) stars. 14
- Figure 1.6. (a) Chemical structure of the HCPE. (b) TEM image of the HCPE nanoparticles. (c) CLSM image of labeled cancer cells. 19
- Figure 1.7. (a) Simulated dendrimer-linear chain complex. (b) TEM and (c) AFM of PSS/4G PAMAM microcapsules. 21
- Figure 1.8. *B. subtilis* cells encapsulated in 4 bilayer thin shells composed of branched silk polyelectrolytes via (a) electrostatic interaction, or (b) hydrogen bonding. Images on the right are confocal microscopy and SEM, respectively. 27
- Figure 3.1. Chemical structure of PDMAEMA star polyelectrolytes (left) and their quaternized salts (right). 39
- Figure 3.2. Schematic representation of the multi-step synthetic procedure that leads to  $A_n(B-C)_n$  heteroarm star block terpolymer. ‘\*’ denotes active sites. 40
- Figure 3.3. Chemical structures of  $\text{PEO}_{113}-(\text{qPDMAEMA}_x)_{4.1}$  miktoarm star polymers. 42
- Figure 3.4 Schematic of LbL assembly of a multilayer coating by sequential adsorption of oppositely charged polyelectrolytes. 44
- Figure 3.5. Schematic of the LbL assembly process on spherical template to fabricate hollow microcapsules. 45

Figure. 3.6. Schematic of the CG-2 SANS diffractometer at ORNL (image from ORNL website). 46

Figure 4.1. SANS data for solutions of PDMAEMA star polyelectrolytes with different number of arms or arm length (1 wt. % at pH 7.0 and 25 °C), the solid lines are fitting with core-shell model. The curves are mutually offset by a factor of 2 for better visualization. 57

Figure 4.2. Kratky plots (a) and pair distance distribution function (b) for PDMAEMA star polyelectrolytes with different number of arms or arm length. The data for linear PDMAEMA<sub>450</sub> are also shown for comparison. 59

Figure 4.3. Characteristic dimensions versus molecular weight for PDMAEMA star polyelectrolytes. From bottom to top:  $R_g$  from core-shell model,  $\nu=0.36\pm 0.02$ ;  $R_g$  from  $p(r)$  analysis,  $\nu=0.35\pm 0.03$ ;  $R_g$  from Kratky analysis,  $\nu=0.36\pm 0.02$ ; effective radius ( $R_{eff}$ ) from MSA structure factor; intermolecular distance (D) from peak position in SANS data. 61

Figure 4.4. The structural changes of PDMAEMA star polyelectrolytes and linear polyelectrolytes at pH around  $pK_a$  upon temperature increase. (For simplification, only one star macromolecule is shown before aggregation.) 64

Figure 4.5. (a) SANS data of quaternized PDMAEMA star polyelectrolytes solution (1 wt. % in D<sub>2</sub>O) with different number of arms or arm length. (b) Kratky plot for the corresponding quaternized PDMAEMA star polyelectrolytes. 66

Figure 4.6. SANS of (PDMAEMA<sub>170</sub>)<sub>18</sub> at pH 7.0 at increasing temperature, the curves are mutually offset by a factor of 1.5 for better visualization (temperature increases from bottom to top). The solid lines (from 25 °C to 45 °C) represent the fitting by core-shell model. (b) Temperature dependent dimension changes from core-shell model, Kratky model and pair distance distribution functions for (PDMAEMA<sub>170</sub>)<sub>18</sub> at pH 7.0. 68

Figure 4.7. SANS data of (PDMAEMA<sub>170</sub>)<sub>18</sub> at pH 5.5 with increasing temperature, the curves are mutually offset by a factor of 1.5 for better visualization (temperature increases from bottom to top). The solid lines (from 25 °C to 50 °C) represent the fitting by core-shell model. (b) Temperature dependent dimension changes from core-shell model, Kratky model and pair distance distribution functions for (PDMAEMA<sub>170</sub>)<sub>18</sub> at pH 5.5. 70

Figure 4.8. SANS data of PDMAEMA<sub>450</sub> at pH 7.0 (a) and pH 5.5 (b) with increasing temperature, the curves are mutually offset by a factor of 1.5 for better visualization (temperature increases from bottom to top). The solid lines are from the combined Ornstein-Zernike and DAB model fittings. 72

Figure S4.1. Kratky plot (a) and pair distance distribution function (b) for (PDMAEMA<sub>170</sub>)<sub>18</sub> star polyelectrolytes at pH 7.0 with increasing temperature. 83

Figure S4.2. Kratky plot (a) and pair distance distribution function (b) for (PDMAEMA<sub>170</sub>)<sub>18</sub> star polyelectrolytes at pH 5.5 with increasing temperature. 84

Figure S4.3. Fitting results from Ornstein-Zernike model and DAB model for PDMAEMA<sub>450</sub> linear polyelectrolytes at pH 7.0 and pH 5.5 with increasing temperature. The lines are just drawn to guide the eyes. 85

Figure S4.4. The changes of solution pH with increasing temperature for (PDMAEMA<sub>170</sub>)<sub>18</sub> and PDMAEMA<sub>450</sub> at a concentration of 1 wt %. The lines are just drawn to guide the eyes. 85

Figure S4.5. pH dependence with temperature for solutions of (PDMAEMA<sub>170</sub>)<sub>9,5</sub> (magenta), (PDMAEMA<sub>170</sub>)<sub>18</sub> (red) and (PDMAEMA<sub>240</sub>)<sub>24</sub> (green) in Millipore water (full lines; all 1.0 g/L; dashed lines: turbidity results). 86

Figure 5.1. (a) Molecular architecture and chemical composition of PS<sub>n</sub>[P2VP-*b*-(PAA-*g*-PNIPAM)]<sub>n</sub>. (b) Molecular models of one arm of the SG2, SG3 and SG4 stars (from top to bottom) in ideal random coil conformation, scale bar is 2 nm. (c) pH dependence of Zeta potential for 0.2 wt.% aqueous solutions of the star-graft quarterpolymers. 93

Figure 5.2. Pressure-area isotherms of SG3 (a) and SG4 (b) stars at 25 °C and different pH conditions (2.5, 5.5, and 8.5), and the subphase is 0.1 M NaCl solution. 96

Figure 5.3. (a) The change of MMA of SG3 and SG4 stars with pH, as well as SG2, SG3 and SG4 stars with increasing temperature (black: SG2, red: SG3, blue: SG4). (b) The change of MMA of SG3 at different pH conditions with increasing temperature (black: pH 2.5, red: pH 5.5, blue: pH 8.5), (c) the change of MMA of SG3 at different ionic conditions with increasing temperature (black: H<sub>2</sub>O, red: 0.1 M NaCl, blue: 0.3 M NaCl). The dash line is a guide for the eyes. 98

Figure 5.4. AFM topography (left) and phase (right) images of SG3 LB monolayer deposited at 25 °C and at 1 mN/m with different pH conditions: (a) pH = 2.5, (b) pH = 5.5, (c) pH = 8.5. The scale bar is 100 nm, Z range is 3 nm (topography) and 8° (phase). 100

Figure 5.5. Schematic of the molecular conformation of stars at air/water interface with different pH conditions (2.5, 5.5 and 8.5), as well as the structural changes of the stars upon increasing temperature. The top row corresponds to the top view, the middle two rows correspond to the side view of the stars at air/water interface, the bottom row represents the conformational change of the star during LB transfer. 102

Figure 5.6. The thickness (a) and the contact angle (b) changes of the SG3 LB monolayers at different pH, temperature and surface pressures. 104

Figure 5.7. Pressure-area isotherms of SG3 stars (a) at pH 5.5 with increasing temperature, (d) at pH 5.5 and different ionic conditions with increasing temperature. Pressure-area isotherms of SG2 (b) and SG4 (c) stars at pH 5.5 condition with increasing temperature. 106

Figure 5.8. (a-d) AFM images of SG3 LB monolayer deposited at pH 5.5 and different temperatures, (a, b) 1 mN/m, (c, d) 10 mN/m. (e-f) AFM images of SG2 LB monolayer film deposited at pH 5.5 and 1 mN/m. (g-h) AFM images of SG4 LB monolayer deposited at pH 5.5 at 1 mN/m. All the scale bars are 100 nm, Z range is 3 nm. Corresponding phase images and cross section analysis are shown in FigureS3. 107

Figure 5.9. (a-d) AFM images of SG3 LB monolayer deposited at pH 2.5 and different temperatures, (a, b) 1 mN/m, (c, d) 10 mN/m. (e-h) AFM images of SG3 LB monolayer deposited at pH 8.5 and different temperatures, (e, f) 1 mN/m, (g, h) 10 mN/m. All the scale bars are 100 nm, Z range is 3 nm. Corresponding phase images and cross section analysis are shown in FigureS8. 112

Figure S5.1. (a) Zeta potential as a function of pH of 0.2 wt% SG3 stars and their precursors without grafted PNIPAM chains, the marked region denotes the precipitation regime for the precursor stars. (b) Potentiometric titration of 0.1 wt% SG3 stars with dropwise addition of 0.1 M NaOH, the first derivative of the pH change with added NaOH volume is also shown. 115

Figure S5.2. Pressure-area isotherms of SG3 at 25 °C and pH 5.5, with multiple compression-expansion cycles. 116

Figure S5.3. (a-d) AFM phase images of SG3 LB monolayer film deposited at pH 5.5 and different temperatures: (a, b) SP = 1, (c, d) SP = 10. (e-f) AFM images of SG2 LB monolayer film deposited at pH 5.5 and SP = 1. (g-h) AFM images of SG4 LB monolayer film deposited at pH 5.5 and SP = 1. All the scale bars are 100 nm, Z range is 8° (SP = 1).or 15° (SP = 10). Cross section analysis of the corresponding height images are shown on the right column (black: 25 °C, red: 45 °C). 117

Figure S5.4. AFM images of SG3 LB monolayer film deposited at pH 5.5 and SP = 20 mN/m, at different temperatures: (a) 25 °C, (b) 35 °C, (c) 45 °C. Scale bar is 100 nm, Z range is 5 nm. 118

Figure S5.5. Pressure-area isotherms of  $PS_n(P2VP-b-PAA)_n$  star block terpolymers at pH 5.5 with increasing temperature. 118

Figure S5.6. Optical density of SG3 star solution (0.1 wt% and pH 5.5) with different ionic strength, the insert image is the SG3 star solution in 1.0 M NaCl. 119

Figure S5.7. Pressure-area isotherms of SG3 at pH 2.5 (a) and pH 8.5 conditions with increasing temperature. 119

Figure S5.8. (a-d) AFM images of SG3 LB monolayer film deposited at pH 2.5 and different temperatures: (a, b) SP = 1, (c, d) SP = 10. (e-h) AFM images of SG3 LB monolayer film deposited at pH 8.5 and different temperatures: (e, f) SP = 1, (g, h) SP = 10. All scale bars are 100 nm, Z range is 8°. Cross section analysis of the corresponding height images are shown on the right column (black: 25 °C, red: 45 °C). 120

Figure 6.1. (a) Chemical structure of PDMAEMA star polymers and (b) the assembly of (PSS/PDMAEMA<sub>18</sub>)<sub>n</sub> LbL microcapsules. 127

Figure 6.2.  $\zeta$ -potential as a function of number of layers during LbL assembly on silica microparticles with alternating (PSS/PDMAEMA<sub>18</sub>) bilayers. 128

Figure 6.3. SEM images of (PSS/PDMAEMA<sub>18</sub>)<sub>n</sub> microcapsules with different number of bilayers: (a, b) 5, (c, d) 8, (e, f) 11. 129

Figure 6.4. TEM images of (PSS/PDMAEMA<sub>18</sub>)<sub>11</sub> microcapsules, the scale bar is 2  $\mu$ m in (a) and 500 nm in (b). 129

Figure 6.5. AFM images of (PSS/PDMAEMA<sub>18</sub>)<sub>n</sub> microcapsule with 5 bilayer (a, b), 8 bilayer (c, d), 11 bilayer (e, f). Z range is 1500 nm (a, c, e) and 50 nm (b, d, f), scale bar is 1  $\mu$ m (a, c, e) and 100 nm (b, d, f). (g) The thickness comparison of microcapsules with different bilayer number. 130

Figure 6.6. CLSM images of (PSS/PDMAEMA<sub>18</sub>)<sub>n</sub> microcapsules prepared from salt solution with 5 bilayers (a), 8 bilayers (b), 11 bilayers (c), (PSS/PDMAEMA<sub>18</sub>)<sub>5</sub> prepared from water solution (d) exposed to FITC-dextran with  $M_w$  of 4 kDa at pH 5. Scale bar in each panel is 5  $\mu$ m. 134

Figure 6.7. Thickness of PSS/PDMAEMA LbL films as a function of number of bilayers, the dotted lines are fitting from linear or exponential model. 136

Figure 6.8. CLSM images of (PSS/PDMAEMA<sub>18</sub>)<sub>8</sub> (a) and (PSS/PDMAEMA<sub>1</sub>)<sub>8</sub> microcapsules (b) exposed to 0.5 M NaCl solution at pH=5 and FITC added. Permeability of (PSS/PDMAEMA<sub>18</sub>)<sub>8</sub> microcapsules in buffer (c) and in 0.5 M NaCl solution (d) to 4 kDa FITC-dextran, the inserts are the representative fluorescent intensity profile over the microcapsule. Scale bar in each panel is 5  $\mu$ m. 137

Figure 6.9. CLSM images of (PSS/PDMAEMA<sub>18</sub>)<sub>n</sub> microcapsules with 5 bilayers (a, b, c), 8 bilayers (d, e, f), 11 bilayers (g, h, i) exposed to FITC solutions at different pH conditions as labeled on each column. The insert in (a) and (c) is the representative fluorescent intensity profile over the microcapsule. Scale bar in each panel is 5  $\mu$ m. 139

Figure 6.10. The structural changes of the (PSS/PDMAEMA<sub>18</sub>) microcapsules to different external stimuli including ionic strength, pH and temperature. 141

Figure 6.11. SEM images of (PSS/PDMAEMA<sub>18</sub>)<sub>11</sub> microcapsules with different pH conditions: (a) pH=5, (b) pH=7, (c) pH=9. 142

Figure 6.12. (PSS/PDMAEMA<sub>18</sub>)<sub>8</sub> microcapsules encapsulation of FITC at pH 9 (a) and release at pH 7 (b); the second cycle of encapsulation and release (c, d). Scale bar is 5  $\mu\text{m}$  in all images. 144

Figure 6.13. (a) Fluorescence intensity of the dialysis bath which contains the FITC molecules permeate from the microcapsules, during the cooling of (PSS/PDMAEMA<sub>18</sub>)<sub>8</sub> microcapsules from 45  $^{\circ}\text{C}$  to 20  $^{\circ}\text{C}$ . (b) Reversibility of the thermo-responsive encapsulation and release as indicated by fluorescence intensity of the dialysis bath. 146

Figure 6.14. Size and morphology changes of (PSS/PDMAEMA<sub>18</sub>)<sub>5</sub> microcapsules with increase of temperature as shown by AFM images. Scale bar is 3  $\mu\text{m}$  for top row, and 1  $\mu\text{m}$  for bottom row, Z range is 500 nm for 20  $^{\circ}\text{C}$  and 40  $^{\circ}\text{C}$  images, 2000 nm for 60  $^{\circ}\text{C}$  images. 148

Figure 6.15 (a) SANS data of (PSS/PDMAEMA<sub>18</sub>)<sub>n</sub> microcapsules with 5 and 8 bilayers at 25  $^{\circ}\text{C}$  and pH 7 condition, solid curves are fitting from lamellar model. (b) SANS curves of (PSS/PDMAEMA<sub>18</sub>)<sub>5</sub> microcapsules at pH 7 condition with increasing temperature, solid curves are fitting from DAB model (25-40  $^{\circ}\text{C}$ ) and lamellar model (45  $^{\circ}\text{C}$ ). The curves are mutually offset by a factor of 2 for better visualization. 149

Figure S6.1. AFM images of PDMAEMA<sub>18</sub> star polyelectrolytes (a, b) and PDMAEMA<sub>1</sub> linear polyelectrolytes (c, d). Scale bar is 1  $\mu\text{m}$  (a, c) and 100 nm (b, d), Z range is 5 nm. 153

Figure S6.2. (a-b) AFM images of (PSS/PDMAEMA<sub>1</sub>)<sub>5</sub> microcapsule, (c-d) AFM images of (PSS/PDMAEMA<sub>1</sub>)<sub>8</sub> microcapsule, (e-f) AFM images of (PSS/PDMAEMA<sub>18</sub>)<sub>11</sub> microcapsule; scale bar is 1  $\mu\text{m}$  (left column) and 200 nm (right column), Z range is 400 nm (left column) and 50 nm (right column). 154

Figure S6.3. CLSM images of (PSS/PDMAEMA<sub>18</sub>)<sub>5</sub> microcapsules fabricated from water solution exposed to FITC-dextran solutions with different molecular weight (a) 70 kDa, (b) 150 kDa, (c) 250 kDa, at pH 5 condition. Scale bar is 5  $\mu\text{m}$ . 155

Figure S6.4. AFM images of (PSS/PDMAEMA<sub>18</sub>)<sub>11</sub> LbL films (a, b) and (PSS/PDMAEMA<sub>1</sub>)<sub>11</sub> LbL films (c, d). The scale bar is 2  $\mu\text{m}$  (left column) and 200 nm (right column), Z range is 30 nm (left column) and 20 nm (right column). 155

Figure S6.5. CLSM images of (PSS/PDMAEMA<sub>1</sub>)<sub>n</sub> microcapsules with 5 bilayers (a, b, c), 8 bilayers (d, e, f), 11 bilayers (g, h, i) exposed to FITC solutions at different pH conditions. Scale bar in each panel is 5  $\mu\text{m}$ . 156

Figure S6.6. CLSM images of (PSS/PDMAEMA<sub>18</sub>)<sub>8</sub> (a, b) and (PSS/PDMAEMA<sub>1</sub>)<sub>8</sub> microcapsules (c, d) exposed to FITC solutions with pH 1 and pH 3. Scale bar is 5 μm.

157

Figure S6.7. CLSM images of (PSS/PDMAEMA<sub>18</sub>)<sub>8</sub> (a, b) and (PSS/PDMAEMA<sub>1</sub>)<sub>8</sub> microcapsules (c, d) exposed to FITC solutions with pH 10 and pH 11. Scale bar is 5 μm.

158

Figure S6.8. Fluorescence intensity of the dialysis bath which contains the FITC molecules permeate from the microcapsules, during the cooling of (PSS/PDMAEMA<sub>18</sub>)<sub>8</sub> microcapsules from 45 °C to 20 °C at pH 6 condition.

158

Figure 7.1. (a) Chemical structure of qPDMAEMA star polyelectrolyte, (b) structural change of qPDMAEMA after adding K<sub>3</sub>Co(CN)<sub>6</sub> and during the photochemical reaction.

166

Figure 7.2. (a-c) AFM images of (PSS/qPDMAEMA<sub>18</sub>)<sub>5</sub> film, (d-f) AFM images of (PSS/qPDMAEMA<sub>18</sub>)<sub>8</sub> film, (g-i) AFM images of (PSS/qPDMAEMA<sub>18</sub>)<sub>11</sub> film; (c, f, i) are phase images. Z-scale is 30nm for topography images, and 30° for phase images.

167

Figure 7.3. (a) Thickness of (PSS/qPDMAEMA<sub>18</sub>)<sub>n</sub> films as a function of bilayer number as measured by ellipsometry. (b) UV-Vis spectra of (PSS/qPDMAEMA<sub>18</sub>)<sub>n</sub> films with different number of layers assembled on quartz substrate. Inset shows the intensity increase of peak at 227 nm with bilayer number.

168

Figure 7.4. (a-c) AFM images of (PSS/qPDMAEMA<sub>5,6</sub>)<sub>5</sub> film, (d-f) AFM images of (PSS/qPDMAEMA<sub>5,6</sub>)<sub>8</sub> film, (g-i) AFM images of (PSS/qPDMAEMA<sub>5,6</sub>)<sub>11</sub> film; (c, f, i) are phase images. Z-scale is 30nm for topography images, and 30° for phase images.

169

Figure 7.5. LbL assembly on silica core and fabrication of (PSS/qPDMAEMA)<sub>n</sub> hollow microcapsule.

170

Figure 7.6. Zeta (ζ)-potential as a function of bilayer number during LbL coating of silica particles with alternating (PSS/ qPDMAEMA<sub>18</sub>) bilayers.

171

Figure 7.7. SEM images of (PSS/qPDMAEMA<sub>18</sub>)<sub>11</sub> (a) and (PSS/qPDMAEMA<sub>5,6</sub>)<sub>11</sub> (b) microcapsules.

172

Figure 7.8. (a) Comparison of thickness of (PSS/qPDMAEMA<sub>18</sub>)<sub>n</sub> with (PSS/qPDMAEMA<sub>5,6</sub>)<sub>n</sub> for both microcapsules and films. (b) Comparison of microroughness of (PSS/qPDMAEMA<sub>18</sub>)<sub>n</sub> and (PSS/qPDMAEMA<sub>5,6</sub>)<sub>n</sub> for microcapsules and films.

173

Figure 7.9. (a-c) AFM images of (PSS/qPDMAEMA<sub>18</sub>)<sub>5</sub> microcapsule, (d-f) AFM images of (PSS/qPDMAEMA<sub>18</sub>)<sub>8</sub> microcapsule, (g-i) AFM images of (PSS/qPDMAEMA<sub>18</sub>)<sub>11</sub>

microcapsule; (c, f, i) are phase images. Z-scale is 200 nm for topography images, and 80° for phase images. 174

Figure 7.10. (a-c) AFM images of (PSS/qPDMAEMA<sub>5,6</sub>)<sub>5</sub> microcapsule, (d-f) AFM images of (PSS/qPDMAEMA<sub>5,6</sub>)<sub>8</sub> microcapsule, (g-i) AFM images of (PSS/qPDMAEMA<sub>5,6</sub>)<sub>11</sub> microcapsule; (c, f, i) are phase images. Z-scale is 200 nm for topography images, and 80° for phase images. 176

Figure 7.11. Confocal images of (PSS/qPDMAEMA<sub>18</sub>)<sub>11</sub> microcapsules exposed to FITC (a), and FITC-dextran solutions with M<sub>w</sub> of 2000 kDa (b), 500 kDa (c), 70 kDa (d). After adding 0.8 mM K<sub>3</sub>Co(CN)<sub>6</sub>, (PSS/qPDMAEMA<sub>18</sub>)<sub>11</sub> microcapsules exposed FITC-dextran solutions with M<sub>w</sub> of 500 kDa (e), 70 kDa (f). Scale bar is 2 μm. 179

Figure 7.12. Permeability of (PSS/qPDMAEMA<sub>18</sub>)<sub>8</sub> microcapsules to 500 kDa FITC-dextran after adding K<sub>3</sub>Co(CN)<sub>6</sub>: (a) without K<sub>3</sub>Co(CN)<sub>6</sub>, (b) 0.08 mM, (c) 0.8 mM, (d) 4 mM of K<sub>3</sub>Co(CN)<sub>6</sub>. Scale bar is 5 μm. 181

Figure 7.13. Responsive behavior of (PSS/qPDMAEMA<sub>18</sub>)<sub>n</sub> microcapsules to multivalent salt and UV irradiation. 184

Figure 7.14. Permeability of (PSS/qPDMAEMA<sub>18</sub>)<sub>8</sub> microcapsules to 500 kDa FITC-dextran, (a) after adding 0.8 mM K<sub>3</sub>Co(CN)<sub>6</sub>, (b) add 0.8 mM K<sub>3</sub>Co(CN)<sub>6</sub>, then irradiate by UV for 45 min, (c) encapsulation of 500 kDa FITC-dextran by adding 0.8 mM K<sub>3</sub>Co(CN)<sub>6</sub>, (d) release of FITC-dextran by 45 min UV irradiation. 186

Figure 7.15. Encapsulation efficiency (defined by the ratio of average fluorescence intensity of microcapsule interior before and after removing surrounding dye) *versus* repeatable UV irradiation cycles. 188

Figure 7.16. SANS data of PSS/qPDMAEMA<sub>18</sub> microcapsules with (square) 5 bilayers, (circle) 8 bilayers, and (triangle) 11 bilayers in D<sub>2</sub>O solution (at 25 °C) that have been fitted with a power law model (a, solid lines) to determine the evolution of the fractal dimension, and Debye-Anderson-Brumberger (DAB) model (b, solid lines) to obtain the correlation length. 190

Figure. 7.17. SANS data of (PSS/qPDMAEMA<sub>18</sub>)<sub>8</sub> and (PSS/qPDMAEMA<sub>18</sub>)<sub>11</sub> microcapsules before and after adding 0.8 mM K<sub>3</sub>Co(CN)<sub>6</sub> (at 25 °C); solids lines are fitting by the power law model, the two curves for (PSS/qPDMAEMA<sub>18</sub>)<sub>8</sub> were shifted upward for clarity. 194

Figure S7.1. (a) Thickness of (PSS/qPDMAEMA<sub>5,6</sub>)<sub>n</sub> films as a function of bilayer number as measured by ellipsometry. (b) UV-Vis spectra of (PSS/qPDMAEMA<sub>5,6</sub>)<sub>n</sub> films with different number of layers assembled on quartz substrate. Inset shows the intensity increase of peak at 227 nm with bilayer number. 197

- Figure S7.2. (a, b) SEM images of (PSS/qPDMAEMA<sub>18</sub>)<sub>5</sub> microcapsules, (c, d) SEM images of (PSS/qPDMAEMA<sub>18</sub>)<sub>8</sub> microcapsules. 198
- Figure S7.3. (a, b) SEM images of (PSS/qPDMAEMA<sub>5,6</sub>)<sub>5</sub> microcapsules, (c, d) SEM images of (PSS/qPDMAEMA<sub>5,6</sub>)<sub>8</sub> microcapsules. 198
- Figure S7.4. (a) SEM images of (PSS/qPDMAEMA<sub>18</sub>)<sub>11</sub> microcapsules, (b) SEM images of (PSS/qPDMAEMA<sub>5,6</sub>)<sub>11</sub> microcapsules. 199
- Figure S7.5. Confocal images of (PSS/qPDMAEMA<sub>18</sub>)<sub>5</sub> microcapsules exposed to FITC (a), and FITC-dextran solutions with Mw of 2000 kDa (b), 500 kDa (c), 70 kDa (d). After adding 0.8 mM K<sub>3</sub>Co(CN)<sub>6</sub>, (PSS/qPDMAEMA<sub>18</sub>)<sub>5</sub> microcapsules exposed FITC-dextran solutions with Mw of 500 kDa (e), 70 kDa (f). Scale bar is 2 μm. 200
- Figure S7.6. Confocal images of (PSS/qPDMAEMA<sub>18</sub>)<sub>8</sub> microcapsules exposed to FITC (a), and FITC-dextran solutions with Mw of 2000 kDa (b), 70 kDa (c). After adding 0.8 mM K<sub>3</sub>Co(CN)<sub>6</sub>, (PSS/qPDMAEMA<sub>18</sub>)<sub>8</sub> microcapsules exposed FITC-dextran solutions with Mw of 70 kDa (d). Scale bar is 2 μm. 201
- Figure S7.7. Confocal microscopy images of (PSS/qPDMAEMA<sub>5,6</sub>)<sub>n</sub> microcapsules in aqueous solution with different number of layers, (a) 5 bilayers, (b) 8 bilayers, (c) 11 bilayers. Scale bar is 2 μm. 201
- Figure S7.8. (PSS/PAH)<sub>5</sub> microcapsules with FITC labeled shell (a) before and (b) after 45 min UV irradiation. Confocal images of (PSS/PAH)<sub>5</sub> microcapsules exposed to 500 kDa FITC-dextran solution (c) before and (d) after 45 min UV irradiation. 203
- Figure S7.9. Confocal microscopy images of (PSS/qPDMAEMA<sub>18</sub>)<sub>8</sub> microcapsules for five cycles of encapsulation and releasing by adding trivalent salt and UV irradiation. (a, b) second cycle, (c, d) third cycle, (e, f) fourth cycle, (g, h) fifth cycle. Scale bar is 5 μm. 204
- Figure S7.10. AFM images of (PSS/qPDMAEMA<sub>18</sub>)<sub>8</sub> capsules before (a) and after (b) adding 0.8 mM K<sub>3</sub>Co(CN)<sub>6</sub>, (c) UV irradiation for 45 min after adding K<sub>3</sub>Co(CN)<sub>6</sub>. Z-scale is 300 nm. 204
- Figure S7.10. AFM images of (PSS/qPDMAEMA<sub>18</sub>)<sub>8</sub> capsules before (a) and after (b) adding 0.8 mM K<sub>3</sub>Co(CN)<sub>6</sub>, (c) UV irradiation for 45 min after adding K<sub>3</sub>Co(CN)<sub>6</sub>. Z-scale is 300 nm. 205
- Figure 8.1. Chemical structure of the (a) SG polymers and (b) tannic acid. 210
- Figure 8.2. Thickness increase with the number of bilayers for (TA/SG)<sub>n</sub> LbL thin films. 212
- Figure 8.3. AFM images of the (a, b) (TA/SG<sub>2</sub>)<sub>15</sub>, (c, d) (TA/SG<sub>2</sub>)<sub>15</sub>, (e, f) (TA/SG<sub>2</sub>)<sub>15</sub> LbL films, the scale bar is 1 μm on the left column, and 100 nm on the right column; the Z range is 200 nm on the left column and 100 nm on the right column. 213

Figure 8.4. (a) Scheme of the LbL fabrication process of (TA/SG3) microcapsules, (b)  $\zeta$ -potential as a function of number of layers during LbL assembly on silica microparticles.

214

Figure 8.5. AFM images of (TA/SG3)<sub>6</sub> microcapsules after drying; Z range is 800 nm in (a) and 500 nm in (b).

215

Figure 8.6. SEM images of (TA/SG3)<sub>6</sub> microcapsules at (a) low and (b) high magnification.

215

Figure 8.7. Permeability of (TA/SG3)<sub>6</sub> microcapsules at different pH condition to 70K FITC-dextran (a, b, c) and 150 K FITC-dextran (d, e, f), the inserts are the representative fluorescent intensity profile over the microcapsule, the scale bar is 5  $\mu$ m.

217

Figure 8.8. The structural changes of the (TA/SG3)<sub>6</sub> microcapsules at different pH conditions, blue curve represents the TA layer.

218

Figure 8.9. (a) UV-Vis spectra of Nile Red in methanol (black) and SG3 with encapsulated Nile Red (red), (b) fluorescence spectra of Nile Red in methanol (black) and SG3 with encapsulated Nile Red (red).

221

Figure 8.10. (a) CLSM images of (TA/SG3)<sub>6</sub> microcapsules with encapsulated Nile Red in the shell, (b) CLSM images of the same sample after heating to 45°C for 15 min, (c) transmission mode image of the same area with b. Scale bar is 5  $\mu$ m.

221

Figure 8.11. (a) CLSM images of the (TA/SG3)<sub>6</sub> microcapsules with encapsulated Nile Red in the shell and FITC-dextran inside the microcapsules, (b) red channel and (c) green channel of the same area in the same sample. (d) (TA/SG3)<sub>6</sub> microcapsules with encapsulated Nile Red and FITC-dextran, (e) release of Nile Red by increasing temperature, (f) subsequent release of FITC-dextran by decrease pH from 7 to 5. The inserts are the representative fluorescent intensity profile over the microcapsule. Scale bar is 5  $\mu$ m.

223

Figure 8.12. Schematic illustration of the programmable encapsulation and release of Nile Red and FITC-dextran from the shell and core region, triggered by temperature and pH change, respectively.

224

Figure S8.1. CLSM images of (TA/SG3)<sub>6</sub> microcapsules at (a) pH 3, (b) pH 5 and (c) pH 7 conditions, and the solution are colored due to FITC addition.

226

Figure S8.2. Zeta potential of SG polymers at different pH conditions, the shaded area indicates the isoelectric region.

226

Figure S8.3. Permeability of (TA/SG3-NR)<sub>6</sub> microcapsules at different pH condition to 20K FITC-dextran (a, b, c) and 70 K FITC-dextran (d, e, f), the inserts are the

- representative fluorescent intensity profile over the microcapsule, the scale bar is 5  $\mu\text{m}$ . 227
- Figure 9.1. Chemical structures of (a)  $\text{PEO}_{113}\text{-(qPDMAEMA}_{60})_{4.1}$  miktoarm star polymer and (b) tannic acid. 230
- Figure 9.2. (a) Formation of polymersomes by mixing cationic miktoarm stars and anionic linear polyelectrolytes. (b) Scheme of the LbL fabrication process of (TA/polymersome) microcapsules. 233
- Figure 9.3. (a) Cryo-TEM image of the polymersomes with the particle diameter histogram, (b) Intensity-weighted size distribution as obtained by DLS (CONTIN;  $60^\circ$ ;  $\lambda = 633 \text{ nm}$ ); insets: extraction of the average hydrodynamic radius  $R_h$  (decay rate  $\Gamma$ , obtained by cumulant analysis, against squared length of scattering vector  $q$ ) and the radius of gyration  $R_g$  (Guinier plot). 234
- Figure 9.4. AFM images of the polymersomes (a, b), and polymersomes with encapsulated Rhodamine b (c, d) in dry state. Z range is 40 nm, and scale bar is 500 nm (a, c), and 100 nm (b, d). 234
- Figure 9.5. UV-Vis (a) and fluorescence (b) spectra of the polymersomes before and after rhodamine B incorporation. 235
- Figure 9.6. (a) Thickness increase with the number of bilayers for  $(\text{TA/polymersome})_n$  LbL thin films, (b)  $\zeta$ -potential as a function of number of layers during LbL assembly on silica microparticles. 236
- Figure 9.7. AFM images of the (a, b)  $(\text{TA/polymersome})_{16}$  LbL films, (c, d)  $(\text{TA/polymersome})_5$  LbL microcapsules. Z range is 300 nm (a, c) and 150 nm (b, d). 237
- Figure 9.8. CLSM images of the  $(\text{TA/polymersome})_5$  (a) and  $(\text{TA/polymersome})_8$  (b) microcapsules, (c, d) green and red channel of the same sample as in b. Scale bar is 5  $\mu\text{m}$ . 238
- Figure 9.9. Permeability of  $(\text{TA/polymersome})_5$  microcapsules at different pH conditions to 70K FITC-dextran, the scale bar is 5  $\mu\text{m}$ . 238
- Figure 9.9. Permeability of  $(\text{TA/polymersome})_5$  microcapsules at different pH conditions to 70K FITC-dextran, the scale bar is 5  $\mu\text{m}$ . 240
- Figure 9.10. CLSM image so the multicomparmental  $(\text{TA/polymersome})_5$  and  $(\text{TA/polymersome})_5$  microcapsules with rhodamine B encapsulated within the polymersomes. Scale bar is 5  $\mu\text{m}$ . 243

## LIST OF SYMBOLS AND ABBREVIATIONS

$\xi$	Correlation Length
$C^*$	Overlap Concentration
$v$	Excluded Volume Parameter
$R_g$	Radius of Gyration
ATRP	Atom Transfer Radical Polymerization
AFM	Atomic Force Microscopy
CLSM	Confocal Laser Scanning Microscopy
CMC	Critical Micelle Concentration
CPB	Cylindrical Polyelectrolyte Brushes
DAB	Debye-Anderson-Brumberger
FITC	Fluorescein Isothiocyanate
HCPE	Hyperbranched Conjugated Polyelectrolyte
IPEC	Interpolyelectrolyte Complex
LB	Langmuir-Blodgett
LbL	Layer-by-Layer
LCST	Low Critical Solution Temperature
MSA	Mean Spherical Approximation
MWNT	Multi-Walled Nanotube
P2VP	Poly(2-vinyl pyridine)
PAA	Poly(acrylic acid)
PAH	Poly(allylamine hydrochloride)
PAMAM	Polyamidoamine
PDMAEMA	Poly2-(dimethylamino)ethyl methacrylate
PE	Polyelectrolyte
PEG	Poly(ethylene glycol)
PEI	Poly(ethylene imine)
PMMA	Poly(methyl methacrylate)
PNIPAM	Poly(N-isopropylacrylamide)
POSS	Polyhedral Oligomeric Silsesquioxane

PS	Polystyrene
PSS	Poly(styrene sulfonate)
PtBA	Poly( <i>tert</i> -butyl acrylate)
RMS	Root Mean Square
SANS	Small Angle Neutron Scattering
SDS	Sodium Dodecylsulfate
SEM	Scanning Electron Microscopy
TA	Tannic acid
TEM	Transmission Electron Microscopy

## SUMMARY

Responsive polymeric nanostructures have attracted much attention in recent years due to their abilities to adapt and respond to external stimuli, and potential applications in bio-sensing, self-healing coatings, drug delivery, tunable catalysis, and bio-imaging. Star polymers have emerged as novel building blocks for such assembled structures due to their unique architectures and multiple responsive properties. A challenging task in this field is how to precisely control the interactions between star polymers and with other components, and maintain the responsive properties of the functional stars in the assembled nanostructures. Therefore, the goal of the proposed work is to understand the responsive properties and interactions of star polymers in different conditions, including solution and interfaces, and utilize them as building blocks for polymeric micro- and nano-structures such as polymersomes, ultrathin films and microcapsules, which have intriguing properties in terms of stability, responsiveness and functionalities compared with conventional linear polymers based structures.

Specifically, in the first place, we studied the solution phase behavior of responsive star polymers by using *in situ* (small angle neutron scattering) SANS, and showed that in semidilute solution, the temperature induced phase separation for thermo-responsive star polymers are significantly different from that of their linear counterparts. The star polymers show limited microphase separation with aggregates composed of several molecules, while the corresponding linear polymers have LSCT (low critical solution temperature) type phase separation.

Secondly, we studied the responsive properties and assembly of amphiphilic star polymers at the air/water interface and in Langmuir-Blodgett monolayer. We found that the confined interface environment leads to different conformational changes and assembly behaviors of the star polymers compared with those in solution state. For instance, when there is a hydrophilic to hydrophobic transition, the polymers tend to go from water subphase to the air/water interface, rather than showing coil to globule transition in aqueous solution.

Thirdly, we utilized the star polymers as major component to fabricate 3D responsive microstructures such as thin shell microcapsules, by using layer-by-layer (LbL) assembly technique, which has rarely been explored before, especially for complex star block copolymers. The assembly microcapsules have hierarchical multicompartmental structure, which enables the encapsulation and release of multiple molecules simultaneously. The shell of the multilayer microcapsules has porous 3D network structure, with fine controlled permeability.

Lastly, for star polymers with multiple responsive properties, we found that their responsiveness is well maintained after being assembled into microstructures, so that the microcapsules have multiple responsive properties. The multiple responses in structure and permeability to external stimuli enable the controlled and programmable delivery of multiple cargo molecules, such as those we demonstrated in this study: microcapsules with pH and temperature dual responsiveness, as well as ionic conditions and UV dual responsive properties.

# CHAPTER 1. INTRODUCTION

## 1.1 General Background

Research activities in the field of branched polymers, centered around designing new architectures, resulted in the appearance of a wide spectrum of novel highly branched molecules including dendrimers, star block copolymers, branched brushes, hyperbranched molecules, and different combinations of branched and linear fragments (dendronized rods, discs, and stems).<sup>1</sup> The critical role of chemical architecture has been demonstrated by comparing dendritic or branched structures to linear polymers.<sup>1,2</sup> Currently, the focus of the research has somewhat shifted from synthetic efforts towards a deeper understanding of the physical properties and structures of these molecules particularly at surfaces and interfaces. An understanding of the behavior of branched polymers at engineered surfaces and interfaces is ultimately beneficial for optimum designs in smart coatings, microreactors, self-healing materials, drug delivery vehicles, and high-performance nanocomposites.<sup>3,4,5</sup>

The molecular shape, size, and properties of branched polymers can be varied as a function of the degree of branching and type/length of branched segments. Intriguing molecular characteristics, such as abundant functional end groups, globular shape, core-shell morphology and highly dense chain structure can offer a new platform for a supramolecular building component of surface science and engineering for assemblies of dynamically stable unimolecular micelles, core/shell type nanoparticles, and nanogels.

On the other hand, highly-branched polymers can also offer an active multi-functional surface and interface in a responsive/predictable manner.<sup>6</sup> Due to the high degree of free end groups and flexible side branches, more diverse conformational transformation and interactions by external stimuli (e.g. pH, temperature, and shear) enable tunable micro and nanoscale assemblies and ordering for the design of multifunctional stimuli-responsive and adaptive thin films and coatings.<sup>7</sup>

## **1.2 Branched Polyelectrolytes and Their Physical Properties**

Majority of previous work on branched polymers focused on traditional neutral polymers, while charged branched polymers or branched polyelectrolytes have not been thoroughly studied so far. Polyelectrolytes (PE) are polymers with ionizable groups in their backbones or side chains, and usually effectively charged in solution due to ionic dissociation controlled by ionic and pH conditions. Due to the dramatic asymmetry in charge, mass, and size between the long polyelectrolyte backbones and the counterions, co-ions, and solvent molecules in solution, polyelectrolytes have rich and significantly different phase behavior compared to conventional neutral macromolecules.<sup>8</sup> Extended chain conformations, a significantly lower critical concentration, and a higher osmotic pressure in solution are examples of those signature differences.<sup>9</sup> The structure and properties of linear polyelectrolytes have been extensively studied during the past several decades,<sup>10</sup> but the understanding of the properties of branched polyelectrolytes with complex chain architectures is still inadequate, especially for complex conditions such as the presence of heterogeneous surfaces and interfaces.

Table 1.1. Property summary of linear and branched polyelectrolytes with various architectures.

Name	Architecture	Synthesis	Properties	Representative examples
Linear PEs	Flexible/semi-flexible linear backbone	Step or chain polymerization, post functionalization	Wide variety of amorphous, crystalline, and LC polymers and electrolytes	8,22,11
Cylindrical PE brushes	a flexible backbone and many grafted shorter side chains	grafting through, grafting to, and grafting from	Large size, low entanglement, lower CMC, rheological modifiers,	58,59,61, 63,67
Star PEs	a central core and multiple polyelectrolyte arms	Core first or arm first method, click chemistry	Lower viscosity, lower crystallinity degree, higher CMC and lower aggregation number	58,74, 80,88, 12
Hyperbranched PEs	random branched polyelectrolyte chains	Step-growth polycondensation, self-condensing, ring-opening polymerization	Lower viscosity, flexible composition and degree of branching, enhanced solubility.	92,93,97, 100,102,13
Dendrimer PEs	A central core with several generations of branches	divergent and convergent growth approach, click chemistry	uniform composition and structure, controlled crystallinity and chirality, Dendritic encapsulation	107,113,116, 14,15,16

Recent advances in polymer chemistry allow the synthesis of a variety of branched polyelectrolytes with well-defined architectures such as cylindrical brushes,<sup>17</sup> dendritic molecules,<sup>18</sup> hyperbranched polymers,<sup>19</sup> pearl-necklace structures,<sup>20</sup> and star block copolymers,<sup>21</sup> with different novel classes of materials introduced continuously (Figure 1.1, Table 1.1). The synthesis, structures, morphologies, and prospective applications of well-known cationic polyelectrolytes have been recently covered by Laschewsky et. al.<sup>22</sup> Water-soluble macromolecular co-assemblies of star-shaped polyelectrolytes with classical ionic groups were reviewed by Müller et al.<sup>23</sup> Various hyperbranched materials and their assemblies at interfaces have been reviewed by Peleshanko et al.<sup>24</sup>

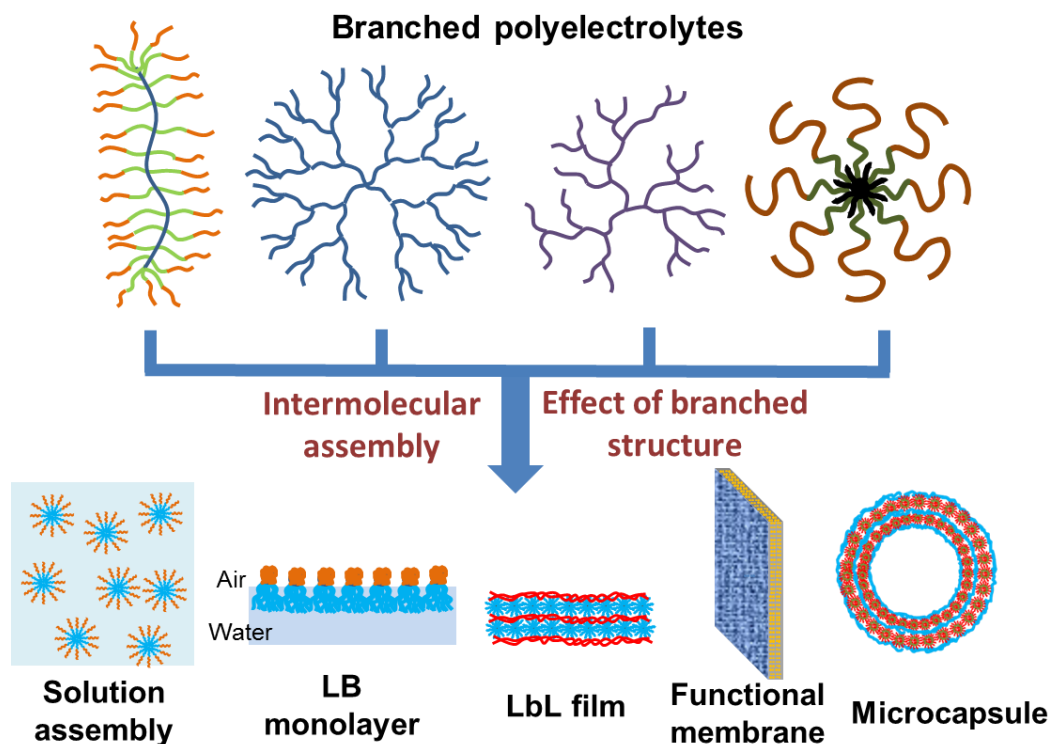


Figure 1.1. Top: structure of major types of branched polyelectrolytes: (from left to right) cylindrical brushes, dendrimers, hyperbranched and star polyelectrolytes. Bottom: representative examples of assembled structures discussed in this chapter.

The chemical structures of common types of cationic and anionic polyelectrolytes are shown in Figure 1.2. Highly branched polyelectrolytes with a low level of entanglements possess novel physical properties when compared with their linear counterparts.<sup>25,26</sup> Star polyelectrolytes frequently show peculiar phase behavior due to a complex balance of intra- and intermolecular interactions.<sup>27, 28, 29, 30</sup> For instance, they have a strong counterion confinement ability, resulting in a high osmotic pressure (caused by the presence of counterions) within the branched polyelectrolytes, which leads to the strong extension of the arms at certain conditions. The branched polyelectrolytes can also be divided into strong and weak polyelectrolytes depending on their ionization ability, both of which can be stimuli-responsive to ionic strength or pH.

## Building Blocks of Conventional Branched Polyelectrolytes

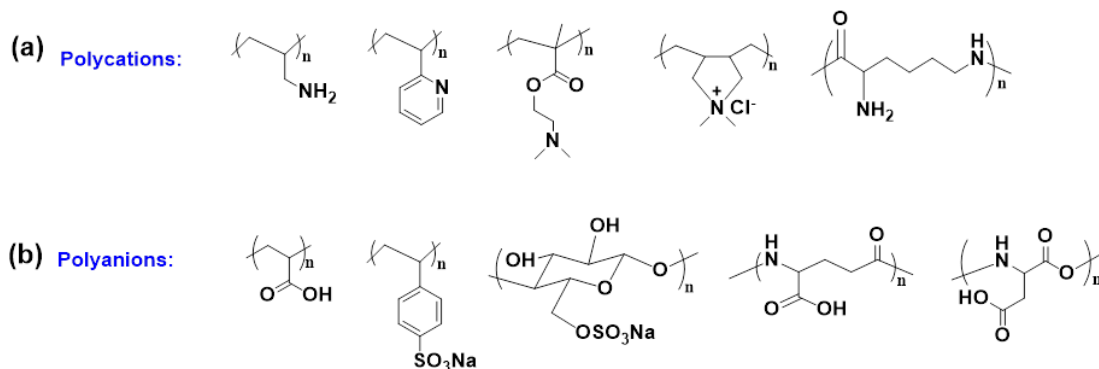


Figure 1.2. Chemical structures of common types of (a) cationic and (b) anionic arms of branched polyelectrolytes.

The crossover from a dilute to a semi-dilute solution regime for polyelectrolytes occurs at much lower polymer concentrations than for solutions of neutral chains.<sup>31</sup> It has been demonstrated that solutions of weak polyelectrolytes exhibit a microphase separation upon a decrease in the solvent quality below the  $\theta$ -point.<sup>32</sup> At appropriate thermodynamic conditions, the system has a tendency to form limited clusters, although true macrophase separation may be inhibited. The most influential factors include counterion concentration and valency, pH, and temperature. Khokhlov et al.<sup>33</sup> showed that for partially charged weak polyelectrolytes, the counterions can be easily transferred between repeating units and from one chain to another, which facilitates phase separation in solution.

Theoretical studies have shown that for star polyelectrolytes, in addition to the steric repulsion, there is a relatively short-range attraction and a secondary repulsive barrier at longer distances.<sup>34</sup> The conformation of spherical polyelectrolyte brushes<sup>35</sup> and star

polyelectrolytes<sup>36</sup> is very sensitive to the ionic condition; for instance, the addition of multivalent ions leads to a collapse in which the surface layer or the arms shrink drastically. The ion exchange and a strong binding of multivalent ions by polyelectrolyte chains is followed by a drop in osmotic pressure inside the brush, which is the driving force for the collapse.<sup>37</sup> Molecular dynamics simulations have shown that the collapse of star polyelectrolytes also depends on the arm number. At a low number of arms, pearl-necklace structures are formed on individual arms. On the other hand, at a higher number of arms, inter-arm bundling is the dominant structural motif.<sup>38</sup>

For polyelectrolyte dendrimers, a theoretical study by Likos et al.<sup>39</sup> showed that Coulombic interactions lead to an increase in size of dendrimer polyelectrolytes due to a combined effect of electrostatic repulsion and the presence of counterions. The bond length between monomers near the center will increase to facilitate a more effective usage of the space in the outer regions of dendrimers. There are also tunable and ultrasoft intermolecular interactions between the centers of the dendrimers. Another study on poly(propyleneimine) dendrimer solutions<sup>40</sup> showed that there is a certain degree of spatial arrangement or a liquid-like ordering in acidic conditions due to electrostatic repulsion with larger-scale intermolecular assemblies in the solution. An increase in the salt concentration in the solution induces a decrease in intermolecular correlations.

Likos et al.<sup>41</sup> studied the complexation behavior of oppositely charged colloidal particles and polyelectrolyte stars with a molecular dynamics approach. The results indicated that

besides electrostatic interactions, entropy controls the adsorption of the stars on a colloidal surface. The functionality of the stars has a significant influence on the adsorption process: higher functionality stars will not adsorb with all their arms anchored on the surface because of the Coulomb interactions between the arms. The maximum load of the PE stars clearly depends on all quantities, i.e. functionality, the length of the arms, and the overall charge of the PE-stars as well as the size and charge of the colloidal particles. Larson et al.<sup>42</sup> used molecular dynamics simulations to show that there are strong interactions of cationic dendrimers with lipid bilayers, resulting in pore formation on the bilayers. On the contrary, linear cationic polyelectrolytes cannot perforate the lipid bilayer because of their deformation into a pancake morphology. Other developments in theory and simulations of the assembly of linear and branched polyelectrolytes have been summarized in several reviews.<sup>43,44</sup>

### **1.3 Assembly of Branched Polyelectrolytes**

Biomacromolecules, such as proteins, nucleic acids and polysaccharides, have high concentrations of ionizable groups and are generally included in the class of polyelectrolytes. Self-assembled structures of those biopolymers play a critical role in biology; for example, the bacterial cell surface is decorated with branched polysaccharides, which can mediate the cell adhesion.<sup>45</sup> Moreover, self-assemblies of biomacromolecules can respond to external stimuli in a sophisticated way, which directly affects biological functions. Synthetic branched polyelectrolytes are close in structure to biomacromolecules, and therefore the self-assembly of branched polyelectrolytes provides an excellent model case for cell biology studies.<sup>46</sup>

Due to the presence of abundant functional terminal groups and tree-like architectures, the assembly of branched polyelectrolytes can occur in various complex ways.<sup>47,48,49</sup> The driving forces for the assembly include covalent-bonding, hydrophobic interactions, hydrogen bonding, electrostatic interactions, charge-transfer interactions, host-guest interactions, and coordination chemistry.<sup>50</sup> The assembled structures also have various morphologies in different states including core-shell particles, capsules, micelles, thin films, and microgels (Figure 1.1).<sup>51,52,53</sup> Nanoarchitectonics is a rising concept in nanomaterials science,<sup>54,55</sup> which refers to the manipulation of nanoscale structural units in an intended configuration.<sup>56</sup> To this end, branched polyelectrolytes can be used for designing advanced materials for device applications.<sup>57</sup>

### **1.3.1 Assembly of Cylindrical Polyelectrolyte Brushes**

Cylindrical polyelectrolyte brushes (CPBs) are composed of a flexible backbone and a large number of shorter grafted side chains which are ionizable (Figure 1.1).<sup>58</sup> The unusual architecture of CPBs gives them some unique properties such as large dimensions of macromolecules, a low entanglement extent, and a lower critical micelle concentration (CMC).<sup>59</sup> Amphiphilic CPBs are able to self-assemble into complex micellar structures in solution, the main difference compared with micelles from linear block copolymer being that the CPB-based micelles are usually larger in size and bear various surface functionalities.

For example, Wooley et al.<sup>60</sup> synthesized heterografted diblock CPBs via a “grafting through” strategy, with one-half of the size chains as PAA and the other half as PS.

When dialyzed against water from DMF solution, which is a good solvent for both types of side chains, the CPBs self-assemble into spherical micelles with an average hydrodynamic diameter of 48 nm and an aggregation number of 60. Another report from the same group<sup>61</sup> showed that CPBs with PS-b-PMA-b-PAA triblock copolymer side chains are able to self-assemble into cylindrical nanostructures when transferred from DMF to water. Such assembly is also reversible by heating or changing the solvent. In another example, CPBs with a polystyrene tail and a cylindrical brush block with poly(acrylic acid) (PAA) side chains were observed to form star-like micelles comprised of four to five macromolecules.<sup>62</sup>

Additionally, the polyelectrolyte chains of CPBs can be used to selectively bind with metal ions to fabricate functional hybrid nanostructures. To this end, Müller et al.<sup>63</sup> synthesized core-shell CPBs with poly(acrylic acid)-block-poly2-(dimethylamino)ethyl methacrylate (PAA-b-PDMAEMA) side chains and used the CPBs as a template for the preparation of rare-earth metal cations incorporated into hybrid nanoparticles, as shown in Figure 1.3. Several different kinds of rare-earth cations ( $Tb^{3+}$ ,  $Eu^{3+}$ ,  $Gd^{3+}$ ) can be incorporated into the PAA block due to the tight chelation; the deposition and cross-linking of tetramethyl orthosilicate on the PDMAEMA blocks result in a stable silica nanoshell.

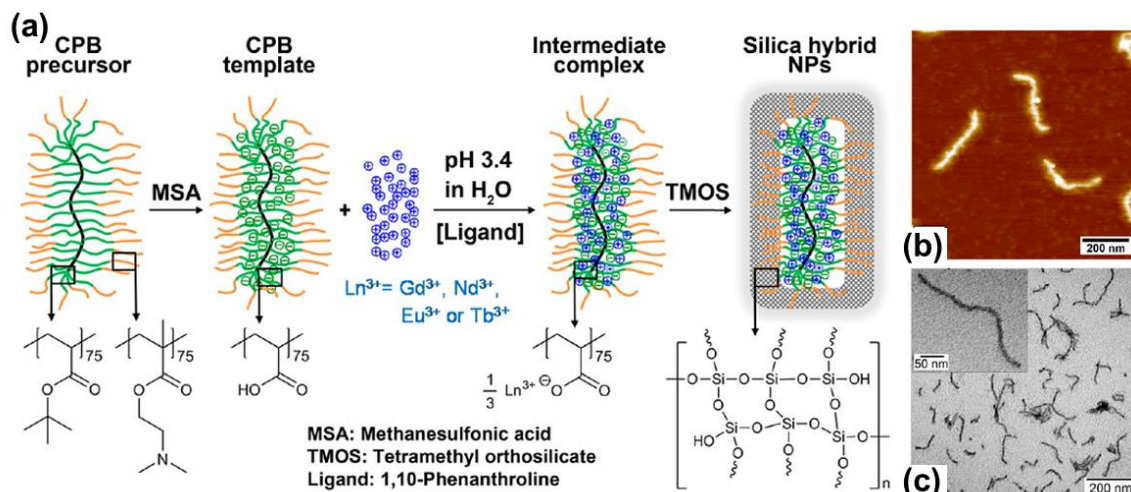


Figure 1.3. (a) Preparation of ion incorporated silica hybrid nanoparticles via template-directed assembly. (b) AFM images of the precursor CPB macromolecules. (c) TEM image of the  $\text{Ln}^{3+}$ -incorporated silica hybrid nanoparticles. Reproduced with permission from reference 63, copyright (2013) American Chemical Society.

It has been found that in a dilute solution, CPBs interact with oppositely charged polyelectrolytes through ion pair formation to form well-defined and stable colloidal nano-assemblies or interpolyelectrolyte complexes (IPECs).<sup>64,65</sup> Molecular dynamics simulations showed that the nano-assemblies adopt pearl necklace morphologies comprised of CPB monomers and the guest polyelectrolyte monomers in an approximately stoichiometric ratio.<sup>66</sup> AFM imaging confirmed such novel complex morphologies on surfaces as well.<sup>67</sup> Furthermore, for IPEC complexes formed by poly{2-(methacryloyloxy)ethyl trimethylammonium iodide} (qPDMAEMA) CPBs and linear poly(styrene sulfonate) (PSS), the morphology can be tuned from worm-like micelles to intermediate pearl-necklace structures and eventually into fully collapsed spheres by increasing the percentage of PSS chains (Figure 1.4). Furthermore, the length of the linear PSS chains also has a significant effect on the complexation phenomenon.<sup>68</sup>

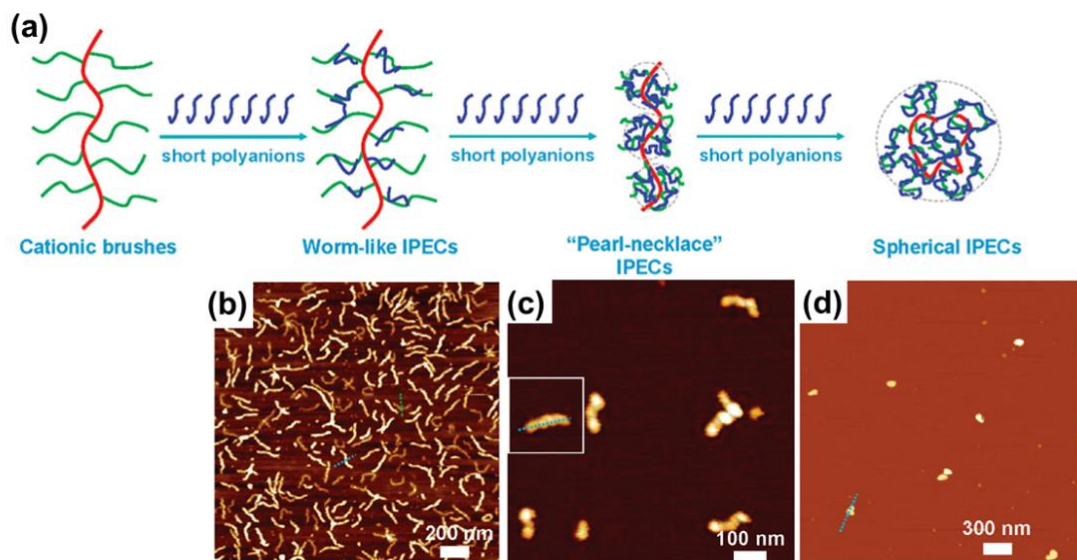


Figure 1.4. (a) Schematic of morphology changes of cationic CPBs and corresponding AFM images (b, c, d) of the worm-like, pearl-necklace and spherical morphologies. Reproduced with permission from reference 68, copyright (2010) American Chemical Society.

CPBs were also used to form complexes with DNA molecules in solution, and the results showed that their complexes coexist with the excess uncomplexed component.<sup>69</sup> Inter-complex bridging with eventual phase separation was observed if the number of complexes became comparable to the number of free molecules. Not only can CPBs interact with large oppositely charged polyelectrolytes to form different kinds of assemblies, they can also interact with smaller counterions in an interesting way. For example, the tetravalent cationic porphyrin binds to the PSS CPBs due to electrostatic and secondary  $\pi$ - $\pi$  interactions.<sup>70</sup> CPB macromolecules can be further interconnected into nanoscale networks. The variable interactions of CPBs with different counterions might lead to various tunable structures. For instance, when interacting with tetravalent double-DABCO (1,4-diazabicyclo2.2.2octane)-based counterions, the PSS CPBs experience a conformational change from worm-like to highly curled structures with an

increasing counterion concentration.<sup>71</sup> Above the charge stoichiometry, the CPBs become interconnected and form stable finite assemblies, which consist of the molecular brushes in curled (bent) conformations.

It has been shown that CPBs with poly(L-lysine) side chains and sodium dodecylsulfate (SDS) can form complexes with intriguing structures.<sup>72</sup> An increasing amount of SDS initiates the complex transformation to a helical conformation with a local  $\beta$ -sheet structure on the side chains, followed by a spherically collapsed structure formation. Further study showed that the surfactant size, ionic conditions, and environmental pH all have significant influence on the shape and size of the supramolecular structures.<sup>73</sup> For example, only surfactants with certain alkyl chain lengths can promote the formation of stable helical complexes with poly(L-lysine)-based CPBs.<sup>73</sup> High ionic strength and acidic or basic pH conditions lead to the disappearance of the helical supramolecular structure.

### **1.3.2 Assembly of Star Polyelectrolytes**

Among different categories of branched polyelectrolytes, star polyelectrolytes constitute a particularly intriguing class of macromolecules with high relevance in soft matter physics, chemistry, and materials science.<sup>74</sup> Star-shaped polyelectrolytes can be considered as branched systems with a well-defined composition and dimensionality of arms, which are relevant to novel colloidal soft nanoparticles with core-shell morphologies.<sup>75,76</sup> Because of their star architecture, these macromolecules show distinct micellar aggregation in bulk, solution, and at interfaces. For instance, star polymers

show a critical micellar concentration which is a few orders of magnitude higher than that of linear counterparts, and the association number is significantly lower than that observed for linear counterparts.<sup>77,78,79</sup>

Star polyelectrolytes with asymmetrical arms can self-assemble in solution to form various novel nanostructures; they are also stimuli-responsive, and their morphology changes dramatically with variable external conditions such as ionic condition, pH or temperature. A recent report by Liu et al.<sup>80</sup> showed that a miktoarm copolymer consisting of 1 PtBA, 1 poly(2-cinnamoyloxyethyl methacrylate) (PCEMA), and an average 1.14 poly(ethylene oxide) (PEO) chains can form vesicles with PtBA cylinders permeating the wall made of PCEMA, yielding unprecedented nanocapsules bearing regularly packed nanochannels (Figure 1.5 a, b). A study on various star polyelectrolyte networks composed of hydrophilic DMAEMA and hydrophobic MMA monomers, with identical topology but different molecular buildups, showed significant differences in structure when swollen with water.<sup>81</sup> Small angle neutron scattering (SANS) measurements showed that for the homopolymer and random copolymer star networks, only relatively small structural units were observed. However, for the heteroarm co-networks, the presence of well-defined hydrophobic domains were observed, indicating pronounced microphase separation in these systems.

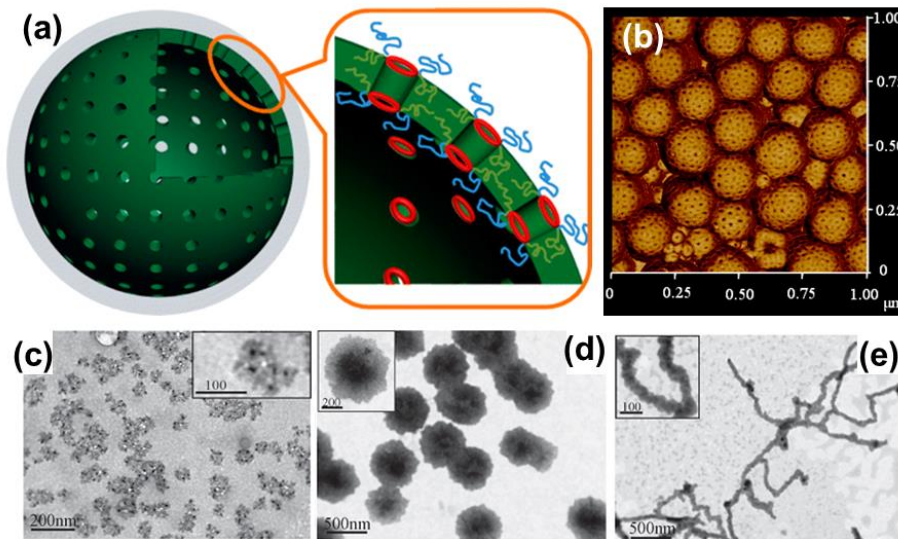


Figure 1.5. (a) Schematics of the vesicles prepared from miktoarm stars with pH-responsive nanochannels. (b) AFM images of cross-linked vesicles. TEM images of the (c) unimolecular micelle, (d) multicore micelle, and (e) worm-like micelle from PS-(P2VP-*b*-PAA) stars. Reproduced with permission from references 80 and 82, copyright (2011) Royal Society of Chemistry, (2014) American Chemical Society.

In another study, Tsitsilianis et al.<sup>82</sup> reported the self-assembly of star terpolymer bearing PS hydrophobic arms and P2VP-*b*-PAA diblock copolymer amphoteric arms in aqueous media. A variety of amphoteric assemblies were observed at different pH conditions of the medium. For instance, below the isoelectric point, the stars can assemble into core-shell unimolecular micelles, worm-like micelles, or multicore large compound micelles (Figure 1.5 c, d, e). Above the isoelectric point, multi-star aggregates, network-like large assemblies, and finally patchy compartmentalized micelles were formed. The authors further demonstrated that the heteroarm stars (PS<sub>22</sub>(P2VP-*b*-PAA)<sub>22</sub>) can be used as an effective dispersing agent for multiwalled carbon nanotubes (MWCNT) in aqueous media, leading to stable MWCNT-star nanohybrids in water with pH responsive properties.<sup>83</sup>

Amphiphilic star polyelectrolytes can further be used at the air-water interface to form monolayers, which can be transferred to a solid substrate using LB technique. For instance, the interfacial assembly of  $PS_nP2VP_n$  and  $PS_n(P2VP-b-PtBA)_n$  star polymers has been recently studied.<sup>84</sup> This study showed that the surface morphology of  $PS_nP2VP_n$  stars strongly depends on subphase conditions. At a low pH, the stars form large circular micelles, which readily transform to labyrinth morphology upon further compression. On the other hand, the  $PS_n(P2VP-b-PtBA)_n$  stars with hydrophobic end blocks maintain a circular, unimolecular micelle morphology at different surface pressures.<sup>85</sup>

In another report,<sup>86</sup> the pH-responsive properties of Langmuir monolayers from  $PS_n(P2VP-b-PAA)_n$  stars were studied at the air-water interface.<sup>87</sup> Star polymers with a small number of arms possess a more pronounced pH-dependent morphology, changing from circular micelles to labyrinth morphology upon monolayer compression. However, star polymers with a larger number of arms possess a stable circular micelle morphology under various pH conditions due to limited interpenetration and suppressed entanglement. A study by Sheiko et al.<sup>88</sup> showed that the phase behavior of branched polymers mixture at the air-water interface is significantly different from that of linear polymers. By taking advantage of the steric repulsion between branched polymers, long-range arrays of perfectly mixed macromolecules with a variety of polymer morphologies have been realized.

Due to the multiple functionalities of star polyelectrolytes, they have been regarded as promising building blocks for functionalized microstructures.<sup>89</sup> For example, Hammond

et al.<sup>90</sup> fabricated nanoporous films from cationic PDMAEMA stars and anionic PAA stars via LbL assembly. The monolayers underwent extensive structural reorganization upon post-fabrication treatment under different pH conditions in contrast to the unchanged morphology observed for their linear counterparts. Finally, Qiao et al.<sup>91</sup> demonstrated that highly ordered, porous honeycomb films can be prepared by the breath-figure technique using dendron-functionalized star polymers as precursors.

### **1.3.3 Assembly of Hyperbranched Polyelectrolytes**

Hyperbranched polyelectrolytes belong to a class of branched macromolecules with random branched polyelectrolyte chains.<sup>92</sup> The interesting physical properties of hyperbranched polyelectrolytes include enhanced solubility and lower viscosity compared with their linear counterparts.<sup>93</sup> The large number of functional groups and chain ends make hyperbranched polyelectrolytes easy to interact with each other. It has been shown that amphiphilic hyperbranched polyelectrolytes with amine groups in the core region and alkyl tails in the shell can self-assemble into nanofibrillar micellar structures at the air-water surface and form nanofibers in the course of crystallization from solution.<sup>94</sup> The monolayer of hyperbranched copolymer was also demonstrated as a potential scaffold for the synthesis of silver nanoparticles.<sup>95</sup> The coupled constraints of the air-liquid interface and the unique morphology of the multifunctional hyperbranched polymer controlled the growth of silver nanoparticles with dimensions of 2-4 nm.

Due to their abundant functional groups, hyperbranched polyelectrolytes have been used to change the surface properties of various nanostructures. The unique globular structures

of the hyperbranched macromolecules offer new possibilities to control phase transitions by the variation of the molecular weight instead of changing the chemical nature of the surface polymer layer. For instance, thermosensitive hyperbranched polyglycerols modified with NIPAM groups were used to coat water-soluble gold nanoparticles through non-covalent bonding, giving rise to soft nanoparticles with readily controllable LCSTs in a very broad temperature range.<sup>96</sup>

In another study, hyperbranched polyethyleneimine was immobilized on the surface of multi-walled nanotubes (MWNTs) via electrostatic interactions between the positively charged protonated amines within the polymer and the carboxyl groups on the chemically oxidized MWNT surface.<sup>97</sup> The branched polyelectrolyte not only provides many sites for the location of protein but also effectively reduces the lateral repulsion of protein species within the adsorbed layer. The new material designed in this study as a biosorbent for the adsorption of proteins provides better selectivity for the adsorption of BSA over the oxidized MWNTs and the MWNTs functionalized by the linear polyelectrolyte.

Hyperbranched polyelectrolytes can also be used to form complexes with oppositely charged polyelectrolytes, nanoparticles, or small molecules. For example, hyperbranched polylysine was used to interact with various anionic sodium alkyl sulfate surfactants electrostatically.<sup>98</sup> The hyperbranched polylysine-surfactant complexes were found to form liquid crystalline (LC) mesophases, and their thermal stability and structure depended both on the molecular weight of the polylysine as well as on the nature of the

anionic surfactant. The LC hyperbranches showed thermotropic behavior and underwent crystal-nematic and nematic-isotropic transitions upon an increase in temperature.

Another important category of hyperbranched polyelectrolytes is hyperbranched conjugated polyelectrolytes (HCPEs), introduced as novel optical, electronic and magnetic materials.<sup>99</sup> These materials exhibit good solubility and excellent processability. The hyperbranched structure is advantageous because of low viscosity, reduced aggregation, high solubility, and photostability as compared to linear conjugated polymers. These materials exhibit a tunable emission color and may be advantageous for disrupted inter- and intramolecular charge-transfer.<sup>100</sup>

For instance, Liu et al.<sup>101</sup> designed and synthesized fluorescent HCPE with a unique core-shell structure for cell imaging. Hyperbranched cationic polyfluorene located in the core region served as a stable light-emitting center, and linear poly(ethylene glycol) (PEG) covering the periphery of the HCPE passivated the macromolecular surface while also providing good cytocompatibility (Figure 1.6). Because of the shape persistence of the rigid core, the HCPE macromolecules form single-molecular nanospheres that facilitate the uptake process for cell imaging.

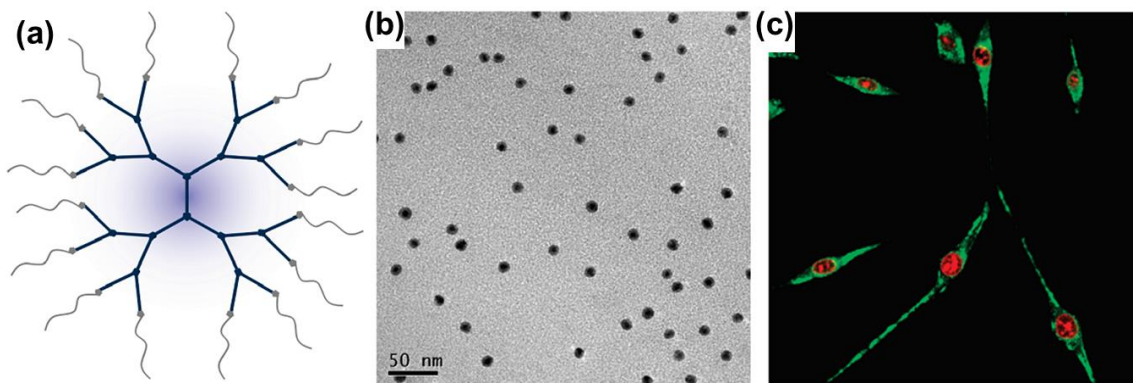


Figure 1.6. (a) Chemical structure of the HCPE. (b) TEM image of the HCPE nanoparticles. (c) CLSM image of labeled cancer cells. Reproduced with permission from reference 101, copyright (2009) American Chemical Society.

HCPE can also interact with oppositely charged metal ions in a selective way for highly sensitive sensing applications. For instance, a series of hyperbranched cationic conjugated polyelectrolytes containing different amounts of phosphorescent Ir(III) complex have been designed and synthesized.<sup>102</sup> These complexes can self-assemble into nanoparticles in aqueous solution with sizes around 100 nm. The energy transfer processes from the host polyfluorene to the guest Ir(III) complex have been observed, and the authors suggested that the hyperbranched polyelectrolytes can be used as light-up heparin probes with good selectivity and high sensitivity. In another example, water-soluble hyperbranched polyfluorenes bearing carboxylate side chains have been synthesized for selective ion interactions.<sup>103</sup> Indeed, the hyperbranched polyelectrolytes with a lower branch unit content (2%) showed excellent solubility and higher fluorescence quantum yield than their linear counterparts. Fluorescence quenching of the hyperbranched polyelectrolytes by different metal ions was also investigated, and they showed high selectivity and sensitivity to  $\text{Hg}^{2+}$  and  $\text{Cu}^{2+}$  ions.

Moreover, HCPEs with oppositely charged segments can interact to form multilayer hybrid structures. For example, Reynolds et al.<sup>104</sup> reported the synthesis of hyperbranched conjugated polyelectrolytes and their self-assembly and application in ionic materials for sensitizing TiO<sub>2</sub> solar cells. The ionic interactions of oppositely charged hyperbranched conjugated polyelectrolytes resulted in an increased chromophore concentration and a resulting enhanced optical density. These changes facilitated efficient light harvesting, which can be of interest for enhanced energy transport and efficient charge migration in hybrid solar cells.

#### **1.3.4 Assembly of Polyelectrolyte Dendrimers**

Polyelectrolyte dendrimers can be used as functionalized building blocks for the fabrication of functional microstructures from different components.<sup>105, 106</sup> The interactions of dendrimers with a linear polymer have been studied both theoretically and experimentally. Gurtovenko et al.<sup>107</sup> used dynamics simulations to investigate the role of electrostatic interactions in molecular complexes comprised of cationic dendrimer polyamidoamine (PAMAM) with oppositely charged linear polyelectrolytes (Figure 1.7 a). Their simulation showed that the complexation leads to a remarkable condensation of the tightly interacted components.

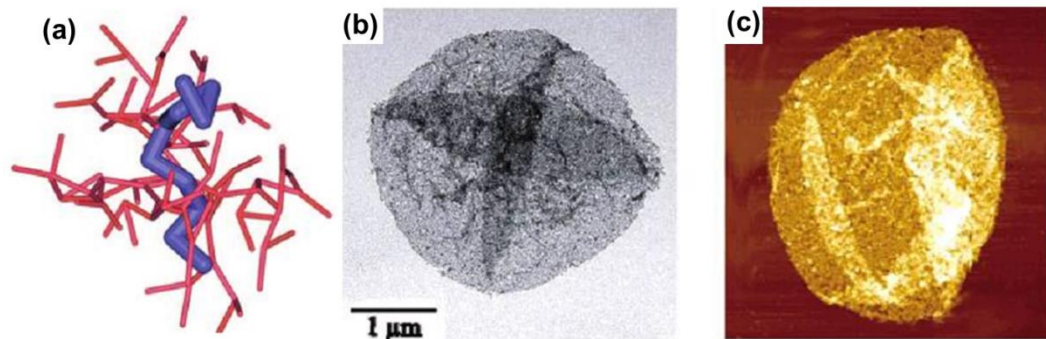


Figure 1.7. (a) Simulated dendrimer-linear chain complex. (b) TEM and (c) AFM of PSS/4G PAMAM microcapsules. Reproduced with permission from references 107 and 116, copyright (2002, 2008) American Chemical Society.

Furthermore, the formation of the molecular complexes results in a considerable dehydration of the chain, which becomes more pronounced when the electrostatic interactions strengthen. Thus, polyelectrolyte dendrimers clearly demonstrate the ability for efficient compaction of guest linear chains and protective screening of the chains from the surrounding medium. A theoretical study by Muthukumar et al.<sup>108</sup> showed that depending on the solution ionic strength and the sizes of the dendrimer and linear chain, their complex can have three different confined conformations: a dendrimer may encapsulate a chain, a chain and a dendrimer may mutually interpenetrate, or a unique “chain-walking” phenomenon (a dendrimer can walk along a longer linear chain) may occur. Thus, it is important to compare the relative size of the target molecules when using dendrimers in controlled delivery.

The PAMAM dendrimer is the most intensively studied type, because of the easy synthesis, low polydispersity and commercial availability.<sup>109, 110</sup> The PAMAM dendrimers are usually positively charged at low pH due to the protonation of amine groups.<sup>111</sup> They can also be transformed to neutral or anionic dendrimers by partial or

complete modification of the dendrimer periphery with neutral or negatively charged groups,<sup>112</sup> which helps lessen the cytotoxicity of PAMAM dendrimers in drug delivery applications.<sup>113</sup>

The assembly of PAMAM dendrimers on oppositely charged latex particles has recently been studied.<sup>114</sup> The results showed that varying the dendrimer content results in the charge changing from negative to positive values through the isoelectric point (IEP). The most intense aggregation was observed near the IEP. The effect of surface charge heterogeneities becomes important for higher dendrimer generations. The adsorption of PAMAM dendrimers onto mica surfaces was investigated as a function of ionic strength, pH, and dendrimer generation.<sup>115</sup> The adsorption was found to follow a diffusion-limited aggregation with formation of nanopatterned surfaces.

PAMAM dendrimers have been used to build multilayer structures via electrostatic interactions. For instance, Caruso et al.<sup>116</sup> fabricated multilayered polyelectrolyte/dendrimer films and microcapsules by using fourth-generation PAMAM dendrimers and linear PSS via LbL deposition (Figure 1.7 b, c). The dendrimer-based ultrathin films and microcapsules can serve as nanoreservoirs for the uptake and release of various compounds. Furthermore, the same group<sup>117</sup> showed that the stability of such microcapsules can be improved by increasing inter- and intra-molecular attractive forces between the PSS chains in the capsules through electrostatic interactions, hydrophobic interactions, and a combination of these.<sup>118</sup> In another report,<sup>119</sup> the surface-modified PSS/4G PAMAM LbL films were assembled through cross-linking and covalent grafting

with fatty-alkyl chains. Subsequently, PEG chains were adsorbed on the dendrimer film surface. Colloid particles coated with the modified LbL films showed reduced adhesion to biological cells.

In another example, *N,N*-disubstituted hydrazine phosphorus-containing dendrimers were used as components to build multilayer microcapsules with oppositely charged polyelectrolytes (PSS or PAH) via electrostatic interaction.<sup>120</sup> The results showed that the dendrimer-based microcapsules were much softer than microcapsules created from conventional linear polyelectrolytes. The softening of these shells is attributed to an enhanced permeability of the polyelectrolyte/dendrimer multilayer shells because the phosphorus-containing dendrimers exhibit a hydrophobic core interior and a hydrophilic charged surface so that the electrostatic interactions and complexation with PSS can take only place at peripheral regions. Using a similar method, the same group also prepared biocompatible DNA/phosphorous dendrimer multilayer microcapsules with potential applications in controlled drug delivery.<sup>121</sup>

PAMAM dendrimers have also been used to fabricate multilayer films and as tailored nanoreactors for the synthesis of metal nanoparticles. For instance, Li et al.<sup>122</sup> prepared LbL thin films with a third-generation PAMAM dendrimer and linear components, PSS or PAA. Furthermore, they grew silver nanoparticles within the films from a corresponding salt solution. The composite multilayer thin films with embedded nanoparticles have a strong negative redox potential with potential applications in catalysis. Similarly, gold nanoparticles were prepared *in situ* inside LbL films comprised

of PAMAM dendrimers and PSS,<sup>123</sup> and there is a 20 nm bathochromic shift in the absorption of the film compared with Au-dendrimer nanocomposites in aqueous solution. Palladium nanoparticles were also prepared within the interior of PAMAM dendrimers. The dendrimer-encapsulated catalysts were used to hydrogenate allyl alcohol and  $\alpha$ -substituted derivatives.<sup>124</sup> LbL films based on PAMAM dendrimers can also be used as a gas-permeable membrane, which show much higher gas flux than similar LbL films from linear polyelectrolytes.<sup>125</sup>

Besides ionic pairing, dendrimers can also be assembled with other molecules via hydrogen bonding. For instance, Zhang et al.<sup>126</sup> reported that carboxyl-terminated polyether dendrimers can be used to fabricate LbL films with linear PVP through hydrogen bonding. By post-formation treatment, the smooth LbL films experience a dramatic structural change from a uniform morphology to a film with a microporous morphology. It was proposed that the partial dissolution of polyether dendrimers and re-adsorption from the multilayer interior and surface into the basic solution and the gradual reconfiguration of linear PVP polymer chains are responsible for the reconfiguration of the initial uniform films.

Multilayered films can also be built from two kinds of oppositely charged dendrimers of different generations.<sup>127</sup> Electrostatic LbL ultrathin films were fabricated from adjacent generation PAMAM dendrimers with surface amine groups and carboxylic groups. As reported, the average thickness of an individual molecular layer in these multilayer films is much smaller than the expected diameter of the ideal spherical dendritic

macromolecules shaped as spherical soft nanoparticles. Therefore, it has been suggested that the self-assembled dendrimers assume a compressed, oblate shape with the axial ratio in the range from 1:3 to 1:6. The high interfacial interaction strength between “sticky” surface groups along with short-range van der Waals forces and long-range capillary forces are considered to be responsible for the formation of compacted multilayer structures.

#### **1.4 Emerging Applications**

Highly branched architectures bring many fundamental differences to the physical and chemical properties and assembly behavior of macromolecules with a high density of inner and terminal ionizable groups compared to conventional linear macromolecules. Recent efforts were focused on the synthesis and characterization of the branched polyelectrolytes for the understanding of their fundamental behavior from a viewpoint of traditional structure-property relationships. In recent years due to the advances in polymer chemistry, branched polyelectrolytes, including cylindrical polyelectrolyte brushes, star polyelectrolytes, hyperbranched polyelectrolytes and polyelectrolyte dendrimers, all with a variety of complex architectures and in reasonable quantities, became widely available. As a result, more studies now focus on exploring the highly branched polyelectrolyte macromolecules for the purposes of assembly and fabrication of functionalized soft nanomaterials with tailored properties and specific applications in mind. Some interesting recent examples will be discussed in this section.

In many cases, the complex structure of branched polyelectrolytes with well-defined inner and outer chemical compositions and typical dimensions from several to tens of

nanometers make them ideal templates for the fabrication of hybrid organic-inorganic nanoparticles with interesting optical, electric, or magnetic properties. The main advantage of using branched polyelectrolytes for such applications are a high monodispersity and versatile compositions which can be tuned for fabrication of various complex, core-shell, hollow, Janus, or multicompartamental metal and semiconductor nanoparticles.<sup>128</sup> CPBs, star polyelectrolytes, and polyelectrolyte dendrimers have all demonstrated novel behavior as prospective efficient nanoreactors for the synthesis of metal nanoparticles via spatially localized chemical reduction.

In the case of drug delivery applications, branched polyelectrolytes, especially dendrimers, are able to act as nanocarriers with controlled loading and unloading abilities if their potential toxicity can be mediated. Moreover, star polyelectrolytes and polyelectrolyte dendrimers can be utilized as major components to assemble ultrathin microcapsules or multilayered films, which have higher loading capacities, more functionalities, and multi-compartmental structures. Furthermore, branched polyelectrolytes have also been used to modify cell surface by forming thin shells. For example, silk fibroin with grafted poly(L-lysine) or poly(L-glutamic acid) side chains were used for cell encapsulation (Figure 1.8).<sup>129</sup> The results showed that shells assembled with polycationic amino acids adversely affected the properties of microbial cells with the formation of large cell aggregates. An excessive cytotoxicity has been noticed in many cases and should be carefully considered. Meanwhile, hydrogen-bonded shells with a high PEG grafting density were the most cytocompatible, and formed stable colloidal suspensions of individual cell encapsulates.

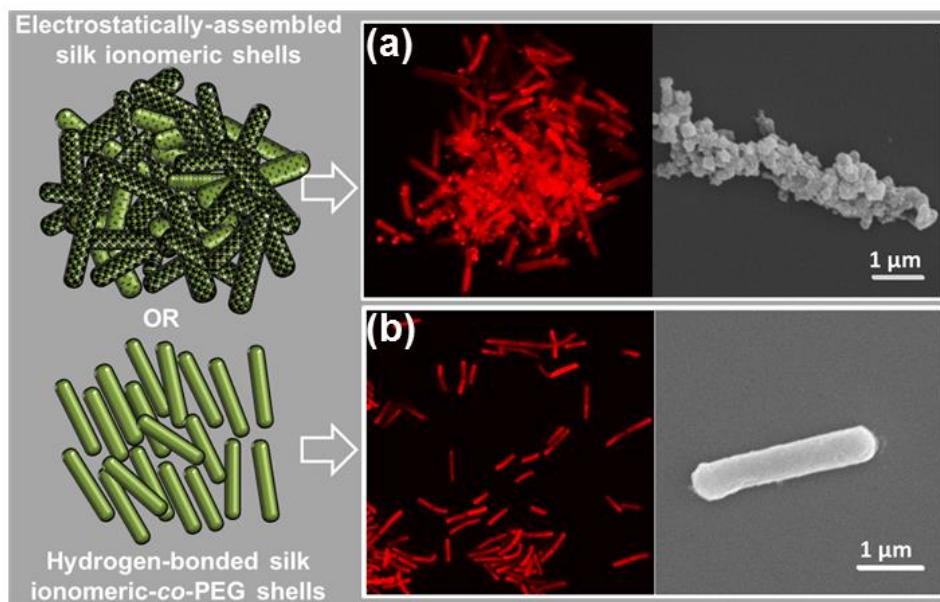


Figure 1.8. *B. subtilis* cells encapsulated in 4 bilayer thin shells composed of branched silk polyelectrolytes via (a) electrostatic interaction, or (b) hydrogen bonding. Images on the right are confocal microscopy and SEM, respectively. Reproduced with permission from reference 129, copyright (2015) American Chemical Society.

Due to the abundance of surface functional groups, branched polyelectrolytes are also good candidates for surface modification and can act as giant surfactant molecules. Star polyelectrolytes and hyperbranched polyelectrolytes have been shown to help the dispersion of individual carbon nanotubes and graphene oxide sheets in solution. For instance, the  $PS_nP2VP_n$  heteroarm star copolymer has been used as an effective dispersing agent for the exfoliation of graphene and the subsequent graphene shuttle between immiscible media such as organic solvent/water and water/ionic liquid.<sup>130</sup> The overall exfoliation yield, including concentration, solubilization yield, monolayer percentage, and large graphene size, is among the highest observed so far using polymeric stabilizers.

Conjugated branched polyelectrolytes have potential for energy harvesting and storage, sensing, and detection applications as well. They can also find applications in cell imaging and the detection of biological species and metal ions. However, these developments are currently limited. In a few examples, hyperbranched conjugated polyelectrolytes have been used as an energy and charge transport material for hybrid solar cells. For instance, Liu et al.<sup>131</sup> reported the synthesis of a gadolinium ion-chelated hyperbranched conjugated polyelectrolyte (HCPE-Gd) which has an average hydrodynamic diameter of 42 nm and a quantum yield of 10% in aqueous solution. The HCPE-Gd can be internalized in cancer cell cytoplasm with good photostability and low cytotoxicity. It can also serve as an efficient dual-modal imaging nanoprobe for *in vivo* cancer diagnosis.

## CHAPTER 2. RESEARCH GOALS AND OVERVIEW

### 2.1 Research Goals

Branched polyelectrolytes possess great advantages for molecular assembly due to the following unique properties. *Firstly*, branched polyelectrolytes do not aggregate as easily compared with their linear counterparts, due to stronger steric hindrance and lower extent of chain entanglement. They can form more ordered and labile phases in solution and at interfaces due to their compact shape. *Secondly*, branched polyelectrolytes with multiple functionalities and enhanced non-covalent interactions enable rich and responsive assembling behavior. *Thirdly*, polyelectrolytes with branched structures frequently behave as well-defined soft 3D objects, their higher-order assembled structures usually have hierarchical, compartmentalized structures, which are very desirable in applications such as drug delivery, controlled delivery, and self-healing.

Despite the great prospects for practical applications of branched polyelectrolytes, there are still several major challenges to be overcome in order to make major successful progress. **First of all**, although the differences between linear and branched polyelectrolytes in terms of conventional physical and chemical properties in solution or melt are well studied, the comparison study of their different behaviors in confined interfaces and their molecular assembly is still lacking.

**On the other hand**, the limited interdiffusion, entanglement, multiple functionalities, and weak intermolecular interactions of highly-branched molecules pose great challenges and unique opportunities in their surface behaviors and controlled assembly. For instance,

when mixing two chemically incompatible linear polymers, typical phase separation occurs. However, one recent study<sup>88</sup> show that two chemically incompatible branched polymers can form perfectly mixed phase at confined interface due to the significant increase in the conformational entropy of the branched polymers with increasing distance between adjacent macromolecules.

**Moreover**, the supramolecular assemblies demonstrated for branched polyelectrolytes are still very limited, and traditional solution assembly cannot generate well-defined structures in many cases. For instance, linear block copolymers can easily form various micelles or patchy nanoparticles structures in selective solvent, but branched or star block copolymers can maintain their unimolecular structures in most cases due to their 3D structure and strong steric hindrance.

**Lastly**, the assembly process of branched polyelectrolytes is still not easily controllable, although this is a common problem for non-covalent bond driven assembly of flexible macromolecules. The stability of the assembled structures is questionable in some cases. Therefore, it is critical to utilize unconventional assembly techniques with better control of the spatial distribution of branched polymers and the interfacial interactions, among which LB and LbL techniques are the most suitable ones.

It is important to note that most previous studies on responsive polymeric structures are focused on one specific type of external stimulus, such as pH, light or temperature, due to the limitation in chemical structure or molecular architecture of the polymers used. The

ability to incorporate dual or even multiple responsiveness into the assembled structure is of great challenge. However, with the multiple functionalities and complex architecture, branched polymers represent a group of very promising candidates to be used to achieve the goal of multiple stimuli-responsive properties. In order to achieve a more controllable way to assemble branched polymers and fabricate complex micro- and nano-structures, it is important to understand how the chemical composition and architecture of different highly-branched entities influence their intra/intermolecular interactions and assembly behaviors under various conditions.

Based on the unique properties, advantages as well as challenges of branched polymers mentioned above, this work will focus on one representative class of them: star-shaped polymers, with emphasis on their structure-property relationship, their controlled assembly through Langmuir-Blodgett and LbL techniques to fabricate functional microstructures.

***The goal of this work*** is to achieve a better understanding of the fundamental principles of the directed assembly of functional star polymers, with an emphasis on complex stars (amphiphilic and star polyelectrolytes) with responsive ionic blocks capable of dramatic conformational changes upon applying external stimuli. Elucidation of intra- and intermolecular organization of these star macromolecules on planar and curved surfaces is critical for understanding how directed assembly can be applied to design organized nanomaterials for prospective applications.

***The key objectives of this study include:***

1. Explore the solution phase behaviors of star polyelectrolytes with responsive properties to external stimuli (such as pH, temperature) using *in situ* SANS measurements at different conditions, in order to achieve deep insight of the structure-property relationship of star polyelectrolytes, and study how the branched architecture affect their conformational changes and aggregation at molecular level.
2. For amphiphilic star block copolymers with stimuli-responsive blocks, their conformational changes and molecular organization will be studied at air/water interface by using Langmuir-Blodgett (LB) technique, which is in complementary to traditional studies in solution state, because the confinement interface environment allows us to precisely control their conformational changes and assembly at 2D space. It also allows us to fabricate organized ultrathin monolayer films.
3. Based on the responsive properties of star polymers, assemble complex, hierarchical, and well-defined responsive layer-by-layer (LbL) structures including ultrathin films and thin shell microcapsules, the driving forces for assembly include electrostatic interactions, hydrophobic interactions and hydrogen bonding. The LbL assembly technique provides an important and versatile way to fabricate functional structures from star-shaped polymers, which are quite challenging to assemble with other methods.

4. Study the dual or multi responsive properties of the assembled 3D microstructures such as thin shell microcapsules, to various stimuli including pH, temperature, ionic condition and light, achieve controlled encapsulation and release of target molecules upon applying external stimuli. The multiresponsive microcapsules are superior to traditional ones that only response to one type of stimulus, because more sophisticated and on-demand release is possible by applying different stimuli at different locations and time.

5. Investigate the internal structure of thin shell microcapsules assembled from branched polymers, as well the structural evolution in terms of fractal dimension and correlation length during external condition changes, by using SANS. The direct structural characterization in solutions state can provide deep insight to the organization of the star polymers as well as their collective structural changes in a confined thin shell.

6. For miktoarm star polymers with small number of arms, explore their solution assembly with oppositely charged linear polymers into vesicles or polymersomes, and use the polymersomes as component to fabricate multilayered structures. The novel polymersomes have unique structure with interpolyelectrolyte complex wall and PEO corona, which are good candidates for drug delivery applications with high loading capacity.

7. Star polymers themselves can act as nanocarriers, so that the LbL microcapsules based on them have multicompartmental hierarchical structure, their capability to delivery two

types of target molecules simultaneously: one type of molecules inside the stars, and another type of molecules in the hollow core of the microcapsules is explored.

In summary, this research focuses on the understanding of multiple responsive behaviors (to pH, temperature, UV illumination, or ionic conditions) of functional star polymers with tunable intermolecular interactions. In addition, adopting functional star polymers as emerging building blocks offers a new approach for fabrication of adaptive and stimuli-responsive micro- and nano-structures due to their intriguing molecular architectures and properties. Significant fundamental questions of how molecular architecture and chemical composition affect the aggregation and assembly behavior, the internal structural and responsive properties of assembled structures will be addressed. Furthermore, we explore how the star polymer based responsive LbL nanostructures can be utilized for controlled encapsulation and release, with superior performances compared with traditional linear polymer based structures.

***The significance and novelty*** of this approach is in elucidating the effects of surface and interface energetics and confinements on the molecular conformation and interaction of these highly-branched well-defined macromolecules with a crowding compact structure. The advanced branch and multicompositional molecular design, in combination with integrated adaptive/responsive chain segments, represents a powerful approach to control the lateral diffusion and phase segregation of novel functional branched building blocks on the surface resulting in generating tunable and ordered complex structural nanodomains in thin films, as well as to tailor their stratified layered nanostructures with

capabilities for switchable morphological heterogeneity and multicompartmental structures.

## **2.2 Organization and Composition of Dissertation**

**Chapter 1** is a critical review of the structure of branched polyelectrolytes, their assembly as well as emerging applications, which defines the general scope of the field, within which this PhD work is focused on.

**Chapter 2** describes the goals and objectives of the work presented in this dissertation. It also contains an overview of the organization of the dissertation, and brief description of each chapter.

**Chapter 3** covers the major experimental techniques used in the work of this dissertation, which includes polymer synthesis, microstructure fabrication as well as materials characterization. In several subsequent chapters the experimental techniques are supplemented with specific protocols used for the particular studies presented.

**Chapter 4** is the solution study on the phase behaviors of responsive PDMAEMA star polyelectrolytes by using *in situ* SANS, and the results show that their temperature induced microphase separation is quite different from that of linear ones.

**Chapter 5** is the study on the interfacial properties and assembly of star-graft quarterpolymers at air/water interface using Langmuir-Blodgett technique, which provides deep insight into the detailed conformational changes and aggregation of amphiphilic star polymers at interface.

**Chapter 6** is about the LbL assembly of PDMAEMA star polyelectrolytes into microcapsules, which are responsive to both pH and temperature, and able to encapsulate and release cargo molecules upon pH and temperature changes.

**Chapter 7** is about the assembly of qPDMAEMA star polyelectrolytes into responsive microstructures, due to the unique ion responsive properties of the qPDMAEMA stars, the microcapsules have the capability to change their structure and permeability upon adding small amount of multivalent counterions and UV irradiation.

**Chapter 8** is about the assembly of core-shell structured star-graft quarter polymers into multicompartmental microcapsules. The microcapsules are able to encapsulate and release two different types of cargo molecules in a precisely controlled manner by changes in pH and temperature.

**Chapter 9** is about the electrostatic force driven assembly of miktoarm star polymers and an oppositely linear polyelectrolytes, which results in stable and robust polymersomes. The polymersomes are further utilized to fabricate hierarchical multilayered

microcapsules, which also have the capability to deliver multiple cargo molecules simultaneously.

**Chapter 10** provides general conclusions for the overall work in the dissertation with a specific focus on broad impact, prospective applications and future directions.

## CHAPTER 3. EXPERIMENTAL TECHNIQUES

### 3.1. Materials: Composition and Chemistry

#### 3.1.1 Star and Linear Polyelectrolytes

The star and linear polyelectrolytes are obtained in the course of collaboration with Prof. Axel H. E. Müller (University of Mainz, Germany). PDMAEMA was synthesized by atom transfer radical polymerization employing a core-first approach.<sup>132</sup> Sugar-based scaffolds as well as silsesquioxane nanoparticles were used as oligofunctional initiators. The rather low efficiency of the initiation sites (30-75%) leads to a moderate arm number distribution of the prepared polyelectrolyte stars. Star polymers with different arm numbers and arm lengths were obtained from each batch by withdrawing a part of the reaction solution at a desired conversion. Poly{2-(methacryloyloxy)ethyl trimethylammonium iodide} is the quaternized ammonium salt of PDMAEMA (qPDMAEMA) (Figure 3.1).

For the quaternization, PDMAEMA was dissolved in acetone and methyl iodide was added at room temperature at a molar ratio of 1.5 compared to amino groups. The mixture was kept stirring overnight to ensure quantitative conversion, acetone was decanted and the polymer was washed several times with acetone. Then quaternized polymer was dissolved in water and dialyzed against pure water for 2 days and finally freeze-dried. The molecular characterization of the polyelectrolytes is summarized in Table 3.1, detailed synthesis steps and characterization has been published earlier.<sup>132</sup>

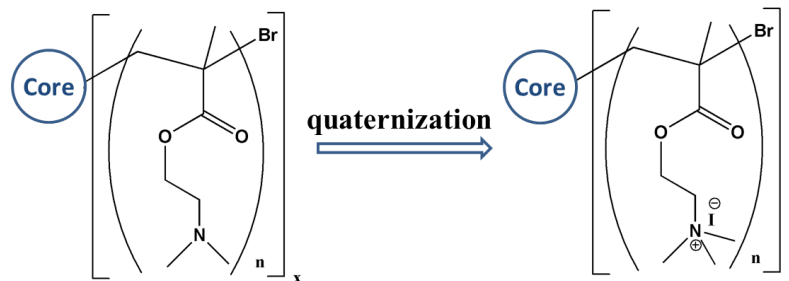


Figure 3.1. Chemical structure of PDMAEMA star polyelectrolytes (left) and their quaternized salts (right).

Table 3.1. Molecular Weight Averages (in g/mol) of PDMAEMA Stars Determined by Different Methods

Sample	$10^{-3}M_n$ , calc <sup>a</sup>	$10^{-3}M_{n,app}$ <sup>b</sup> ( $PDI_{app}$ )	$10^{-3}M_w$ <sup>c</sup> ( $\langle R_g^2 \rangle_z^{0.5}$ )	$PDI$ <sup>d</sup>
(PDMAEMA <sub>170</sub> ) <sub>5.6</sub>	150	108 (1.14)	155 (-)	1.03
(PDMAEMA <sub>170</sub> ) <sub>9.5</sub>	250	162 (1.11)	300 (-)	1.20
(PDMAEMA <sub>170</sub> ) <sub>18</sub>	490	253 (1.12)	690 (17)	1.41
(PDMAEMA <sub>240</sub> ) <sub>24</sub>	950	371 (1.24)	1360 (29)	1.43

<sup>a</sup> Number-average molecular weight ( $M_n$ ) calculated from conversion  $\chi_{p,NMR}$ . <sup>b</sup> Apparent  $M_n$  determined by gel permeation chromatography with linear poly(styrene) standards. <sup>c</sup> Weight average molecular weight ( $M_w$ ) and root of z-average of mean-squared radius of gyration ( $R_g$ ) determined by static light scattering (SLS) in acetone. <sup>d</sup> Polydispersity index (PDI) determined by ratio of  $M_w$ (SLS) and  $M_n$  (conversion).

### 3.1.2 Amphiphilic Star Block Copolymers

The star block copolymers are synthesized by Prof. Constantinos Tsitsilianis (University of Patras, Greece) in the course of collaboration. The  $A_n(B-C)_n$  heteroarm star block terpolymer was synthesized by a multi-step, one pot, sequential anionic living polymerization procedure which constitutes an extension of the so-called “in-out” method.<sup>133</sup> According to Figure 3.2, the first generation of arms is formed in the first step by reacting sBuLi with styrene. These “living” linear PS chains were used in a subsequent step to initiate the polymerization of a given amount of a suitable

bisunsaturated monomer (e.g., divinylbenzene) acting as a crosslinking agent. A “living” PS star-shaped polymer was thus formed bearing within its crosslinked core, an equal number of active sites with its arms. In the third step, a second generation of arms was grown from the core upon the addition of 2VP. The sites located now at the ends of the second generation of P2VP arms were “living” and were used to polymerize the third monomer (*t*-BA) leading therefore to the  $A_n(B-C)_n$  heteroarm star block terpolymer. The star terpolymer, consisting of poly(acrylic acid) blocks, was resulted by acid catalyzed hydrolysis of the ester groups of the precursor terpolymer bearing the protected poly(*tert*-butylacrylate) blocks. The de-protection reaction was carried out in 1,4-dioxane with a 10 fold excess of hydrochloric acid at 80°C for 24 h.

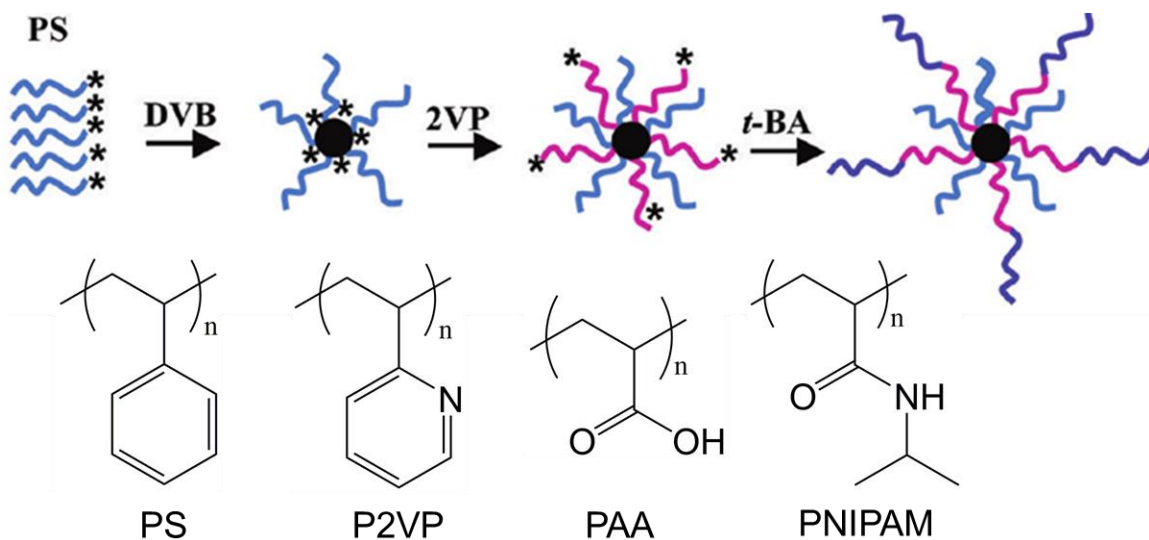


Figure 3.2. Schematic representation of the multi-step synthetic procedure that leads to  $A_n(B-C)_n$  heteroarm star block terpolymer. “\*” denotes active sites.

Finally, the  $PS_n[P2VP-b-(PAA-g-PNIPAM)]_n$  multifunctional star-graft quarterpolymers were synthesized by grafting of the carboxylate groups of PAA with PNIPAM-NH<sub>2</sub> chains. All samples have been characterized by a combination of gel permeation

chromatography,  $^1\text{H}$  NMR, and light scattering in accordance with the approach published elsewhere and summarized in Table 3.2.<sup>134</sup>

Table 3.2 Characterization data of the  $\text{PS}_n[\text{P2VP-}b\text{-(PAA-}g\text{-PNIPAM)}]_n$  heteroarm star-graft quarterpolymers.

Polymer topology	number of 2VP-PAA arms <sup>a</sup>	$M_w$ of star precursor <sup>b</sup>	$M_w$ star-graft <sup>c</sup>	PNIPAM chains per PAA arm <sup>d</sup>	PNIPAM graft weight fraction <sup>d</sup>
$\text{S}_9(\text{V-}b\text{-A-}g\text{-N}_{3.4})_9$	9.2	199000	372558	3.43	0.46
$\text{S}_9(\text{V-}b\text{-A-}g\text{-N}_{4.5})_9$			426194	4.49	0.53
$\text{S}_9(\text{V-}b\text{-A-}g\text{-N}_{11})_9$			759648	11.08	0.74
$\text{S}_{22}(\text{V-}b\text{-A-}g\text{-N}_4)_{22}$	21.7	572000	1049400	4.00	0.45

<sup>a</sup> by light scattering of  $\text{PS}_n$  star precursor, <sup>b</sup> by light scattering of heteroarm  $\text{PS}_n(\text{P2VP-PtBA})_n$  and assuming quantitative deprotection of tBA moieties, <sup>c</sup> calculated from  $M_w$  of  $\text{PS}_n(\text{P2VP-PAA})_n$  precursor and PNIPAM weight fraction, <sup>d</sup> by  $^1\text{H-NMR}$ .

### 3.1.3 Miktoarm Star Polymers

Miktoarm star polymers were synthesized by Dr. Felix Plamper from RWTH Aachen University, Germany in the course of collaboration. The miktoarm star polymer consisting of one poly-(ethylene oxide) (PEO) and on average 4.1 shorter PDMAEMA or poly{2-(methacryloyloxy)ethyl trimethylammonium iodide} (qPDMAEMA) arms. qPDMAEMA is a water-soluble, strong polyelectrolyte, which phase-separates in the presence of multivalent anionic counterions (Figure 3.3). The polymer was synthesized by atom transfer radical polymerization (ATRP) of a PEO and dipentaerythritol-based macroinitiator, aiming for five PDMAEMA grafts. The pendant amino groups of miktoarm star PEO-PDMAEMA<sub>4.1</sub> were quaternized with methyl iodide, leading to PEO-qPDMAEMA<sub>4.1</sub> star polymers. The completeness of quaternization was verified by elemental analysis. The synthesis and detailed characterization are explained in a

previous publication,<sup>135</sup> two sets of miktoarm star polymers with various length of the grafted PDMAEMA or qPDMAEMA chains were obtained. The overall formula was determined to  $\text{PEO}_{113}\text{-(PDMAEMA}_x\text{)}_{4.1}$  or  $\text{PEO}_{113}\text{-(qPDMAEMA}_x\text{)}_{4.1}$ , indicating the number-average degree of polymerization for the PEO arm is 113 and for one PDMAEMA or qPDMAEMA chain ( $x=60, 84$  or  $140$ ).

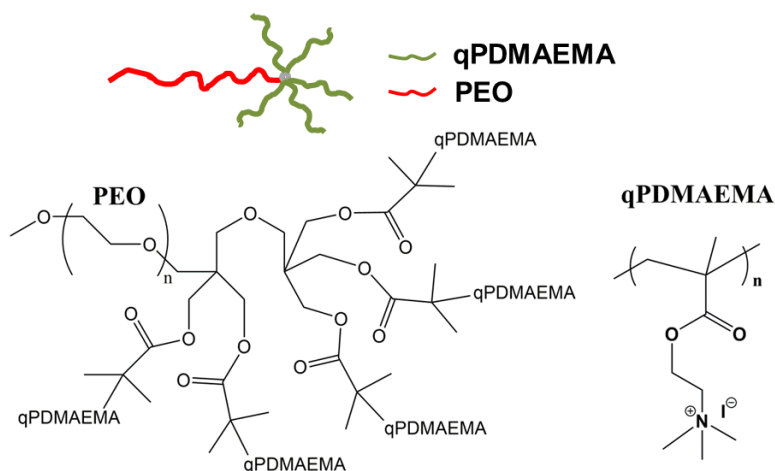


Figure 3.3. Chemical structure of  $\text{PEO}_{113}\text{-(qPDMAEMA}_x\text{)}_{4.1}$  miktoarm star polymers.

## 3.2 Fabrication of Microstructures

### 3.2.1 Preparation of LB Monolayer Film

Freshly cut silicon substrates with dimensions 1 cm x 2 cm and 100 orientation (Semiconductor Processing) and a native silicon dioxide layer having a 1.6 nm thickness are cleaned with piranha solution (3:1 concentrated sulfuric acid and hydrogen peroxide mixture) in accordance with usual procedure.<sup>136</sup> Subsequently, it is abundantly rinsed with Nanopure water (18.2 M $\Omega$  cm) and dried with a dry nitrogen stream. Pretreated substrates serve as a hydrophilic base for film deposition.

The LB studies are conducted using a KSV2000 minitrough, according to the usual procedure adapted in our lab.<sup>137</sup> Star polymers are dissolved in a nonselective solvent of chloroform/methanol mixture (90/10 % in vol/vol) (HPLC grade), with a concentration of 0.1-0.5 mg/ml. The LB minitrough is filled with Nanopure water, and the pH of the water subphase is adjusted by using hydrochloric acid (HCl) and sodium hydroxide (NaOH). Then 60-120  $\mu\text{L}$  polymer solution is dropwise dispersed evenly onto the surface of the water, and leave for 30 minutes to allow the evaporation of the organic solvent. Compression of the monolayers is conducted at a speed of 5 mm/min. The Langmuir monolayers are transferred from the air-water interface by vertically pulling out the substrate submerged in the water subphase at a rate of 2 mm/min. The limiting cross sectional area  $A_0$  is determined by the steepest tangent rise in the surface pressure, which indicates the formation of a condensed monolayer.<sup>138</sup>

### **3.2.2 Preparation of LbL Thin Films**

Polyelectrolytes are dissolved in Nanopure water or in 0.01M Tris HCl buffer solution. The pH of all the solutions is adjusted by the addition of 0.1 M HCl or 0.1 M NaOH aqueous solution to control the charge density of polyelectrolytes.

Spin-assisted LbL films are prepared by using sequential spin-casting at 3000 rpm for 30 sec and rinse twice with nanopure water between depositions of polyelectrolyte layers, in accordance with usual procedure in our lab.<sup>139</sup> LbL films are further dried at room temperature for 2 hours before experimental measurements. The dip-assisted LbL process (Figure 3.4) is performed by alternate immersion of the substrates in

polyelectrolyte solutions for 15 min, followed by rinsing two times with the same pH buffer solution.

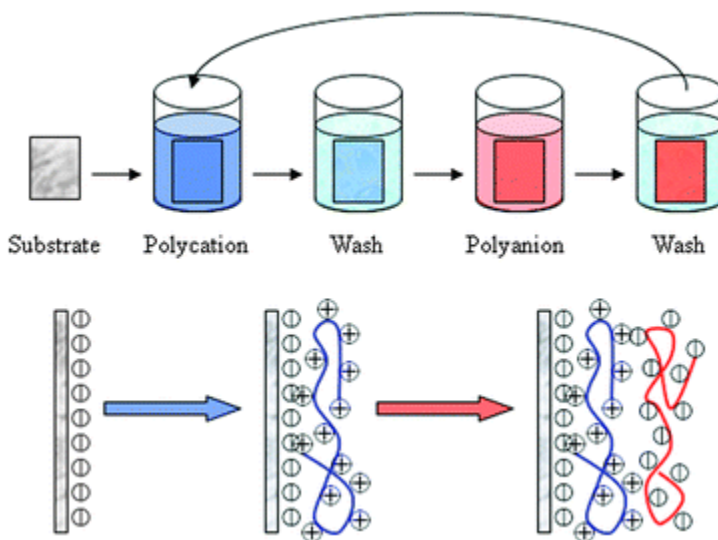


Figure 3.4 Schematic of LbL assembly of a multilayer coating by sequential adsorption of oppositely charged polyelectrolytes.<sup>140</sup>

### 3.2.3 Preparation of LbL Microcapsules

The preparation of LbL microcapsules consists of the following steps (Figure 3.5): the bare, negatively charged silica particles with average diameter of 4  $\mu\text{m}$  were first coated with PEI pre-layer (if necessary) by incubating in 1.5 mL of PEI solution (1.0 mg/mL) for 15 min, followed by two centrifugation (3000 rpm for 3 min)/wash cycles. Subsequently, the silica particles were incubated in 1.5 mL anionic polyelectrolyte solution (0.2 mg/mL) for 15 min, followed by two centrifugation (3000 rpm for 3 min)/wash cycles. 1.5 mL of cationic polyelectrolyte solution was then added to the silica particles and 15 min was allowed for adsorption, also followed by two centrifugation (3000 rpm for 3 min)/wash cycles. The anionic and cationic polyelectrolyte adsorption steps were repeated until the desired number of layers was built on silica particles. Hollow microcapsules were finally obtained by dissolving silica

cores in 0.5% HF solution for 2h, followed by dialysis in nanopure water for 36 hours with repeated change of water.

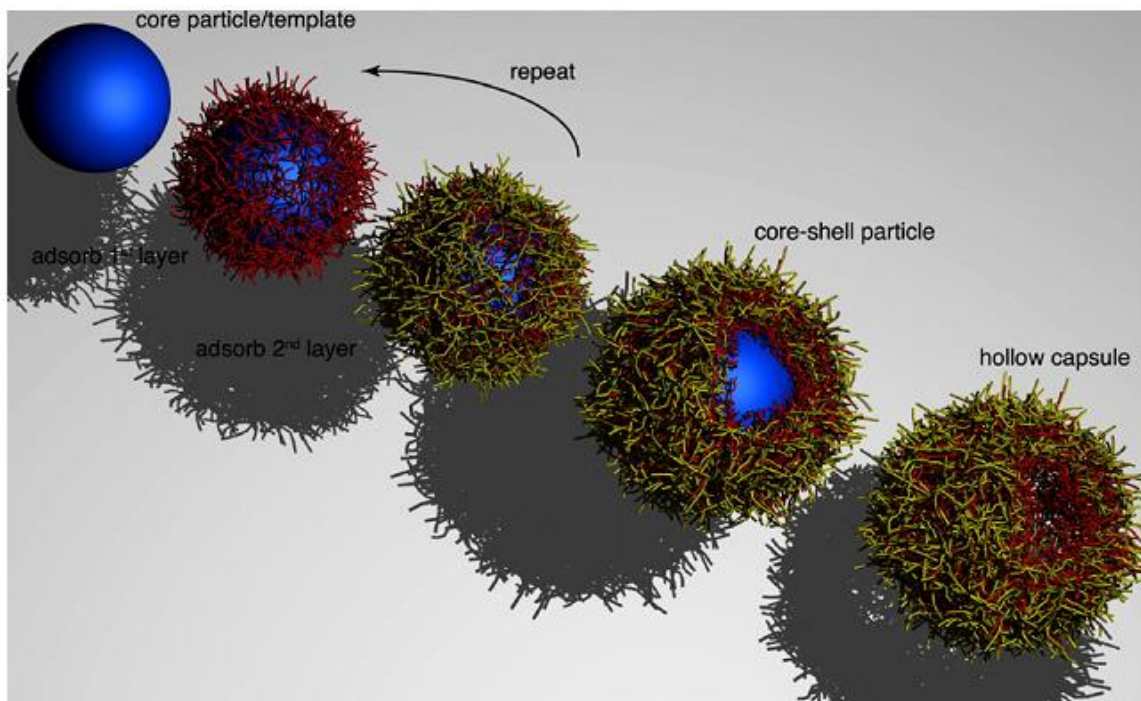


Figure 3.5. Schematic of the LbL assembly process on spherical template to fabricate hollow microcapsules.<sup>141</sup>

### 3.3 Characterization of Solution and Microstructures

#### 3.3.1 Characterization of Star Polymer Solution by SANS

SANS measurements were conducted at Oak Ridge National Laboratory (ORNL) on the CG2 (GP-SANS) instrument (Figure. 3.6) with a wavelength of  $\lambda = 4.7 \text{ \AA}$  ( $\Delta\lambda/\lambda \sim 0.14$ ). Polyelectrolyte solutions were loaded into 2 mm thick quartz cells. Quartz cells were mounted in a temperature-controlled sample holder (temperature stability and gradients are better than  $\pm 0.1 \text{ }^\circ\text{C}$ ), and the samples were allowed to stabilize at a preset temperature for 10 min at given temperature before each measurement. Polymer concentration in our experiments was chosen to be 1 wt % in order to keep high signal-to-noise ratio and minimize possible interactions between the stars and large scale aggregate

formation. Two sample-detector distances were used (1.0 and 18.5 m with a 40 cm detector offset), which resulted in a range of scattering vectors  $q$  ( $q = 4\pi \cdot \sin\theta/\lambda$ , where  $2\theta$  is the scattering angle) covered in the experiment from  $0.004 \text{ \AA}^{-1}$  to  $0.6 \text{ \AA}^{-1}$ . The data were corrected for instrumental background and detector efficiency and converted to an absolute scale (cross section  $I(q)$  in units of  $\text{cm}^{-1}$ ) by means of a pre-calibrated secondary standard, Al-4.<sup>142</sup> Scattering from the solvent was subsequently subtracted proportionally to its volume fraction. In addition to PDMAEMA star polyelectrolytes, we also studied the solution behaviors of linear PDMAEMA with the changes of pH and temperature.

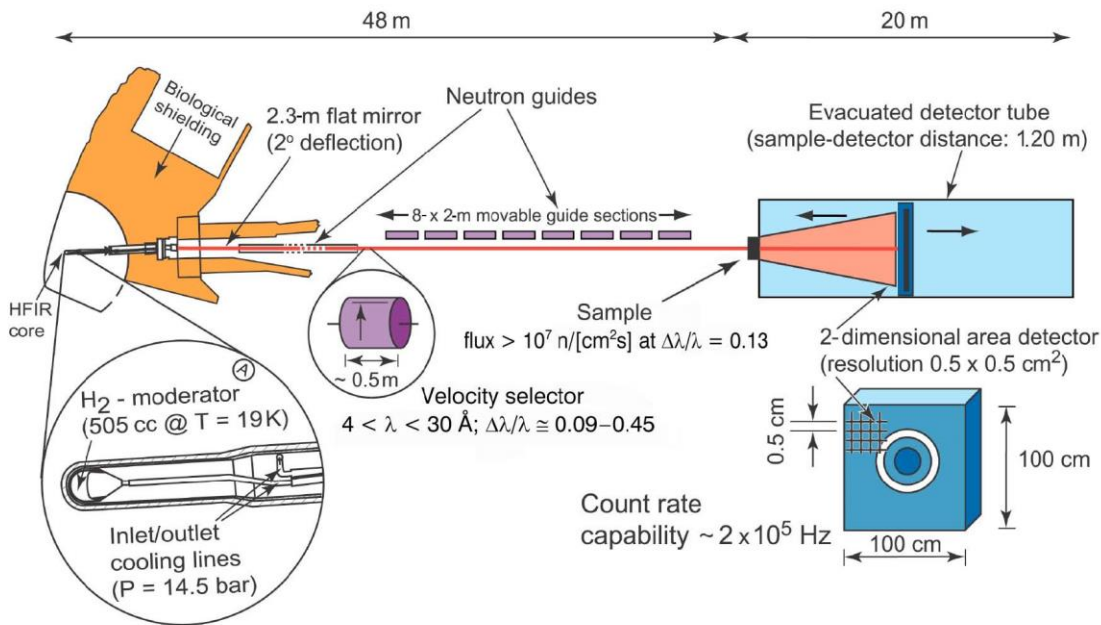


Figure. 3.6. Schematic of the CG-2 SANS diffractometer at ORNL (image from ORNL website).

### 3.3.2 Characterization of Thin Films and Microcapsules

**Atomic Force Microscopy (AFM)** Surface morphology of the hollow microcapsules and thin films was studied using AFM. AFM images were obtained using a Dimension-3000 (Digital Instruments) microscope in the “light” tapping mode according to the well-established procedure.<sup>143,144</sup> For capsule sample preparation, a drop of microcapsule

suspension was placed onto a pre-cleaned silicon wafer and dried in air prior to AFM imaging. Thickness of the microcapsules was determined as half of the height of the collapsed flat regions of dried microcapsules from generated height histograms by NanoScope software.<sup>145</sup>

***Ellipsometry*** Film assembly as well as thickness was determined using M-2000U spectroscopic ellipsometer (Woollam). Prior to the measurements, samples were dried with nitrogen stream. Thickness value of the LbL film was obtained by fitting measured raw data with Cauchy model. Thickness measurements are conducted on at least three different homogeneous surfaces for each sample showing standard deviation within  $\pm 8\%$  level.

***UV-Visible Spectroscopy*** UV-2450 spectrophotometer (Shimadzu) was used to monitor the absorbance increments of the films on quartz slides. Data were evaluated after the spectrum of the piranha-treated blank quartz sample was subtracted from each of the measured spectra.

***Scanning Electron Microscopy (SEM)*** SEM imaging of hollow microcapsules was performed on a Hitachi S-3400-II scanning electron microscope with electric current of 10 kV in vacuum ( $<1$  Pa). Microcapsules air-dried on silicon wafers and were then sputter-coated with gold before imaging.

***Transmission Electron Microscopy (TEM)*** TEM was done using a JEOL 100CX operated at 100 kV with samples drop cast on carbon–formvar-coated copper grids (Ted Pella, Inc.).

***Zeta-Potential Measurements*** Surface potentials of bare and coated silica particles were measured from aqueous solutions on Zetasizer Nano-ZS equipment (Malvern). Each value of the zeta-potential was obtained at ambient conditions by averaging three independent measurements of 35 sub-runs each.

***Confocal Laser Scanning Microscopy (CLSM)*** Confocal images of capsules were obtained with an LSM 510 UV Vis laser scanning microscope (Zeiss, Germany) equipped with C-Apochromat 63× oil immersion objective. The excitation/emission wavelengths were 488/515 nm. Microcapsules were visualized through addition of fluorescein isothiocyanate (FITC) to the capsule suspension. A drop of hollow capsule suspension was added to Lab-Tek chamber (Electron Microscopy Sciences), which was then filled with 0.01 M Tris-HCl buffer. Microcapsules were allowed to settle down and then analyzed. To investigate the permeability of microcapsules, a drop of dispersion of hollow capsules was added to Lab-Tek chamber, which was then half-filled with 0.01 M Tris-HCl buffer and then mixed with FITC-dextran solution of different molecular weight (1 mg/mL).

## CHAPTER 4. SOLUTION PHASE BEHAVIORS OF RESPONSIVE STAR POLYELECTROLYTES

### 4.1 Introduction

Recent advances in polymer chemistry allow the synthesis of branched polyelectrolytes with well-defined structures, such as polyelectrolyte brushes,<sup>146</sup> dendritic polyelectrolytes,<sup>147</sup> hyperbranched polyelectrolytes,<sup>148</sup> ,<sup>149</sup> pearl-necklace polyelectrolytes<sup>20</sup> and star polyelectrolytes.<sup>150,151,152,153</sup> Among many different kinds of branched polyelectrolytes, star polyelectrolytes constitute a particular class of macromolecules with high relevance in soft matter physics, chemistry, and materials science.<sup>21</sup> Due to the unique architecture of star polyelectrolytes, their conformational state can be complicated and affected by the degree of charging, the salt concentration, the valency of counterions and co-ions, as well as the temperature and pH of the solution.<sup>150,154,155</sup> Star and linear polyelectrolytes frequently show peculiar phase behavior due to complex balance of intra- and intermolecular ionic interactions. For instance, the crossover from a dilute to a semi-dilute solution regime occurs at much lower polymer concentrations than for solutions of neutral chains.<sup>156,157</sup> Muthukumar et al.<sup>158</sup> reported a novel mechanism of phase separation upon temperature change for aqueous solutions of poly(sodium 4-styrenesulfonate) (PSS), where an enrichment of polymer aggregates of well-defined size occurs in the very early stage of nucleation, which is then followed by a growth process in the formation of the new phase. In the latter stage, the polymer aggregates formed in the early stage act as the templating nuclei with the daughter phases have different polymer charges from that of the mother phase.<sup>159</sup>

Theoretical studies have shown that in addition to the steric repulsion between star polymers, there are also a relatively short range attraction and a secondary repulsive barrier at longer distance.<sup>160</sup> It has been demonstrated that solutions of weakly charged polyelectrolytes exhibit a microphase separation upon a decrease in the solvent quality below the  $\theta$ -point.<sup>161</sup> At appropriate thermodynamic conditions, the system has a tendency to form clustered regions, however, true macrophase separation might be inhibited. The affecting factors include counterion concentration and valency, pH and temperature, amongst others. The role of temperature in the solution behavior of linear polyelectrolytes has been considered.<sup>162</sup> The correlation length for concentration fluctuations in aqueous solutions of PSS with added salt was determined, and the critical behavior was observed upon lowering the temperature to phase boundaries. Studies by Khokhlov et al.<sup>163</sup> showed that for partially charged weak polyelectrolytes the counterions can easily transfer between repeating units and from one chain to another, which facilitates the phase separation in solution. A study on polyelectrolyte micelles also showed that with increasing packing fraction and minimal screening conditions, the micelle stars shrink and the corona layers eventually interdigitate, and this effect is most pronounced for higher corona charge.<sup>164</sup> Another study on thermo-responsive micelles also showed that the shell collapses upon heating, followed by intermicellar aggregation and densification.<sup>165</sup>

On the other hand, the temperature effects on the interactions and phase behavior of star polyelectrolytes have hardly received any attention. Considering recent utilization of star polyelectrolytes for building hollow microcapsules,<sup>166, 167</sup> conformal coatings<sup>52</sup> with

tunable properties as well as in gene delivery,<sup>168</sup> the elucidation of the responsive behavior of star polyelectrolytes in solution becomes important.<sup>169</sup> For the investigation of the temperature behavior of polyelectrolyte solution, classical macroscopic methods such as turbidimetry cannot be applied to monitor local conformational and aggregation behavior. The characteristic dimensions and internal morphology can be obtained from the neutron scattering data, which is sensitive to inner morphology if a high contrast is achieved in deuterated environment. Small-angle neutron scattering (SANS) has been used to study the thermo-responsive properties of block copolymers,<sup>170</sup> gels,<sup>171</sup> microgel colloids,<sup>172</sup> micelles,<sup>173</sup> and other related soft materials.<sup>174</sup> For instance, Moore et al.<sup>175</sup> studied the aggregation behavior of thermally responsive star block copolymers where the interior block of N-isopropylacrylamide (NIPAM) can collapse when heated above its low critical solution temperature (LCST).

In this chapter, we discuss the solution behavior of novel star polyelectrolytes poly(*N,N*-dimethylaminoethyl methacrylate) (PDMAEMA) with dual-responsive properties by using *in situ* SANS measurements at different temperatures and pH values around  $pK_a$  when they are partially charged ( $pK_a$  is 5.8 for (PDMAEMA<sub>170</sub>)<sub>18</sub>).<sup>132</sup> Since PDMAEMA is a weak polyelectrolyte, the protonation/deprotonation equilibrium depends on the pH conditions and solution temperature.<sup>176</sup> We observed that PDMAEMA star polyelectrolytes in semi-diluted solution form core-shell microphase separated micelles with limited short-range intermolecular ordering. Upon heating from room temperature to 45-50 °C, a modest contraction of brush-like shells was observed, which was induced by the reduced osmotic pressure with changes in local pH. In this temperature range,

their dense collapsed cores remain almost unchanged while the arm chains in their loose shells undergo significant densification and contraction (about 50%). At even higher temperature ( $>45\text{ }^{\circ}\text{C}$ ), but well below cloud point at these pH conditions ( $>80\text{ }^{\circ}\text{C}$ )<sup>176</sup> the limited intermolecular aggregation has been detected. This behavior is in striking contrast with the common macroscopic phase separation of their linear PDMAEMA counterparts studied here under the same conditions.

## 4.2 Experimental Section

### Materials

PDMAEMA star polymers were synthesized by atom transfer radical polymerization of 2-(*N,N*-dimethylamino)ethyl methacrylate employing a core-first route with functionalized polyhedral oligomeric silsesquioxane (POSS) core (described earlier<sup>132</sup>). The chemical structure is shown in Figure 3.1. Sugar-based scaffolds as well as silsesquioxane nanoparticles were used as multifunctional initiators. Subsequent quaternization of the obtained PDMAEMA stars yielded their star-shaped quaternized ammonium salts (qPDMAEMA). The rather low efficiency of the initiation sites (30-75%) leads to a moderate arm number distribution of the prepared polyelectrolyte stars. Here, we used PDMAEMA star polymers with arm numbers of 9.5, 18 and 24 (number average), the number-average degree of polymerization per arm is 170, 170 and 240, respectively (Table 4.1). Therefore, they are named as (PDMAEMA<sub>170</sub>)<sub>9.5</sub>, (PDMAEMA<sub>170</sub>)<sub>18</sub> and (PDMAEMA<sub>240</sub>)<sub>24</sub>, with the number-average molecular weight of 250, 490 and 950 kg/mol, and polydispersity index of 1.20, 1.41 and 1.43, respectively.

To assure high scattering contrast, D<sub>2</sub>O (99.9%) was used to dissolve star polyelectrolytes for SANS experiments (Cambridge Isotope Laboratories). Sodium deuterioxide (40 wt. % in D<sub>2</sub>O, 99 atom % D) and deuterium chloride (99 atom % D) were purchased from Sigma-Aldrich, and used to adjust the pH of the samples.

## **SANS Experiments**

SANS measurements were described in detail in Chapter 3. The molecular models of arm chains were built using Materials Studio with energy minimization combined with cycles of molecular dynamics.

## **4.3 Results**

### **4.3.1 SANS Data Analysis Notes**

As known, the SANS data from star polymers usually show two distinguishable scattering regimes, with the scattering at lower  $q$  range stems from the overall shape of the stars and intermolecular ordering, scattering at higher  $q$  value is determined by a secondary sub-structure, which corresponds to the intramolecular density distribution and blob structure.<sup>177</sup> Thus, a combination of the two appropriate models is usually required to analyze SANS experimental data in the whole  $q$  range. Spherical core-shell model provides the form factor  $P(q)$  with core-shell structure, and the appearance of the distinct maximum allows for the evaluation of the intermolecular distances in partially ordered solutions.<sup>178</sup> The intermolecular interactions can also be accounted with mean spherical approximation (MSA),<sup>179</sup> the MSA structure factor is suitable for systems consisting of charged, spheroidal objects in a dielectric medium. When combined with the appropriate

form factor (core-shell model in our case), allows the inclusion of interparticle effects due to the screened Coulomb repulsion between charged particles.<sup>180</sup>

The blob sub-structure for star polyelectrolytes needs to be analyzed with a mass fractal model. The use of the mass fractal model to parameterize scattering at higher  $q$  range in addition to a model describing the overall size of the star polymers has been reported before.<sup>181</sup> The mass fractal model calculates the scattering from fractal-like aggregates based on the Mildner reference.<sup>182</sup> In addition to the shape-dependent model, the SANS data for PDMAEMA stars can be analyzed by the generalized Kratky analysis, which provides an additional independent way to estimate the radius of gyration of the stars by plotting  $I(q)q^{1/\nu}$  vs  $q$ , where  $\nu$  is the excluded volume parameter.<sup>183</sup> From the peak position  $q_{\max}$  in Kratky plots, the radius of gyration can be calculated. The scattering from semi-diluted solution of linear PDMAEMA without well-defined molecular shape can be treated in terms of a hierarchical structure with two length scales: the low  $q$ -range (Debye-Anderson-Brumberger (DAB) behavior) and the high  $q$ -range (Ornstein-Zernike behavior). DAB model is used to calculate the scattering from a randomly distributed, two-phase system and gives the long-range correlation length ( $L$ ), which is a measure of the average distance between contributing phases.<sup>184</sup> Ornstein-Zernike model gives the correlation length ( $\xi$ ) of the chains,<sup>185</sup> which is related to the entanglement distance (blob size). The two contributions can be treated separately and added to give the total scattering intensity in the two-correlation-length model.<sup>186</sup>

Finally, the pair distance distribution function  $p(r)$  employed here is calculated by using a modified version of the process described by Moore et al<sup>187</sup>, where  $I(q)$  is related to the real space  $p(r)$  by Fourier transform. As known,  $p(r)$  is a histogram of all distances between point pairs within the particles weighted by the excess scattering density (which can be both positive and negative) at the points, which can be used to determine the overall shape and size of the scattering object.

#### 4.3.2 Structure Study of PDMAEMA Stars in Semi-Dilute Solution

First, we estimate the state of the star polyelectrolyte solutions under investigation here. According to Daoud and Cotton,<sup>188</sup> the overlap concentration of star polymers depends on the length of arm chain, and for relatively long arms (as is the case for all our PDMAEMA star polyelectrolytes), the overlap concentration  $C^* \sim N^{-4/5} f^{2/5} v^{-3/5} l^{-3}$ , where  $N$  is the degree of polymerization of each arm,  $f$  is the arm number,  $v$  is the excluded volume exponent, and  $l$  is the monomer size. Based on this equation, all the star polyelectrolytes solution concentrations used in our SANS study are lower than  $C^*$ : the (PDMAEMA<sub>170</sub>)<sub>18</sub> concentration of 5.8 vol. % is below  $C^* = 7.5$  vol. %, (PDMAEMA<sub>170</sub>)<sub>9.5</sub> concentration of 4.3 vol. % is below  $C^* = 5.8$  vol. %, and (PDMAEMA<sub>240</sub>)<sub>24</sub> concentration of 5.6 vol. % is below  $C^* = 6.4$  vol. %. This calculations show that all our solutions are below concentrated solution regime without overlap of the neighboring stars that enable the study of scattering from individual star macromolecules. On the other hand, for charged polyelectrolytes the crossover from dilute to semi-dilute regime occurs at lower concentrations than that in solutions of neutral chains due to stronger intermolecular interactions. Therefore, all of the PDMAEMA stars in our study are in the semi-dilute regime with the intermolecular

interactions playing an important role and the overall the scattering originated from both form-factors of individual stars and the intermolecular interference related to the close proximity of neighboring stars.<sup>189</sup>

In fact, the SANS data of all PDMAEMA stars show two distinguishable scattering regimes with the broad maximum at lower  $q$  stemming from the interference between PDMAEMA stars and scattering peak at higher  $q$  due to the internal structure of individual stars (Figure 4.1). Such characteristic diffuse scattering has been reported for many polyelectrolyte systems and is attributed to the contributions from short-range ordered polyelectrolyte structures and a form-factor related to internal morphology.<sup>190,191</sup> In contrast, SANS for linear counterpart shows more diffuse scattering and significant intensity increase at lower  $q$ , which is characteristic of semi-diluted polymer solution of random coils (Figure 4.1).

The core-shell model combined with MSA structure factor (interparticle interference effects due to Coulomb repulsion) allows excellent fitting results for the experimental data in the whole  $q$  range (Figure 4.1, solid lines).<sup>180</sup> From the MSA structure factor, the effective radius ( $R_{\text{eff}}$ ) of the PDMAEMA star polymers can also be obtained (Table 4.1). In the case of charged spherical particles, as a consequence of the presence of the electrical double layer, the excluded volume of the particles defined by an effective radius is significantly larger than their actual radius of gyration and is responsible for large intermolecular distances as will be discussed below (Table 4.1).

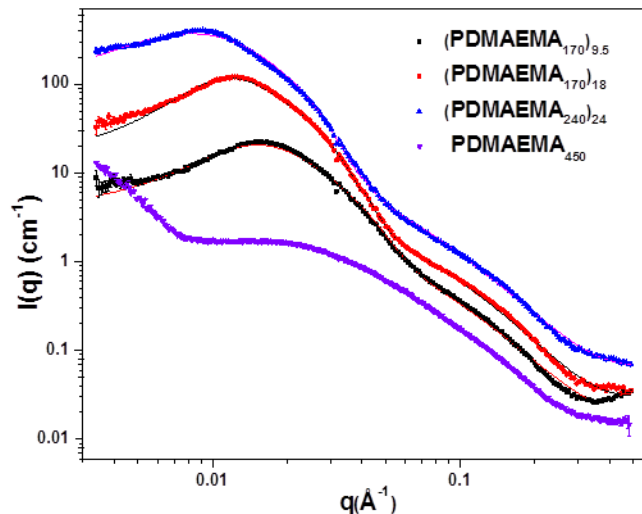


Figure 4.1. SANS data for solutions of PDMAEMA star polyelectrolytes with different number of arms or arm length (1 wt. % at pH 7.0 and 25 °C), the solid lines are fitting with core-shell model. The curves are mutually offset by a factor of 2 for better visualization.

Table 4.1. Structural parameters for PDMAEMA star polyelectrolytes and their quaternized salts with different number of arms or arm length, all units are in nm.

Sample	$M_w^a$	Core radius	Shell thickness	Overall R	$R_g$ (Kratky)	$R_g$ (p(r))	Effective radius <sup>b</sup>	D (peak position) <sup>c</sup>
(PDMAEMA <sub>170</sub> ) <sub>9.5</sub>	$3.00 \times 10^5$	$3.5 \pm 0.2$	$3.7 \pm 0.3$	$7.2 \pm 0.5$	$7.5 \pm 0.3$	$7.0 \pm 0.4$	11.0	37.8
(PDMAEMA <sub>170</sub> ) <sub>18</sub>	$6.90 \times 10^5$	$5.2 \pm 0.2$	$4.8 \pm 0.2$	$10.0 \pm 0.4$	$10.4 \pm 0.3$	$9.0 \pm 0.5$	15.2	49.9
(PDMAEMA <sub>240</sub> ) <sub>24</sub>	$1.36 \times 10^6$	$6.1 \pm 0.3$	$6.2 \pm 0.5$	$12.3 \pm 0.8$	$12.8 \pm 0.4$	$12.0 \pm 0.4$	23.0	65.8
(qPDMAEMA <sub>170</sub> ) <sub>9.5</sub>	$5.76 \times 10^5$	/	/	/	$10.9 \pm 0.4$	/	/	41.5
(qPDMAEMA <sub>170</sub> ) <sub>18</sub>	$1.10 \times 10^6$	/	/	/	$15.1 \pm 0.3$	/	/	56
(qPDMAEMA <sub>240</sub> ) <sub>24</sub>	$2.21 \times 10^6$	/	/	/	$17.3 \pm 0.4$	/	/	65.8

<sup>a</sup> Weight average molecular weight ( $M_w$ ) determined by static light scattering (SLS) in acetone.

<sup>b</sup> The effective radius values are from MSA structure factor (Appendix).

<sup>c</sup> The distance D is calculated from the peak position at low q range in Figure 4.1a.

The Kratky plots for PDMAEMA stars show a pronounced maximum, which can be used for the evaluation of the molecular dimensions under isotropic approximation (Figure 4.2a).<sup>192</sup> When  $I(q)q^{1/\nu}$  vs  $q$  was plotted with a horizontal asymptotic behavior at high  $q$  range, the excluded volume parameter  $\nu$  is found to be 0.6. This value for PDMAEMA

stars indicates that within the blobs, the arm chains can be described as random coils in a good solvent with standard excluded volume behavior unperturbed by the interactions with other branches.<sup>193</sup> The intensity of the characteristic peak in Kratky plot increases with the increasing number of arms of PDMAEMA stars indicating more compact inner structure. The radius of gyration,  $R_g$ , can be estimated by using relationship  $R_g = \sqrt{3}/q_{max}$ , where  $q_{max}$  is position of the peak at Kratky plot (Table 4.1, Figure 4.2a).<sup>192</sup>  $R_g$  systematically increases from 7.5 nm to 12.8 nm for PDMAEMA stars with increasing number of arms (or increasing molecular weight) (Table 4.1). For linear PDMAEMA<sub>450</sub> there is no obvious peak in the Kratky plot indicating random coiled state (Figure 4.2a).

The pair distance distribution function  $p(r)$  for all stars possess symmetrical shape with correlations vanishing at the maximum distance which is defined as the effective diameter  $D$  ( $D \approx 2R$  where  $R$  is defined as a peak position) (Figure 4.2b). The symmetrical shape of the  $p(r)$  of PDMAEMA star polyelectrolytes indicates spherical structures.<sup>194,195</sup> The increase of the number of arms results in the increasing correlation density and shift of the peak position to higher values (Figure 4.2b). The  $R_g$  obtained from the  $p(r)$  peak position is in good agreement with the Kratky analysis (within standard deviation) (Table 4.1). The  $p(r)$  analysis is not suitable for linear PDMAEMA at the same condition due to very low density variation within these scattering units.

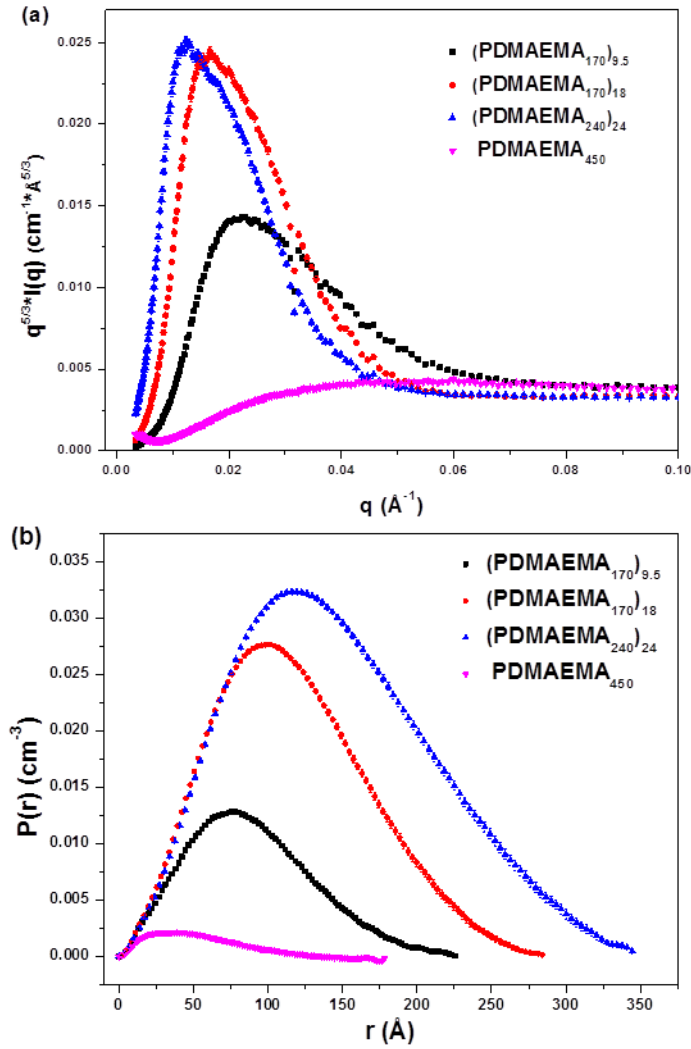


Figure 4.2. Kratky plots (a) and pair distance distribution function (b) for PDMAEMA star polyelectrolytes with different number of arms or arm length. The data for linear PDMAEMA<sub>450</sub> are also shown for comparison.

### Comparison with theoretical calculation

The dimensional calculations from different methods can be compared with theoretical estimations at some limiting cases (Table 4.2). For a star macromolecules in dilute solution with random coil conformation, the equation proposed by Borisov et al.<sup>37</sup> can be employed for the estimation of the effective dimensions:

$$R \sim aN^{\nu}p^{(1-\nu)/2}$$

where  $a$  is the monomer size,  $N$  is the degree of polymerization of each arm,  $p$  is the arm number and  $v$  is the scaling exponent. Two other limiting cases are random coil and fully extended conformation for all arms. The total radius of gyration of the star polymer can be evaluated by combining  $2 R_g$  with  $R_c$ , where  $R_c$  is the radius of the POSS core exploited for synthesis of star polyelectrolytes (around 0.75 nm) (Table 4.2).

Theoretical effective radii evaluated under different assumptions for star and linear chains vary in the wide range from 8 nm to 17 nm for the stars with the lowest molecular weight to 11 nm to 24 nm for the stars with the highest molecular weight (Table 4.2). From comparison with experimental values, it is apparent that the star dimensions with extended arms will exceed any experimental values and, thus, excludes extended conformation from further consideration. On the other hand, simple random coil model for all arms does not reflect the trends observed in the experiment and, thus, should be excluded from consideration as well (Table 4.2). For another limiting case of a spherical particle with uniform density and the same mass as the PDMAEMA star, the calculated radius is about 67% of the experimental radius (e.g., 6.7 nm vs 10.0 nm for (PDMAEMA<sub>170</sub>)<sub>18</sub>), which indicates that the stars are highly swollen and far from being densely-packed spheres (Table 4.2). Finally, the theoretical molecular dimensions calculated considering actual star architecture constraints and random coil conformations of arms with excluded volume are still systematically (about 30%) higher than the dimensions obtained from all experimental models.

Table 4.2. Theoretical dimensions estimated for PDMAEMA star polyelectrolytes under different model assumptions, the unit is nm.

Sample	R (theory) <sup>a</sup>	R <sub>g</sub> (random coil) <sup>b</sup>	R <sub>g</sub> (fully extended) <sup>c</sup>	R (uniform sphere) <sup>d</sup>
(PDMAEMA <sub>170</sub> ) <sub>9.5</sub>	12.2	8.1	17.1	5.2
(PDMAEMA <sub>170</sub> ) <sub>18</sub>	14.9	8.1	17.1	6.7
(PDMAEMA <sub>240</sub> ) <sub>24</sub>	18.3	11.2	23.9	8.2
PDMAEMA <sub>450</sub>	/	7.2	25.1	/

<sup>a</sup> The theoretical radius was calculated from the equation proposed by Borisov et al.<sup>190</sup>

<sup>b,c</sup> The R<sub>g</sub> data were calculated based on the molecular models from Materials Studio software.

<sup>d</sup> The radius are calculated by assuming a sphere with uniform density and the same mass as PDMAEMA star.

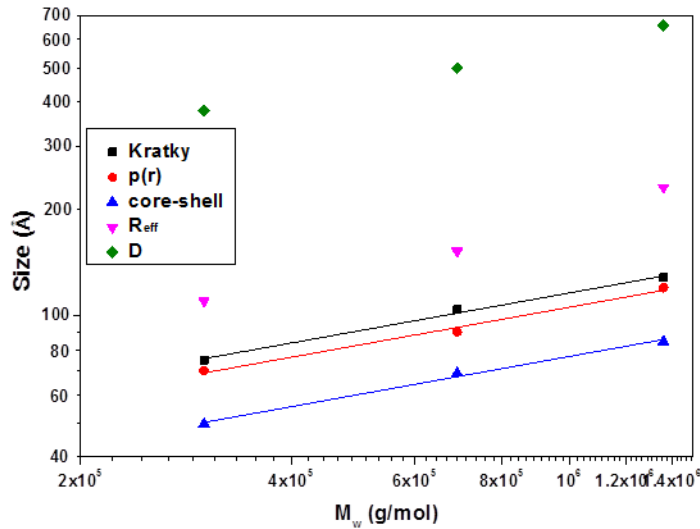


Figure 4.3. Characteristic dimensions versus molecular weight for PDMAEMA star polyelectrolytes. From bottom to top: R<sub>g</sub> from core-shell model,  $\nu=0.36\pm0.02$ ; R<sub>g</sub> from p(r) analysis,  $\nu=0.35\pm0.03$ ; R<sub>g</sub> from Kratky analysis,  $\nu=0.36\pm0.02$ ; effective radius (R<sub>eff</sub>) from MSA structure factor; intermolecular distance (D) from peak position in SANS data.

A log-log plot of experimental R<sub>g</sub> versus M<sub>w</sub> for PDMAEMA star polyelectrolytes is shown in Figure 4.3 (M<sub>w</sub> was taken from light scattering measurements<sup>176</sup>). As known, the radius of gyration is expected to scale with molecular weight as  $R_g = k M_w^\nu$ , where  $\nu$  is 1/3 for dense homogeneous sphere and 0.6 for chains with excluded volume in a good

solvent.<sup>196,197</sup> Our experimental data for PDMAEMA stars shows an exponent  $\nu$  being close to 0.36 for all stars that again indicates the structure is close to dense but swollen spherical particles.

Overall, the analysis of all models considered above indicates that neither random coil/extended distribution or simple dense spherical particles describe experimental results consistently and the estimated star dimensions in dilute solution are usually systematically than those measured experimentally. Therefore, an alternative model of collapsed arms with consideration of the inner structure should be used. For further analysis, we exploited a common core-shell model with a non-uniform density distribution of star polyelectrolytes as theoretically suggested for microphase-separated stars.<sup>198</sup>

Indeed, the fitting of the scattering data with core-shell model combined with MSA structural factor is applicable to all stars studied here (Figure 4.1). Overall, charge-corrected effective diameter of stars from this model is within 11-23 nm, which is close to the star dimensions estimated from Borisov et al<sup>190</sup> (Tables 4.2). This analysis shows that the core radius and shell thickness increase with the number of arms and arm length: core radius increases from 3.5 nm to 6.1 nm and the shell thickness increases from 3.7 nm to 6.2 nm (Table 4.1). The core dimensions are smaller than that estimated for fully collapsed arms (5.2 nm to 8.2 nm, Table 4.2) indicating the presence of significant fraction of loose chain fragments. Moreover, mass fractal model which describes the blob sub-structure of the arm chains shows that the correlation length is around 1.7 nm

and the excluded volume parameter of around 0.6, which again indicates the random coil structure within the blobs.

During the fitting process with core-shell model, both the core radius and shell thickness are fitting parameters, the scattering length density (SLD) of the core and shell regions is first estimated from the comparison of  $R_g$  values (Kratky analysis) with theoretical dimension as a starting value. Then the obtained core radius and shell thickness are fixed, SLD of the core or the shell is set to be the variable to get a more accurate value, after that the radius and thickness are fitted again with the obtained SLD values. The results show that SLD of the shell regions is much higher than that of core region, around  $5.0 \times 10^{-6} \text{ \AA}^{-2}$  for all PDMAEMA stars due to the presence of the  $D_2O$  with high SLD. On the other hand, SLD for cores is  $1.4 \times 10^{-6} \text{ \AA}^{-2}$  for  $(PDMAEMA_{170})_{9.5}$  and even lower,  $1.1 \times 10^{-6} \text{ \AA}^{-2}$  for  $(PDMAEMA_{170})_{18}$  and  $(PDMAEMA_{240})_{24}$  stars.

Such significant difference indicates that the core region has higher concentration of polymer chains and very little solvent content as compared to the shell region with high concentration of deuterated water (Figure 4.4). Such a core-shell model corresponds to quasi-micelle morphology with microphase separation of arms with loose brush-like shells and melt-like morphology of collapsed segments in dense cores due to dominating hydrophobic interactions.<sup>198</sup> Indeed, an estimation of the inner composition of PDMAEMA stars in the regime studied here can be based on the SLD values for bulk materials,<sup>199</sup> core, and shell regions. The volume fraction of solvent (deuterated water) in the core region was estimated to be around 6 % further confirming dense packing of the

collapsed chains. On the other hand, star shells contain up to 76 % of solvent that reflects their highly swollen state (Figure 4.4). Moreover, from direct comparison of chain dimensions evaluated in random coil and extended states one can conclude that chains localized in shells regions are in partially coiled, semi-brush regime.

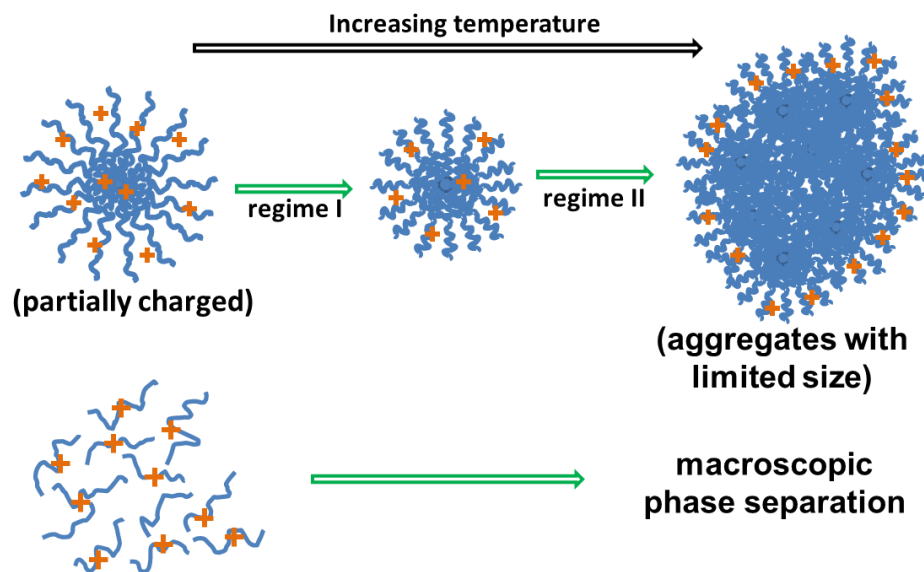


Figure 4.4. The structural changes of PDMAEMA star polyelectrolytes and linear polyelectrolytes at pH around  $pK_a$  upon temperature increase. (For simplification, only one star macromolecule is shown before aggregation.)

Finally, the presence of the broad peaks in the low  $q$  range on SANS curves of star polyelectrolytes indicates a short range ordering of charged stars in a semi-diluted regime in contrast to linear PDMAEMA macromolecules (Figure 4.1). The formation of partially ordered stars has been observed for some star macromolecules and suggested to be controlled by long-range repulsive intermolecular interactions.<sup>190</sup> All peaks are very broad that corresponds to the spatial correlation expanded only over very few neighboring stars. For PDMAEMA stars with different number of arms and arm lengths, the position of the broad peak shifts to the lower  $q$ , which indicates the increasing distance between the stars (Figure 4.3). Distance between stars is within 38 nm - 66 nm,

which is larger than the effective dimensions of star macromolecules (22 nm - 46 nm). These values further confirm the semi-dilute regime with partially ordered individual stars interacting with each other but being far from close contact and overlap.<sup>180</sup>

### **Comparison with fully charged star polyelectrolytes**

The structural differences between weak and strong star polyelectrolytes were also studied by using the quaternized ammonium salts of the PDMAEMA stars obtained by quaternization with methyl iodide.<sup>176</sup> In contrast to the weak star polyelectrolytes considered above, the SANS for qPDMAEMA stars show sharper peaks indicating better intermolecular ordering with significant upturn at low  $q$  (Figure 4.5a). The peaks are shifted to lower  $q$  indicating increased separation of star macromolecules as a result of increased repulsion (Table 4.1). The excessive zero-angle scattering ( $q < 0.08 \text{ \AA}^{-1}$ ) indicates large-scale concentration fluctuations and increasing osmotic pressure within solutions of highly charged stars.<sup>200,180</sup>

Because of expanded state of highly charged stars and higher ordering, core-shell models and pair distance distribution approach are not applicable for these solutions. Kratky analysis shows much sharper peaks, which are significantly shifted to lower  $q$  indicating increase in effective molecular dimensions along with narrowing size dispersion (Figure 4.5b). Moreover, the excluded volume parameter  $v$  in Kratky plots increases to 0.7, which indicates the more expanded local blob structure due to the increasing electrostatic repulsion and osmotic pressure within the star macromolecules.<sup>201</sup>

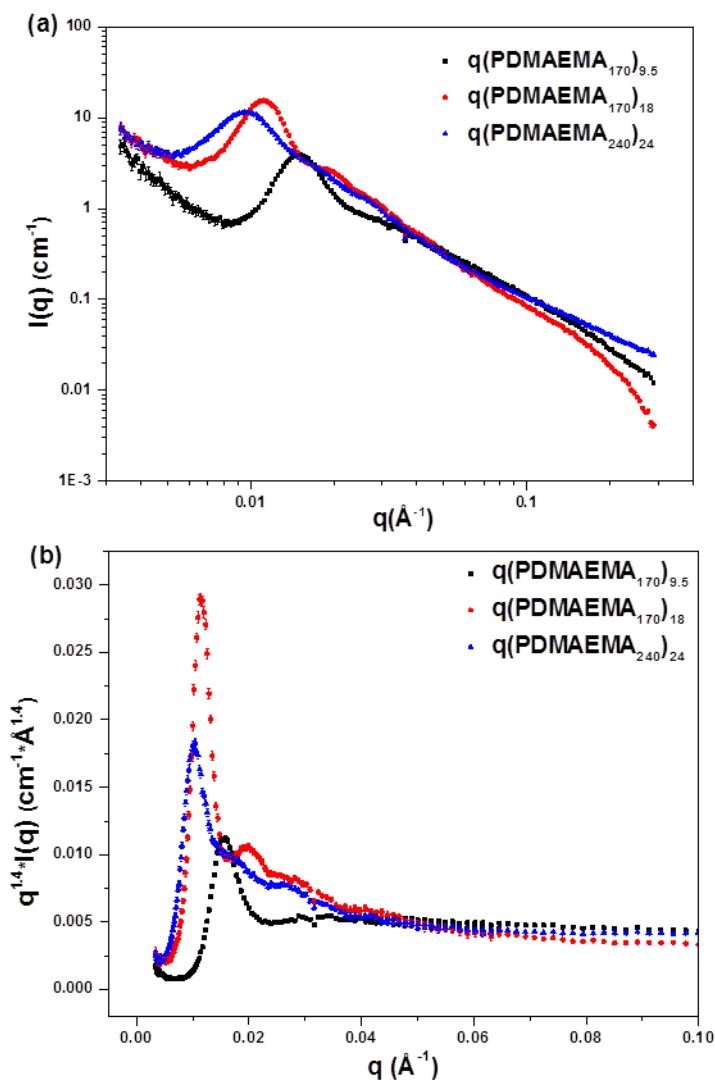


Figure 4.5. (a) SANS data of quaternized PDMAEMA star polyelectrolytes solution (1 wt. % in  $\text{D}_2\text{O}$ ) with different number of arms or arm length. (b) Kratky plot for the corresponding quaternized PDMAEMA star polyelectrolytes.

### 4.3.3 Thermo-Responsiveness of PDMAEMA Star Polyelectrolytes

For further analysis of the thermo-responsive behaviors of star polyelectrolyte solutions at different pH conditions, we selected one type of star polyelectrolyte,  $(\text{PDMAEMA}_{170})_{18}$ , with intermediate arm length and number of arms, the  $\text{pK}_a$  of which is around 5.8.<sup>176</sup> At pH values close to  $\text{pK}_a$ ,  $(\text{PDMAEMA}_{170})_{18}$  stars are partially charged

and the charge density decreases with increasing pH value. It is worth to note that at high pH conditions when the charge density is low, PDMAEMA stars show typical LCST behavior upon increasing temperature.<sup>176</sup> The LCST point is 31 °C at pH 9 but increases to above 80 °C for pH below 7 that is too close to boiling point and cannot be achieved.

The SANS curves was first collected at pH 7.0, which is above the  $pK_a$  for PDMAEMA star polyelectrolytes (Figure 4.6a). In the temperature range from 25 °C to 70 °C dramatic change are observed. Two temperature regimes can be clearly visible: in regime I, from 25 to 45 °C, the scattering curves are similar to that obtained at room temperature with diffuse peak. However, starting from 50 °C the SANS curves changed significantly with low-q scattering dramatically increasing and shifting to lower q (Figure 4.6a).

Kratky analysis of scattering data and pair distance distribution in the temperature regime I show a consistent shift of the peak position towards higher q values and  $p(r)$  maximum position to lower radial values. Therefore, in this temperature regime,  $R_g$  shows a gradual decrease by about 20% up to 45 °C (Figure 4.6b). Moreover, core-shell modeling also confirms the contraction of star macromolecules but additionally shows that the core size remains virtually unchanged, around 5.1 nm, while the shell gradually collapsed with the thickness decreasing by 40% from 4.8 nm to about 2.5 nm at the highest temperature of 45 °C for this regime.

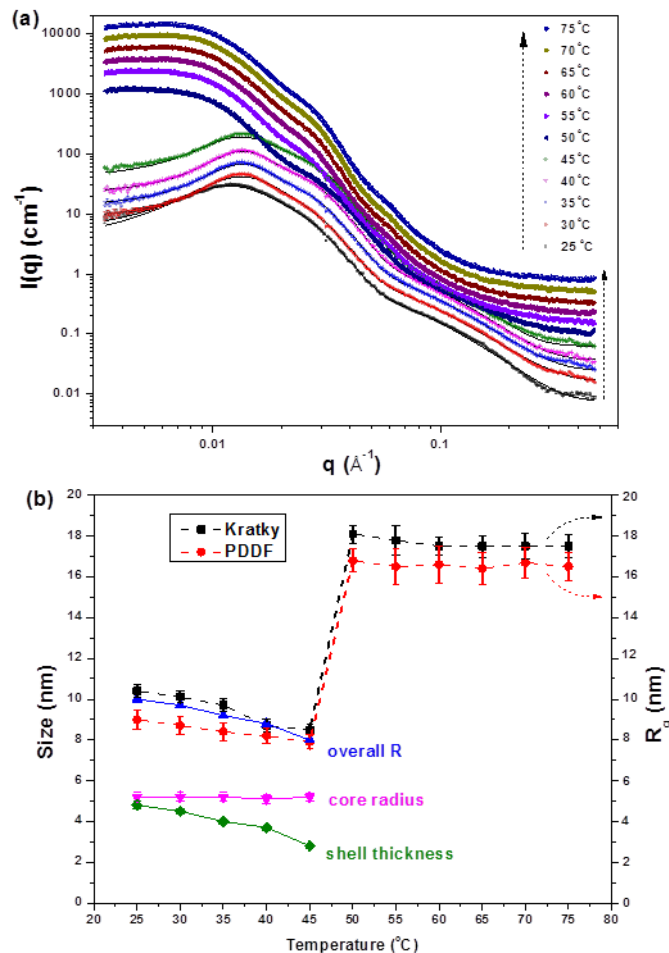


Figure 4.6. SANS of  $(\text{PDMAEMA}_{170})_{18}$  at pH 7.0 at increasing temperature, the curves are mutually offset by a factor of 1.5 for better visualization (temperature increases from bottom to top). The solid lines (from 25 °C to 45 °C) represent the fitting by core-shell model. (b) Temperature dependent dimension changes from core-shell model, Kratky model and pair distance distribution functions for  $(\text{PDMAEMA}_{170})_{18}$  at pH 7.0.

In the temperature regime II (above 50 °C), the diffuse character of scattering makes it unsuitable for using the core-shell model and, thus, only Kratky plots and  $p(r)$  analysis have been employed. These analyses show that the  $R_g$  increases significantly from 8.5 nm at 45 °C to 18.1 nm at 50 °C within very narrow temperature range, and remains virtually unchanged at even higher temperatures (Figure 4.6b). Such dramatic and sharp

change in the characteristic molecular dimensions can be associated with intramolecular microphase separation, as will be discussed later.

SANS measurements were also conducted at pH 5.5, which is slightly below  $pK_a$ , so that the star polyelectrolytes are charged to a higher extent. Similarly to the pH 7 condition discussed above, two distinct temperature regimes are observed in the temperature range from 25 °C to 50 °C and from 55 °C to 75 °C (Figure 4.7a). Similarly, Kratky and  $p(r)$  analysis show a consistent decrease in  $R_g$  with temperature within the first regime, with the core dimensions remain almost constant, around 5.3 nm, and shell gradually collapses by about 30% (Figure 4.7b). Furthermore, at temperatures above 55 °C, the  $R_g$  increases by 50%, to 12.2 nm within narrow temperature interval, and then remains virtually constant at higher temperatures (Figure 4.7b). Overall, the transition temperature is slightly shifted to higher temperature and dimensional changes are less dramatic at lower pH.

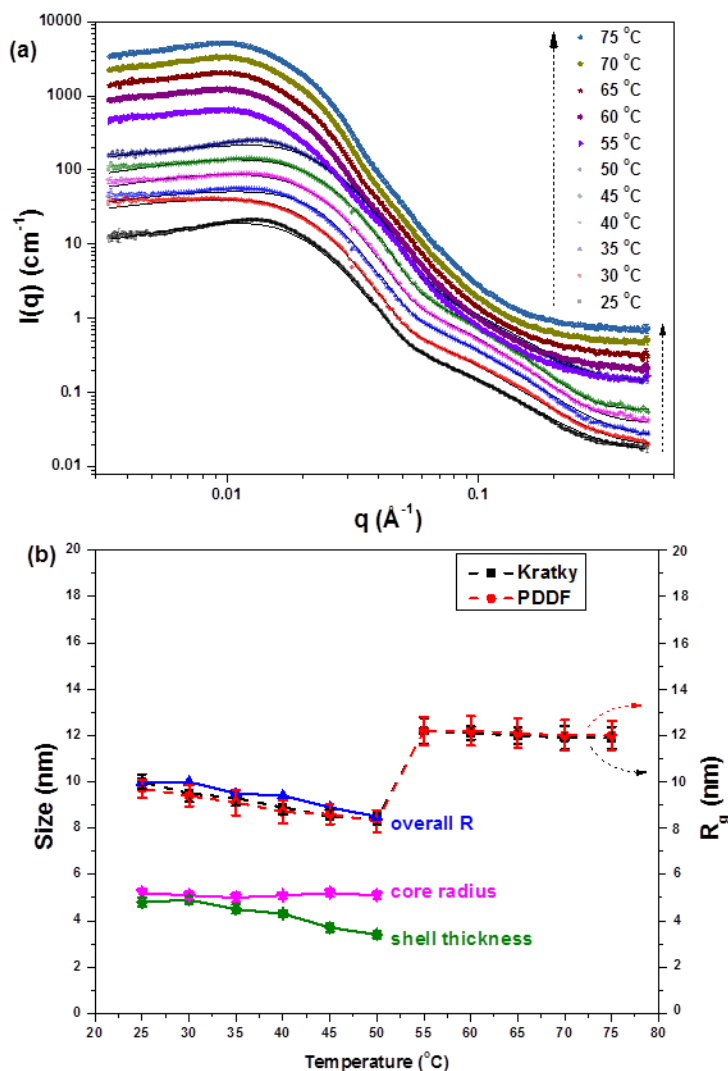


Figure 4.7. SANS data of  $(\text{PDMAEMA}_{170})_{18}$  at pH 5.5 with increasing temperature, the curves are mutually offset by a factor of 1.5 for better visualization (temperature increases from bottom to top). The solid lines (from 25 °C to 50 °C) represent the fitting by core-shell model. (b) Temperature dependent dimension changes from core-shell model, Kratky model and pair distance distribution functions for  $(\text{PDMAEMA}_{170})_{18}$  at pH 5.5.

#### 4.3.4 Comparison with Linear PDMAEMA Polyelectrolytes

Finally, we conducted comparative study of linear PDMAEMA at the same concentration, temperature range, and pH conditions (Figure 4.8). At both pH values studied here, a broad diffuse scattering in the intermediate  $q$  range and increasing scattering intensity at

lower  $q$  are observed below 45 °C. When the temperature increases to 45 °C and above, a significant increase in scattering intensity is observed at low  $q$ . Fitting of the scattering data for linear PDMAEMA was conducted with Ornstein-Zernike model that gives the short-range correlation length,  $\xi$ , of around 1.7 nm at 25 °C with modest variation in a whole temperature range (1.7 nm - 2.4 nm). This is close to the characteristic dimensions of blobs in solutions of star polymers.<sup>180</sup> On the other hand, the DAB model which is applicable here only to SANS curves at elevated temperatures and low  $q$  range, gives the long-range correlation length  $L$  of above 100 nm (at pH 7.0 condition) at 45 °C which further increases at higher temperature and achieves the limit of resolution in this study. The results at lower pH condition (pH 5.5) show similar trends with smaller absolute values.

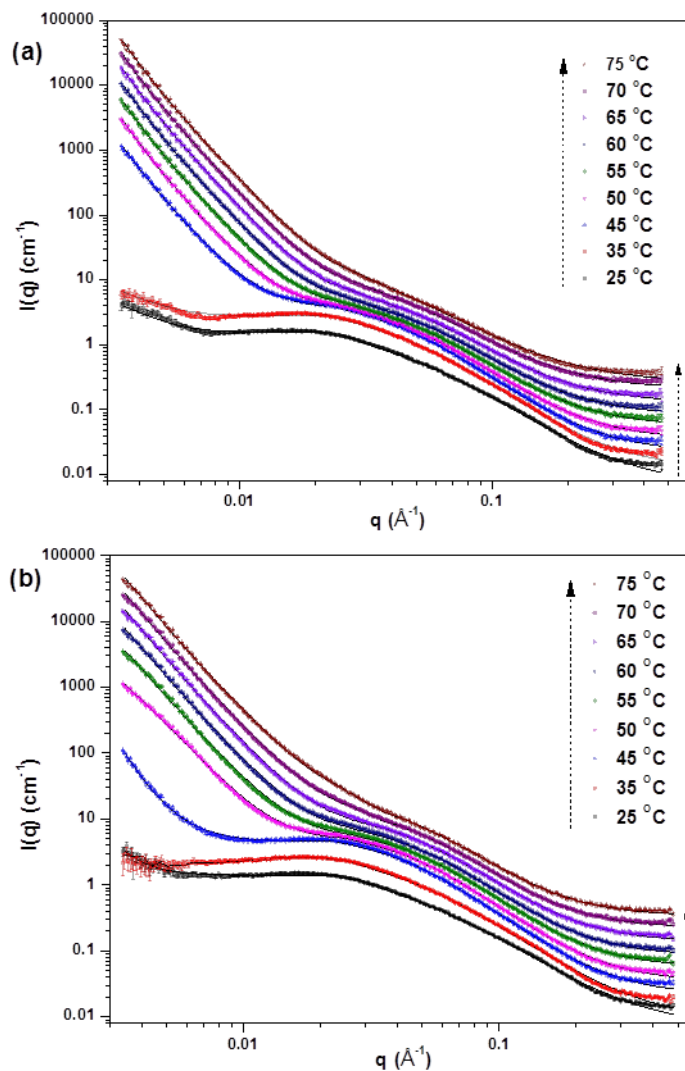


Figure 4.8. SANS data of PDMAEMA<sub>450</sub> at pH 7.0 (a) and pH 5.5 (b) with increasing temperature, the curves are mutually offset by a factor of 1.5 for better visualization (temperature increases from bottom to top). The solid lines are from the combined Ornstein-Zernike and DAB model fittings.

#### 4.3.5 General Discussion

Before general discussion it is worth to note that PDMAEMA polyelectrolytes at pH 5.5, which is slightly lower than the  $pK_a$ , are more charged than at pH 7.0. In addition, since the use of buffer is detrimental in a salt-free system,<sup>176</sup> the pH value in the salt free solution decreases with increasing temperature (e.g., from 7.0 at 25 °C to 5.7 at 75 °C),

which also plays a role in the observed phenomena. Moreover, the pH vs temperature curves for (PDMAEMA<sub>170</sub>)<sub>18</sub> solution shows a kink at around 50 °C, which is close to the transition temperatures between regimes I and II detected in this study. The pH dependence with temperature of PDMAEMA stars with different number of arms in dilute water solution has similar characters.<sup>202</sup>

The results of the dimensional changes for PDMAEMA star polyelectrolytes in semi-dilute solution can be understood in terms of local variations of the balance between intermolecular and intramolecular interactions. General schematics of molecular transformations suggested in this study for star polyelectrolytes are presented in Figure 4.4. Firstly, we suggest that at room temperature, star macromolecules in semi-dilute solution possess core-shell morphology with higher density collapsed cores and less dense shells composed of highly swollen arms as discussed before. In the temperature regime I, the arm chains gradually collapse mainly due to the decrease in the osmotic pressure within stars and the decrease of solvent quality with increasing temperature. Indeed, it has been demonstrated that in semi-dilute solution, temperature increase results in the decreasing concentration of confined counterions and thus, the osmotic pressure decreases within the stars.<sup>203</sup> Moreover, with the increase of temperature, the pH value of PDMAEMA solution slightly decreases that causes the star macromolecules becoming more deprotonated and certain amount of protons are released to the solution. As a result, the charge density of arm chains decreases to a certain extent, which also contributes to the decreased electrostatic repulsion and increased hydrophobic interactions that promotes arm collapse in the outer shells.

At a certain temperature, the sudden transition to a regime dominated by hydrophobic interactions occurs which results in the formation of limited intermolecular aggregates (aggregation number below 10, similar to theoretical estimation<sup>204</sup>) (Scheme 1). During this sharp transition, the strong screening of charges and the increased hydrophobic interaction as well as the attractive force between ion pairs synergistically lead to the limited intermolecular aggregation of neighboring stars. Moreover, the partially charged PDMAEMA star polyelectrolytes contain annealed charges, which can move from one repeat unit to another in an optimum way so that to minimize the loss in translational entropy of the counterions.<sup>163</sup> The annealed charge redistribution results in microphase separation with the formation of hydrophobic clusters consisting of several densely packed hydrophobic domains surrounded by charged hydrophilic regions swollen by solvent, such aggregate structures help them remain stable upon further increase in temperature without macroscopic phase separation,<sup>205</sup> similar phenomenon has also been observed for amphiphilic polyelectrolyte hydrogels before.<sup>206</sup>

The screening of charges by increased counterion condensation and hydrophobic interactions can be considered as the main causes for such aggregation in this temperature regime. The compact structure of star polyelectrolytes provides strong steric repulsion, which effectively prevents large-scale aggregation due to the intermolecular interactions. No macroscopic phase separation occurs and LCST is out-of-reach according to previous studies but the observed limited aggregation can be considered as “pre-transitional” behavior below the phase boundary.<sup>176</sup>

Finally, the effect of pH on the state of PDMAEMA star polyelectrolyte solutions has been revealed in this study as well. Indeed, the size of intramolecular aggregates decreases at pH 5.5 condition due to the stronger electrostatic repulsion, the transition temperature for the microphase separation also increases, and the aggregation number decreases from 10 at pH 7.0 to around 3 at pH 5.5. In contrast, the temperature behavior of solution of linear PDMAEMA polyelectrolytes is very different from that of star PDMAEMA. The high scattering intensity at low- $q$  indicates the presence of large-scale inhomogeneities observed for semi-dilute polyelectrolyte solutions.<sup>207</sup> Significant increase in this scattering at low  $q$  range at elevated temperature indicates large-scale phase separation, which has been further proven by DAB model analysis. As a result, linear PDMAEMA solutions exhibit macroscopic condensation caused by dominating hydrophobic interactions in contrast to core-shell star polyelectrolytes under the same conditions (Figure 4.4).

The structural behavior observed here are underpinned by recent studies, which show that the conformation of polyelectrolyte stars in aqueous solution is controlled by hydrophobic interactions, which promote a collapse of the arms, while the electrostatic forces lead to a swelling of the chains in outer loose shells.<sup>198</sup> In a semi-dilute PDMAEMA star polyelectrolyte solution, electrostatic repulsion results in the partially collapsed arm chains and the size of stars is also smaller compared with that in dilute solution.<sup>175</sup> Moreover, salt- and buffer-free solutions provide negligible electrostatic screening that might further explain the absence of a phase boundary for PDMAEMA

star polyelectrolyte in pure water solution at 0.1 g/L within the experimental window (20 °C to 80 °C).<sup>176</sup>

Indeed, polyelectrolyte brushes possess smaller dimensions at increasing concentration due to the increased counterion adsorption and/or Donnan salt partitioning between the coronal layer and the surrounding medium.<sup>164</sup> Simulation studies showed that for strongly charged polyelectrolyte chains under poor solvent condition in a salt-free solution, the polyelectrolyte concentration plays a vital role in the balance between electrostatic and hydrophobic interactions.<sup>208,209</sup> At low polymer concentration, the polyelectrolyte chains form necklaces of beads connected by strings as solvent quality decreases. At high polyelectrolyte density there is a crossover from dominating electrostatic interaction to a regime where the hydrophobic interactions dominate because of the electrostatic interactions are screened on length scales larger than the correlation length.

The effects of increasing temperature (or decrease of solvent quality) on star polymers were reported, which result in coil-to-globule transition or shrinkage of the stars.<sup>175,210</sup> Moreover, a molecular dynamics study of polyelectrolyte stars showed that the  $R_g$  value consistently decreases with decreasing solvent quality.<sup>211</sup> Another study<sup>203</sup> showed that if the Coulomb interaction strength exceeds a critical value, counterions condense on the chain and ion pairs are formed, so that the charges on the chains are largely screened and the ion pairs also possess a net attraction.<sup>212</sup> The counterion condensation leads to inhomogeneous charge redistribution, and the resulting attractive interaction leads to the

collapse of polyelectrolyte chains and eventually to the formation of intermolecular aggregates.

#### **4.4 Conclusions**

Poly(*N,N*-dimethylaminoethyl methacrylate) (PDMAEMA) star polyelectrolytes with dual , thermo and pH, responsive properties have been studied by *in situ* small-angle neutron scattering at different temperatures and pH conditions in order to reveal their conformational changes in semi-dilute solution. At pH value close to the  $pK_a$ , all PDMAEMA stars studied here are partially charged and show a core-shell quasi-micellar morphology caused by microphase separation with the collapsed core region possessing high monomer density and the hydrated loose brush shell region. Upon increasing the temperature, the PDMAEMA star polyelectrolytes first experience a contraction in the loose shell region while the core size remains almost unchanged, and then start to form intermolecular aggregates within narrow temperature range. With decreasing pH value, the transition temperature increases and the size of the aggregates decreases (average aggregation number decrease from 10 to 3). We suggest that these changes are triggered by the decrease in solvent quality with increasing temperature, which leads to the transition from an electrostatically dominated regime to a regime dominated by hydrophobic interactions. The observed phenomenon is in striking contrast with behavior of linear PDMAEMA polyelectrolytes, which show macrophase separation with increasing temperature under the same conditions.

## Appendix: Supporting Information

### Core-shell model and intermolecular scattering

A spherical core-shell model, which provides the form factor  $P(q)$  for a spherical particle with core-shell structure normalized by the particle volume:<sup>213</sup>

$$P(q) = \frac{\text{scale}}{V_s} \left[ 3V_c(\rho_c - \rho_s) \frac{[\sin(qr_c) - qr_c \cos(qr_c)]}{(qr_c)^3} + 3V_s(\rho_s - \rho_{\text{solv}}) \frac{[\sin(qr_s) - qr_s \cos(qr_s)]}{(qr_s)^3} \right]^2 \quad (1)$$

where  $V_s$  is the volume of the outer shell,  $V_c$  is the volume of the core,  $r_s$  is the radius of the shell,  $r_c$  is the radius of the core,  $\rho_c$  is the scattering length density of the core,  $\rho_s$  is the scattering length density of the shell, and  $\rho_{\text{solv}}$  is the scattering length density of the solvent. The outermost radius (radius plus thickness) is used as the effective radius toward  $S(q)$  when  $P(q)*S(q)$  is applied. The intermolecular interactions can be taken into account by using the structure factor based on mean spherical approximation (MSA) by Hayter et al.<sup>214</sup> The MSA structure factor is suitable for systems consisting of charged, spheroidal objects in a dielectric medium, and can be combined with appropriate form factor (core-shell model in our case).

### Mass Fractal Model

The fractal dimensionality of an ideal random structure exhibiting self-similarity implies that the intensity of radiation scattered at small scattering vectors should have a power-law dependence on the magnitude of the scattering vector. However for any real system,

the scattering law must be modified by the introduction of a correlation length which reflects the finite overall size of the system.<sup>215</sup>

$$I(q) = scale \times P(q)S(q) + background \quad (2)$$

$$P(q) = -F(qR)^2 \quad (3)$$

$$F(x) = \frac{3[\sin(x) - x\cos(x)]}{x^3} \quad (4)$$

$$S(q) = \frac{\Gamma(D-1)\xi^{(D-1)}}{[1+(q\xi)^2]^{(D-1)/2}} \frac{\sin[(D-1)\tan^{-1}(q\xi)]}{q} \quad (5)$$

where R is the radius of the building block, which corresponds to monomer size in our case; D is the mass fractal dimension;  $\xi$  is the correlation length.

### Kratky Plot Analysis

The Kratky representation provides an additional independent way to estimate the radius of gyration of the stars. In the region around the peak, the form factor can be approximated by the Gaussian star form factor of Benoit:<sup>216</sup>

$$P(q) = \frac{2}{fv^4} (v^2 - [1 - \exp(-v^2)]) + \frac{f-1}{2} [1 - \exp(-v^2)]^2 \quad (6)$$

$$\text{where } v = \left(\frac{f}{3f-2}\right)^{1/2} qR_g \quad (7)$$

This form factor is in principle describing star polymers under  $\theta$  solvent conditions, but excluded volume effects for swollen chains are not affecting the Q range around the peak.<sup>217</sup> The position of the maximum of the Benoit form factor,  $v_{\max}$ , can be calculated from the first derivative of expression (6) with respect to  $v$ , and for star polymer with large number of arms ( $f \gg 1$ ),  $v_{\max} \approx 1$ . Radius of gyration can then be calculated by comparing  $v_{\max}$  to the experimentally obtained  $q_{\max}$ , after rearrangement of equation (7) we can get

$$R_g = \left(\frac{3f-2}{f}\right)^{1/2} \frac{v_{\max}}{q_{\max}} \text{ or } R_g = \frac{\sqrt{3}}{q_{\max}}$$

Previous studies<sup>218</sup> showed the values obtained are very close to those from the Zimm evaluation. Therefore, for star polymers whose Guinier regime could not be accessed easily, it is justified to take  $R_g$  value from the Kratky evaluation.

### **Pair Distance Distribution Function:**

The scattering intensity  $I(q)$  is related to the real space pair distance distribution function  $p(r)$  by the following Fourier transformation, which enables the determination of the overall shape and size of the scattering objects. This method allows simultaneous determination of the form factor and structure factor without assuming a model for the shape of the particles, and previous study showed that taking into account the structure factor in fitting the data for arborescent polymers did not change the final result for  $p(r)$ , so no structure factor was considered in the data analysis.<sup>219</sup>

The pair distance distribution function  $p(r)$  goes to zero at  $r = D_{\max}$ , where  $D_{\max}$  is the maximum distance within the scattering objects.<sup>220</sup>

$$I(Q) = \int p(r) \frac{\sin 2\pi r q}{2\pi r q} dr \quad (8)$$

and  $p(r) = \sum_{i=1}^N c_i \varphi_i(r)$ , where  $\varphi_n(r) = 2rs \sin(\pi r n / D_{\max})$

then  $I(Q)$  can be written as

$$I(q) = \sum_{i=1}^N c_i \phi_i(q) \quad (9)$$

where  $\phi_i(q) = \int \varphi_i(r) \frac{\sin 2\pi r q}{2\pi r q} dr$

The coefficient of each base function is found by minimizing the following:

$$\chi^2 = \sum_{i=1}^{N_{pts}} \frac{(I_i^{obs} - I(q_i))^2}{\sigma_i^2} + \alpha \int \frac{d^2 p(r)}{dr^2} dr \quad (10)$$

The second term is a regularization term to ensure that the output is smooth, the minimization is done with a simple linear least square fit.

### **Ornstein-Zernike and Debye-Anderson-Brumberger (DAB) model**

The Ornstein-Zernike model suggests the following functional form:<sup>221</sup>

$$I(q) = \frac{scale}{1+q^2\zeta^2} + B \quad (15)$$

where B is the background and  $\zeta$  is the correlation length of the concentration fluctuation. For example,  $\xi$  is equal to the entanglement distance for a semi-dilute polymer solution and it is equal to the end-to-end distance for very dilute polymers.

The scattering cross section for phase-separated linear PDMAEMA at elevated temperature is treated as a hierarchical structure with two length scales in two distinct q ranges: low q range (DAB behavior) and the high q range (Ornstein-Zernike behavior). DAB model is used to calculate the scattering from a randomly distributed, two-phase system and gives the correlation length (L), which is a measure of the average spacing between regions of the two phases, and the scattering intensity can be expressed by:<sup>222</sup>

$$I(q) = \frac{scale}{(1+q^2L^2)^2} + B \quad (16)$$

where B is the background.

### **Guinier-Porod Model**

The Guinier-Porod model can empirically model widely different structures and provide useful information from the scattering from a nonspherical object.<sup>223</sup> The scattering intensity is given by the two contributions:

$$I(q) = \frac{G}{q^s} \exp\left(\frac{-q^2 R_g^2}{3-s}\right) \quad (11), \text{ for } q < q_1$$

$$I(q) = \frac{D}{q^d} \quad (12), \text{ for } q > q_1$$

$q$  is the scattering variable,  $I(q)$  is the scattered intensity,  $R_g$  is the radius of gyration,  $d$  is the Porod exponent,  $G$  and  $D$  are the Guinier and Porod scale factors, respectively. A dimensionality parameter  $3-s$  is defined, and is 3 for spherical objects, 2 for rods, and 1 for plates. With the requirement that the values of the Guinier and Porod terms and their slopes (derivatives) be continuous at a value  $q_1$ , the following relationships are obtained:

$$q_1 = \frac{1}{R_g} \left(\frac{3d}{2}\right)^{1/2} \quad (13)$$

$$D = I(q)Q_1^d = \frac{G}{q^s} \exp\left(\frac{-q^2 R_g^2}{3-s}\right) \frac{1}{R_g^d} \left(\frac{3d}{2}\right)^{d/2} \quad (14)$$

Note that the value of  $q_1$  does not have to be set; it is calculated internally using the above two equations.

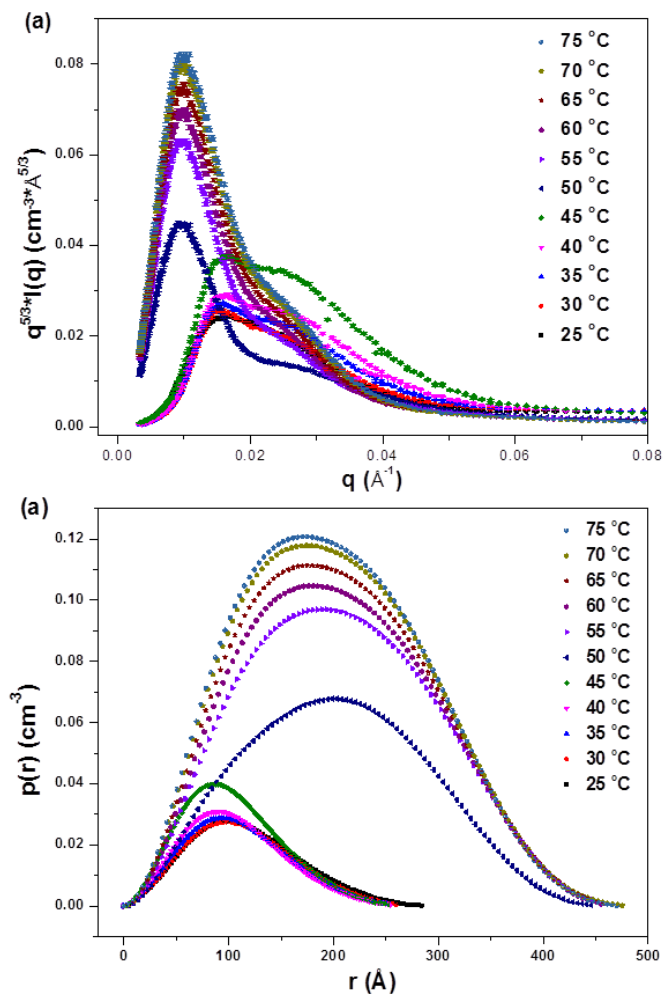


Figure S4.1. Kratky plot (a) and pair distance distribution function (b) for (PDMAEMA<sub>170</sub>)<sub>18</sub> star polyelectrolytes at pH 7.0 with increasing temperature.

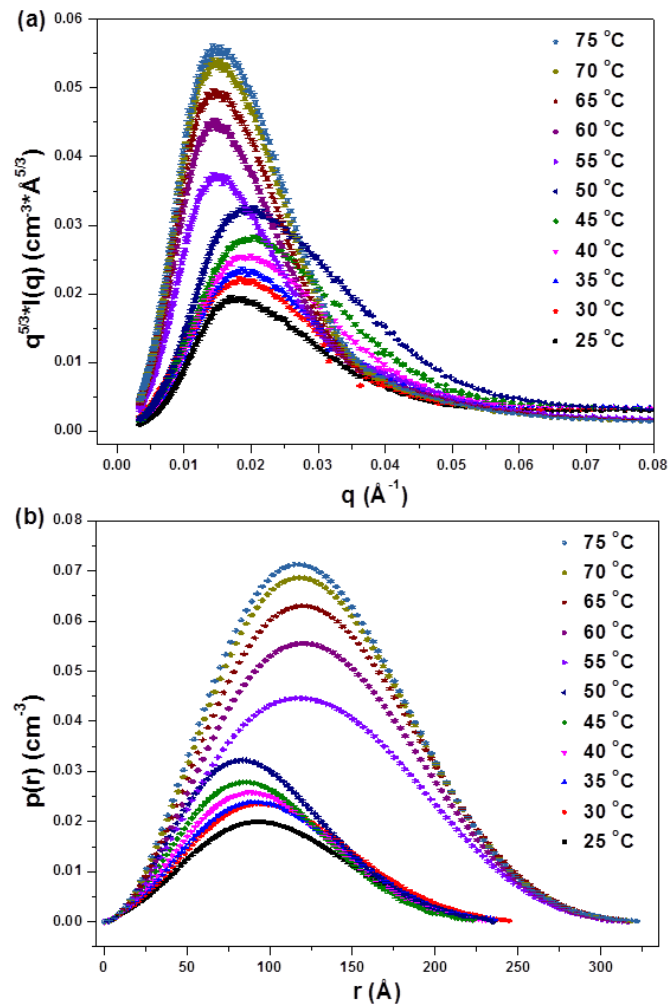


Figure S4.2. Kratky plot (a) and pair distance distribution function (b) for (PDMAEMA<sub>170</sub>)<sub>18</sub> star polyelectrolytes at pH 5.5 with increasing temperature.

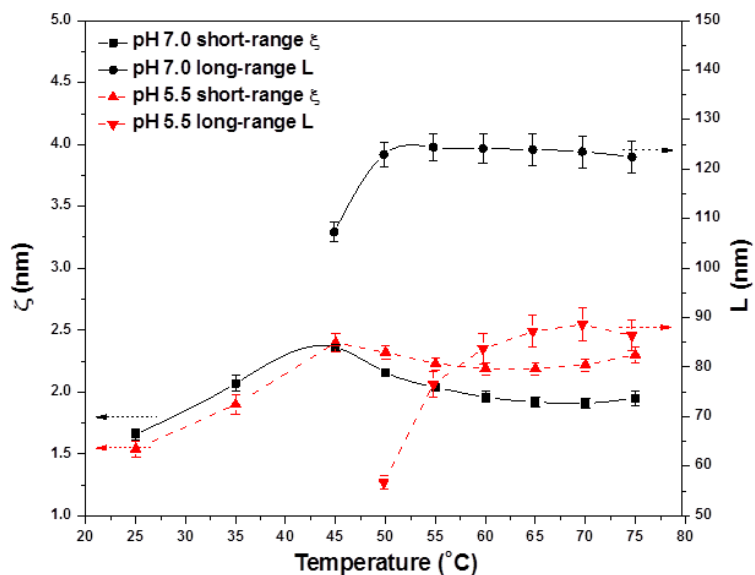


Figure S4.3. Fitting results from Ornstein-Zernike model and DAB model for PDMAEMA<sub>450</sub> linear polyelectrolytes at pH 7.0 and pH 5.5 with increasing temperature. The lines are just drawn to guide the eyes.

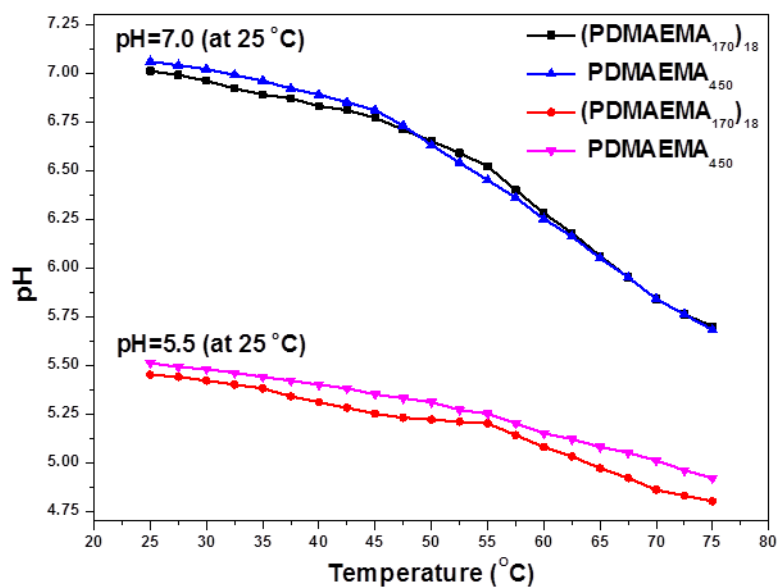


Figure S4.4. The changes of solution pH with increasing temperature for (PDMAEMA<sub>170</sub>)<sub>18</sub> and PDMAEMA<sub>450</sub> at a concentration of 1 wt %. The lines are just drawn to guide the eyes.

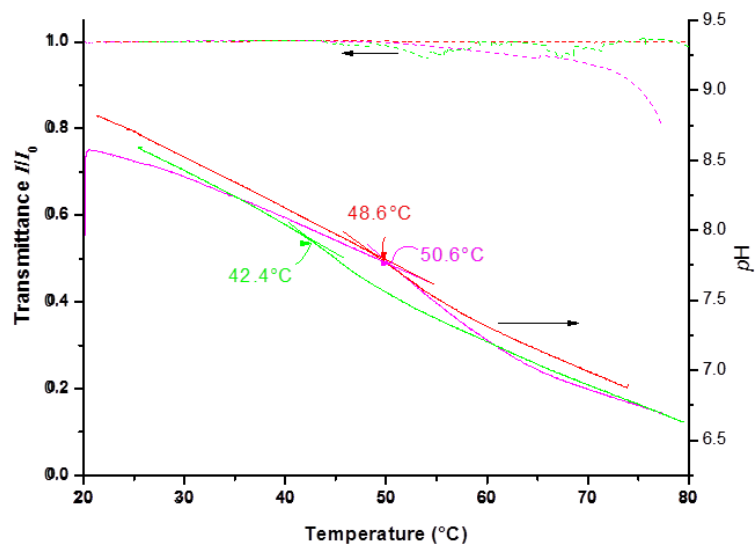


Figure S4.5. pH dependence with temperature for solutions of (PDMAEMA<sub>170</sub>)<sub>9,5</sub> (magenta), (PDMAEMA<sub>170</sub>)<sub>18</sub> (red) and (PDMAEMA<sub>240</sub>)<sub>24</sub> (green) in Millipore water (full lines; all 1.0 g/L; dashed lines: turbidity results)

## CHAPTER 5. INTERFACIAL RESPONSIVE PROPERTIES AND ASSEMBLY OF STAR-GRAFT QUARTERPOLYMERS

### 5.1 Introduction

Recent advances in polymer chemistry enable the synthesis of complex star block copolymers with well-defined architectures and multiple functionalities.<sup>224</sup> When the arms of star block copolymers are composed of stimuli-responsive chains, the stars become a unique class of responsive materials,<sup>225</sup> because their responsive properties are quite distinct from their linear counterparts due to the spatial confinement and complex intramolecular interactions of the different arms.<sup>226,89</sup> In order to systematically study the responsive properties and assembly of star block copolymers at the molecular level,<sup>85</sup> their confinement at interface is necessary,<sup>227</sup> and allows to control the intermolecular interactions precisely.<sup>24,228</sup> For example, the segmental orientation of a dye labeled poly(methyl methacrylate) (PMMA) single chain in two dimensional space can be studied by Langmuir–Blodgett (LB) technique and defocus fluorescence imaging with high accuracy.<sup>229</sup> Langmuir monolayers of thermally-responsive linear pentablock copolymer at the air/water interface showed that the surface morphology of the monolayer depend on the sub-phase pH and temperature and the corresponding reorganization of the central and terminal blocks.<sup>230</sup> Reversible response is only observed at pH close to  $pK_a$ , the surface area of the copolymers increases by 10% when the temperature increases from 25 °C to 50 °C.

However, multicomponent amphiphilic star block copolymers are much less studied at air/water interface,<sup>231</sup> and the majority of the star macromolecules studied are responsive

only to one specific stimulus.<sup>232</sup> For example, study on arborescent PS-g-PEO copolymers at the air/water interface showed that with the increase of temperature, the star polymers start to associate and form clusters or ribbon-like superstructures.<sup>233</sup> Such reorganization is due to the conformational changes of PEO chains and increased van der Waals force between PS chains. Three-arm star block copolymers with PS core and PEO arms formed 2D micelle-like aggregates at low surface pressure,<sup>234</sup> and these domains underwent aggregation including micellar chaining upon compression. The role of architecture of amphiphilic star polymers has been studied by using star block copolymers composed of PEO core and PS arm or the reversed structure.<sup>235</sup> The results showed that when PEO is the core, there is a stronger intra- and intermolecular aggregation; while when PEO resides in the corona, spreading occurs.

Similar aggregation behavior was also observed for micelles from branched molecules.<sup>21</sup> For instance, Goedel et al.<sup>236</sup> reported that for Janus micelles with PS and PMMA arms and cross-linked polybutadiene core can form uniform circular domain at the air/water interface, and each spherical domain is composed of approximately 7 molecules. The PMMA chains spread out on the substrate, while the hydrophobic PS and PB chains are effectively dewetted from the surface and form aggregates. Study on heteroarm star polymers with PEO and PS arms of different lengths showed that the ratio of hydrophobic/hydrophilic arms has significant effect on their assembly at the air/water interface.<sup>237</sup> Low PEO content leads to stripe and netlike morphologies, moderate PEO content leads to ordered 2D circular domains, and high PEO content results in smooth uniform monolayers.<sup>238</sup>

On the other hand, Langmuir monolayers from amphiphilic heteroarm star polymers containing 12 alternating PS and PAA arms were studied,<sup>239</sup> and the results showed that the PS and PAA arms segregated at the opposite side of the air/water interface, and the stars spontaneously formed pancake-like micelles at low surface pressure. Another study<sup>240</sup> reported the surface behavior of the star block polymers and their precursors, including  $PS_nP2VP_n$  star copolymers and  $PS_n(P2VP-b-PtBA)_n$  star terpolymers. Results showed that the surface morphology of  $PS_nP2VP_n$  stars strongly depend on subphase pH: at low pH the stars form large circular micelles, which are readily transformed to the labyrinth morphology upon further compression.  $PS_n(P2VP-b-PtBA)_n$  stars with hydrophobic end blocks maintain circular unimolecular micelle morphology at different surface pressures.

Thermo-responsiveness is one of the most interesting categories of stimuli-responsive polymers.<sup>154</sup> The most extensively investigated thermo-responsive polymer is poly(N-isopropylacrylamide) (PNIPMA) with a lower critical solution temperature (LCST) at around 33°C. PNIPAM containing copolymers have been widely used to form micelles,<sup>241</sup> hydrogels,<sup>242</sup> thin films<sup>243</sup> and microcapsules.<sup>244</sup> However, there are only few reports about their thermo-response at the air/water interface.<sup>245</sup> It is found that although the driving force for the responsive behavior of PNIPAM is the same both in solution and at interface, the conformational changes and the extent of reorganization are different and can be manipulated by packing density, compression rate and subphase conditions.<sup>246</sup>

In this report, we discuss novel star-graft quarterpolymers  $\text{PS}_n[\text{P2VP-}b\text{-(PAA-}g\text{-PNIPAM)}]_n$ , which are responsive to multiple external stimuli such as pH, temperature and ionic strength due to the presence of ampholytic P2VP-*b*-PAA arms and grafted PNIPAM blocks (Figure 5.1). The conformational changes as well as the aggregation behavior within Langmuir and Langmuir-Blodgett (LB) monolayers are monitored by  $\pi$ -A isotherms, atomic force microscopy (AFM), ellipsometry and contact angle measurements. The increase in either pH or temperature leads to a larger molecular surface area of the stars, while the former is due to the changes in ionization degree of PAA and P2VP blocks, and the latter is due to the rise of PNIPAM chains from subphase to the interface during LCST transition. The results provide an insight to the responsive behavior of complex star block copolymers in stimuli controlled assembly under interfacial constraints.<sup>247</sup>

## 5.2 Experimental Section

**Material.** The  $\text{PS}_n(\text{P2VP-}b\text{-PAA})_n$  heteroarm star block terpolymers were synthesized via a one-pot/four-step sequential “living” anionic polymerization procedure (an extended “in-out” method), which was described in detail elsewhere.<sup>248</sup> Briefly, *sec*-BuLi was used as the initiator to prepare “living” PS chains in the first step, then the PS chains were used to polymerized a small quantity of DVB, resulting in a living star-shaped PS bearing active sites in the PDVB core. Then the “living” star polymers were used to initiate polymerization of 2VP, leading to a second generation of P2VP arms. Finally, *t*BA was polymerized from the end of each P2VP arms. The  $\text{PS}_n(\text{P2VP-}b\text{-PAA})_n$  terpolymers were obtained after acidic hydrolysis of the *Pt*BA blocks. In order to graft

PNIPAM chains to the PAA blocks, PNIPAM-NH<sub>2</sub> chains with M<sub>n</sub> of 5500 (purchased from Aldrich) were grafted to the carboxylate groups of PAA in the presence of 1-Ethyl-3-(3-dimethylaminopropyl) carbodiimide (EDC). The detailed characterization of the final star-graft quarterpolymers PS<sub>n</sub>[P2VP-*b*-(PAA-*g*-PNIPAM)]<sub>n</sub> can be found in<sup>249</sup> and some characteristics are summarized in Table 3.2.

***Electrophoresis and Titration*** Zeta-potential measurements were carried out at 25 °C by Zetasizer Nano-ZS equipment (Malvern). The excitation light source was a 4 mW He–Ne laser with wavelength of 633 nm and the intensity of the scattered light was measured at 173°. A series of PS<sub>n</sub>[P2VP-*b*-(PAA-*g*-PNIPAM)]<sub>n</sub> solutions of different pH values (from 1 to 12) and at a concentration of 0.2 wt% were prepared in H<sub>2</sub>O for the electrophoresis measurements. Potentiometric titrations were performed with a Schott Lab 850 pH meter, star-graft quarterpolymers solution in nanopure water with a concentration of 1 mg/mL was prepared, and 0.1 M HCl was added until the pH reached to 3.00. Aliquots of 5 μL of 0.1 M NaOH were added dropwise to the solution continuously under stirring to pH 11.0. The pH value was recorded after each 5 μL of NaOH was added.

***Molecular Model*** The simplified molecular models of free chains were built with Accelrys Materials Studio 3.1. The energy of the structures were minimized using the Discover tool (CVFF force field), combined with cycles of molecular dynamics.

## 5.3 Results and Discussion

### 5.3.1 Molecular Structure and Solution Properties

The star-graft quarterpolymers  $PS_n[P2VP-b-(PAA-g-PNIPAM)]_n$  have two class of arms, one is PS arm with degree of polymerization (DP) of 33, the other is P2VP-*b*-PAA block copolymer with grafted PNIPAM (DP=48) chains on PAA block (DP of P2VP: ~130, DP of PAA: 69 or 119) (Figure 5.1a). In this study, we choose three star-graft quarterpolymers with the same chemical composition but different arm number or PNIPAM grafting density. Briefly, SG2 has 9 PS arms and 9 P2VP-*b*-(PAA-*g*-PNIPAM) arms, with 4.5 PNIPAM chains per PAA block on average; SG3 has the same number of arms, but 11.0 PNIPAM chains per PAA block; and SG4 has 22 PS arms and 22 P2VP-*b*-(PAA-*g*-PNIPAM) arms, with 4.0 PNIPAM chains per PAA block. The detailed information of star composition can be found in Table 3.2 and Table S5.1, and the molecular models of one arm in ideal random coil conformation are presented in Figure 5.1b.

The hydrophilic block copolymer arms consist of oppositely charged P2VP and PAA, which can interact with each other through electrostatic or hydrogen bonding depending on the pH condition. At acidic conditions, the P2VP block is protonated and positively charged, in basic condition PAA is deprotonated and behaving as negatively charged polyelectrolyte, but in the isoelectric region, the two blocks interact with each other electrostatically and are mutually neutralized.<sup>250</sup> The zeta potential of the SG3 stars and their precursor stars at different pH conditions are shown in FigureS5.1a, which shows that the isoelectric region is between 4 and 7. Potentiometric titration was also performed

on the SG3 stars (FigureS5.1b), the titration curve shows a biphasic feature, and the isoelectric point estimated from the curve is 5.8, the isoelectric region is pH 4.20 - 7.5 that supports the zeta-potential measurements.

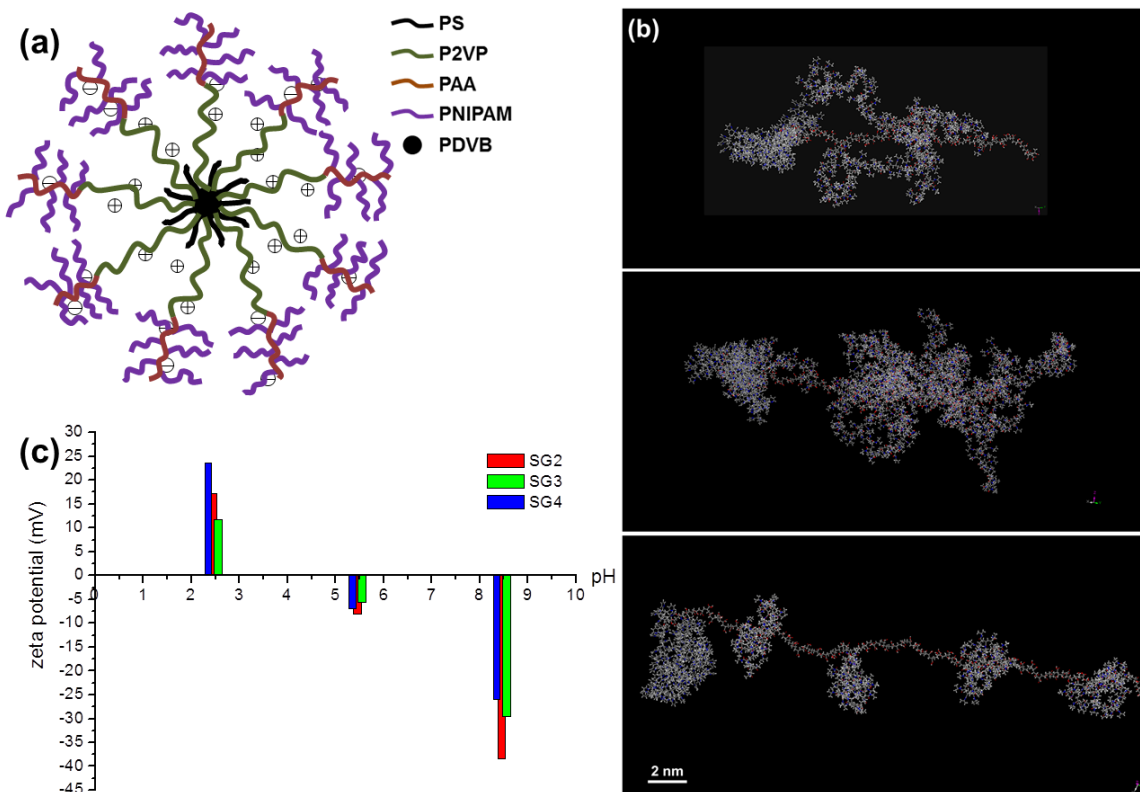


Figure 5.1. (a) Molecular architecture and chemical composition of  $PS_n[P2VP-b-(PAA-g-PNIPAM)]_n$ . (b) Molecular models of one arm of the SG2, SG3 and SG4 stars (from top to bottom) in ideal random coil conformation, scale bar is 2 nm. (c) pH dependence of Zeta potential for 0.2 wt.% aqueous solutions of the star-graft quarterpolymers.

The solution properties of  $PS_n(P2VP-b-PAA)_n$  star terpolymers have been reported earlier.<sup>248</sup> At low pH condition, the stars self-assemble into multicore micelles, and the driving force for self-assembly is mainly intermolecular hydrogen bonding between PAA blocks. Moreover, the hydrogen bonding between PAA blocks is suppressed at elevated temperature. In the isoelectric region, the stars precipitate from solution due to strong intramolecular electrostatic attraction. When the pH increases to basic condition, the

stars transform from bis-hydrophilic (P2VP and PAA) to bis-hydrophobic (PS and P2VP), with charged PAA corona and PS/P2VP concentric compartmented hydrophobic core.

Similar to the precursor,  $PS_n(P2VP-b-PAA)_n$  stars discussed above, the phase behavior and solution properties of the  $PS_n[P2VP-b-(PAA-g-PNIPAM)]_n$  stars are also strongly pH dependent. The P2VP and PAA blocks undergo ionization to different extent depending on the pH condition, which leads to different overall charging state of the star-graft quarterpolymers. As shown in Figure 5.1c, at pH 2.5 the zeta potential of the SG4 is around +24 mV due to the positively charge P2VP blocks, at pH 5.5 the zeta potential is around -6 mV due to the neutralization of PAA and PVP, and at pH 8.5 the zeta potential is around -26 mV due to the negatively charged PAA blocks as reported elsewhere.<sup>249</sup>

Upon increasing temperature of dilute solution of the star-graft polymers studied here, intermolecular association was observed above a critical temperature due to the coil-to-globule transition of PNIPAM chains and increased hydrophobic interaction.<sup>249</sup> The cloud points for SG2 and SG3 stars are around 35 °C at pH 2.5 and pH 5.5. While at pH 8.5 there is no cloud point detected for SG2 stars, the cloud points of SG3 stars shift to higher temperature, the main reason is due to the increased electrostatic repulsion from the charged PAA blocks in the shell region at high pH condition. For higher concentration (3 wt.%) solution of the star-graft quarterpolymers, there is a sol-gel transition upon increasing temperature, which strongly depend on the pH, ionic strength and PNIPAM graft density.

### 5.3.2 Langmuir Monolayers: pH-Responsive Behaviors at the Air/Water Interface

Study on the pH-responsive behavior of the precursor  $PS_n(P2VP-b-PAA)_n$  stars at air/water interface showed that the limiting molecular surface area is the highest at the isoelectric region due to the pancake conformation of star macromolecules with widely spread arms at the air/water interface.<sup>251</sup> Star polymers with a small number of arms (9) show pronounced pH-dependent reorganization, changing from circular micelles to labyrinth morphology upon compression. On the other hand, 22 arm star polymers have stable circular micelles morphology under various pH conditions due to the limited interpenetration and suppressed entanglement of crowded arms.

For the  $PS_n[P2VP-b-(PAA-g-PNIPAM)]_n$  stars, due to the grafted PNIPAM chains, their pH responsive behaviors at the air/water interface is more complicated. It can be seen that the  $\pi$ -A isotherms (Figure 5.2a) follow similar, S-shaped trend upon compression, the surface pressure slowly increases at high molecular areas, followed by a sharp increase as the Langmuir monolayer is further compressed, and finally experience a second slow increase stage. Based upon our previous studies and AFM results which will be discussed later, we suggest that at high molecular area (low pressure), the SG3 stars are well separated and have relatively extended chain conformation, limited intermolecular aggregates are also possible due to the attractive interaction between the hydrophobic blocks. With the further decrease of molecular surface area, the stars form a dense monolayer, leading to a sharp increase in surface pressure. Finally, further compression initiates PNIPAM chains to gradually desorb from the interface and submerge in the aqueous subphase to form tails.<sup>246</sup> There is also obvious isotherm

hysteresis during the compression-expansion cycles (Figure S5.2), which is due to the intermolecular interaction and chain entanglement during compression, the arms do not have enough time to recover to their initial conformation during expansion. Moreover, the conformational difference would be smaller during multiple cycles of compression and expansion and, eventually, a quasi-static monolayer state may be achieved.

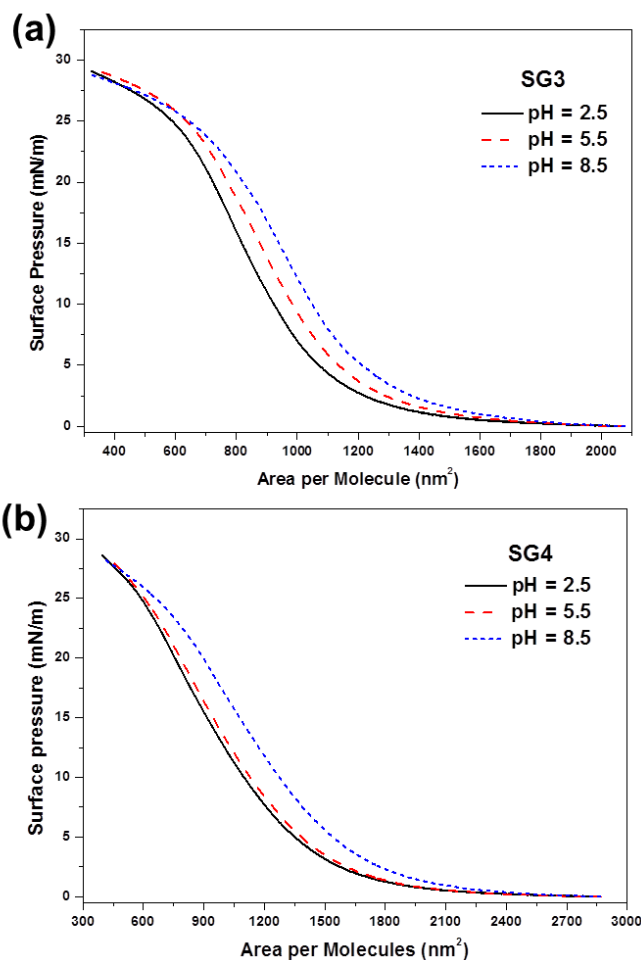


Figure 5.2. Pressure-area isotherms of SG3 (a) and SG4 (b) stars at 25 °C and different pH conditions (2.5, 5.5, and 8.5), and the subphase is 0.1 M NaCl solution.

With the increase of pH from 2.5 to 8.5, the molecular surface area of the stars at the same surface pressure has an increase trend (Figure 5.2a). The limiting mean molecular area (MMA) of SG3, which was determined by extrapolating the steeply rising part of the

curves to zero surface pressure, increases by 16.6 % from pH 2.5 to pH 8.5 (Figure 5.3a). From the limiting MMA, the calculated radii of the SG3 stars are in the range from 18.5 to 20.0 nm at different pH conditions. On the other hand, the molecular model of one arm of the SG3 star has a size of 20.0 nm in ideal random coil conformation (Figure 5.1b) (without considering the ionization of PAA or P2VP), and 43.4 nm at fully extended chain conformation. Therefore, the overall size of the SG3 star at the air/water interface upon compression is close to the size of a neutral star molecule when the arms are in ideal random coil conformation.

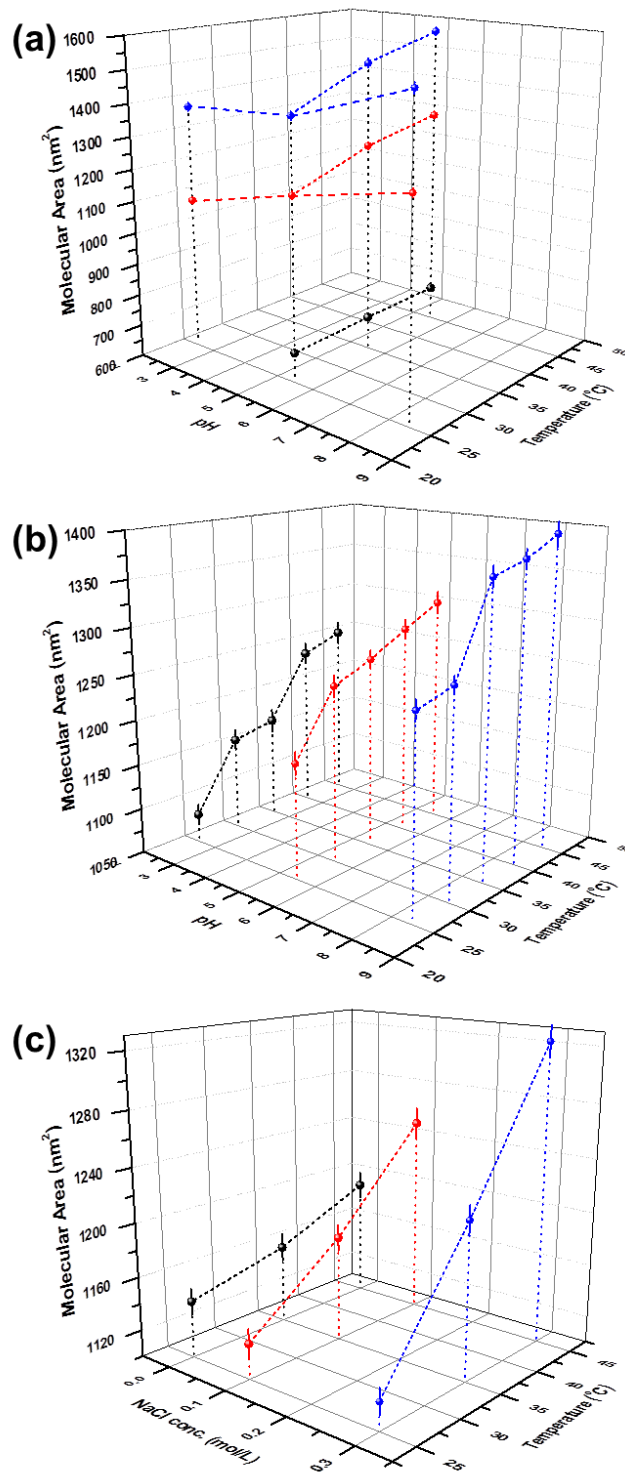


Figure 5.3. (a) The change of MMA of SG3 and SG4 stars with pH, as well as SG2, SG3 and SG4 stars with increasing temperature (black: SG2, red: SG3, blue: SG4). (b) The change of MMA of SG3 at different pH conditions with increasing temperature (black: pH 2.5, red: pH 5.5, blue: pH 8.5), (c) the change of MMA of SG3 at different ionic conditions with increasing temperature (black: H<sub>2</sub>O, red: 0.1 M NaCl, blue: 0.3 M NaCl). The dash line is a guide for the eyes.

It is worth to note that LB monolayers discussed here were obtained by transferring the monolayer at the air/water interface to a hydrophilic surface of a silicon wafer at different conditions (pH, temperature, surface pressure). The transfer ratios are very close to 1.0 in all cases, which indicate the transfers are reliable and repeatable without changes in materials during transfer. As known, for linear and crystalline polymers, it is possible that the Langmuir deposition might lead to some changes of the orientation<sup>252</sup> and crystallinity<sup>253</sup> of the chains but does not affect much less ordered polymers such as star polymers.<sup>254</sup> Moreover, previous studies in our group have utilized X-ray reflectivity to study Langmuir monolayers of branched polymers at the air/water interface in comparison to the LB monolayer.<sup>255,256</sup> The results showed that the organization or assembly of the star polymers is not affected by the transfer process with the star polymers becoming somewhat squashed after transferring to the air/solid interface as suggested in this study as well (Figure 5.5).

Furthermore, the LB monolayers show a high density of granule structures in all three different pH conditions (Figure 5.4). But the size and height of the granules are quite different: they are compact at pH 2.5, while more flat and spread at pH 5.5 condition. To consider the significant differences of the interfacial assembly at different pH conditions, we compare the theoretical number of star macromolecules with the actual number of granule domains as obtained from AFM images, in order to get the average aggregation number ( $\Gamma$ ) of each granule. It has been showed that  $\Gamma=A/(N_g*\sigma)$ , where A is the scanned area of the AFM image,  $N_g$  is the number of granule domains obtained from the AFM image, and  $\sigma$  is the mean molecular area of the stars during transfer as obtained

from the isotherm.<sup>234</sup> The results show that at pH 2.5, the granules or micelles are composed of 2.0 star macromolecules on average, at pH 5.5 the micelle size increases and they are composed of 4.5 stars. But at pH 8.5 the very fine granules are mostly composed of a single star molecule.

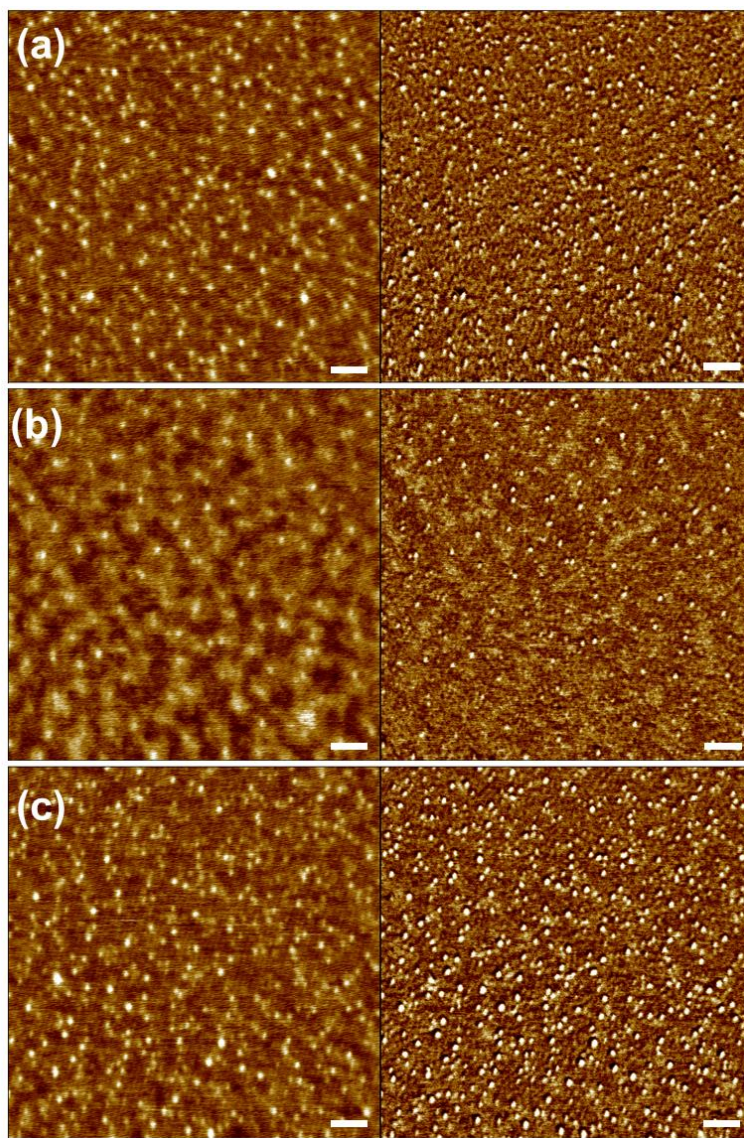


Figure 5.4. AFM topography (left) and phase (right) images of SG3 LB monolayer deposited at 25 °C and at 1 mN/m with different pH conditions: (a) pH = 2.5, (b) pH = 5.5, (c) pH = 8.5. The scale bar is 100 nm, Z range is 3 nm (topography) and 8° (phase).

The pH-dependent molecular surface area and the aggregation behavior are controlled by the ionization degree of the P2VP and PAA blocks as depicted in models in Figure 5.5. At pH 8.5, the P2VP blocks are essentially neutral and hydrophobic, so they blocks tend to adopt compact coil conformation and stay at the air/water interface.<sup>257</sup> At the same time, the outer PAA blocks are highly charged, so they are highly extended in the subphase due to strong electrostatic repulsion. Therefore, at basic pH condition, the molecular surface area of the stars is larger and they remain isolated due to the highly charged repulsive shell. At pH 2.5, the P2VP blocks are highly charged and tend to submerge into the water subphase even at low surface pressure. On the other hand, the PAA blocks form hydrogen bonding with the PNIPAM chains, which results in a collapsed chain ends, or a collapsed shell for the stars, which can shield the positive charge of P2VP blocks to a certain extent, as a result, the molecular area of the stars is smaller at acid conditions, and they tend to form intermolecular aggregates composed of two star macromolecules on average as discussed earlier. This also explains the  $\xi$ -potential of the star-graft quartepolymers decreases with the PNIPAM graft density (Figure 5.1c).

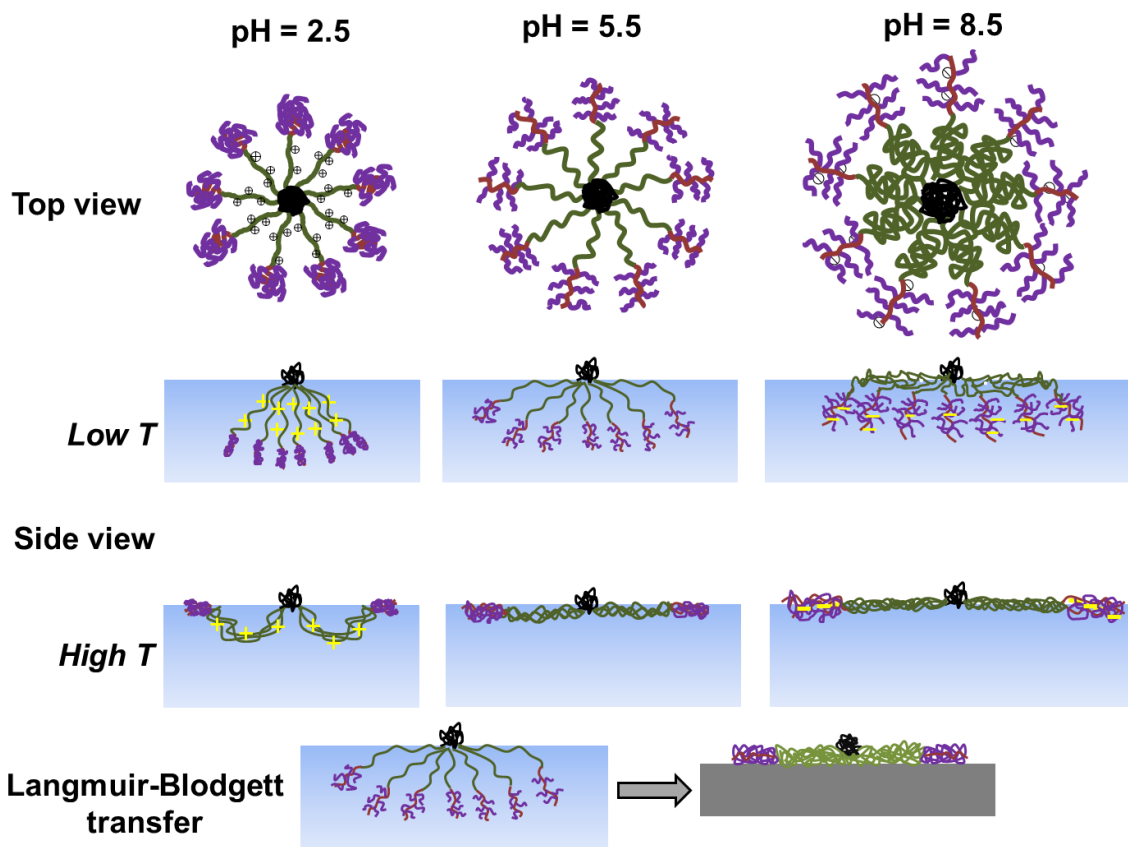


Figure 5.5. Schematic of the molecular conformation of stars at air/water interface with different pH conditions (2.5, 5.5 and 8.5), as well as the structural changes of the stars upon increasing temperature. The top row corresponds to the top view, the middle two rows correspond to the side view of the stars at air/water interface, the bottom row represents the conformational change of the star during LB transfer.

Lastly, at pH 5.5 which falls in the isoelectric region, the overall star is essentially neutral and the molecular area is in between those of pH 2.5 and pH 8.5 conditions. Also at pH 5.5 the stars have a stronger tendency to aggregate due to the reduced electrostatic repulsion (Figure 5.5). One important effect of the introduction of PNIPAM chains on the PAA block is that they can effectively shield the charges on the PAA blocks. For the  $PS_n(P2VP-b-PAA)_n$  precursor stars, in the isoelectric region (pH between 4.2 and 7), the partially charged P2VP blocks and PAA blocks interact with each other electrostatically, resulting in a pancake like structure with the highest molecular area at the interface.

However, for the  $PS_n[P2VP-b-(PAA-g-PNIPAM)]_n$  stars at pH 5.5 condition, the PNIPAM chains largely prevent the intramolecular electrostatic interaction between PAA and P2VP, and enhance the overall solubility of the stars.

The thickness of the SG3 LB monolayer is within 1.0 to 2.0 nm, and controlled by the pH condition and temperature of the monolayer formation. The thickness decreases with increasing subphase pH or temperature, and also depends on the surface pressure (Figure 5.6a). The monolayer deposited at 10 mN/m is much thicker (by 30% - 80%) than that at the lower surface pressure of 1 mN/m. The LB monolayer deposited at pH 2.5 is modestly hydrophobic with the average contact angle of  $52.2^\circ \pm 0.6^\circ$ , and more hydrophilic at pH 8.5 (the average contact angle decreases to  $40.6^\circ \pm 1.0^\circ$ ) (Figure 5.6b). The reason for such difference is that at acidic condition the stars have compact structure with the smallest molecular surface area, thus hydrophilic arms are squeezed within subphase and hydrophobic cores are exposed at the topmost surface (Figure 5.5).<sup>258</sup>

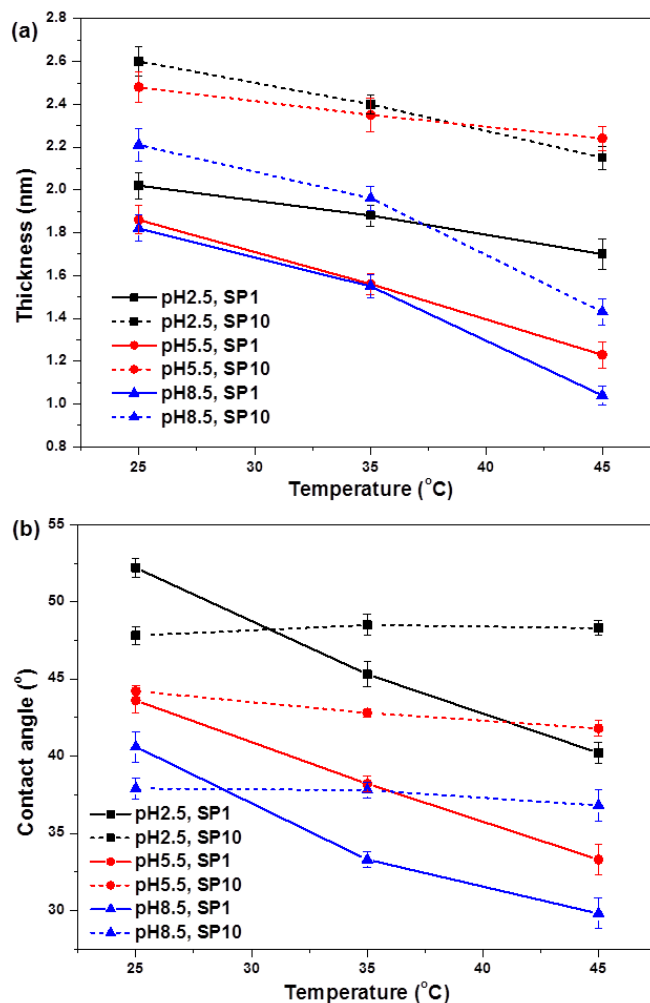


Figure 5.6. The thickness (a) and the contact angle (b) changes of the SG3 LB monolayers at different pH, temperature and surface pressures.

The arm number of the stars is found to have influence on their pH-responsive behavior (Figure 5.2b). The larger number of arms restricts the molecular organization within Langmuir monolayers, so the surface behavior is less dependent on pH condition of the subphase. The 22 arms in SG4 star have a much higher molecular surface area as compared to 9 armed SG3 stars. On the other hand, the changes in isotherms of 22 armed SG4 stars with pH condition are less pronounced. The limiting molecular surface area showed a 11.3 % increase for pH increasing from 2.5 to pH 8.5 (for SG3 the increase is 16.6 %) (Figure 5.3a).

The pH responsive behavior of Langmuir monolayers from  $\text{PS}_n[\text{P2VP-}b\text{-(PAA-}g\text{-PNIPAM)}]_n$  stars is different from that of simple linear block copolymers or other branched block copolymers reported earlier.<sup>251</sup> For example, linear PS-P2VP block copolymer forms LB monolayers with isolated circular micelles at high pH.<sup>257</sup> At low pH, the micelles interact with each other and form a laced network of circular micelles. The aggregation behavior of surface micelles within Langmuir monolayers is strongly dependent on the ionic strength of the sub-phase, which affects the balance between hydrophobic-hydrophobic attraction and electrostatic-driven repulsion. Another study on PS-*b*-PAA dendrimer-like copolymers showed that at basic conditions when the carboxylic acid groups are deprotonated, the copolymer is highly water soluble and cannot form stable monolayer.<sup>259</sup> At acidic conditions, the block copolymer is surface active, and there is a pancake to brush transition upon compression due to the submergence of PAA chains in the water sub-phase, which is accompanied by aggregation of the dendrimers with the low aggregation numbers.

### **5.3.3 Thermo-Responsive Behavior of Stars at Interfaces.**

The  $\pi$ -A isotherms of the  $\text{PS}_n[\text{P2VP-}b\text{-(PAA-}g\text{-PNIPAM)}]_n$  stars at different temperatures are shown in Figure 5.7. For the SG3 monolayer, at the same surface pressure, the molecular area gradually increases with temperature, and the limiting MMA shows a 11.0% increase at temperature increasing from 25°C to 45°C (Figure 5.3b). The increase in molecular surface area with temperature is actually in contrary to that of linear PNIPAM chains in bulk solution, which exhibit a sharp coil-to-globule transition

resulting in decreasing size.<sup>260</sup> This indicates that the hydrophobic-hydrophobic interactions between the methyl groups, which are the driving force for the coil-to-globule transition at LCST, are largely masked when PNIPAM chains are located at the air/water interface and their mobility is constrained by requirement for their localization outside of water subphase above LCST transition (Figure 5.5).

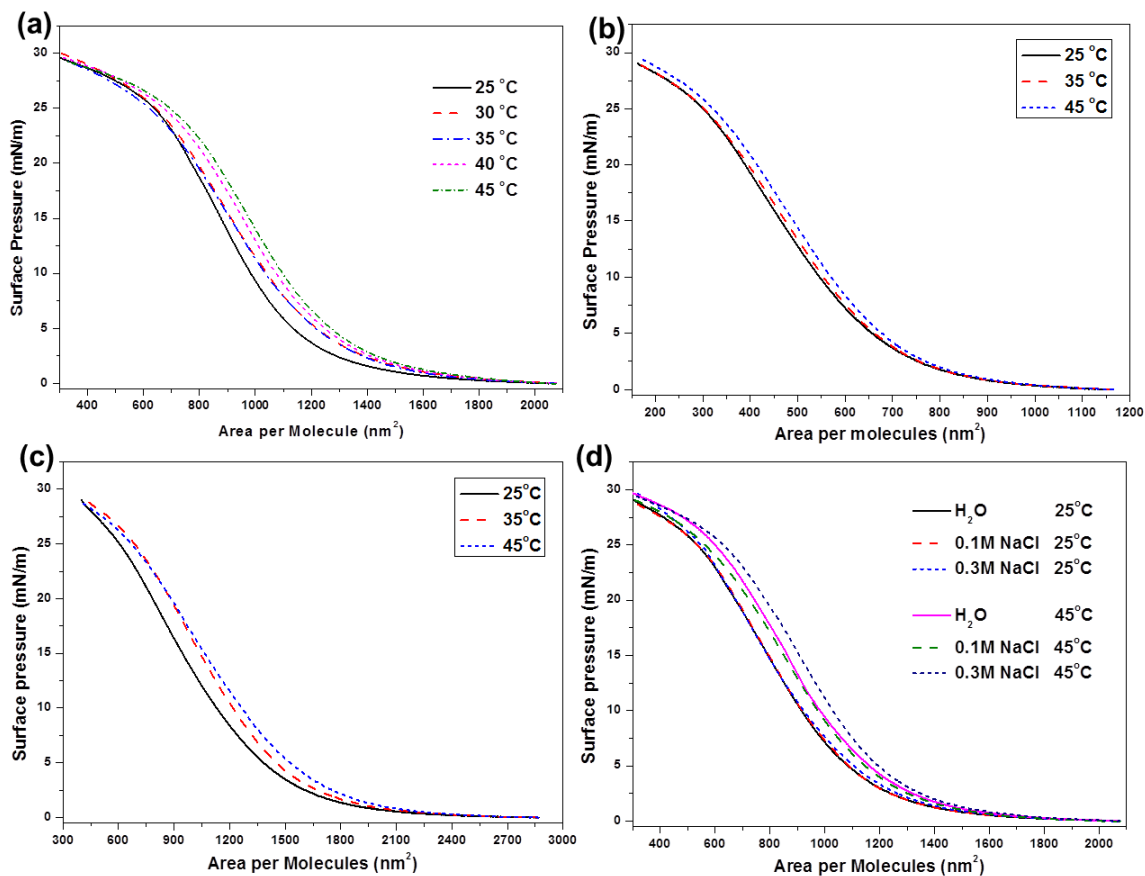


Figure 5.7. Pressure-area isotherms of SG3 stars (a) at pH 5.5 with increasing temperature, (d) at pH 5.5 and different ionic conditions with increasing temperature. Pressure-area isotherms of SG2 (b) and SG4 (c) stars at pH 5.5 condition with increasing temperature.

The morphology of this monolayer deposited at different temperatures at pH 5.5 is shown in Figure 5.8. At low surface pressure of 1 mN/m, the monolayer is composed of molecular aggregates with the aggregation numbers of 4-5. With the increase of

temperature from 25°C to 45°C, the aggregation number remains almost the same, but the lateral size of the granules increases and their average height decreases (see also Figure S 5.3). The root mean square (RMS) microroughness of the 1  $\mu\text{m}^2$  area decreases from 0.26 nm at 25°C to 0.20 nm at 45°C. With the increasing surface pressure, the density of the aggregates significantly increases which results in increasing microroughness to 0.45 nm (Figure 5.8c, d). The average height of the aggregates also increases but the average aggregation number does not change significantly.<sup>261</sup> Further compression to higher surface pressure (20 mN/m) results in higher density of granulated domains (Figure S5.4), and the morphological changes with temperature follows the similar trend.

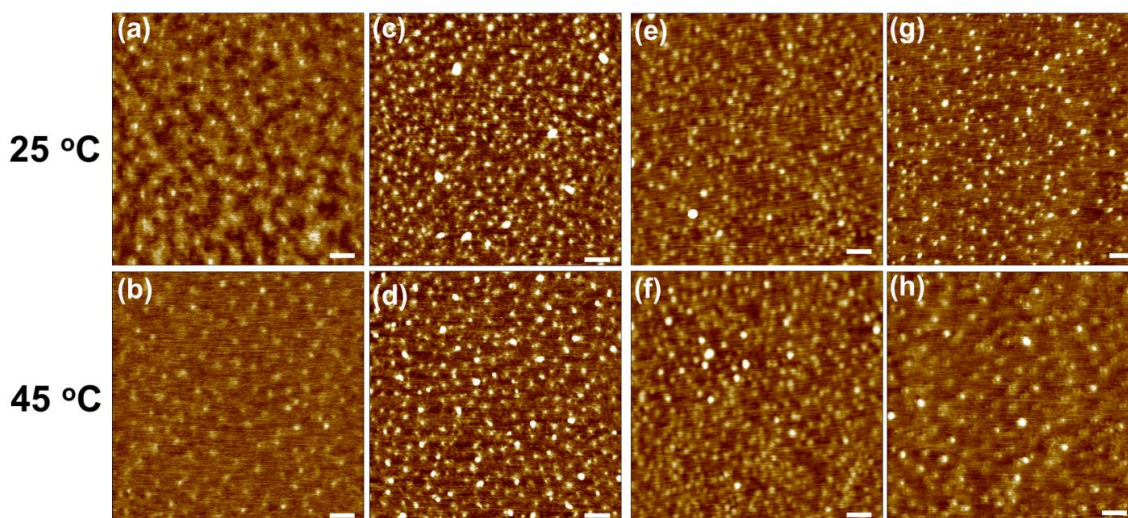


Figure 5.8. (a-d) AFM images of SG3 LB monolayer deposited at pH 5.5 and different temperatures, (a, b) 1 mN/m, (c, d) 10 mN/m. (e-f) AFM images of SG2 LB monolayer film deposited at pH 5.5 and 1 mN/m. (g-h) AFM images of SG4 LB monolayer deposited at pH 5.5 at 1 mN/m. All the scale bars are 100 nm, Z range is 3 nm. Corresponding phase images and cross section analysis are shown in Figure S5.3.

Moreover, the overall thickness of the SG3 monolayers decreases with the increasing temperature and the monolayer surface becomes more hydrophilic (for example, LB monolayer deposited at 1 mN/m shows a decreased contact angle from  $43.6^\circ \pm 0.8^\circ$  to

$33.3^\circ \pm 1.0^\circ$ .) (Figure 5.6a, b). For LB monolayers deposited at 10 mN/m, the decrease in thickness is not accompanied by an increase in hydrophilicity, which is probably due to the limited structural reconstruction of the LB films upon heating compared with that of lower surface pressure.

### **5.3.4 Effect of Graft Density and Arm Number on the Thermo-Responsive**

#### **Behaviors**

The  $\pi$ -A isotherms of SG2 monolayer are shown in Figure 5.7b. The limiting MMA at the same surface pressure also increases with temperature, but the increase is less pronounced compared to that of SG3 stars (Figure 5.3a). The limiting MMA extrapolated from the isotherms shows a 2.0 % increase from 25 °C ( $693.7 \text{ nm}^2$ ) to 45 °C ( $707.4 \text{ nm}^2$ ). The LCST transition leads to a smaller molecular surface area change due to the fact that the SG2 stars have only 4.5 PNIPAM chains per PAA arm, which is significantly smaller than the 11.0 PNIPAM chains per PAA arm for SG3 stars. Control experiments on the precursor  $\text{PS}_9(\text{P2VP-}b\text{-PAA})_9$  stars without PNIPAM arms at different temperatures show unchanged isotherms thus confirming that other molecular components do not contribute significantly in thermo-responsive behaviors (Figure S5.5). The surface morphology of the monolayers of SG2 with much smaller molecular weight shows a higher density of granule domains (Figure 5.8e, f). The aggregation number at 25 °C is 2.5, which is lower than that of SG3 stars (4.5) due to lower density of PNIPAM shell which can shield the charges on P2VP or PAA chains, thus, decrease the intermolecular electrostatic repulsion. At higher temperature, the SG2 stars have a tendency to form larger aggregates, as shown in Figure 5.8f. The aggregation number

increases to 3.2 from 25 °C to 45 °C due to the increased hydrophobic interactions and higher mobility of chains with lower grafting density.

With the increase of arm number, the branched polymers become closer to soft nanoparticles with strong steric and entropic repulsion.<sup>262</sup> The SG4 star (PS<sub>22</sub>[P2VP-*b*-(PAA-*g*-PNIPAM)]<sub>22</sub>) possesses 22 PS arms and 22 block copolymer arms with the PNIPAM graft density close to those at SG2 star macromolecules (4.0 PNIPAM chains per PAA arm, on average) (Table 3.2). The  $\pi$ -A isotherms of SG4 stars with increasing temperature show increasing MMA with temperature (Figure 5.7c). Due to the large number of arms, the molecular surface area of SG4 is significantly larger than that of SG2 and SG3 stars that corresponds to the increasing molecular weight of star macromolecules (Table 3.2). Furthermore, the limiting MMA of SG4 increases from 1903 nm<sup>2</sup> at 25 °C to 2033 nm<sup>2</sup> at 45 °C, an increase of 6.8 % (Figure 5.3a). The surface of the SG4 monolayer contains larger granular aggregates (Figure 5.8g, h). With the increase of the deposition temperature, the lateral size of granules increases while the height decreases, as indicated by the cross section analysis (Figure S5.3). The average aggregation number does not change at the elevated temperature and stays around 2.0. Overall, larger number arms of the star-graft quarterpolymers significantly increases molecular surface area needed for a macromolecule interfacial packing and promotes larger changes in the limiting MMA with increasing temperature, while the aggregation number is less dependent on temperature due to crowded architecture of stars with increased number of arms.

### **5.3.5 Effect of Ionic Strength and pH on the Thermo-Responsive Behavior.**

As discussed in previous sections, the ionization degree of the P2VP and PAA blocks has significant influence on the interfacial behaviors on the star-graft quarterpolymers, and it is well known that the ionic strength of the solution is an important factor controlling the ionization of polyelectrolytes. The isotherms of SG3 monolayers at the same pH of 5.5 with three different ionic conditions: pure H<sub>2</sub>O, 0.1 M NaCl and 0.3 M NaCl are shown in Figure 5.7d. It can be seen that at 25 °C, the SG3 stars show almost identical isotherms, which means they have similar limiting MMA (Figure 5.3c). At elevated temperature, the molecular surface area of SG3 increases for increasing temperature from 25 °C to 45 °C with the effect being much more pronounced at higher salt concentration.

The main reason for the ionic strength dependent thermo-response is that the LCST of PNIPAM chains gradually decreases with increasing ionic strength, which means the temperature response is more pronounced at higher ionic strength. In terms of the star-graft quarterpolymers studied here, the more pronounced hydrophilic to hydrophobic transition leads to a higher extent rise of the PNIPAM chains from water to the interface. On the other hand, the increase in the ionic strength weakens the intramolecular electrostatic interactions due to the charge screening effect. This effect can also contribute to the more extended chain conformation and thus larger molecular surface area increase at the air/water interface. Further increase in ionic strength (close or above 1.0 M) leads to more significant charge shielding, so that hydrophobic interaction will dominate, and intermolecular aggregation starts to appear, eventually leads to precipitation of the star polymers from the solution (Figure S5.6).

To consider the role of sub-phase pH, we choose SG3 at acidic (pH 2.5) and basic (pH 8.5) conditions in comparison with pH 5.5 discussed above. As clear from the isotherm data (Figure S5.7), the molecular area at the same surface pressure increases with temperature at all pH conditions: as temperature increases from 25 °C to 45 °C, an increase in MMA is 13.4 % at pH 2.5, 11.0% at pH 5.5, and 10.7% at pH 8.5. The higher surface area increase at acidic conditions can be related to the fact that the PAA blocks are close to neutral state and interact with PNIPAM chains via hydrogen bonding. As a result, the stars have collapsed shell and the PNIPAM chains are in close proximity with each other (Figure 5.5), which facilitates the hydrophilic to hydrophobic transition, thus the increase in MMA is the largest. On the other hand, the surface morphology differs for the LB monolayers deposited at different pH conditions (Figure 5.9). At pH 2.5 and low surface pressure of 1 mN/m, the LB monolayer of SG3 stars shows high density of distinct granular aggregates. At elevated temperature of 45 °C, the granules become smoother and their size increases significantly although their concentration decreases due probably to coalescence of smaller granules. The average aggregation number of granules increases from 2.0 at 25 °C to 5.5 at 45 °C. At higher surface pressure of 10 mN/m, the aggregation number of each granule does not change much with increasing temperature.

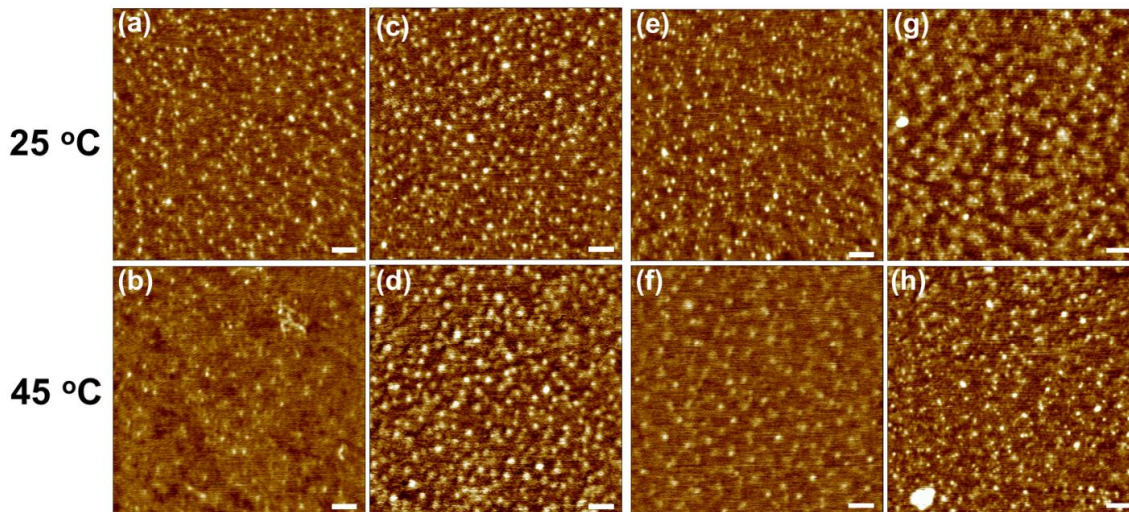


Figure 5.9. (a-d) AFM images of SG3 LB monolayer deposited at pH 2.5 and different temperatures, (a, b) 1 mN/m, (c, d) 10 mN/m. (e-h) AFM images of SG3 LB monolayer deposited at pH 8.5 and different temperatures, (e, f) 1 mN/m, (g, h) 10 mN/m. All the scale bars are 100 nm, Z range is 3 nm. Corresponding phase images and cross section analysis are shown in Figure S5.8.

At basic pH of 8.5, the PAA outer blocks are highly charged that prevent star aggregation and promotes the formation of unimolecular micelles (the aggregation number is around 1.0) at low temperature and at low surface pressure (Figure 5.9e). At elevated temperature, the SG3 stars start to aggregate and form larger micelles with the average aggregation number of 3.3 at 45 °C (Figure 5.9f). At the higher surface pressure of 10 mN/m, the SG3 stars tend to form rod-like aggregates with the aggregation number above 10 (Figure 5.9g, h, Figure S5.8). In the framework of general models proposed in Figure 5.5, at basic condition, the inner P2VP blocks are essentially neutral and assume compact globule conformation,<sup>263</sup> while the PAA blocks are highly charged and extended. Thus, the SG3 stars have a dense neutral core surrounded by a charged shell which is submerged in the aqueous subphase at low temperature. At high surface pressure, the star-graft quarterpolymers are forced to be in close contact with each other, if the

compressive forces are high enough to overcome the electrostatic repulsion, large micelles with neutral core and charged corona will form. Moreover, the overall thickness of the SG3 monolayers decreases with the increasing temperature and monolayer surfaces become more hydrophilic (at 1 mN/m a  $10^\circ$  decrease in contact angle is observed) (Figure 5.6a, b).

## 5.4 Conclusions

The ampholytic star-graft quarterpolymers  $PS_n[P2VP-b-(PAA-g-PNIPAM)]_n$  studied here at the air/water and air/solid interface show that they have multiple responsiveness to pH, temperature and ionic strength, with unusual conformational changes and assembly behavior at different conditions. The overall size of the stars increases with subphase pH, due to the different ionization state of PAA and P2VP blocks. On the other hand, the thermo-responsive behavior at LCST transition depends on a series of factors, including pH, ionic strength, PNIPAM graft ratio, the arm number, and the surface pressure. Higher ionic strength of the subphase leads to more pronounced thermo-responsiveness due to the shift of LCST to lower value. At acidic and basic conditions, the aggregation number of the star micelles increases with temperature, while at the isoelectric region it remains almost the same due to the metastable micellar structure of the aggregates. Finally, higher grafting ratio of PNIPAM chains on the PAA arms leads to higher sensitivity of fine granular micellar aggregates in LCST region. The assembly of multi-responsive star-graft polymers with their ability to reversibly change their morphology can lead to applications in smart coating, drug carrier and microreactors, which are the objectives for further study.

## Appendix: Supporting Information

Table S5.1. Molecular characteristics of the  $PS_n(P2VP-b-PAA)_n$  star block terpolymers

Sample	No. of arms <sup>a</sup>	PS		P2VP		PAA		$\Phi_{P2VP}^e$	$M_w$ , total <sup>f</sup>
		$M_w^b$	DP	$M_w^c$	DP	$M_w^d$	DP		
$S_9(V-b-A)_9$	9.2	3400	33	13,200	126	4968	69	0.61	199,000
$S_{22}(V-b-A)_{22}$	21.7	3500	34	14,300	136	8568	119	0.54	572,000

<sup>a</sup> Average number of arms of each kind by SLS.

<sup>b</sup> By SEC.

<sup>c</sup> Calculated by subtracting the  $M_w$  of the  $PS_n$  from that of  $PS_nP2VP_n$  and dividing by the number of arms.

<sup>d</sup> Calculated, by subtracting the  $M_w$  of the  $PS_nP2VP_n$  from that of  $PS_n(P2VP-b-PtBA)_n$  and dividing by  $n$ , considering quantitative hydrolysis of tBA to AA.

<sup>e</sup> P2VP weight fraction.

<sup>f</sup>  $M_w$  of heteroarm star terpolymer (calculated).

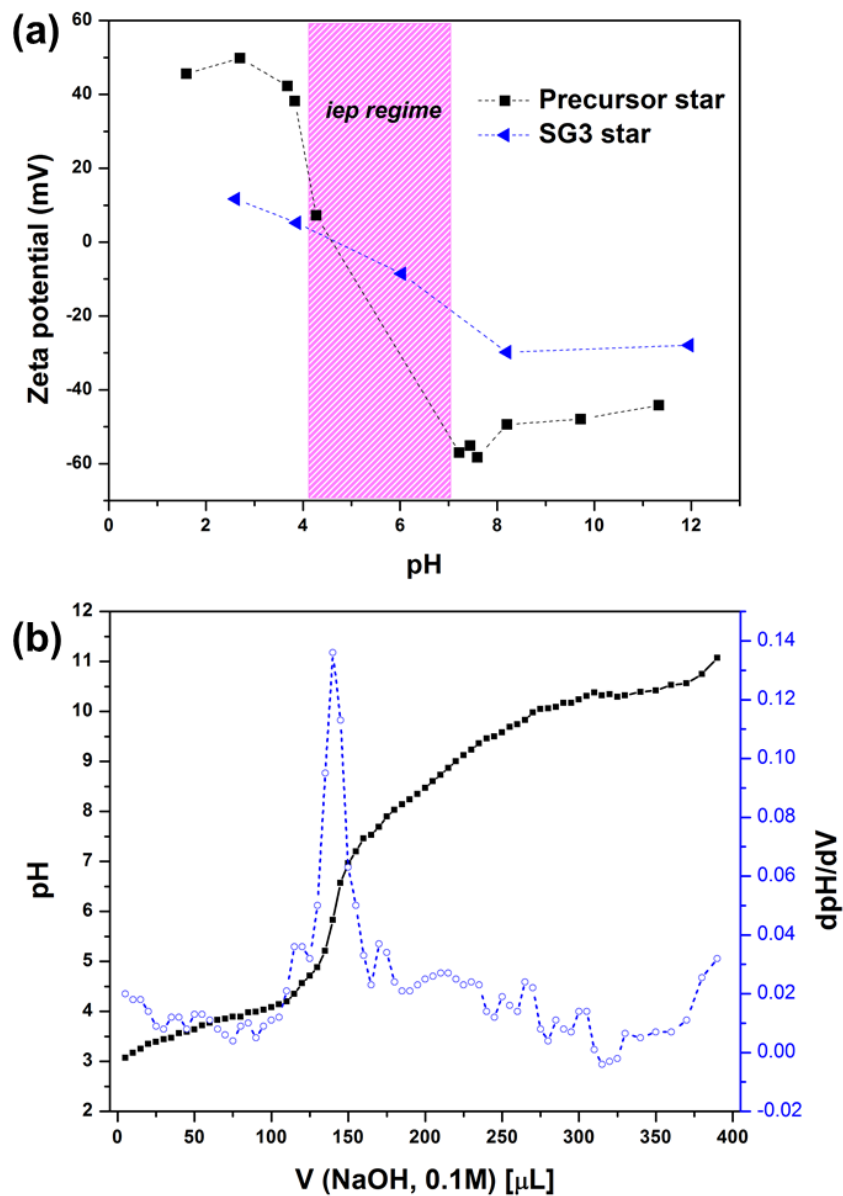


Figure S5.1. (a) Zeta potential as a function of pH of 0.2 wt% SG3 stars and their precursors without grafted PNIPAM chains, the marked region denotes the precipitation regime for the precursor stars. (b) Potentiometric titration of 0.1 wt% SG3 stars with dropwise addition of 0.1 M NaOH, the first derivative of the pH change with added NaOH volume is also shown.

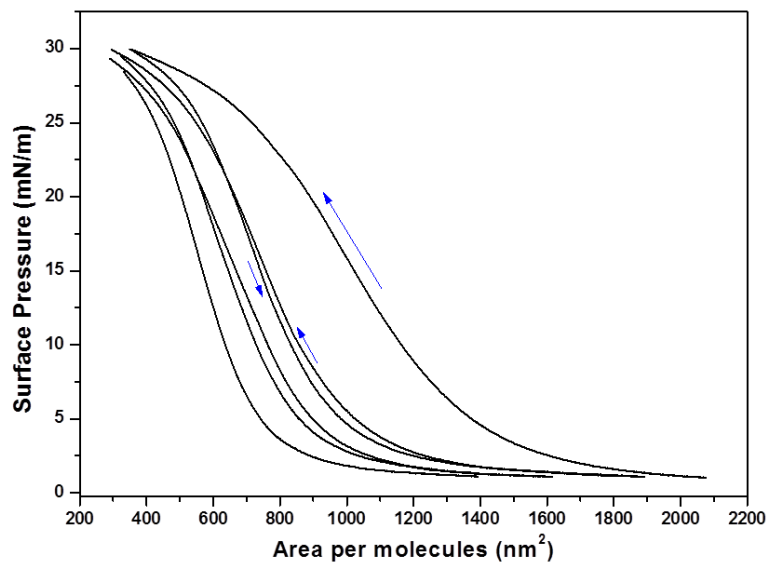


Figure S5.2. Pressure-area isotherms of SG3 at 25 °C and pH 5.5, with multiple compression-expansion cycles.

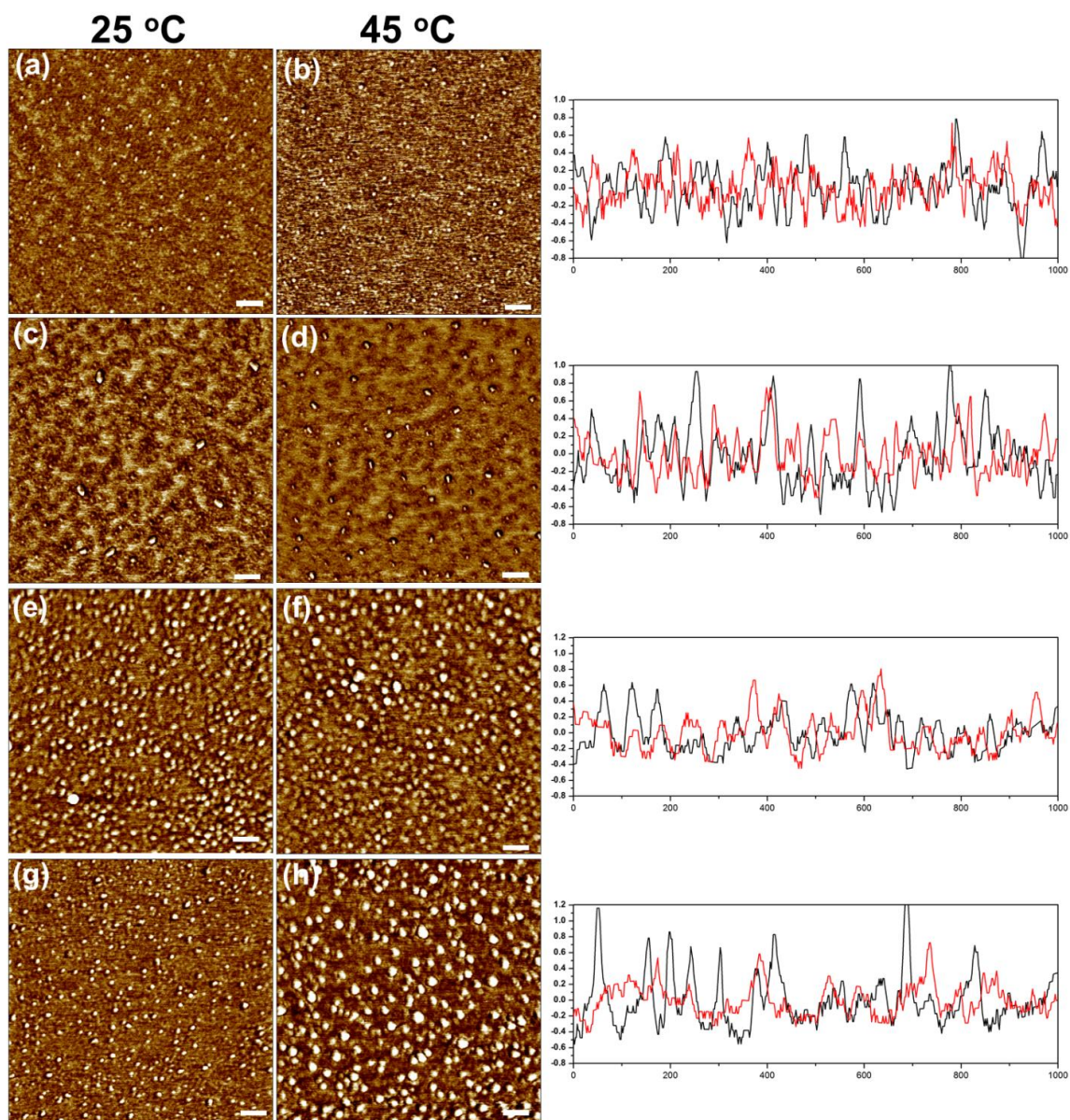


Figure S5.3. (a-d) AFM phase images of SG3 LB monolayer film deposited at pH 5.5 and different temperatures: (a, b) SP = 1, (c, d) SP = 10. (e-f) AFM images of SG2 LB monolayer film deposited at pH 5.5 and SP = 1. (g-h) AFM images of SG4 LB monolayer film deposited at pH 5.5 and SP = 1. All the scale bars are 100 nm, Z range is  $8^\circ$  (SP = 1) or  $15^\circ$  (SP = 10). Cross section analysis of the corresponding height images are shown on the right column (black: 25 °C, red: 45 °C).

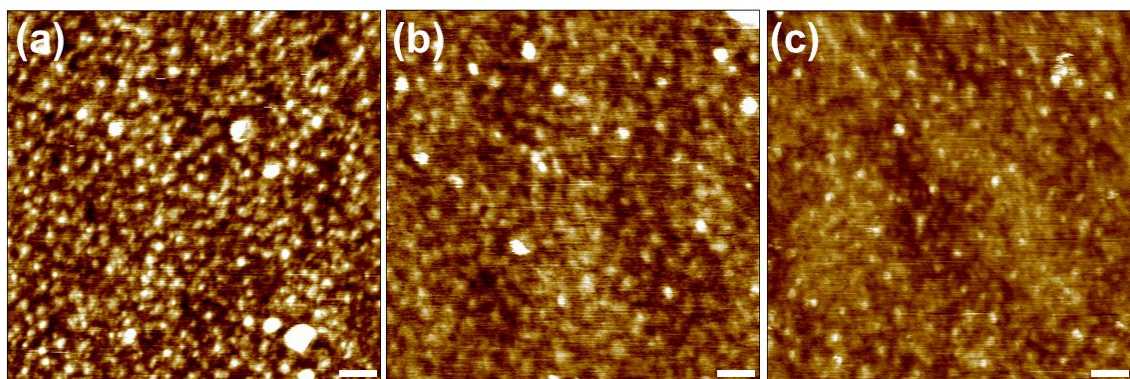


Figure S5.4. AFM images of SG3 LB monolayer film deposited at pH 5.5 and SP = 20 mN/m, at different temperatures: (a) 25 °C, (b) 35 °C, (c) 45 °C. Scale bar is 100 nm, Z range is 5 nm.

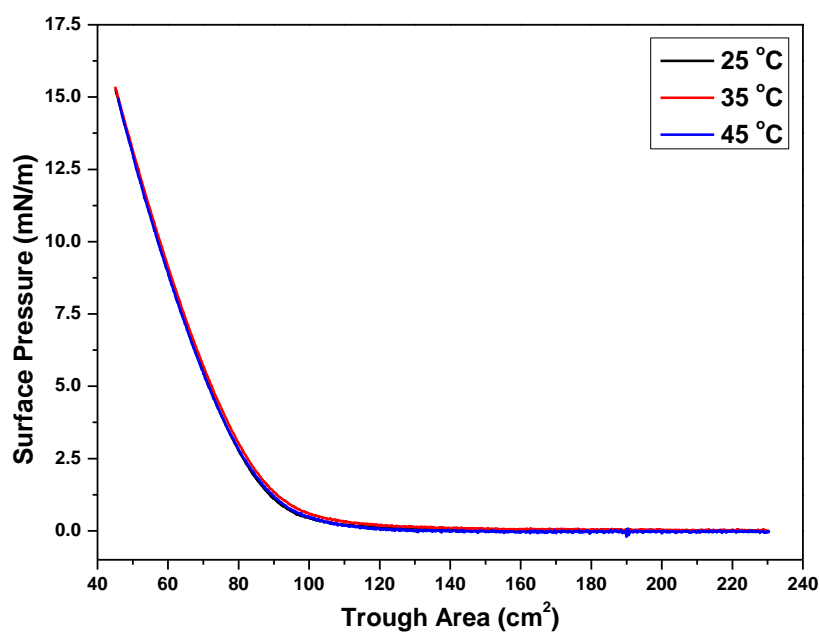


Figure S5.5. Pressure-area isotherms of PS<sub>n</sub>(P2VP-*b*-PAA)<sub>n</sub> star block terpolymers at pH 5.5 with increasing temperature.

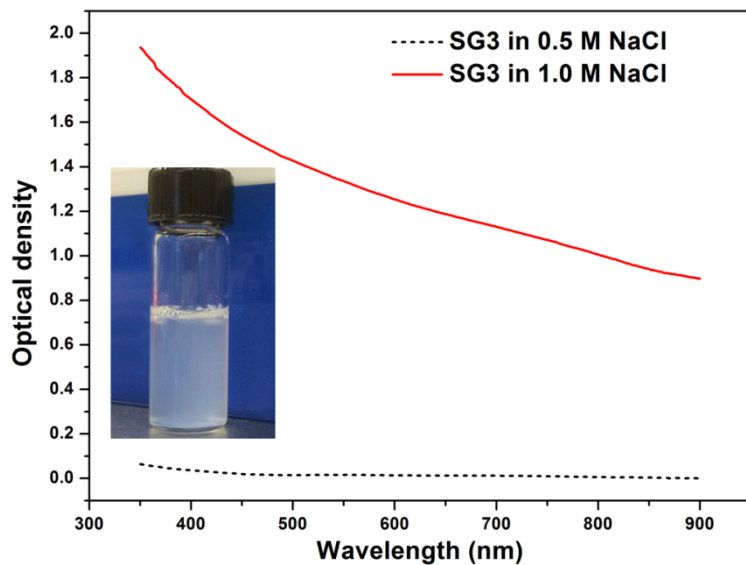


Figure S5.6. Optical density of SG3 star solution (0.1 wt% and pH 5.5) with different ionic strength, the insert image is the SG3 star solution in 1.0 M NaCl.

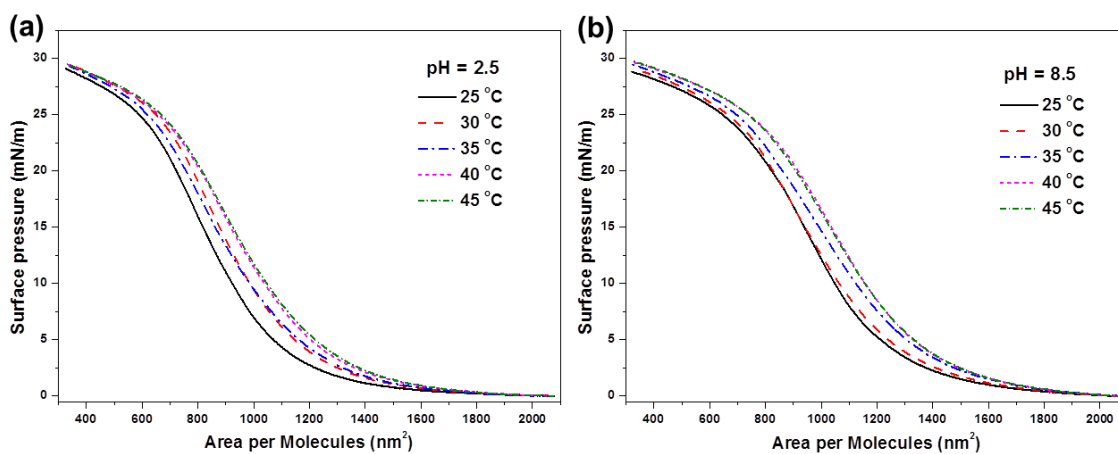


Figure S5.7. Pressure-area isotherms of SG3 at pH 2.5 (a) and pH 8.5 conditions with increasing temperature.

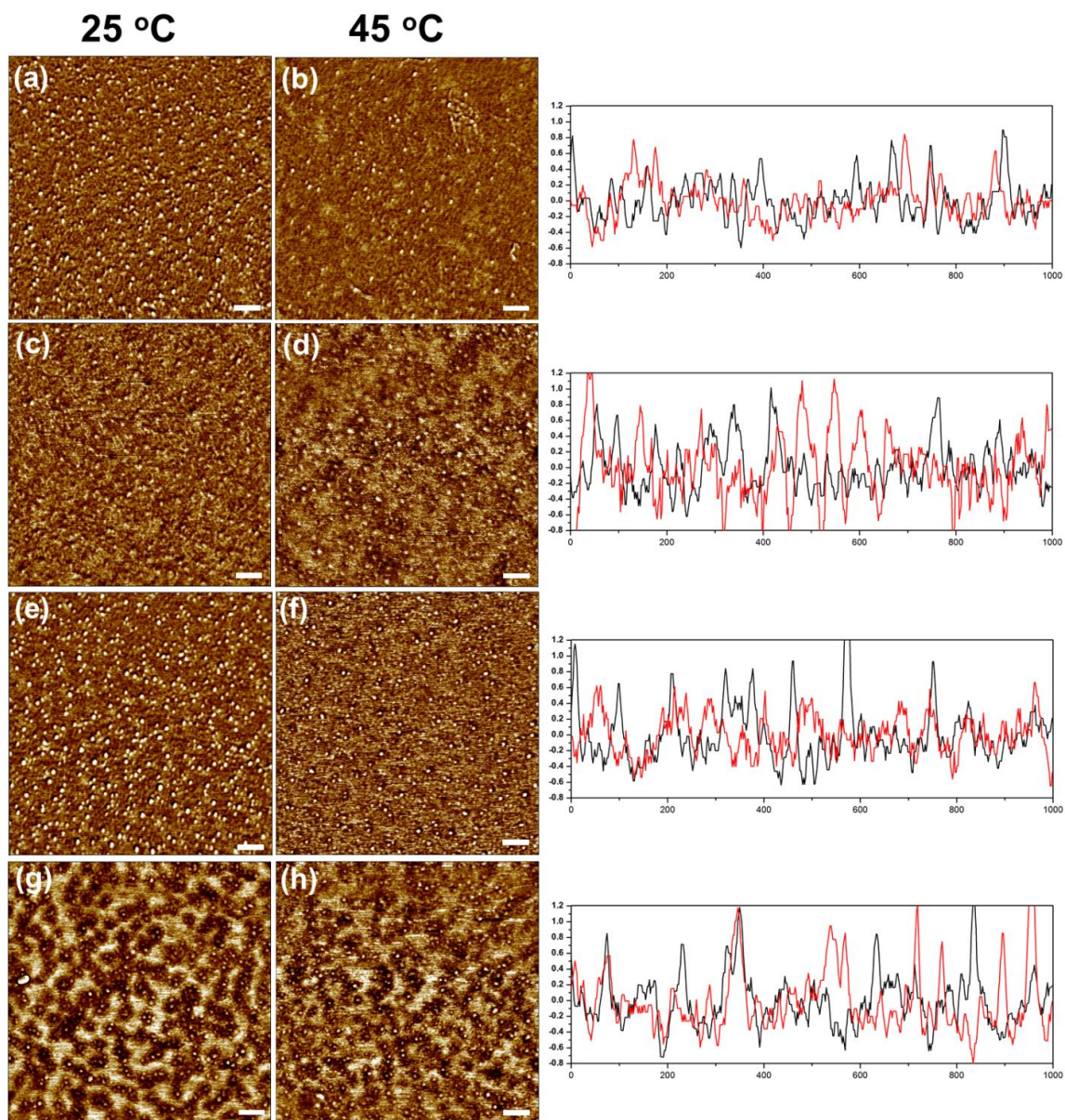


Figure S5.8. (a-d) AFM images of SG3 LB monolayer film deposited at pH 2.5 and different temperatures: (a, b) SP = 1, (c, d) SP = 10. (e-h) AFM images of SG3 LB monolayer film deposited at pH 8.5 and different temperatures: (e, f) SP = 1, (g, h) SP = 10. All scale bars are 100 nm, Z range is  $8^\circ$ . Cross section analysis of the corresponding height images are shown on the right column (black: 25 °C, red: 45 °C).

## CHAPTER 6. pH- AND THERMO- DUAL RESPONSIVE MICROCAPSULES BASED ON PDMAEMA STAR POLYMERS

### 6.1 Introduction

Stimuli-responsive polymeric structures have attracted much attention in recent years due to their diverse range of potential applications.<sup>154</sup> There are many different categories of responsive polymeric structures, such as brushes,<sup>264</sup> thin films,<sup>265</sup> micro- and nano-gels,<sup>266</sup> micelles,<sup>267,268</sup> hybrid particles,<sup>269,270</sup> nanotubes,<sup>271</sup> microcapsules,<sup>141</sup> biomaterial sheets,<sup>272</sup> thin shells for cells.<sup>273, 274</sup> Among these different materials, responsive microcapsules have their unique and superior properties, such as easy fabrication, high stability, high loading capacity, and controlled release of cargo molecules.<sup>275</sup> During the past decade, layer-by-layer (LbL) assembly has emerged to be an important tool to fabricate microcapsules because of its many advantages, such as high versatility, uniformity, broad choice of materials, and facile incorporation of multiple functionalities.<sup>276,277,278,279</sup>

LbL microcapsules and shells with stimuli-responsive properties have been studied intensively in recent years due to their emerging applications in drug delivery, tissue engineering, implantation, coatings, and biosensors.<sup>280</sup> Traditional stimuli used to modulate the structure and properties of LbL microcapsules include pH and ionic strength.<sup>281,282</sup> Usually for microcapsules composed of weak polyelectrolytes, because the charge density and electrostatic interaction within the shell change with pH value, rendering their structure and permeability pH-responsive.<sup>283</sup> Due to the charge screening effect with the increasing ionic strength, the electrostatic interaction between oppositely

charged polyelectrolytes decreases,<sup>284</sup> which leads to an increased permeability of the microcapsules with a polyelectrolyte multilayer shell.<sup>285</sup>

Besides pH and ionic strength, other environmental stimuli such as light,<sup>286</sup> magnetic or electric fields,<sup>287,288</sup> chemical stimuli,<sup>289</sup> ultrasound<sup>290</sup> and temperature<sup>291</sup> are also highly attractive.<sup>292</sup> Generally, these stimuli can be remotely controlled and require only mild changes in the environment, making them more desirable in certain applications. Most of the previous work in this field is focused on responsiveness to a specific type of stimulus,<sup>293</sup> the integration of responsiveness to the novel stimuli with that to traditional stimuli (pH, ionic strength) has received little attention so far. On the other hand, in order to satisfy the requirements of some more demanding tasks,<sup>294</sup> and to have smart systems that can react to different stimuli at the desired location, condition, and time, the integration of multi-responsive properties into one single type of microcapsule is a very attractive option.<sup>295</sup> Moreover, in many practical applications the change in environment is often includes several interrelated factors, and a change in one factor often induces the variation of others. Therefore, the ability to respond to several external stimuli simultaneously or in orthogonal way is of significant interest.

Several previous reports describe multi-responsive microcapsules. For instance, Chu *et al.*<sup>296</sup> reported the temperature-magnetic field dual responsive microcapsules that rely on the incorporation of magnetic nanoparticles. Gao *et al.*<sup>297</sup> showed that by using the host-guest interaction, LbL microcapsules can possess multi-responsiveness to pH, ionic strength, and selectively-binding molecules, but such host-guest interaction can only

apply to limited specific molecules. Pich *et al.*<sup>298</sup> reported composite microcapsules with responsive microgel particles embedded in the shell, which respond to temperature and solvent concentration, but the responses takes a long time. Despite the great potential of multi-responsive microcapsules, there are still many fundamental and practical issues to be addressed. For example, the role of polymer architecture on the responsiveness of polymeric microcapsules; the effects of organization and interaction of the building blocks within the microcapsule shell on their responsive properties; the potential interaction or crosstalk among different external stimuli, and precise morphological changes which accompany apparent microcapsule variations.

For the purpose of fabricating multi-functional or multi-responsive microstructures, star polymers stand out as an excellent candidate material because they have the advantages of having multiple functionalities<sup>299</sup> flexible compositions and unique responses caused by well-defined macromolecular segments.<sup>21</sup> Due to the unique branched architecture and peculiar intermolecular interactions of star polymers,<sup>300</sup> they can bring unique internal structure and significantly different physical properties to the fabricated microstructures including microcapsules.<sup>301</sup> For example, star-shaped polystyrene-*block*-poly(2-pyridine) (PS<sub>n</sub>P2VP<sub>n</sub>) block copolymers have been used to fabricate LbL microcapsules,<sup>167</sup> the prepared microcapsules have a multicompartmental shell structure with densely packed hydrophobic domains within the hydrophilic matrix. Poly{2-(methacryloyloxy)ethyl trimethylammonium iodide} (qPDMAEMA) star polyelectrolytes have also been used in LbL assembly of microcapsules, and due to the unique response of qPDMAEMA stars to multivalent salt, the permeability of the

microcapsules can be reversibly tuned by the counterion valency and UV irradiation. However, those previous studies on microcapsules with star polymer components have not demonstrated multiple responsive behaviors.

Herein, we utilize PDMAEMA star polyelectrolytes with dual response to pH and temperature to fabricate LbL microcapsules. PDMAEMA is a well-known water-soluble and stimuli-responsive polyelectrolyte with a wide range of applications.<sup>302</sup> As a weak polyelectrolyte, its charge density depends on the solution pH. With decreasing pH value, the ionization degree of the amino groups is higher, therefore the polymer has a higher charge density, and previous studies showed that the (PDMAEMA<sub>170</sub>)<sub>18</sub> star polyelectrolytes has a pK<sub>a</sub> of 5.8.<sup>176</sup> The prepared microcapsules based on PDMAEMA stars are very robust and their structure and permeability are readily responsive to external stimuli such as pH, temperature, and ionic strength. The pH-controlled permeable-impermeable transition occurs in a very narrow pH range, which is superior to most previous reports.<sup>303,304</sup> Taking advantage of the thermo-responsive properties, a highly efficient and reversible loading-unloading pattern under cross-correlated stimuli can be achieved.

## 6.2 Experimental Section

**Materials.** Poly(ethylene imine) (PEI) was purchased from Polysciences. Poly(sodium 4-styrenesulfonate) (PSS, M<sub>w</sub>=70,000 kg/mol) were purchased from Sigma-Aldrich. All commercial polyelectrolytes were used without further purification. Silica particles with a diameter of 4.0 ± 0.2 μm and 10% dispersion in water were obtained from Polysciences. Hydrofluoric acid (48–51%) was purchased from BDH Aristar. Tris-HCl (1.0 M) was

purchased from Rockland and was diluted to 0.01 M in ultrapure pure water with pH adjusted by HCl or NaOH for use.

***Synthesis of PDMAEMA star polyelectrolytes*** PDMAEMA star polymers were synthesized by atom transfer radical polymerization of 2-(*N,N*-dimethylamino)ethyl methacrylate employing a core-first route with functionalized polyhedral oligomeric silsesquioxane (POSS) core as described earlier<sup>132</sup> (Scheme 1). Silsesquioxane nanoparticles were used as multifunctional initiators, the rather low efficiency of the initiation sites (30-75%) leads to a moderate arm number distribution of the prepared polyelectrolyte stars. Here, we used PDMAEMA star polymers with 18 arms, with the number-average degree of polymerization (DP) per arm of 170,  $M_n$  of 910 kDa and a (polydispersity index) PDI of 1.2. The linear PDMAEMA used in this study for comparative purposes has a DP of 450,  $M_n$  of 28.8 kDa, and a PDI of 1.98.

***Preparation of LbL microcapsules and films.*** PSS and PDMAEMA star polyelectrolyte were each dissolved in 0.1 M NaCl solution with the concentration of 0.2 mg/mL. PEI solution (1.0 mg/mL) in DI water was used to deposit the pre-layer. The preparation of LbL (PSS/PDMAEMA)<sub>n</sub> microcapsules is shown in Scheme 1b: the bare, negatively charged silica particles with average diameter of 4.0  $\mu\text{m}$  were first coated with a PEI prelayer by incubating in 1.5 mL of PEI solution (1.0 mg/mL) for 15 min, followed by two centrifugation (3000 rpm for 3 min)/wash cycles. Subsequently, the silica particles were incubated in 1.5 mL PSS solution (0.2 mg/mL) for 15 min, followed by two centrifugation (3000 rpm for 3 min)/wash cycles. 1.5 mL of PDMAEMA star

polyelectrolyte solution was then added and 15 min was allowed for adsorption, also followed by two centrifugation/wash cycles. The adsorption steps were repeated until the desired number of layers was built on silica particles. Hollow microcapsules were finally obtained by dissolving silica cores in 1% HF solution for 2h, followed by dialysis in Nanopure water for 2 days with repeated change of water. The LbL films were prepared by dip-assisted LbL method: the silicon substrate was alternately immersed in PSS and PDMAEMA polyelectrolyte solution for 15 min, followed by two times rinsing with water or 0.01 M Tris-HCl buffer.

## **6.3 Results and Discussion**

### **6.3.1 Fabrication of LbL Microcapsules**

The star architecture provides many unique properties compared with the linear counterparts, and for the sake of comparison, both star and linear PDMAEMA were used to as the polycations respectively, and poly(sodium 4-styrenesulfonate) (PSS) was used as the polyanion, to fabricate LbL microcapsules via electrostatic interaction (Figure 6.1). The LbL microcapsules are named as  $(\text{PSS}/\text{PDMAEMA}_{18})_n$  or  $(\text{PSS}/\text{PDMAEMA}_1)_n$ , where the subscript 18 refers to the PDMAEMA star with 18 arms, while the subscript 1 refers to linear PDMAEMA, and n indicates the number of bilayers.

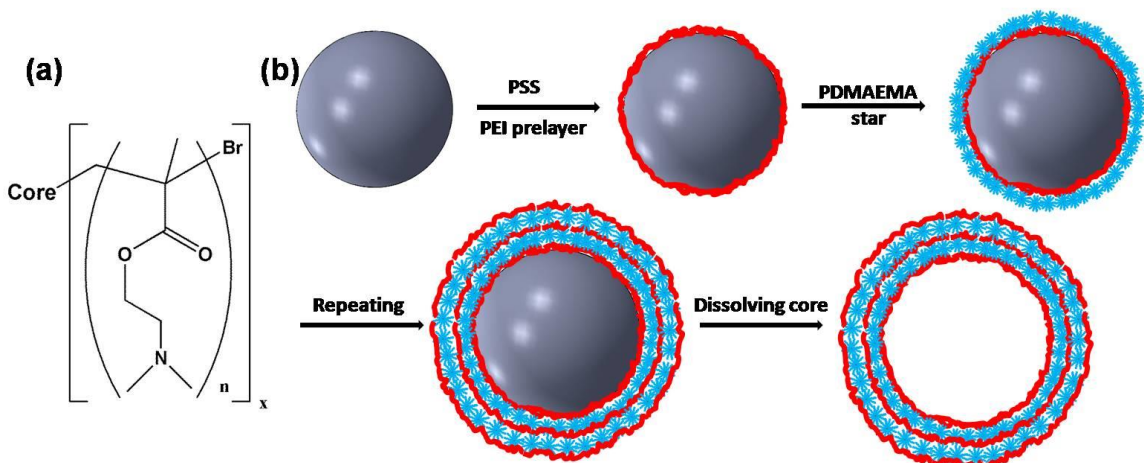


Figure 6.1. (a) Chemical structure of PDMAEMA star polymers and (b) the assembly of (PSS/PDMAEMA<sub>18</sub>)<sub>n</sub> LbL microcapsules.

The LbL assembly of PSS and PDMAEMA stars was conducted at pH 5 condition, since at this condition the PDMAEMA stars have higher charge content and the electrostatic interaction with anionic PSS is stronger, which is beneficial to the assembly process. The two polyelectrolyte components were dissolved in 0.1M NaCl solution, due to the presence of salt, the charge on the polyelectrolyte backbones was partially screened, which has significant influence on the structure and permeability of the resulting hollow microcapsules, as will be discussed later.

Electrophoresis experiments were conducted to monitor the LbL growth of PSS and PDMAEMA star polyelectrolytes (Figure 6.2). The  $\zeta$ -potential of bare silica particle at pH 5 buffer was around -9.8 mV. A  $\zeta$ -potential of *ca.* -52.0 mV was obtained for microcapsules when PSS was the outmost layer of film on silica core. On the other hand, a  $\zeta$ -potential of *ca.* +42.7 mV was observed when PDMAEMA<sub>18</sub> star polyelectrolyte was the outmost layer. Overall, the alternating surface charge of coated silica particles serves

as strong evidence that consistent assembly of anionic PSS and cationic PDMAEMA components took place during the fabrication process.<sup>305,306</sup>

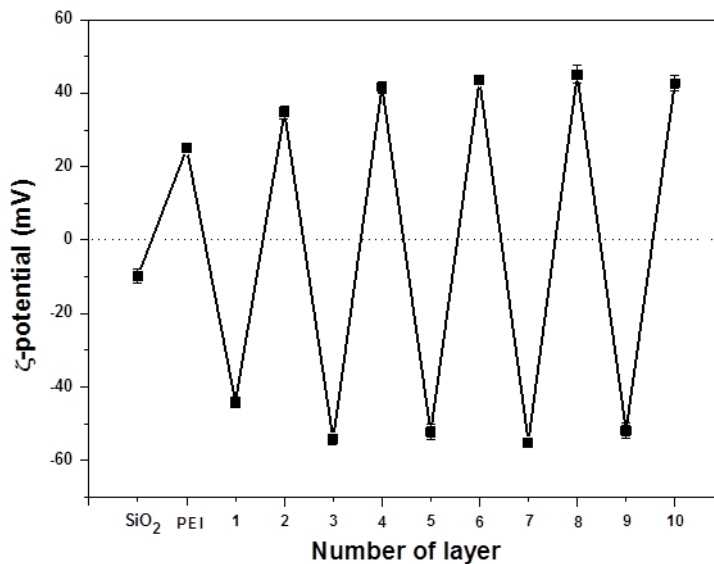


Figure 6.2.  $\zeta$ -potential as a function of number of layers during LbL assembly on silica microparticles with alternating (PSS/PDMAEMA<sub>18</sub>) bilayers.

### 6.3.2 Morphology of (PSS/PDMAEMA)<sub>n</sub> LbL Microcapsules

From the scanning electron microscope (SEM) images in Figure 6.3, it can be seen that the hollow microcapsules collapse after drying with formation of random wrinkles. With the increase of number of bilayers, the contact area of the collapsed microcapsules with the substrate decreases and wrinkles on the surface also become larger. Figure 6.4 shows representative transmission electron microscopy (TEM) images of (PSS/PDMAEMA<sub>18</sub>)<sub>11</sub> microcapsules, where it can be seen clearly that the microcapsules are hollow without any residue core materials inside.

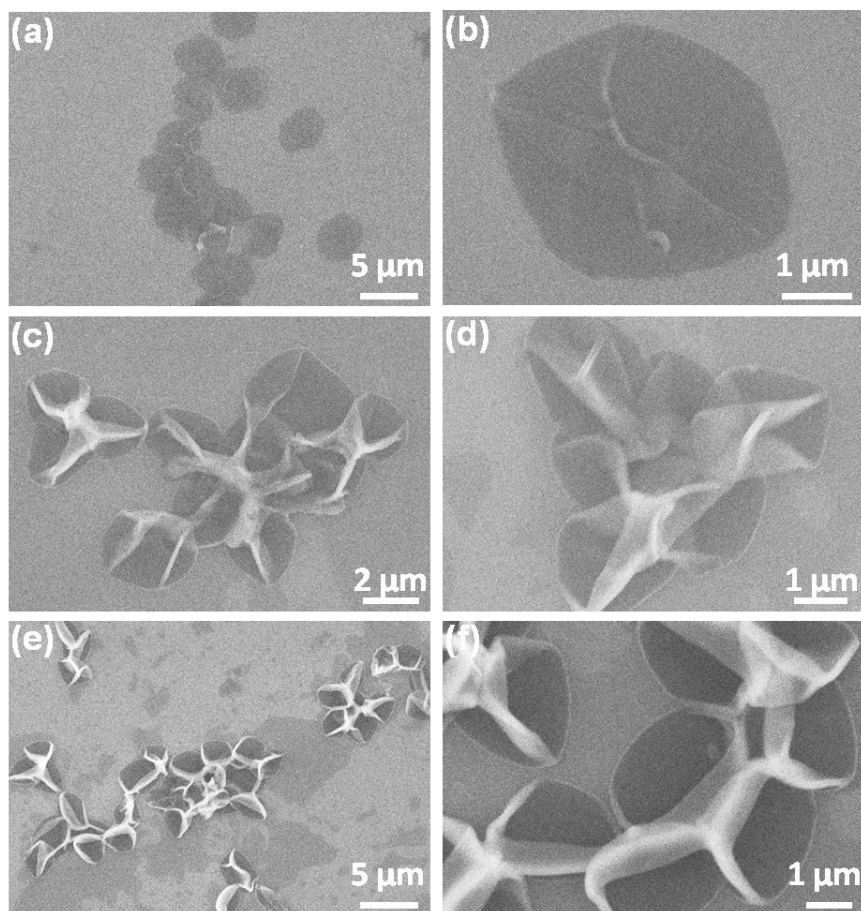


Figure 6.3. SEM images of  $(\text{PSS}/\text{PDMAEMA}_{18})_n$  microcapsules with different number of bilayers: (a, b) 5, (c, d) 8, (e, f) 11.

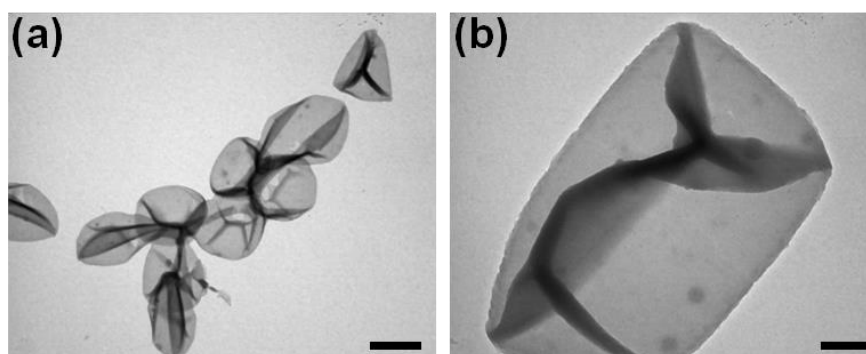


Figure 6.4. TEM images of  $(\text{PSS}/\text{PDMAEMA}_{18})_{11}$  microcapsules, the scale bar is 2  $\mu\text{m}$  in (a) and 500 nm in (b).

Further surface analysis was conducted using atomic force microscopy (AFM), as shown in Figure 6.5. The left column images show the whole microcapsules with increasing number of bilayer. From a smaller area scan depicted in the right column of Figure 6.5, it can be seen that the surface possesses a highly dense granular morphology, where the average size of individual granules (30 ~ 40 nm) matches dimensions of PDMAEMA stars (Figure S6.1).

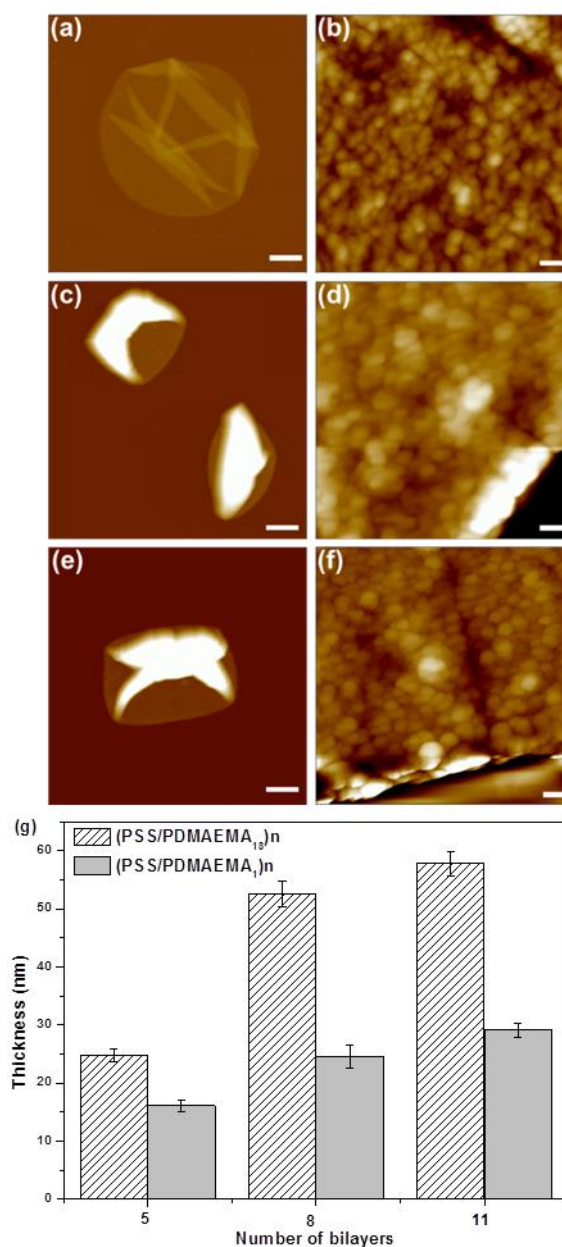


Figure 6.5. AFM images of (PSS/PDMAEMA<sub>18</sub>)<sub>n</sub> microcapsule with 5 bilayer (a, b), 8 bilayer (c, d), 11 bilayer (e, f). Z range is 1500 nm (a, c, e) and 50 nm (b, d, f), scale bar is 1 μm (a, c, e) and 100 nm (b, d, f). (g) The thickness comparison of microcapsules with different bilayer number.

The data on thickness of the microcapsules in dry state is summarized in Figure 6.5g. The thickness of the microcapsules increases significantly from 5 bilayers to 8 and 11 bilayers. In contrast, microcapsules from linear PDMAEMA and PSS have significantly thinner shell. It can also be seen from Figure 6.5 that with the increase of bilayer number, the number of wrinkles on the dried microcapsules decreases, while the wrinkles become larger, some of them covers almost half of the whole collapsed microcapsules.

The main reason for thicker shell of (PSS/PDMAEMA<sub>18</sub>)<sub>n</sub> microcapsule is that star PDMAEMA have more abundant functional groups and chain ends, therefore, their electrostatic interaction with PSS is stronger and the amount of adsorbed polyelectrolytes in each layer on the silica core is more than that of microcapsules from linear PDMAEMA. On the other hand, the thicker shell of the star PDMAEMA based microcapsules leads to better mechanical stability, the shell becomes more rigid and less easy to deform, which allows the microcapsules to be persistent against local capillary forces during the drying process. As a result, the microcapsules only partially collapse, with large wrinkle on the surface (Figure 6.5c and e). On the contrary, (PSS/PDMAEMA<sub>1</sub>)<sub>n</sub> microcapsules with lower mechanical stability collapse completely on the substrate (Figure S6.2).

The main reason for such big difference in wall thickness for star and linear PDMAEMA microcapsules is that PSS/PDMAEMA<sub>18</sub> microcapsules shrink significantly during

drying, and the shrinkage happens to a larger extent with the increase of layer numbers. For instance, the average size of the microcapsules in dry state is  $4.47 \pm 0.33$ ,  $3.04 \pm 0.29$  and  $2.92 \pm 0.26$   $\mu\text{m}$  for PSS/PDMAEMA<sub>18</sub> microcapsules with 5, 8 and 11 bilayers, respectively. While for microcapsules made from linear PDMAEMA, their size remains almost constant at round  $3.90$   $\mu\text{m}$  (Figure S6.2).

### **6.3.3 The Effects of Ionic Strength and Polymer Architecture on Microcapsule**

#### **Behavior**

We found a significant influence of the ionic strength of the solution used to prepare the microcapsules on their properties. To study this effect, we used two different polyelectrolyte solutions: one with 0.2 mg/mL polyelectrolytes dissolved in 0.1 M NaCl solution with adjusted pH, the other with 0.2 mg/mL polyelectrolytes dissolved in pure water with adjusted pH. It is worth to mention that all microcapsules, regardless which solution was used for their preparation, were dialyzed in pure water after core dissolution. This procedure should remove almost all of the salt even from the LBL multilayers, leading to a “frozen” structure of the shell, which is cross-linked by electrostatic interaction and remains stable when exposed to salt-free condition afterwards.

The microcapsule permeability was measured by using fluorescein isothiocyanate (FITC) or FITC labeled dextrans of various molecular weights as fluorescent probes in 0.01 M Tris-HCl buffer with adjusted pH. If the pore size of the microcapsules shell is larger than the size of the fluorescent probe, then the fluorescent intensity would be almost the same for the interior and exterior of the microcapsules, otherwise the interior would be dark and the background appears bright. The (PSS/PDMAEMA<sub>18</sub>) microcapsules have

quite low permeability, as shown in Figure 6.6, FITC-dextran with  $M_w$  of 4 kDa cannot permeate into the microcapsules, while FITC molecules are able to go through the shell at  $\text{pH} \leq 7$  condition. Considering the hydrodynamic diameter of FITC-dextran (4K) is approximately 2.8 nm, and that of FITC is 1.1 nm,<sup>307</sup> the average pore size of the (PSS/PDMAEMA) microcapsules is estimated to be between these two values (around 2 nm). This result is in accordance with a previous study,<sup>285</sup> which also showed that for microcapsules fabricated from salt solution with relatively thicker shells, the mesh size is in the order of a few nanometers.

On the other hand, the (PSS/PDMAEMA<sub>18</sub>)<sub>5</sub> microcapsules prepared from pure water solution have much higher permeability, as shown in Figure 6.6, FITC-dextran with  $M_w$  up to 250 kDa (hydrodynamic diameter: 22.9 nm) can still diffuse inside (Figure S6.3), which means the pore size is in the range of 20~30 nm, which is around 10 times higher than those prepared from 0.1 M NaCl solution. Due to the screening of charges and more compact chain conformation in salt solution, the LbL shell would be thicker and more condense with smaller mesh size. While in aqueous solution without salt, the polyelectrolytes should assume a stretched conformation due to the electrostatic repulsion between charged arms, thus forming a highly porous interpenetrating network with irregular pores distributed through the entire shell. Another important consequence is that the microcapsules prepared from water solution tend to aggregate easily (Figure 6.6d), while those from salt solution are well dispersed.

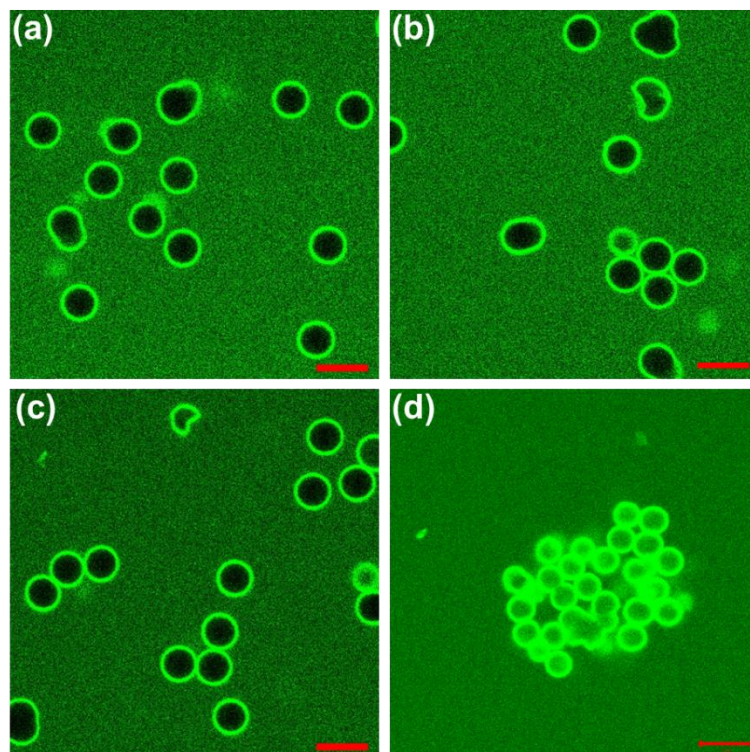


Figure 6.6. CLSM images of  $(\text{PSS}/\text{PDMAEMA}_{18})_n$  microcapsules prepared from salt solution with 5 bilayers (a), 8 bilayers (b), 11 bilayers (c),  $(\text{PSS}/\text{PDMAEMA}_{18})_5$  prepared from water solution (d) exposed to FITC-dextran with  $M_w$  of 4 kDa at pH 5. Scale bar in each panel is 5  $\mu\text{m}$ .

Moreover, the average size of the hollow  $(\text{PSS}/\text{PDMAEMA}_{18})_5$  microcapsules prepared from water solution ( $2.66 \pm 0.11 \mu\text{m}$ ) is significantly smaller than those prepared from salt solution ( $3.65 \pm 0.13 \mu\text{m}$ ), which can also be attributed to more rigid chain conformation in the multilayer shell, there are much stronger unbalanced stress within the shell during core dissolution, which would lead to shrinkage of the overall size. The ability to tune the permeability of microcapsules several micrometers in size down to the nanometer scale makes the more robust  $(\text{PSS}/\text{PDMAEMA}_{18})$  microcapsules interesting candidates for many potential applications. Therefore, in the rest of the paper, the microcapsules are all prepared from 0.1 M NaCl polyelectrolyte solution unless specifically stated.

To further investigate the effect of the star architecture on the assembly process, we also measured the thickness and surface morphology of the analogous LbL films on planar substrates (Figure 6.7). The LbL films from star and linear PDMAEMA in salt solution have very different growth modes: the PSS/PDMAEMA<sub>18</sub> LbL film exhibits non-linear growth in thickness, while PSS/PDMAEMA<sub>1</sub> LbL film shows conventional linear growth. The non-linear growth can be attributed to sub-surface diffusion resulting in the increase of film surface roughness with the number of deposited layers.<sup>52</sup> Indeed, AFM images show that the surface of PSS/PDMAEMA<sub>18</sub> LbL film is highly grainy but uniform without any vermiculate pattern, and the root mean square (RMS) roughness is 4.0 nm in a 4 μm<sup>2</sup> area (Figure S6.4).<sup>308</sup> For PSS/PDMAEMA<sub>1</sub> LbL film, the surface is much smoother with RMS roughness of 1.8 nm in a 4 μm<sup>2</sup> area, which indicates the conventional build up process with alternate overcompensation of the surface charge after each deposition.<sup>309</sup> On the other hand, the LbL films prepared from water solution have linear growth pattern for both star and linear PDMAEMA, and their thickness is much smaller compared with those prepared from salt solution. The absence of charge screening and more stretched conformation prevent excessive build-up process.

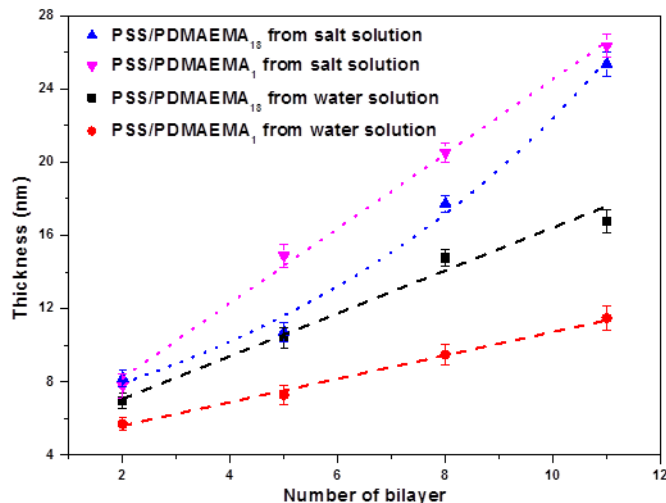


Figure 6.7. Thickness of PSS/PDMAEMA LbL films as a function of number of bilayers, the dotted lines are fitting from linear or exponential model.

Finally, the (PSS/PDMAEMA<sub>18</sub>)<sub>8</sub> and (PSS/PDMAEMA<sub>1</sub>)<sub>8</sub> microcapsules were exposed to FITC solution at pH 5 with different concentration of NaCl, as shown in Figure 6.8(a, b). It can be seen that (PSS/PDMAEMA<sub>18</sub>)<sub>8</sub> microcapsules are stable in high ionic strength condition, while (PSS/PDMAEMA<sub>1</sub>)<sub>8</sub> microcapsules tend to aggregate and be deformed, which happens to a higher extent with the increase of salt concentration. We suggest that due to the abundance of charged sites on star PDMAEMA chains, they can maintain a relatively highly charged state in spite of the shielding effect compared with the linear counterpart, therefore, the (PSS/PDMAEMA<sub>18</sub>)<sub>n</sub> microcapsules are less likely to aggregate.<sup>311</sup> On the other hand, the salt induces polyelectrolyte rearrangements which can result in the formation of local defects on the shell,<sup>316</sup> and the exposure to high salt concentration would lead to an osmotic pressure induced compression. As a result, a significant portion of (PSS/PDMAEMA<sub>1</sub>)<sub>8</sub> microcapsules are deformed to crescent shape in 0.5 M NaCl solution. Star PDMAEMA has more crosslinking sites with PSS, and the

microcapsules have a thicker and stable shell, which makes them more resistant to such kind of deformation.

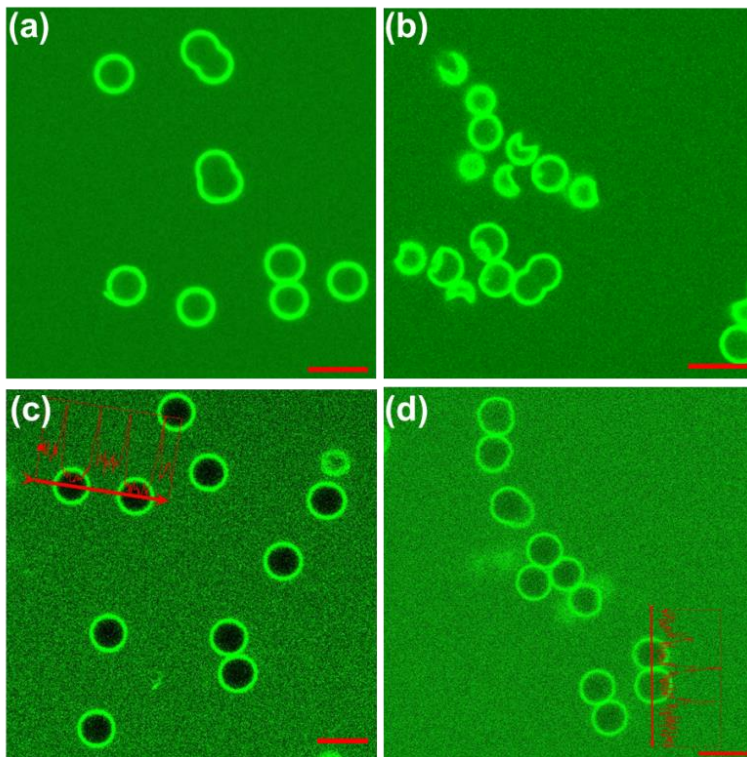


Figure 6.8. CLSM images of (PSS/PDMAEMA<sub>18</sub>)<sub>8</sub> (a) and (PSS/PDMAEMA<sub>1</sub>)<sub>8</sub> microcapsules (b) exposed to 0.5 M NaCl solution at pH=5 and FITC added. Permeability of (PSS/PDMAEMA<sub>18</sub>)<sub>8</sub> microcapsules in buffer (c) and in 0.5 M NaCl solution (d) to 4 kDa FITC-dextran, the inserts are the representative fluorescent intensity profile over the microcapsule. Scale bar in each panel is 5  $\mu$ m.

Ionic strength can also be used to tune the permeability of the star PDMAEMA based microcapsules, as shown in Figure 6.8c, d. FITC-dextran with  $M_w$  of 4 kDa is impermeable to (PSS/PDMAEMA<sub>18</sub>)<sub>8</sub> microcapsules in 0.01 M Tris-HCl buffer with pH 5, but when the microcapsules were exposed to 0.5 M NaCl solution, they became much more permeable. The reason of which is also due to the salt induced polyelectrolyte rearrangements, the chains become more mobile and local defects can be generated.

Because of the higher stability of the star PDMAEMA based LbL microcapsules, in the following study we focus on the  $(\text{PSS}/\text{PDMAEMA}_{18})_n$  microcapsules.

#### **6.3.4 pH-Response of $(\text{PSS}/\text{PDMAEMA}_{18})$ LbL Microcapsules**

Taking advantage of the pH-dependent behavior of PDMAEMA, the structure and permeability of the corresponding LbL microcapsules are also expected to change with pH. Indeed, as shown in Figure 6.9, at  $\text{pH} \leq 7$  conditions, the FITC is able to diffuse into the  $(\text{PSS}/\text{PDMAEMA}_{18})$  microcapsules however, as the pH increases, the permeability of the microcapsules decreases. For  $(\text{PSS}/\text{PDMAEMA}_{18})_5$  microcapsules, the transition from permeable to impermeable state happens at pH 9, and the same is true for  $(\text{PSS}/\text{PDMAEMA}_{18})_8$  microcapsules. While for  $(\text{PSS}/\text{PDMAEMA}_{18})_{11}$  microcapsules, due to the increased shell thickness, the transition already happens at pH 8.

The permeability test results are summarized in Table 6.1. For the sake of comparison, we also studied the responsiveness of microcapsules based on linear PDMAEMA. As shown in Figure S6.5, the  $(\text{PSS}/\text{PDMAEMA}_1)_n$  microcapsules show similar trend of permeability changes with increasing pH.

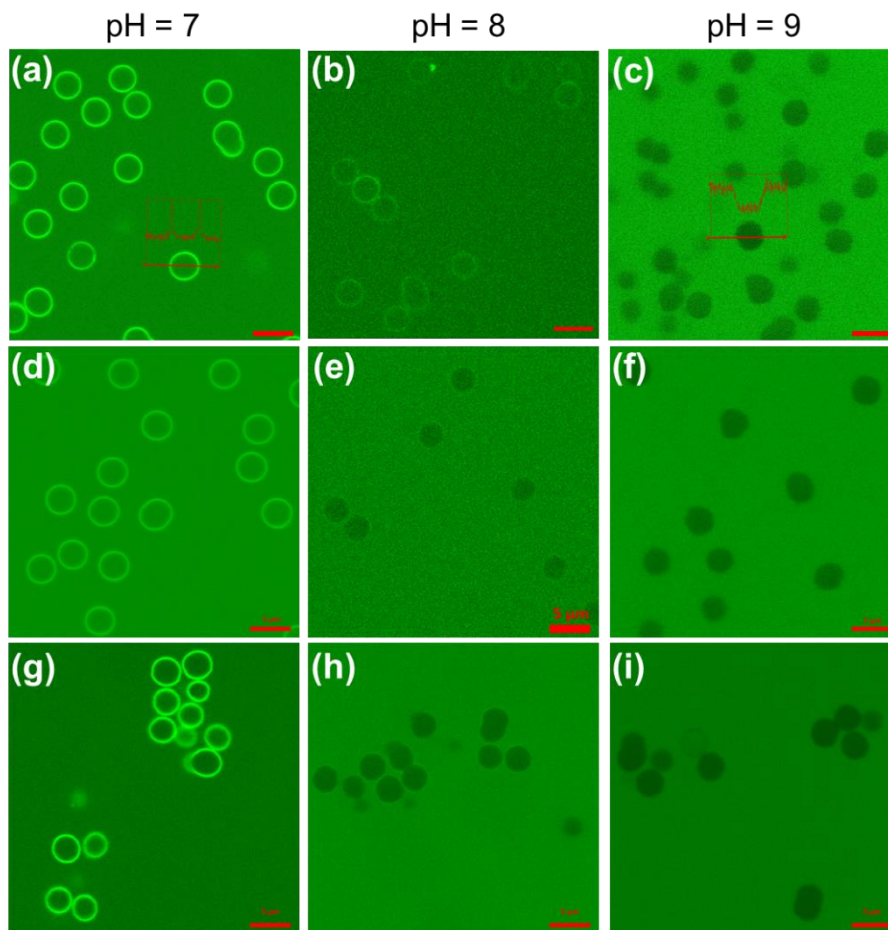


Figure 6.9. CLSM images of (PSS/PDMAEMA<sub>18</sub>)<sub>n</sub> microcapsules with 5 bilayers (a, b, c), 8 bilayers (d, e, f), 11 bilayers (g, h, i) exposed to FITC solutions at different pH conditions as labeled on each column. The insert in (a) and (c) is the representative fluorescent intensity profile over the microcapsule. Scale bar in each panel is 5 μm.

Table 6.1. Permeability of (PSS/PDMAEMA<sub>18</sub>)<sub>n</sub> and (PSS/PDMAEMA<sub>1</sub>)<sub>n</sub> microcapsules to FITC at different pH conditions (“+”: permeable, “-” not permeable).

Sample	pH = 3	pH = 5	pH = 7	pH = 8	pH = 9
(PSS/PDMAEMA <sub>18</sub> ) <sub>5</sub>	+	+	+	+	-
(PSS/PDMAEMA <sub>18</sub> ) <sub>8</sub>	+	+	+	-	-
(PSS/PDMAEMA <sub>18</sub> ) <sub>11</sub>	+	+	+	-	-

As known, the electrostatic crosslinks within the polyelectrolyte multilayer shell are dynamic and sensitive to pH and electrostatic screening, which allows the chains to undergo certain reorganization due to the breaking and reforming of ionic cross-links that hold the multilayer shell together.<sup>310</sup> This reorganization process has been found to lead to reversible pore opening or closing in certain weak polyelectrolyte multilayer films.<sup>311</sup> At low pH value, the majority of the free amino groups on PDMAEMA chains are charged, which would cause the chains to extend due to the electrostatic repulsion, as a result, the spacing between the chains in the multilayer system is larger, in other words, the microcapsules have higher permeability, which allows the facile diffusion of FITC.<sup>311</sup> The (PSS/PDMAEMA<sub>18</sub>)<sub>n</sub> microcapsules are very stable at acid condition down to pH=1 (Figure S6.6).

With the increase of pH value, the charge density on PDMAEMA chain dimensions decrease, as a result, the electrostatic repulsion force decreases, which leads to the contraction of the flexible chains. Since the PSS chains are closely bound to PDMAEMA, the contraction of PDMAEMA chains would also force the whole multilayer shell to contract, which results in a denser shell and lower permeability as depicted in Figure 6.10.

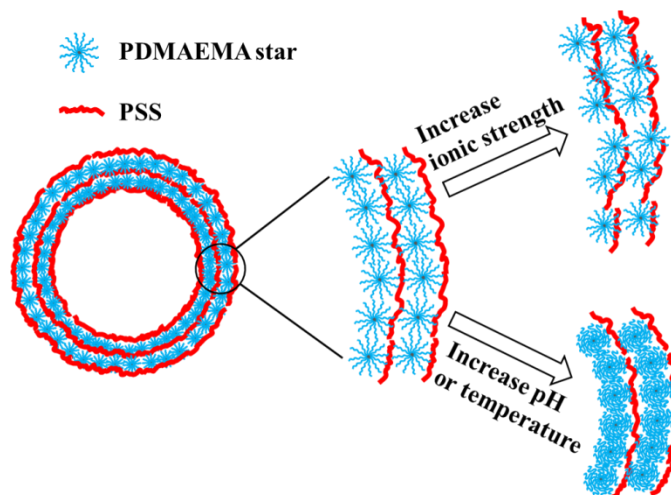


Figure 6.10. The structural changes of the (PSS/PDMAEMA<sub>18</sub>) microcapsules to different external stimuli including ionic strength, pH and temperature.

On the other hand, the density of ionic crosslinks also decreases with increasing pH, leading to a more flexible membrane, and possible defects in the microcapsule shell are filled by the more dynamic chains. The critical value for the permeation of FITC molecules is in between pH 8 or 9 depending on the shell thickness (Figure 6.9). The overall size of the microcapsule also gradually decreases with increasing pH, for example, the average size of (PSS/PDMAEMA<sub>18</sub>)<sub>8</sub> microcapsules decreases from 3.65  $\mu\text{m}$  ( $\pm 0.10$ ) at pH 7 to 3.33  $\mu\text{m}$  ( $\pm 0.12$ ) at pH 9, as measured by CLSM in solution state. The morphology of the microcapsules in dry state from their suspension with different pH values provides additional evidences to the dimensional changes.

As shown in Figure 6.11, (PSS/PDMAEMA<sub>18</sub>)<sub>11</sub> microcapsules have relatively thin shell and flat surface at pH 5, and the shell gradually become denser with large wrinkles forming on the surface at pH 7. Eventually, the microcapsules have thick and rigid shell which tends not to collapse during drying, so that the spherical shape is largely retained

and the shells are partially broken during drying. At the same time, the size of the microcapsules in dry state also decreases with increasing pH.

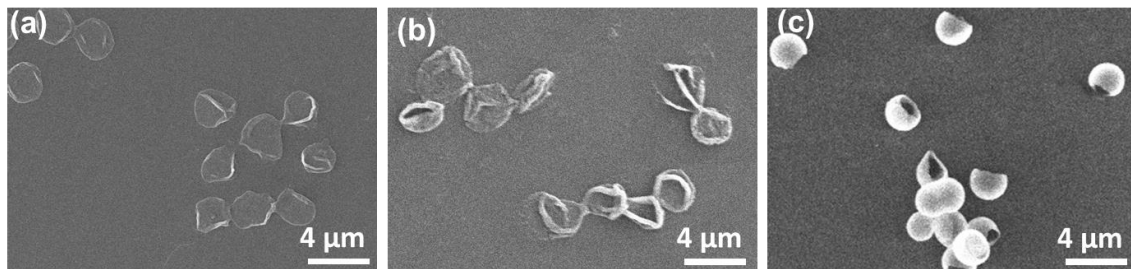


Figure 6.11. SEM images of (PSS/PDMAEMA<sub>18</sub>)<sub>11</sub> microcapsules with different pH conditions: (a) pH=5, (b) pH=7, (c) pH=9.

If the pH value further increases to above 9, the shell integrity would be compromised and FITC can permeate through the damaged region into the microcapsules. As can be seen from Figure S6.7, at pH 10 condition about half of the (PSS/PDMAEMA<sub>18</sub>)<sub>8</sub> microcapsules are broken and FITC can diffuse inside. With further increase of pH to 11, most of the microcapsules are damaged and almost no intact spherical microcapsules can be found. The PSS/PDMAEMA<sub>18</sub> microcapsules have higher stability in such extreme pH conditions compared with (PSS/PDMAEMA<sub>1</sub>)<sub>8</sub> microcapsules (Figure S6.7).

Another interesting phenomenon observed in this study is that not only the permeability of target molecules inside the microcapsules can be controlled by pH, but also the incorporation of target molecules into the shell is influenced by pH conditions. It can be seen from Figure 6.9 that at pH 7, the FITC molecules can be readily absorbed on the shell, which show higher fluorescence intensity than the background. When the pH value increases to 8, less FITC molecules are bound to the shell, and at pH 9 the shell is not

visible, which means FITC cannot attach to the shell. FITC is negatively charged in the pH range used for our study, so that they can bind with PDMAEMA chains through electrostatic interaction. When the charge density of PDMAEMA decreases with increasing pH value, the interaction between FITC and PDMAEMA also decreases, resulting in a reduced FITC absorption.

Taking advantage of the pH responsive permeability of  $(\text{PSS}/\text{PDMAEMA}_{18})_n$  microcapsules, we also performed encapsulation and release of FITC molecules in solution (Figure 6.12). By exposing the  $(\text{PSS}/\text{PDMAEMA}_{18})_8$  microcapsules to FITC solution at pH 7, the dye molecules can readily permeate inside, then after collecting the microcapsules through centrifugation and replacing the supernatant with pH 9 buffer, the permeability of the microcapsules decreases so that the FITC can be encapsulated with the background dye removed. The encapsulated FITC can be quickly released by exposing the microcapsules to pH 7 buffer again. The encapsulation and release are completely reversible and can be done multiple times with high efficiency (Figure 6.12).

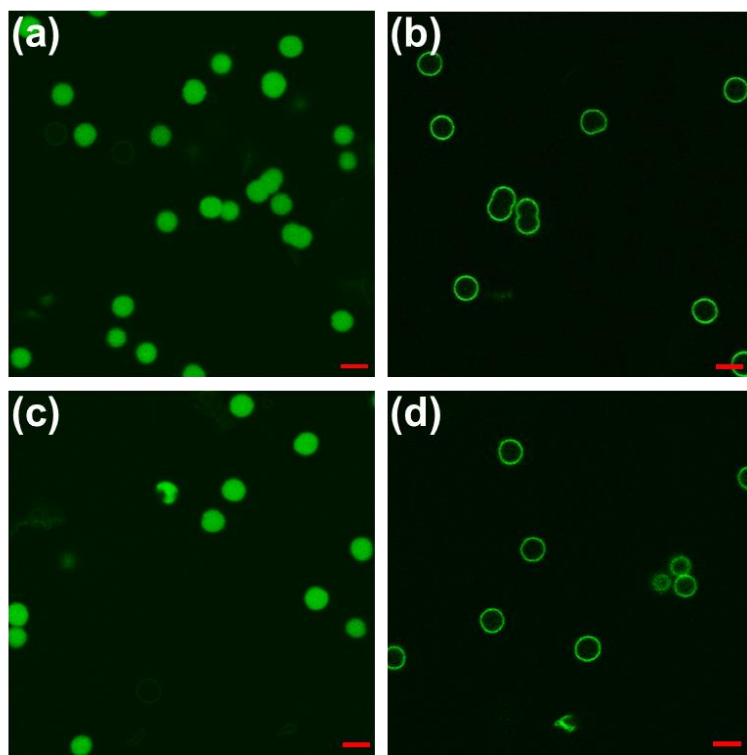


Figure 6.12. (PSS/PDMAEMA<sub>18</sub>)<sub>8</sub> microcapsules encapsulation of FITC at pH 9 (a) and release at pH 7 (b); the second cycle of encapsulation and release (c, d). Scale bar is 5  $\mu\text{m}$  in all images.

### 6.3.5 Temperature Response of (PSS/PDMAEMA<sub>18</sub>) Microcapsules

PDMAEMA is a well-studied water soluble thermo-responsive polyelectrolyte, and the cloud points of PDMAEMA containing solutions strongly decrease with increasing pH.<sup>312</sup> With the increase of temperature, water becomes a bad solvent for PDMAEMA, the hydrogen bonding between PDMAEMA chains and water weakens, and the hydrophobic interaction increases,<sup>313</sup> so that the arms of PDMAEMA stars shrink to a more collapsed conformation,<sup>314</sup> which leads to changes in the structure and permeability of the microcapsule.

As shown in the previous section, the transition of (PSS/PDMAEMA<sub>18</sub>) microcapsules from being permeable to being impermeable to FITC molecules occurs between pH 8 to 9. Therefore, for following study, we chose pH 7 as the condition to load FITC dye molecules inside the microcapsules. The encapsulation was done by incubating the microcapsules in solution containing FITC dye at room temperature. The solution was then transferred to a dialysis tube in pH 7 buffer bath at a preset temperature of 45 °C with constant stirring. Dialysis at 45 °C was continued until the concentration of FITC in the buffer was very low and remained unchanged, as monitored by a fluorophotometer.

Then the whole system was cooled down to a series of preset temperatures (40 °C, 35 °C, 30 °C, 25 °C, 20 °C) consecutively, at each preset temperature the buffer bath was equilibrated for 15 min, then the fluorescence intensity of the bath which contains the FITC molecules permeate from the microcapsules was measured. The results are shown in Figure 6.13a, it can be seen that the intensity of the FITC emission peak of (518 nm) increases as the cooling proceeds.

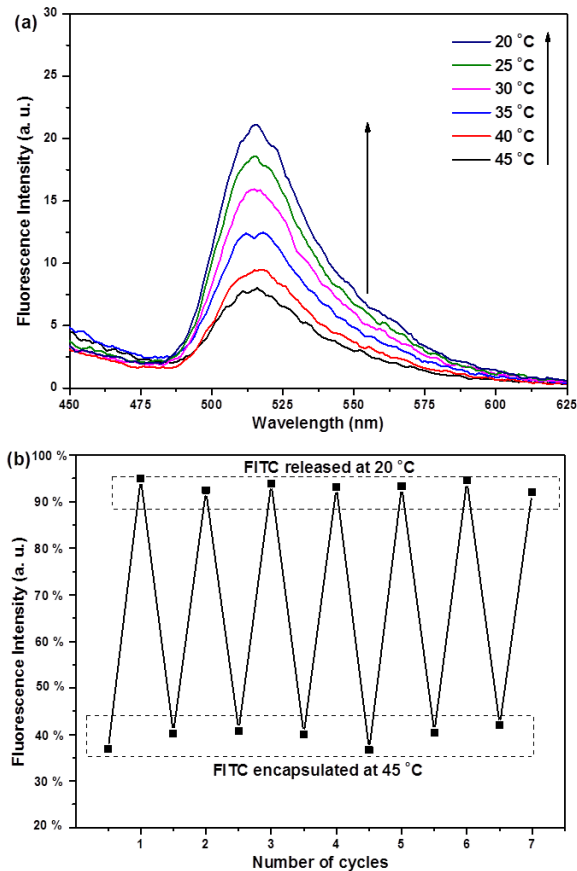


Figure 6.13. (a) Fluorescence intensity of the dialysis bath which contains the FITC molecules permeate from the microcapsules, during the cooling of (PSS/PDMAEMA<sub>18</sub>)<sub>8</sub> microcapsules from 45 °C to 20 °C. (b) Reversibility of the thermo-responsive encapsulation and release as indicated by fluorescence intensity of the dialysis bath.

The results give strong indication that FITC dye was successfully encapsulated and retained inside the microcapsules at 45 °C but can be subsequently released by decreasing the temperature (Figure 6.13). With the decrease of temperature, the PDMAEMA stars can recover from their collapsed state, therefore, the shell of microcapsules also become more swollen and permeable for FITC. The thermo-responsive encapsulation and release is also completely reversible, as shown in Figure 6.13b. FITC molecules can be encapsulated inside the microcapsules at 45 °C and be released at 20 °C with high

efficiency in a cyclical fashion. Such temperature-induced loading-unloading cycling can be repeated for numerous (more than 10) times

Moreover, it has been found that pH conditions also affect the thermo-responsive behavior of microcapsules, proving direct cross-correlation of two independent stimuli. As shown in Figure S6.8, when the encapsulation and release are performed at a lower pH condition (pH=6), the encapsulation efficiency somewhat decreases, as indicated by the relative fluorescent intensity changes during cooling at the same condition. The reason for this can be related to the earlier pH responsiveness discussion; basically, at lower pH condition the permeability of PSS/PDMAEMA<sub>18</sub> microcapsules is higher, so that less amount of FITC molecules can be encapsulated at the same temperature.

The thermo-responsiveness has also been proved by the changes in size and morphology of the microcapsules as measured by AFM. From Figure 6.14 it can be seen that the average overall size of the dried microcapsules shrink from 4.47 ( $\pm$  0.31)  $\mu\text{m}$  at 20  $^{\circ}\text{C}$ , to 3.42 ( $\pm$  0.18)  $\mu\text{m}$  at 40  $^{\circ}\text{C}$ , and 2.07 ( $\pm$  0.16)  $\mu\text{m}$  at 60  $^{\circ}\text{C}$ . At the same time, the average thickness of the microcapsules increases from 24.8 ( $\pm$  1.1) nm at 20  $^{\circ}\text{C}$ , to 29.4 ( $\pm$  2.6) nm at 40  $^{\circ}\text{C}$ , and 76.0 ( $\pm$  7.9) nm at 60  $^{\circ}\text{C}$ . The significant size reduction and densification of shell caused by changing hydrophobic-hydrophilic balance corroborate the permeability changes of the microcapsules with increasing temperature.

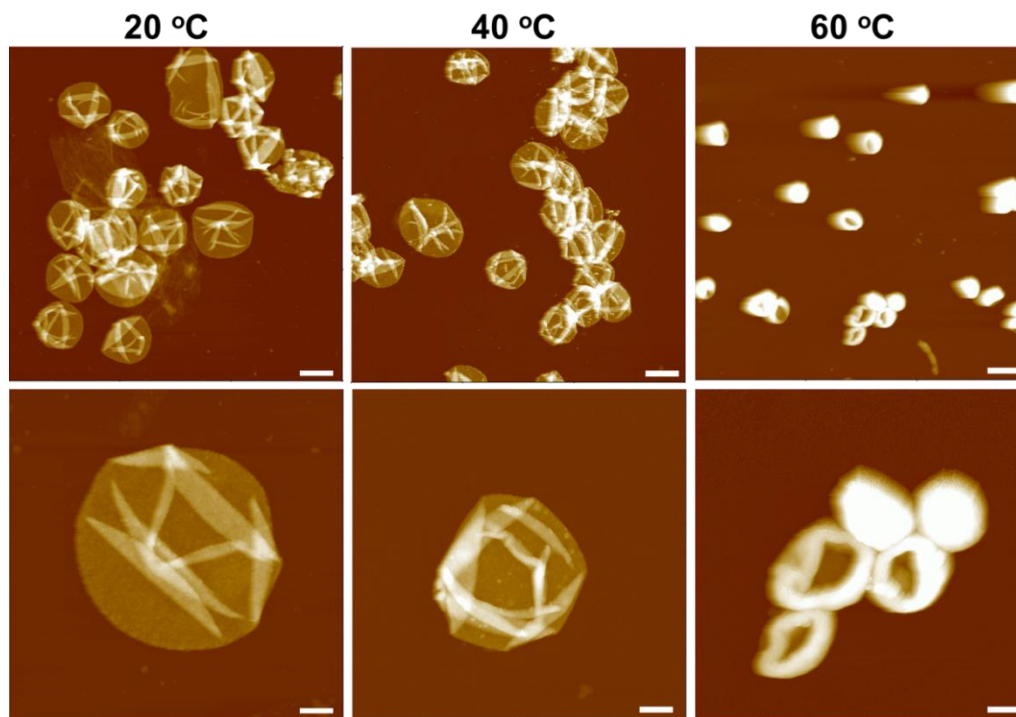


Figure 6.14. Size and morphology changes of (PSS/PDMAEMA<sub>18</sub>)<sub>5</sub> microcapsules with increase of temperature as shown by AFM images. Scale bar is 3  $\mu\text{m}$  for top row, and 1  $\mu\text{m}$  for bottom row, Z range is 500 nm for 20  $^{\circ}\text{C}$  and 40  $^{\circ}\text{C}$  images, 2000 nm for 60  $^{\circ}\text{C}$  images.

Our results of the thermo-responsiveness of microcapsules based on responsive PDMAEMA star polyelectrolyte are unique and superior in certain aspects compared with previous studies on conventional LbL microcapsules. A study on PSS/PAH microcapsules<sup>315</sup> indicates that the capsule size decreases when heated, the density and volume of the microcapsules shell remained approximately constant. But the magnitude of the observed decrease in the former case is much lower compared with our results. In another study the annealing at high temperature (40  $^{\circ}\text{C}$ ) even lead to the swelling of the microcapsules.<sup>316</sup>

### 6.3.6 SANS Study on the Structural Changes of Microcapsules

As discussed before, the conformational changes and organization of star polyelectrolytes within confined multilayers are the main driving forces for the responsiveness to external stimuli. In order to elucidate the detailed structural changes of  $(\text{PSS}/\text{PDMAEMA})_n$  microcapsules during external stimuli, we also conducted SANS measurements on the microcapsule solutions.

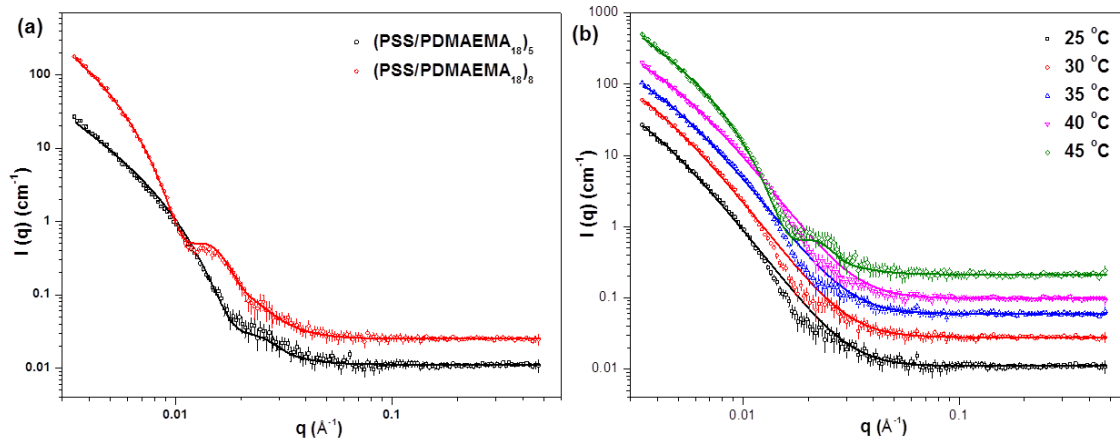


Figure 6.15 (a) SANS data of  $(\text{PSS}/\text{PDMAEMA}_{18})_n$  microcapsules with 5 and 8 bilayers at 25 °C and pH 7 condition, solid curves are fitting from lamellar model. (b) SANS curves of  $(\text{PSS}/\text{PDMAEMA}_{18})_5$  microcapsules at pH 7 condition with increasing temperature, solid curves are fitting from DAB model (25-40 °C) and lamellar model (45 °C). The curves are mutually offset by a factor of 2 for better visualization.

Figure 6.15 shows the SANS data from microcapsules with different number of bilayers. It can be seen that for thinner shells, the scattering curve has a monotonically decreasing trend with increasing  $q$ , while for microcapsules with 8 bilayers, there are obviously characteristic humps in the  $q$  range from 0.01 to  $0.05 \text{ \AA}^{-1}$ . The reason for such a difference is that the shell consisting of 5 bilayers is thin enough to be considered as a simple two phase system composed of a hydrogenated polyelectrolyte shell and  $\text{D}_2\text{O}$  inside. Fitting from the power law model gives a surface fractal dimension of 2.60, which corresponds to surface fractal structure; the DAB model fitting gives a correlation

length of 35.6 nm (Figure 6.15b), which also matches with the result from the permeability studies.

Microcapsules with a much thicker shell of 8 bilayers have complex hierarchical internal structures, which prevents a simple power law model or DAB model to give a satisfactory fitting. In fact, such characteristic humps in the middle  $q$  range are an indication of lamellar-like structures.<sup>317</sup> Although well-defined lamellar layering is probably not the accurate description of the shell structure, the result indicates the thicker shell may have reorganized to microphase separated internal structures.

The lamellar model provides the scattering intensity for a lamellar phase where a uniform scattering length density and random distribution in solution are assumed.<sup>318</sup>

The scattering intensity is expressed as:

$$I(q) = 2\pi \frac{P(q)}{\delta q^2}, \quad (6.1)$$

and the form factor is

$$P(q) = \frac{2\Delta\rho^2}{q^2} (1 - \cos(q\delta)), \quad (6.2)$$

where  $\delta$  is the lamellar thickness. Fitting by the lamellar model gives a thickness of 57.8 nm for the 8 bilayer shells and 33.0 nm for the 5 bilayer shell, which confirms the increase in shell thickness with increasing number of layers, the results also match well with thickness from AFM measurements. The interdiffusion of polyelectrolyte chains as well as the increased thickness and roughness with bilayer number are the probable driving forces for the appearance of lamellar-like shell structure.

On the other hand, *in situ* SANS measurements were conducted for (PSS/PDMAEMA<sub>18</sub>)<sub>5</sub> microcapsules with increasing temperature, which are shown in Figure 6.15b. It can be seen that from 25 °C to 40 °C, the overall shapes of the scattering curves are similar, but fitting from power law and DAB models is able to provide insightful information. Power law model fitting shows that the surface fractal dimension gradually increases from 2.60 (25 °C) to 2.63 (30 °C), 2.80 (35 °C) and 2.84 (40 °C), which means that the shell structure has a densification trend with temperature, although still in the surface fractal range. Accordingly, DAB model fitting shows that the correlation length decreases from 35.6 nm (25 °C) to 33.8 nm (30 °C), 28.2 nm (35 °C) and 26.3 (40 °C), which provides direct evidence about the permeability decrease of the microcapsule with increasing temperature.

Moreover, when the temperature further increases to 45 °C, the scattering curve undergoes a significant change in shape, which is similar to the thicker, lamellar-like structure as we discussed for the 8 bilayer microcapsules above. Fitting by the lamellar model for the 45 °C scattering curve gives a thickness of 38.3 nm. Such a transition provides another strong evidence that increasing temperature leads to densification of the shell, which has both a thickness increase and mesh size decrease.

## 6.4 Conclusions

In conclusion, responsive PDMAEMA star polyelectrolytes (to pH and temperature) were successfully used as main component to fabricate LbL microcapsules. The microcapsules are able to respond to multiple external stimuli, such as ionic strength, pH, and

temperature. With increasing pH, the permeability of microcapsules decreases, and the transition from “open” to “close” state for target molecules can be accurately tuned within a narrow pH range. Furthermore, due to the thermo-responsiveness of PDMAEMA stars, the overall size and permeability of the microcapsules decreases with increasing temperature, a reversible encapsulation and release of cargo molecules by temperature changes can be achieved. The organization and interaction of star polyelectrolytes within confined multilayer structure are the main driving forces for the multiple responsive behaviors. SANS measurements give direct evidence to the structural evolution of the microcapsule shell under different conditions.

This study is the first demonstration of multi-responsive microcapsules and provides insights to the interaction and assembly of star polyelectrolytes in multilayered systems. The microcapsules based on responsive star polyelectrolytes provide a robust and smart platform to enable the controlled loading and unloading of target molecules under multiple stimuli. For example, the star polyelectrolytes can serve as nanocarriers for target molecule I, and target molecule II can be encapsulated in the hollow core region of microcapsules, then by applying different stimuli simultaneously or consecutively, the target molecules can be released in a controlled and logic way, which is superior to most conventional polyelectrolyte microcapsules. Moreover, the ability of the LbL microstructure to translate multiple external stimuli into physical response has the potential to be used as multi-input logic gates and polymer memory device,<sup>319</sup> which was demonstrated mostly for small molecules or polymers before.

## Appendix: Supporting Information

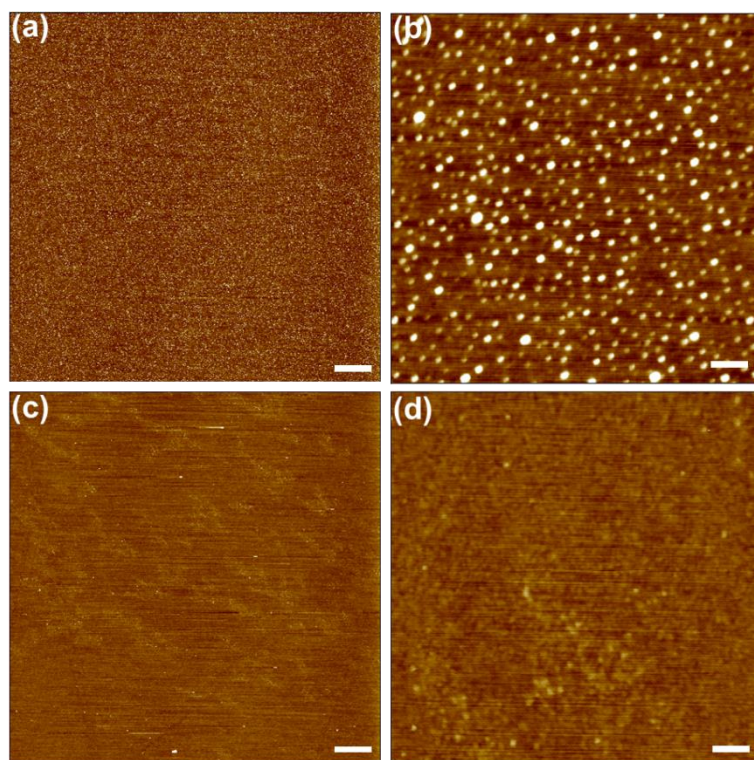


Figure S6.1. AFM images of PDMAEMA<sub>18</sub> star polyelectrolytes (a, b) and PDMAEMA<sub>1</sub> linear polyelectrolytes (c, d). Scale bar is 1 μm (a, c) and 100 nm (b, d), Z range is 5 nm.

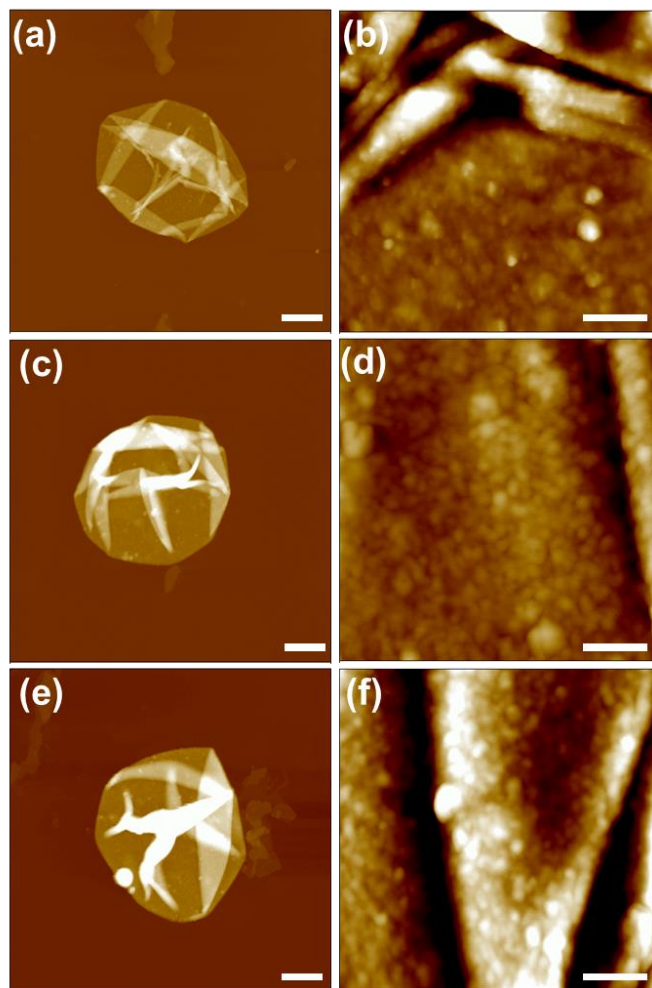


Figure S6.2. (a-b) AFM images of  $(\text{PSS}/\text{PDMAEMA}_1)_5$  microcapsule, (c-d) AFM images of  $(\text{PSS}/\text{PDMAEMA}_1)_8$  microcapsule, (e-f) AFM images of  $(\text{PSS}/\text{PDMAEMA}_{18})_{11}$  microcapsule; scale bar is  $1\ \mu\text{m}$  (left column) and  $200\ \text{nm}$  (right column), Z range is  $400\ \text{nm}$  (left column) and  $50\ \text{nm}$  (right column).

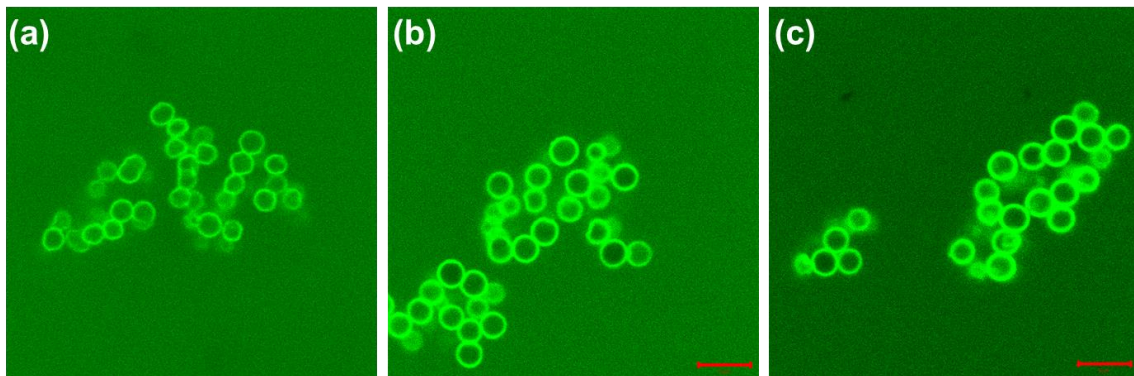


Figure S6.3. CLSM images of (PSS/PDMAEMA<sub>18</sub>)<sub>5</sub> microcapsules fabricated from water solution exposed to FITC-dextran solutions with different molecular weight (a) 70 kDa, (b) 150 kDa, (c) 250 kDa, at pH 5 condition. Scale bar is 5  $\mu$ m.

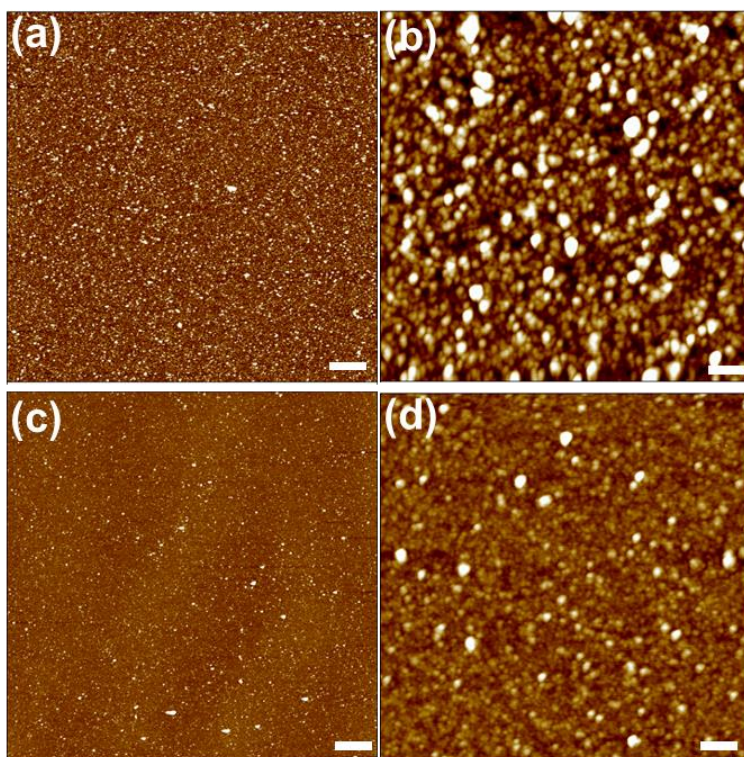


Figure S6.4. AFM images of (PSS/PDMAEMA<sub>18</sub>)<sub>11</sub> LbL films (a, b) and (PSS/PDMAEMA<sub>1</sub>)<sub>11</sub> LbL films (c, d). The scale bar is 2  $\mu$ m (left column) and 200 nm (right column), Z range is 30 nm (left column) and 20 nm (right column).

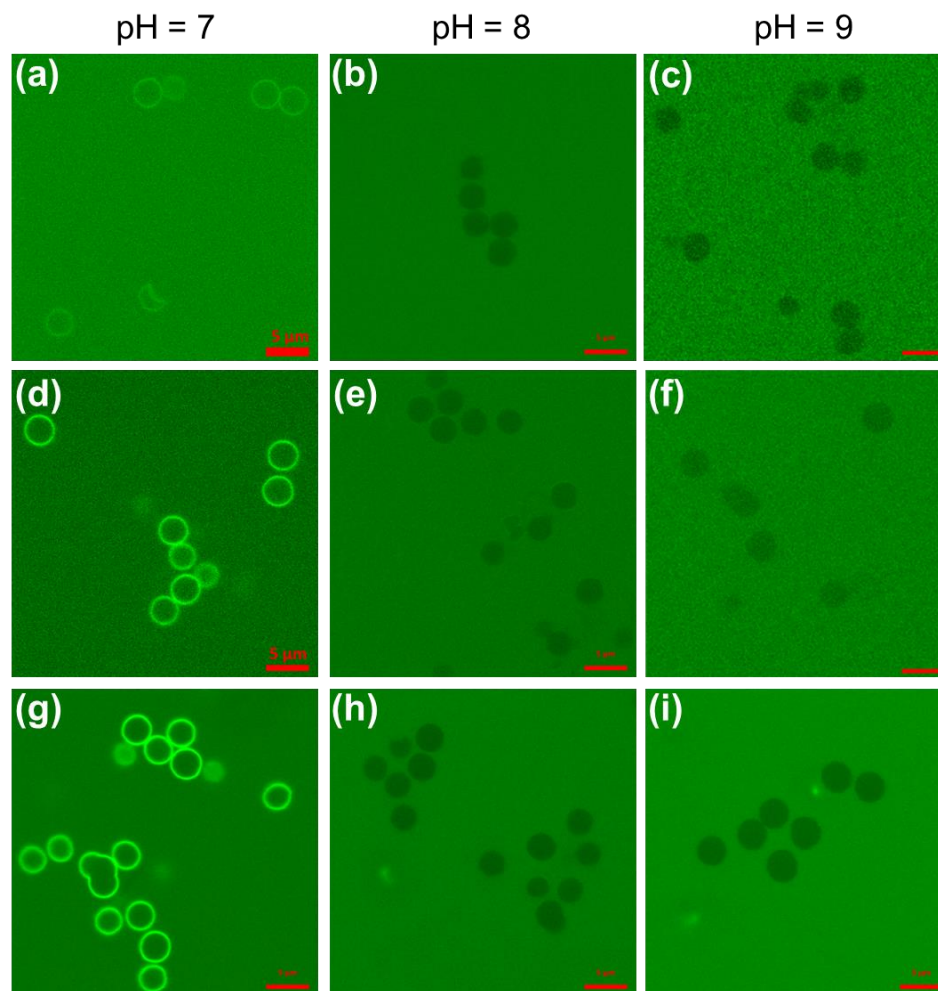


Figure S6.5. CLSM images of  $(\text{PSS}/\text{PDMAEMA}_1)_n$  microcapsules with 5 bilayers (a, b, c), 8 bilayers (d, e, f), 11 bilayers (g, h, i) exposed to FITC solutions at different pH conditions. Scale bar in each panel is 5  $\mu\text{m}$ .

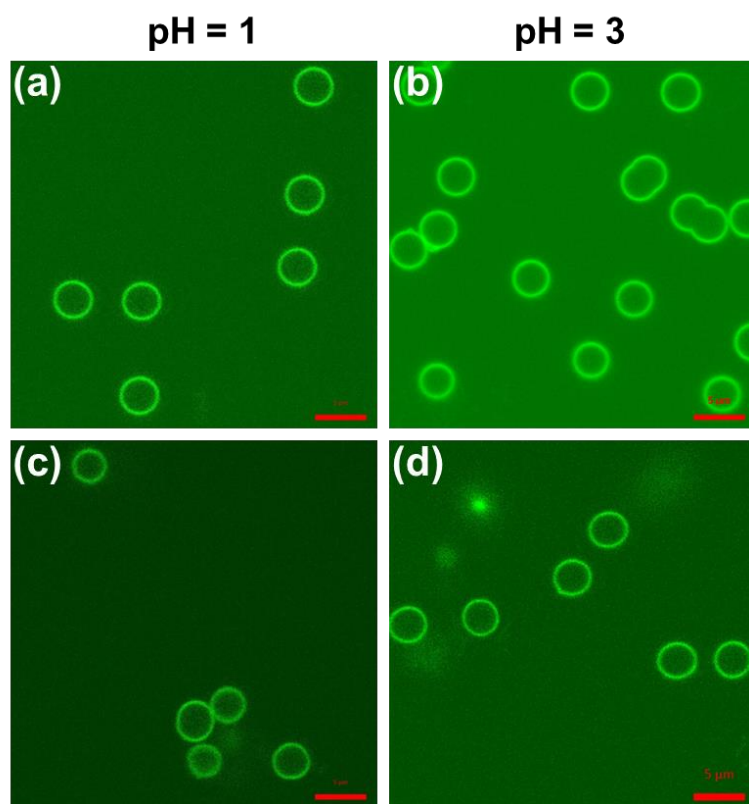


Figure S6.6. CLSM images of (PSS/PDMAEMA<sub>18</sub>)<sub>8</sub> (a, b) and (PSS/PDMAEMA<sub>1</sub>)<sub>8</sub> microcapsules (c, d) exposed to FITC solutions with pH 1 and pH 3. Scale bar is 5 μm.

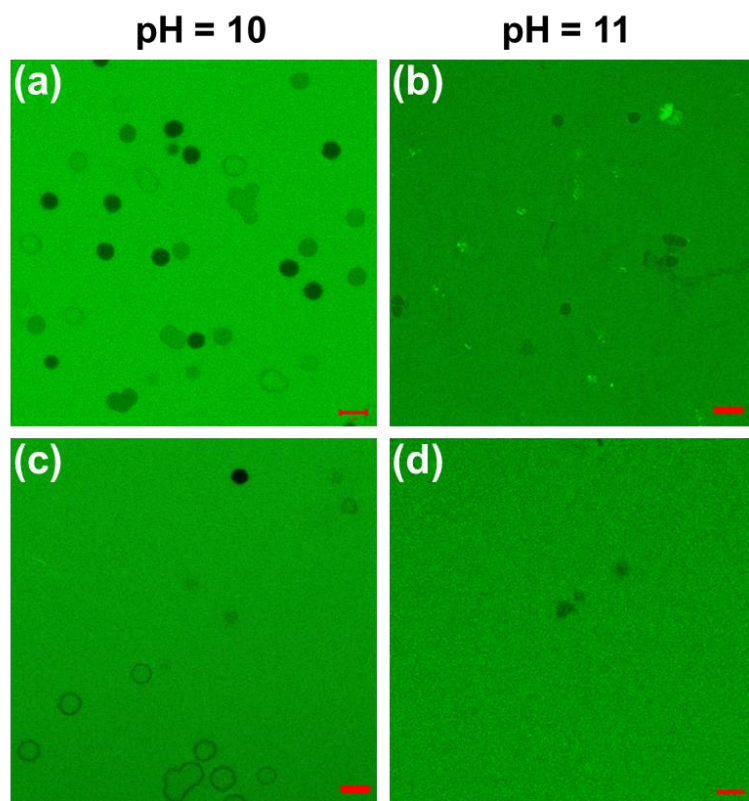


Figure S6.7. CLSM images of (PSS/PDMAEMA<sub>18</sub>)<sub>8</sub> (a, b) and (PSS/PDMAEMA<sub>1</sub>)<sub>8</sub> microcapsules (c, d) exposed to FITC solutions with pH 10 and pH 11. Scale bar is 5  $\mu\text{m}$ .

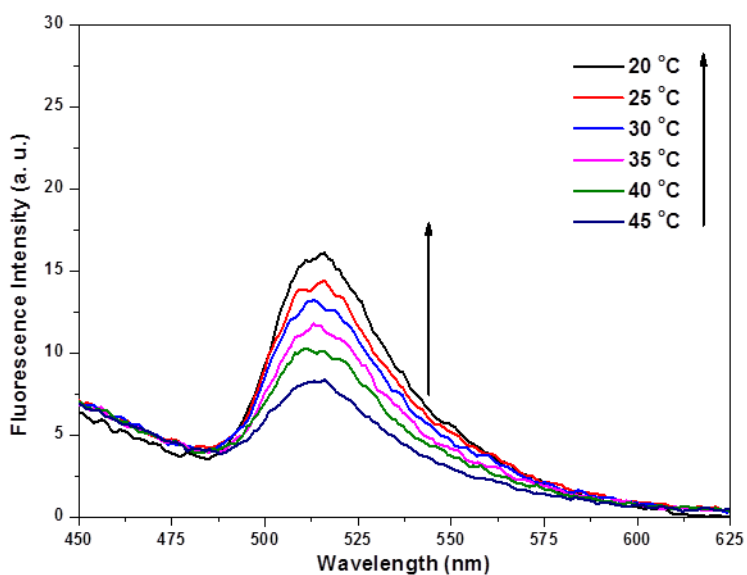


Figure S6.8. Fluorescence intensity of the dialysis bath which contains the FITC molecules permeate from the microcapsules, during the cooling of (PSS/PDMAEMA<sub>18</sub>)<sub>8</sub> microcapsules from 45 °C to 20 °C at pH 6 condition.

## CHAPTER 7. ION AND UV RESPONSIVE MICROCAPSEULS BASED ON QPDMAEMA STAR POLYMERS

### 7.1 Introduction

Responsive materials assembled from nanostructured building blocks have attracted much attention in recent years due to their abilities to adapt and respond to stimuli in surrounding environments.<sup>154</sup> These materials are playing an increasingly important role in fields such as controlled release,<sup>320</sup> tissue engineering, biosensors and catalytic systems. Among the many approaches to fabricate responsive polymeric structures, layer-by-layer (LbL) assembly is a highly versatile technique to produce organized structures with desirable properties from many different kinds of materials, such as polymers,<sup>321</sup> nanoparticles, DNA, proteins and viruses.<sup>322</sup> Microcapsules prepared *via* LbL techniques have attracted particular interests because their properties can be readily tailored during and after the preparation process.<sup>323</sup> In addition, multiple functionalities can be introduced during the step-wise formation, thus creating a novel platform with unprecedented structures and functions.<sup>324</sup>

Stimuli-responsive behavior of microcapsules can be achieved in various ways by specific stimuli such as pH, salt, light, ultrasonic and magnetic fields, which can trigger cargo release at the desired location, condition, and time.<sup>325</sup> Microcapsules composed of weak polyelectrolytes are generally responsive to pH of the environment.<sup>326</sup> When the pH of the environment becomes lower (in case of polyacid) or higher (in case of polybase) than the  $pK_a$ , the polyelectrolytes become uncharged thus resulting in the increasing permeability.<sup>327</sup> This process can be reversible in most cases when the pH of

the environment goes back to the original value. However, the pH responsive approach cannot be remotely controlled and most of pH responsive microcapsules are not able to perform satisfactorily in terms of subtle pH change. Another interesting category of responsive microcapsules is magnetic field responsive. By embedding magnetic particles into the polymer shells of microcapsules, the LbL shells can be disturbed, and consequently, allows the permeation of target molecules through the microcapsule wall.<sup>328</sup> But the long exposure time and strong magnetic field requirement are major challenges.

Light-induced release of polymeric microcapsules has attracted much attention in recent years due to their potential applications in diverse delivery areas.<sup>329</sup> Previous research on light-responsive microcapsules can be divided into three main categories. Firstly, microcapsules containing metal nanoparticles such as TiO<sub>2</sub>, silver and gold,<sup>330</sup> which can either destructively or non-destructively change the permeability and mechanical properties of microcapsules,<sup>331</sup> mostly due to the strong light absorption of the nanoparticles. Unfortunately, the potential toxicity of metal nanoparticles might limit their application in some fields and most of the approaches are destructive. The second category is microcapsules contains fluorescent and functional dyes,<sup>332</sup> which can be responsive to visible or IR irradiation. Finally, UV irradiation can change the permeability of microcapsules by photooxidation or optical photoisomerization.<sup>333</sup> But the light responsive properties for these microcapsules are compromised by the fact that only about half of the microcapsules have the ability to encapsulate model substances after UV irradiation, and the approaches are destructive to the microcapsules (but not

necessary for organic exterior), thus multiple loading-unloading cycles of these microcapsules cannot be completed.

The modulation of the polyelectrolyte microcapsule's permeability by changing the salt concentration in the surroundings is commonly observed for polyelectrolyte-based LbL microcapsules.<sup>334</sup> Salt-induced permeability change of microcapsules shell is generated from the shielding of charges on the polyelectrolytes that reduces the interaction between adjacent layers with opposite charges, thus facilitating the diffusion of macromolecules through the multilayer walls. The combination of salt and UV responsive properties can be possibly achieved by using salt with photochemical property, so that the change in permeability of microcapsule shell induced by the addition of salt can be recovered by decomposing the salt using photochemical reaction. To achieve this goal, the polymers used to compose the microcapsule shell need to be very sensitive to the salt, especially having dramatically different behaviors in the presence of different salt ions before and after the photochemical reaction. Highly branched polyelectrolytes can be considered as the material of choice for the assembly of ion-sensitive shells, among which star polyelectrolytes are excellent candidates for such microcapsules due to their extremely high sensitivity to ionic environment.<sup>335</sup> Compared to dendrimers and other branched polymers, star polymers have the advantages of facile synthesis,<sup>336</sup> flexible compositions and tunable sizes.<sup>337</sup>

There are several pioneering works on microcapsules made from branched polyelectrolyte macromolecules. Poly(amidoamine) dendrimers have been used to

prepare hollow capsules by LbL technique with poly(sodium 4-styrenesulfonate) (PSS),<sup>338</sup> however the capsules were unstable toward core removal procedure and the yield was low. Microcapsules composed of cationic phosphorus dendrimers and PSS were able to selectively encapsulating Cy5 dye molecules *via* DNA hybridization.<sup>339</sup> The mechanical properties of DNA/phosphorus dendrimers based microcapsules have been studied, and it was found that these microcapsules were softer than microcapsules assembled from linear flexible polyelectrolytes.<sup>340</sup> Hollow microcapsules with shell constructed entirely from a cationic/zwitterionic pairs of pH-responsive block copolymer micelles have also been successfully prepared, it was shown that the core/shell structure of the micelles remains intact after LbL assembly.<sup>341</sup>

Herein, we introduce novel LbL microcapsules based on responsive star polyelectrolytes with unique non-destructive, remote, reversible, light-induced tunability of shell permeability in high contrast with traditional methods which are usually destructive and require adding toxic nanoparticles to shell composition. Taking advantage of star polyelectrolyte's unique response to ionic environment, we can effectively modulate the conformation of qPDMAEMA stars by adding multivalent salt and controlling its state by mild photo-induced chemical reaction, thus readily tuning the permeability of microcapsules. By using the photochemical reaction,  $\text{Co}(\text{CN})_6^{3-}$ , trivalent counterions can be decomposed into monovalent and divalent ions that dramatically affect the conformation of qPDMAEMA star polyelectrolytes and porosity of LbL shells.<sup>46</sup> In contrast to previous approaches, the path suggested here results in reversible, remote, non-destructive light-triggering changes in microcapsules permeability.

## 7.2 Experimental Section

**Materials.** Poly(ethylene imine) (PEI) was purchased from Polysciences. PSS ( $M_w=70K$ ) and poly(allylamine hydrochloride) (PAH,  $M_w=58K$ ) were purchased from Sigma-Aldrich. All commercial polyelectrolytes were used without further purification. Potassium hexacyanocobaltate (III) was also purchased from Sigma-Aldrich, with a total impurity  $\leq 0.1\%$ . Silica particles with diameter of  $4.0 \pm 0.2 \mu\text{m}$  and 10% dispersion in water were obtained from Polysciences. Hydrofluoric acid (48–51%) was purchased from BDH Aristar.

**Synthesis of *qPDMAEMA star polyelectrolytes.*** Poly{2-(methacryloyloxy)ethyl trimethylammonium iodide} (*qPDMAEMA*) is the quaternized ammonium salt of poly2-(N,N-dimethylamino)ethyl methacrylate (*PDMAEMA*). *PDMAEMA* was synthesized by atom transfer radical polymerization employing a core-first approach.<sup>47</sup> Sugar-based scaffolds as well as silsesquioxane nanoparticles were used as oligofunctional initiators. The rather low efficiency of the initiation sites (30-75%) leads to a moderate arm number distribution of the prepared polyelectrolyte stars. For quaternization, *PDMAEMA* was dissolved in acetone and methyl iodide was added at room temperature at a molar ratio of 1.5 compared to amino groups. The mixture was kept stirring overnight to ensure quantitative conversion. Acetone was decanted and the polymer was washed several times with acetone. Then quaternized polymer was dissolved in water and dialyzed against pure water for 2 days and finally freeze-dried. Here we used star *qPDMAEMA* with an arm number of 18 (number average, polydispersity index (PDI) in arm number distribution  $\approx 1.4$ ) and a number-average degree of polymerization per arm of 170 (PDI

of arm = 1.2), number average molecular weight is 910K. qPDMAEMA<sub>5,6</sub> also has a number-average degree of polymerization per arm of 170 (PDI of arm = 1.2), number average molecular weight is 280K. Detailed synthesis steps and characterization has been published earlier.<sup>132</sup>

***Preparation of LbL films and microcapsules.*** PSS and qPDMAEMA star polyelectrolyte are dissolved in 0.01 M Tris-HCl buffer (pH = 7) with the concentration of 0.2 mg/mL. PEI solution (1.0 mg/mL) in 0.01M Tris-HCl buffer was used to deposit the pre-layer. Silicon wafer was cleaned with pirana solution (3:1 concentrated sulfuric acid and hydrogen peroxide mixture. *Caution strong oxidizer!*) according to the known procedure.<sup>342</sup> Then it was rinsed with abundant nanopure water and dried with a nitrogen stream. LbL films were prepared by dip-assisted method: the silicon substrate was alternately immersed in PSS and qPDMAEMA star polyelectrolyte solution for 15 min, followed by two times rinsing with 0.01 M Tris-HCl buffer. For most of studies, we prepared LbL film with bilayer numbers of 5, 8 and 11, all of which have PSS as the outmost layer.

The preparation of LbL (PSS/qPDMAEMA)<sub>n</sub> microcapsules is shown in Scheme 2: the bare, negatively charged silica particles with average diameter of 4 μm were first coated with PEI prelayer by incubating in 1.5 mL of PEI solution (1.0 mg/mL) for 15 min, followed by two centrifugation (3000 rpm for 3 min)/wash cycles. Subsequently, the silica particles were incubated in 1.5 mL PSS solution (0.2 mg/mL) for 15 min, followed by two centrifugation (3000 rpm for 3 min)/wash cycles. 1.5 mL of qPDMAEMA star

polyelectrolyte solution was then added to the silica particles and 15 min was allowed for adsorption, also followed by two centrifugation cycles. The PSS and qPDMAEMA star polyelectrolyte adsorption steps were repeated until the desired number of layers was built on silica particles. Hollow microcapsules were finally obtained by dissolving silica cores in 0.5% HF solution for 2h, followed by dialysis in nanopure water for 36h with repeated change of water.

## **7.3 Results and Discussion**

### **7.3.1 Properties of qPDMAEMA Star Polyelectrolytes and the LbL Thin Films**

The chemical structure of the qPDMAEMA star polyelectrolyte is shown in Figure 7.1a. qPDMAEMA is the quaternized ammonium salt of PDMAEMA, which was synthesized by polymerizing DMAEMA by atom transfer radical polymerization employing a core-first strategy. The oligofunctional initiators used here were sugar-based scaffolds as well as silsesquioxane nanoparticles. At very low ionic strength the hydrodynamic radius of qPDMAEMA<sub>18</sub> is 24 nm, which is about 56% of the contour length of a single arm (42.5 nm), indicating a considerable stretching due to Coulombic repulsion and high osmotic pressure inside the star.<sup>47</sup> As previously reported,<sup>36</sup> when multivalent counterions are added to star polyelectrolyte solution, the arms of the star polyelectrolytes would retract (Figure 7.1b). The addition of trivalent hexacyanocobaltate(III) ions leads to collapse of qPDMAEMA star polyelectrolyte even at low concentrations. Moreover, qPDMAEMA star can recover to expanded state from collapsed state by transforming the trivalent hexacyanocobaltate(III) ions into a mixture of mono- and divalent ions by UV irradiation, as shown in Figure 7.1b. Therefore, the conformation and interaction of qPDMAEMA

star polyelectrolyte can be switched by controlling the state of multivalent salts with UV irradiation. To take advantage of the unique responsive behaviors of qPDMAEMA star polyelectrolyte and extend its application, we study the properties of planar films first.

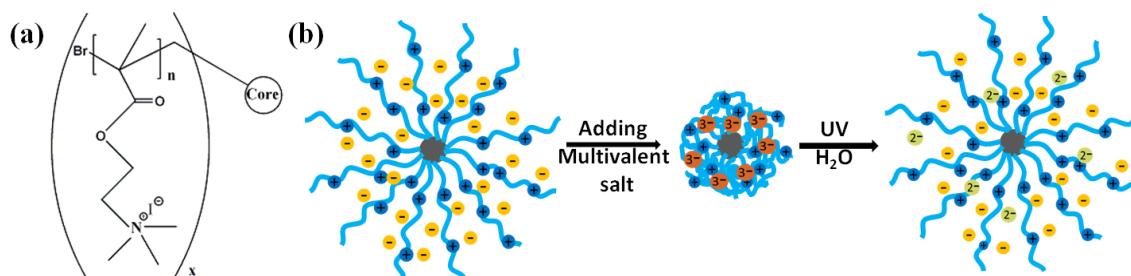


Figure 7.1. (a) Chemical structure of qPDMAEMA star polyelectrolyte, (b) structural change of qPDMAEMA after adding  $K_3Co(CN)_6$  and during the photochemical reaction.

### **(PSS/qPDMAEMA)<sub>n</sub> LbL thin films**

To study the effects of the number of arms of star polyelectrolytes on their self-assembly behavior, two sets of LbL films with 5, 8 and 11 bilayers have been prepared from PSS and 18 and 5.6 armed qPDMAEMA star polyelectrolytes:  $(PSS/qPDMAEMA_{18})_n$  and  $(PSS/qPDMAEMA_{5.6})_n$ . In this designation, for instance,  $(PSS/qPDMAEMA_{18})_8$  represents a film (or microcapsule) of 8 bilayers made with 18 arm qPDMAEMA star polyelectrolyte.

AFM images of the  $PSS/qPDMAEMA_{18}$  films with three different numbers of layers are shown in Figure 7.2. The films are uniform that confirms the relatively strong interaction between  $qPDMAEMA_{18}$  and PSS components. From high resolution AFM topography and phase images, it can be seen that fine granular structures are uniformly distributed throughout the surface. The average size of the granules is below 30 nm, with the height

around 2.5 nm, which are close to expected dimensions of qPDMAEMA star polyelectrolytes with extended arms. The density of granule structures on the surface of LbL films gradually increases with the number of layers, while the overall roughness of the films remains almost constant, around 1.7 nm (as measured on  $1 \times 1 \mu\text{m}$  area). The microroughness of  $(\text{PSS}/\text{qPDMAEMA}_{18})_n$  films is higher than that of uniform LbL films made by linear polyelectrolyte (usually below 1 nm) due to more pronounced aggregation of star polyelectrolytes.

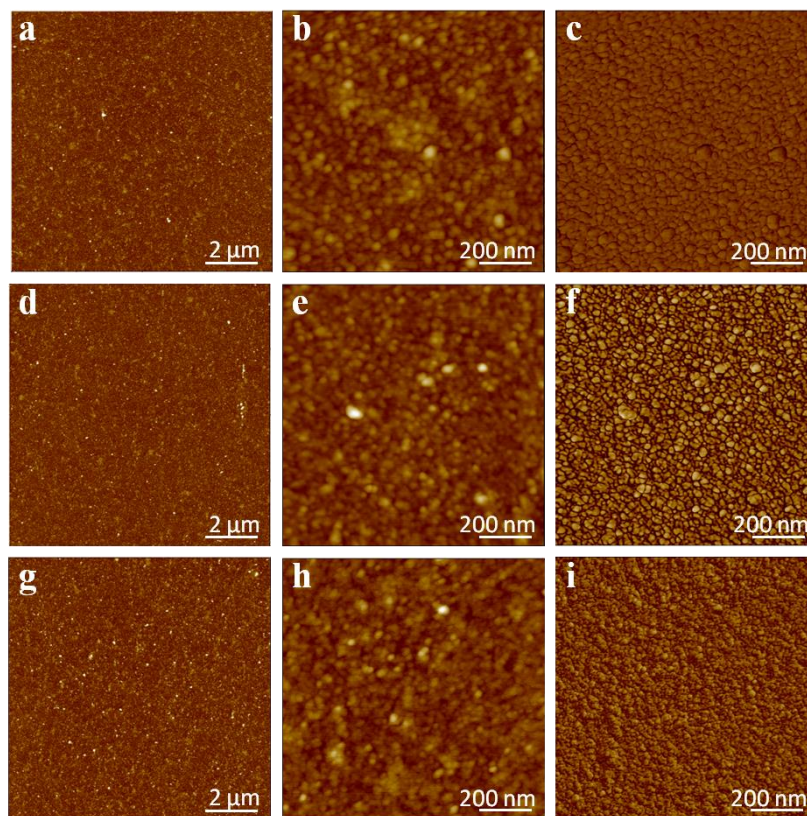


Figure 7.2. (a-c) AFM images of  $(\text{PSS}/\text{qPDMAEMA}_{18})_5$  film, (d-f) AFM images of  $(\text{PSS}/\text{qPDMAEMA}_{18})_8$  film, (g-i) AFM images of  $(\text{PSS}/\text{qPDMAEMA}_{18})_{11}$  film; (c, f, i) are phase images. Z-scale is 30nm for topography images, and  $30^\circ$  for phase images.

Figure 7.3 shows the thickness buildup of  $(\text{PSS}/\text{qPDMAEMA}_{18})_n$  films as obtained from UV absorption and ellipsometry. From UV absorption it is clear that the increase of

number of layers results in a virtually linear growth of film thickness.<sup>343</sup> Both total thickness and the characteristic peak in 227nm which is attributed to the phenyl ring in PSS linearly increase with the number of layers.

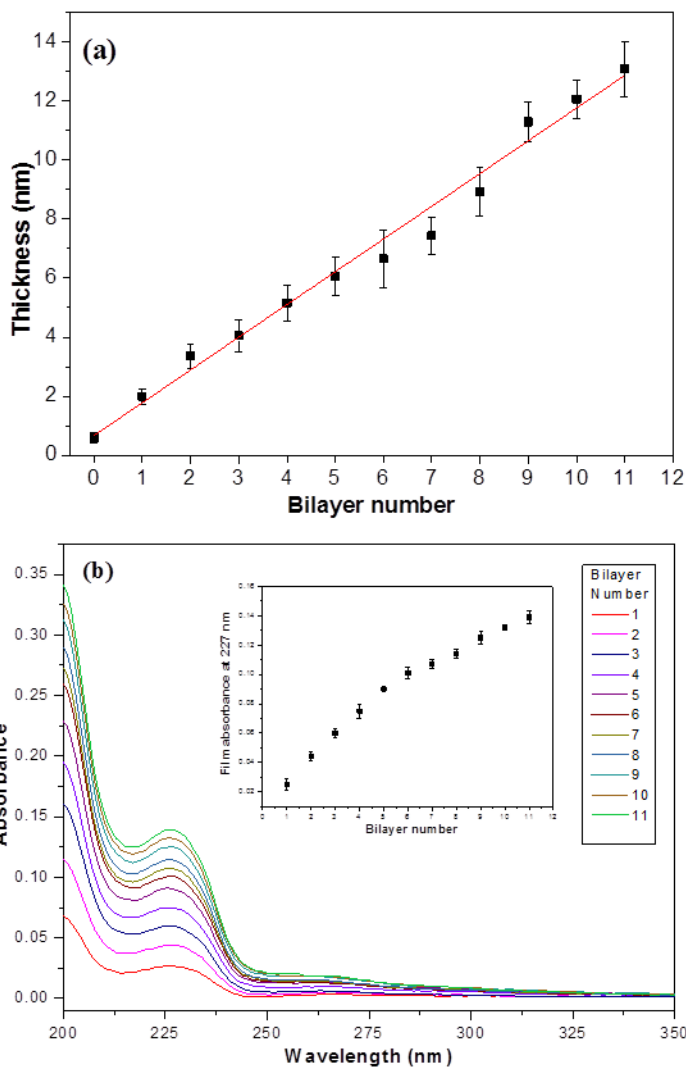


Figure 7.3. (a) Thickness of  $(\text{PSS}/\text{qPDMAEMA}_{18})_n$  films as a function of bilayer number as measured by ellipsometry. (b) UV-Vis spectra of  $(\text{PSS}/\text{qPDMAEMA}_{18})_n$  films with different number of layers assembled on quartz substrate. Inset shows the intensity increase of peak at 227 nm with bilayer number.

AFM images for the  $(\text{PSS}/\text{qPDMAEMA}_{5.6})_n$  films show different characteristics compared with that of  $(\text{PSS}/\text{qPDMAEMA}_{18})_n$  films (Figure 7.4). The high resolution

AFM topography and phase images of (PSS/qPDMAEMA<sub>5.6</sub>)<sub>5</sub> films show uniform distribution of granular aggregates. The average size of these granule structures (below 20 nm) is smaller than that of the 18 arm qPDMAEMA star polyelectrolytes. With the increased of number of layers, some larger-scale aggregation occurs as can be clearly seen for 8 and 11 bilayer films. This process is confirmed by the increased microroughness of (PSS/qPDMAEMA<sub>5.6</sub>)<sub>n</sub> films with 5, 8 and 11 bilayers from 1.1 to 2.2 and 3.9 nm, respectively.

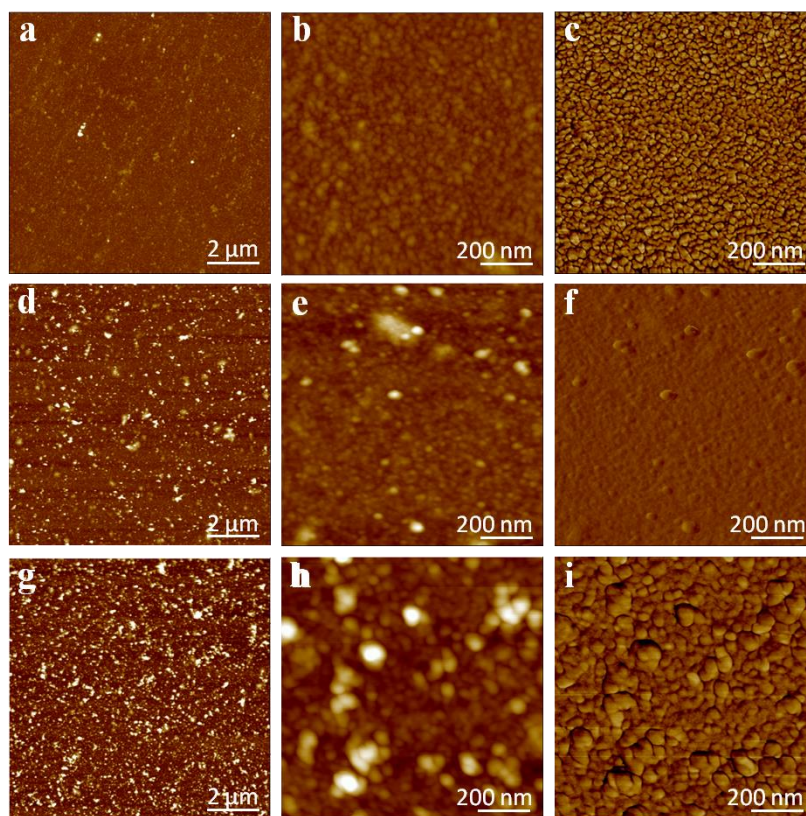


Figure 7.4. (a-c) AFM images of (PSS/qPDMAEMA<sub>5.6</sub>)<sub>5</sub> film, (d-f) AFM images of (PSS/qPDMAEMA<sub>5.6</sub>)<sub>8</sub> film, (g-i) AFM images of (PSS/qPDMAEMA<sub>5.6</sub>)<sub>11</sub> film; (c, f, i) are phase images. Z-scale is 30nm for topography images, and 30° for phase images.

Despite the appearance of large aggregates on the film surface, the average thickness of (PSS/qPDMAEMA<sub>5.6</sub>)<sub>n</sub> films grows linearly with layer number, as proven by the

thickness data from ellipsometry measurement. The UV absorbance intensity at 227 nm increases almost linearly with increasing layer number indicating consistent growth of LbL films. For the same number of layers, the (PSS/qPDMAEMA<sub>5.6</sub>)<sub>n</sub> film is slightly thinner than the (PSS/qPDMAEMA<sub>18</sub>)<sub>n</sub> film, due to lower molecular weight of 5.6 arm star polymer.

### 7.3.2 Morphology of (PSS/ qPDMAEMA)<sub>n</sub> LbL Microcapsules

The common preparation routine for (PSS/qPDMAEMA)<sub>n</sub> microcapsules is shown in Figure 7.5. Similar to (PSS/qPDMAEMA)<sub>n</sub> films, we also prepared LbL microcapsules using two different qPDMAEMA star polyelectrolytes with 5.6 arms and 18 arms and with 5, 8 and 11 bilayer shells.

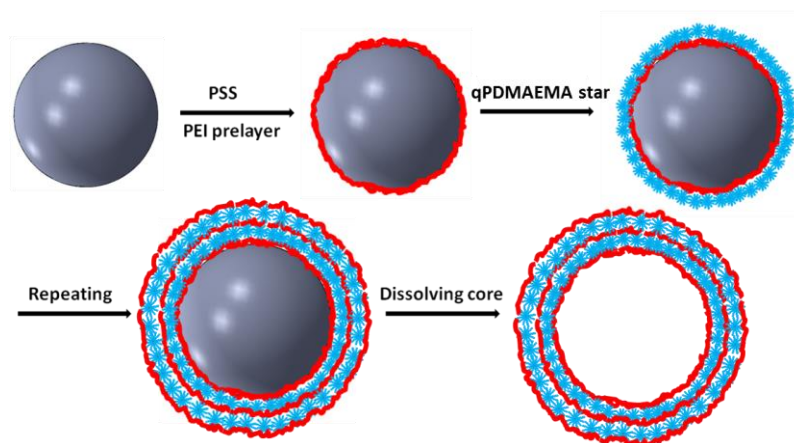


Figure 7.5. LbL assembly on silica core and fabrication of (PSS/qPDMAEMA)<sub>n</sub> hollow microcapsule.

Electrophoresis experiment was conducted to monitor the LbL growth of PSS and qPDMAEMA star polyelectrolytes. As shown in Figure 7.6, the  $\zeta$ -potential of bare silica particle was *ca.* -70 mV. A  $\zeta$ -potential of *ca.* -75 mV was obtained for microcapsules when PSS was the outmost layer of film on silica core. On the other hand, a positive  $\zeta$ -

potential of +72 mV was observed when qPDMAEMA<sub>18</sub> star polyelectrolyte was the outermost layer. On the whole, the alternating surface charge of coated silica particles was strong evidence that consistent LbL assembly of anionic PSS and cationic qPDMAEMA components took place during the fabrication process.

SEM images of (PSS/qPDMAEMA<sub>18</sub>)<sub>11</sub> and (PSS/qPDMAEMA<sub>5.6</sub>)<sub>11</sub> microcapsules are shown in Figure 7.7, it can be seen that all of the different kinds of microcapsules are uniform in size. The average thicknesses for (PSS/qPDMAEMA<sub>18</sub>) microcapsules with 5, 8, 11 bilayers are 12.8, 16.1 and 21.6 nm, respectively, which is higher than that of planar films with the same number of layer (see comparison in Figure 7.8a). The average bilayer thicknesses of (PSS/qPDMAEMA<sub>18</sub>)<sub>n</sub> films and microcapsules in dry state are 1.2 nm and 2.0 nm, respectively. The rougher silica particles resulted in larger adsorbed amount as discussed in earlier reports.<sup>344</sup>

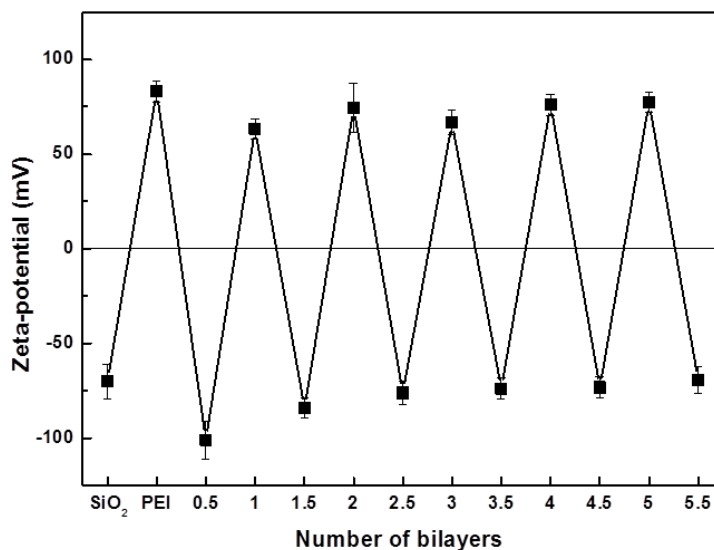


Figure 7.6. Zeta ( $\zeta$ )-potential as a function of bilayer number during LbL coating of silica particles with alternating (PSS/ qPDMAEMA<sub>18</sub>) bilayers.

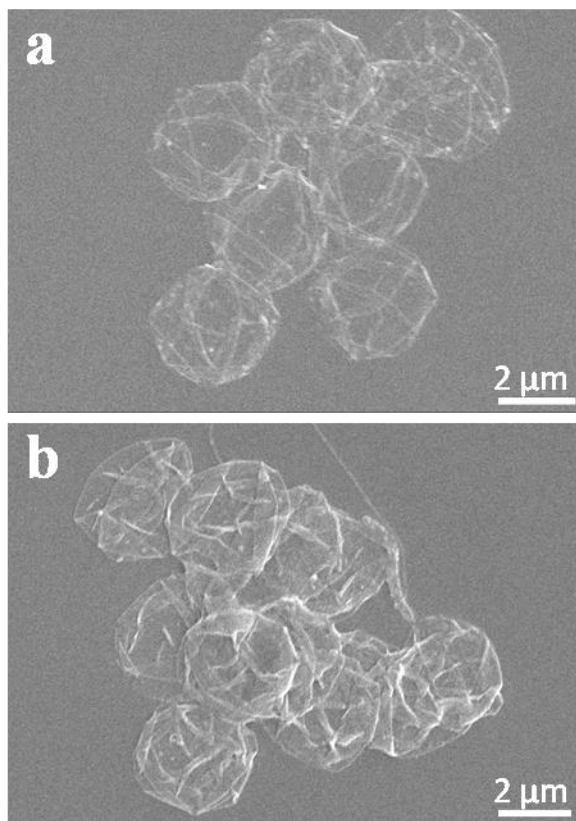


Figure 7.7. SEM images of (PSS/qPDMAEMA<sub>18</sub>)<sub>11</sub> (a) and (PSS/qPDMAEMA<sub>5.6</sub>)<sub>11</sub> (b) microcapsules.

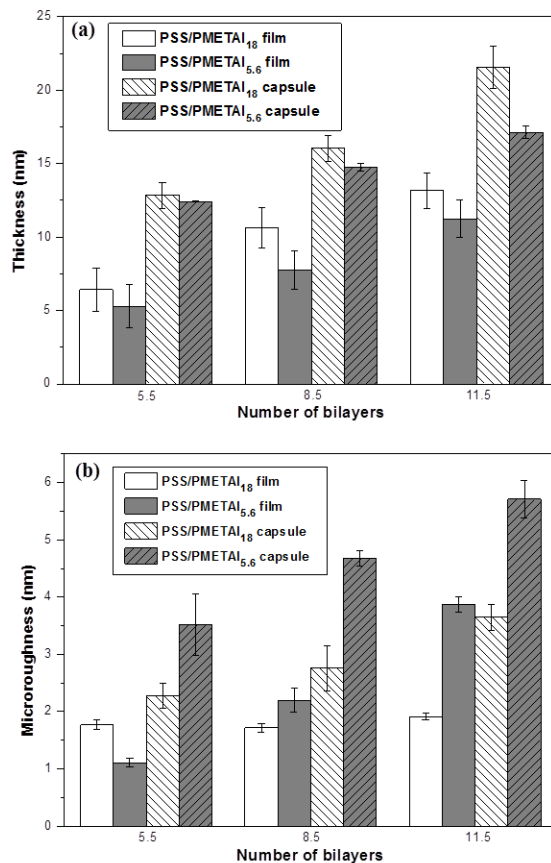


Figure 7.8. (a) Comparison of thickness of  $(\text{PSS}/\text{qPDMAEMA}_{18})_n$  with  $(\text{PSS}/\text{qPDMAEMA}_{5,6})_n$  for both microcapsules and films. (b) Comparison of microroughness of  $(\text{PSS}/\text{qPDMAEMA}_{18})_n$  and  $(\text{PSS}/\text{qPDMAEMA}_{5,6})_n$  for microcapsules and films.

Stable and monodisperse microcapsules were produced upon removal of silica cores, although a certain amount of shrinkage was observed. From confocal microscopy images it can be seen that the average diameter of hollow  $(\text{PSS}/\text{qPDMAEMA})_n$  microcapsules was  $3.0 \mu\text{m}$ , compared with  $4.0 \mu\text{m}$  diameter of the original silica particles. Such shrinkage of microcapsules based on highly branched polymers is in accordance with previous research and is related to partial collapse of the inner porous network upon core removal.<sup>345</sup>

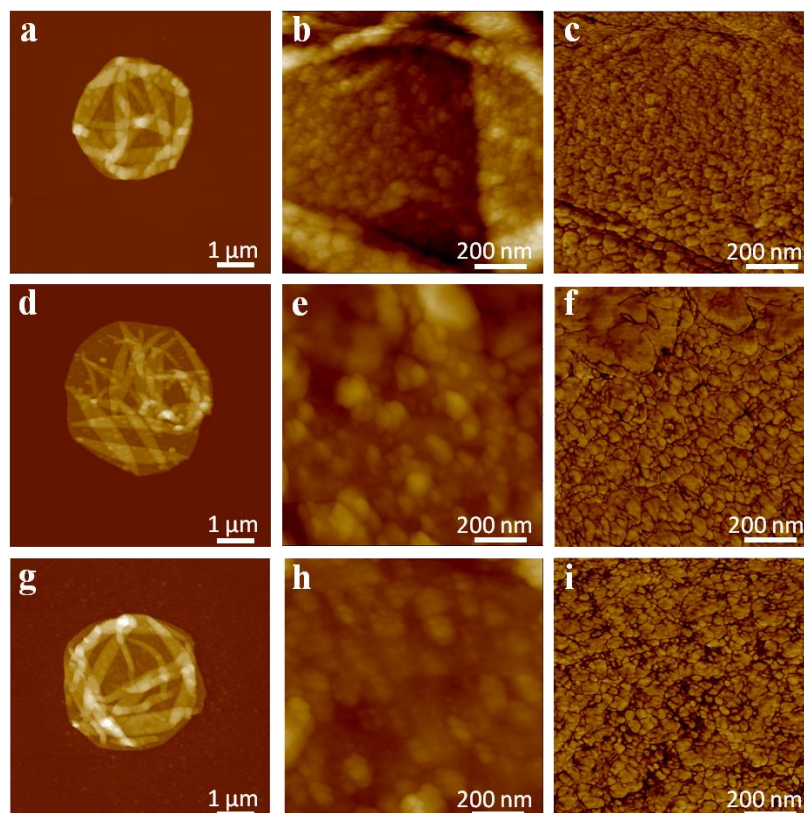


Figure 7.9. (a-c) AFM images of (PSS/qPDMAEMA<sub>18</sub>)<sub>5</sub> microcapsule, (d-f) AFM images of (PSS/qPDMAEMA<sub>18</sub>)<sub>8</sub> microcapsule, (g-i) AFM images of (PSS/qPDMAEMA<sub>18</sub>)<sub>11</sub> microcapsule; (c, f, i) are phase images. Z-scale is 200 nm for topography images, and 80° for phase images.

Figure 7.9 shows AFM images of dried (PSS/qPDMAEMA<sub>18</sub>)<sub>n</sub> hollow microcapsules with 5, 8, 11 bilayers. The large scale images show that the microcapsules are quite robust even after drying, preserve their near spherical shape and avoid aggregation due to strong Coulombic repulsion. Characteristic grainy morphology with occasional wrinkles and folded shells is visible for all three microcapsules with different number of layers. Similar to the morphology of films, high density of grains is visible with uniform distribution of aggregated nanostructures, a common feature for LbL shells with weakly interacting components. The overall roughness of (PSS/qPDMAEMA<sub>18</sub>)<sub>n</sub> microcapsules

is higher than that of films (see Figure 7.8b) with the roughness of microcapsules with 5, 8 and 11 bilayers increasing to 2.3, 2.8 and 3.6 nm, respectively.

Figure 7.10 shows the AFM images of  $(\text{PSS}/\text{qPDMAEMA}_{5,6})_n$  microcapsules with 5, 8, 11 bilayers. The thickness of microcapsules with 5, 8, 11 bilayers is 12.4, 14.8 and 17.1 nm, respectively (Figure 7.8a). Similar with that of  $(\text{PSS}/\text{qPDMAEMA}_{5,6})_n$  films, high resolution topography and phase images of microcapsules show a grainy surface morphology, increased porosity, as well as larger-scale aggregation. Such an aggregation significantly increases the microroughness of microcapsules as compared with that of  $(\text{PSS}/\text{qPDMAEMA}_{18})_n$ , and indicates less regular LbL growth. The microroughness of  $(\text{PSS}/\text{qPDMAEMA}_{5,6})$  microcapsules with 5, 8 and 11 bilayers is 3.5, 4.7 and 5.7 nm, respectively (Figure 7.8b). We suggest that the higher microroughness of these microcapsules and increasing porosity might affect the permeability of the microcapsules, as will be discussed in the following section.

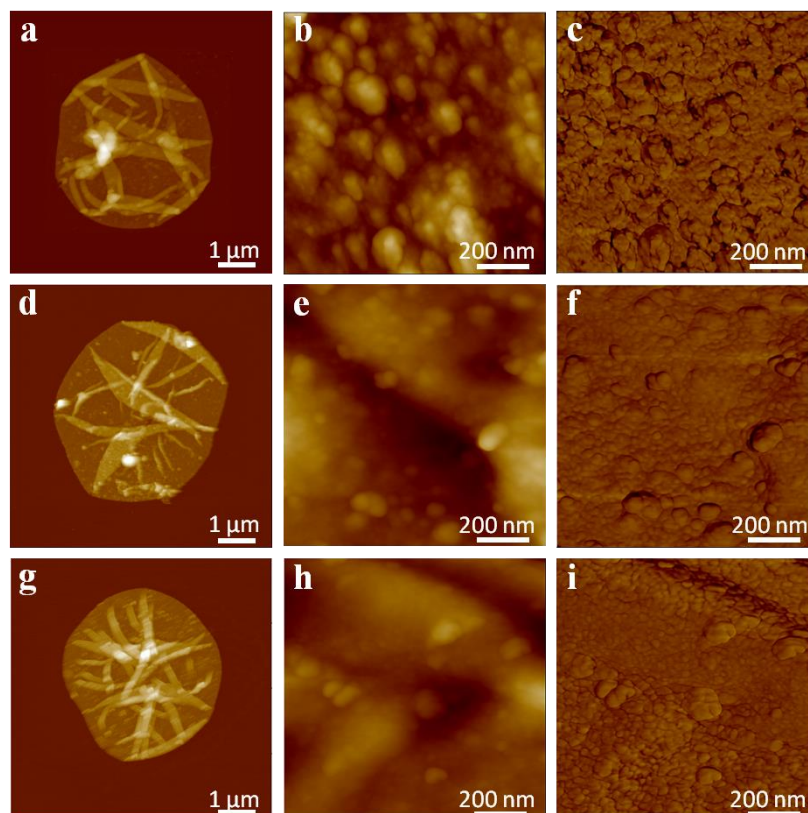


Figure 7.10. (a-c) AFM images of (PSS/qPDMAEMA<sub>5.6</sub>)<sub>5</sub> microcapsule, (d-f) AFM images of (PSS/qPDMAEMA<sub>5.6</sub>)<sub>8</sub> microcapsule, (g-i) AFM images of (PSS/qPDMAEMA<sub>5.6</sub>)<sub>11</sub> microcapsule; (c, f, i) are phase images. Z-scale is 200 nm for topography images, and 80° for phase images.

### 7.3.3 Controlled Permeability of (PSS/ qPDMAEMA)<sub>n</sub> Microcapsules

Fluorescein isothiocyanate (FITC)-labeled dextrans of various molecular weights were used as fluorescent probe to study the permeability of microcapsules with confocal microscopy (Table 7.1). As expected for diffusion controlled processes, the permeability of microcapsules decreases with the increase of layer number. For (PSS/qPDMAEMA<sub>18</sub>) microcapsules with 5 and 8 bilayers, FITC-dextran with molecular weight of 2000 kDa and below is able to permeate through the shells. For (PSS/qPDMAEMA<sub>18</sub>)<sub>11</sub>

microcapsules, FITC-dextran with molecular weight of 500 kDa and below can permeate through the shells, while 2000 kDa FITC-dextran cannot.

Table 7.1. Permeability of (PSS/qPDMAEMA<sub>18</sub>)<sub>n</sub> capsules to FITC-dextrans with different molecular weight (“+”: permeable, “-” non permeable).

Sample	FITC-dextran 70kDa	FITC-dextran 250kDa	FITC-dextran 500kDa	FITC-dextran 2000kDa
(PSS/qPDMAEMA <sub>18</sub> ) <sub>5</sub> in buffer	+	+	+	+
(PSS/qPDMAEMA <sub>18</sub> ) <sub>5</sub> after adding 0.8 mM K <sub>3</sub> Co(CN) <sub>6</sub>	-	-	-	-
(PSS/qPDMAEMA <sub>18</sub> ) <sub>8</sub> in buffer	+	+	+	+
(PSS/qPDMAEMA <sub>18</sub> ) <sub>8</sub> after adding 0.8 mM K <sub>3</sub> Co(CN) <sub>6</sub>	-	-	-	-
(PSS/qPDMAEMA <sub>18</sub> ) <sub>11</sub> in buffer	+	+	+	-
(PSS/qPDMAEMA <sub>18</sub> ) <sub>11</sub> after adding 0.8 mM K <sub>3</sub> Co(CN) <sub>6</sub>	-	-	-	-

Confocal microscopy images of (PSS/qPDMAEMA<sub>18</sub>)<sub>11</sub> microcapsules with different molecular weight FITC-dextran are shown in Figure 7.11. For (PSS/qPDMAEMA<sub>5,6</sub>)<sub>n</sub> microcapsules, the confocal microscopy images show that microcapsules with different number of layers are also very stable and uniform during changing the environment of the surrounding. Considering that the reported hydrodynamic diameters of 2000kDa and 500 kDa FITC-dextran are 53.8 nm and 31.8 nm,<sup>346</sup> respectively, the mesh size of (PSS/qPDMAEMA<sub>18</sub>)<sub>5</sub>, (PSS/qPDMAEMA<sub>18</sub>)<sub>8</sub> and (PSS/qPDMAEMA<sub>18</sub>)<sub>11</sub> shells should fall within 30-50 nm range. This result is in accordance with previous permeability study

of microcapsule with very thin shells and from weak hydrogen bonded components or proteins.<sup>347</sup> On the other hand, these pore sizes are much larger than the common pore dimensions for conventional polyelectrolyte-based LbL shells (few nm across).

The incorporation of branched polyelectrolytes in LbL shells, which are known to exhibit conformational changes in the presence of counterions, has been exploited to tune permeability of microcapsules. Indeed, previous studies showed that the addition of trivalent ions ( $\text{La}^{3+}$ ) might lead to a collapsed polyelectrolyte brush, which is caused by a reduction of the interior osmotic pressure.<sup>35</sup> Plamper *et al.* demonstrated that the arms of cationic star polyelectrolyte (which is also 18 armed qPDMAEMA) retract when adding multivalent counterions and that trivalent hexacyanocobaltate (III) ions leads to the collapse of qPDMAEMA<sub>18</sub> stars even at very low concentrations. Molecular dynamic simulations and AFM observations have also shown that the dendrimers and star polymers can collapse upon addition of multivalent salt ions.<sup>348</sup>

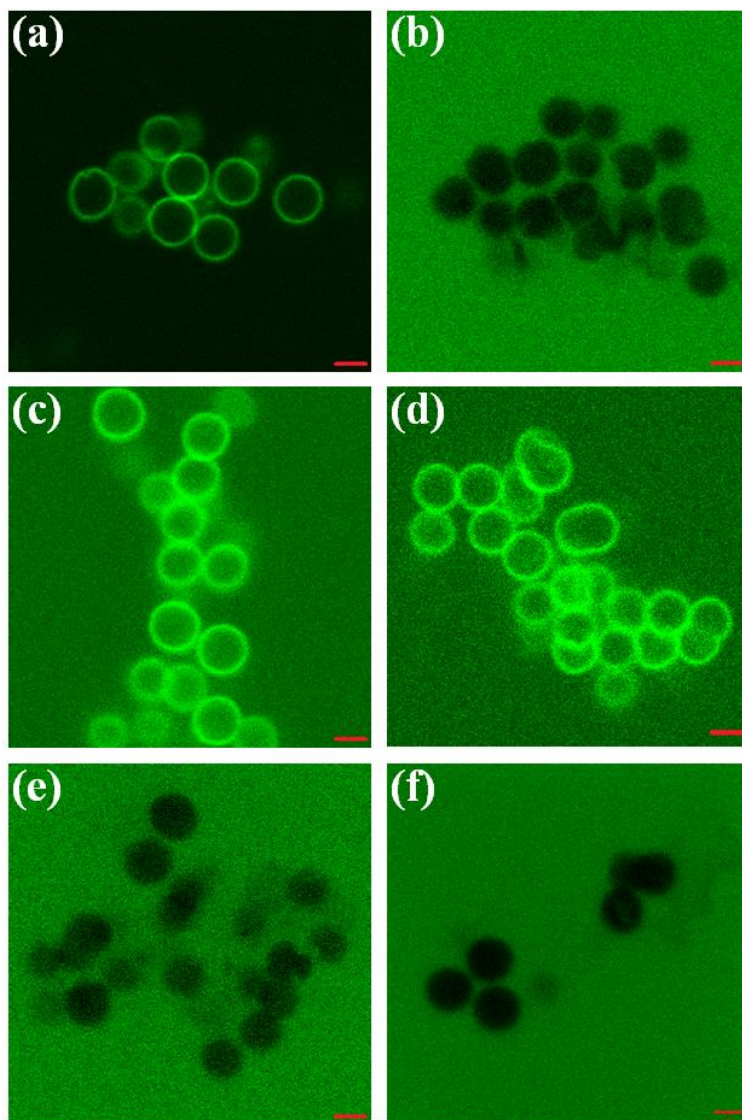


Figure 7.11. Confocal images of  $(\text{PSS}/\text{qPDMAEMA}_{18})_{11}$  microcapsules exposed to FITC (a), and FITC-dextran solutions with  $M_w$  of 2000 kDa (b), 500 kDa (c), 70 kDa (d). After adding 0.8 mM  $\text{K}_3\text{Co}(\text{CN})_6$ ,  $(\text{PSS}/\text{qPDMAEMA}_{18})_{11}$  microcapsules exposed FITC-dextran solutions with  $M_w$  of 500 kDa (e), 70 kDa (f). Scale bar is 2  $\mu\text{m}$ .

In this study, adding hexacyanocobaltate (III) ions ( $\text{Co}(\text{CN})_6^{3-}$ ) to the solution of  $(\text{PSS}/\text{qPDMAEMA}_{18})_n$  microcapsules was used to tune the permeability of microcapsule shells. First, we found that before adding  $\text{K}_3\text{Co}(\text{CN})_6$  to the solution,  $(\text{PSS}/\text{qPDMAEMA}_{18})_n$  microcapsules showed a high permeability. Figure 7.11e, f shows the confocal microscopy images of  $(\text{PSS}/\text{qPDMAEMA}_{18})_{11}$  microcapsules with 500kDa

and 70kDa FITC-dextran after adding  $K_3Co(CN)_6$ , respectively. After adding trivalent salt ions at a concentration of 0.8 mM, the permeability of  $(PSS/qPDMAEMA_{18})_n$  microcapsules dramatically decreases with threshold level decreasing to molecular weight of 70kDa. Considering that the hydrodynamic diameter of 70kDa dextran is around 13.0 nm, we can conclude that the pore dimensions the  $(PSS/qPDMAEMA_{18})_n$  shells reduced by a factor of 3 under these conditions. Additionally, the average size of  $(PSS/qPDMAEMA_{18})_n$  microcapsules in solution state decreased from 3.0  $\mu m$  to 2.6  $\mu m$  after adding 0.8 mM trivalent salt, thus further confirming densification of the shells.

On the other hand, the concentration of  $K_3Co(CN)_6$  also plays an important role in the permeability of  $(PSS/qPDMAEMA_{18})_n$  microcapsules. At very low concentration ( $<0.1$  mM) the permeability of  $(PSS/qPDMAEMA_{18})_8$  only decreases by a small extent, so that less 500kDa FITC-dextran can diffuse across the shell (Figure 7.12b). At the  $K_3Co(CN)_6$  concentration of around 0.8 mM,  $(PSS/qPDMAEMA_{18})_8$  microcapsules are impermeable for 500kDa FITC-dextran (Figure 7.12c). If the concentration of added  $K_3Co(CN)_6$  is further increased, for instance to 4 mM, the effect in closing the pores of  $(PSS/qPDMAEMA_{18})_n$  capsules decreases and shells become permeable to a certain extent (Figure 7.12d).

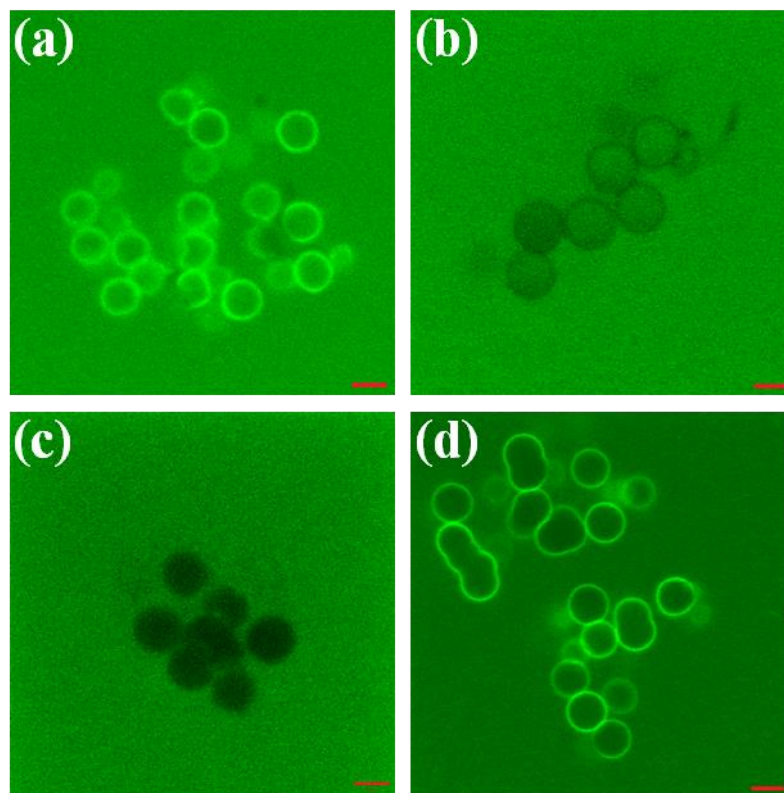


Figure 7.12. Permeability of  $(\text{PSS}/\text{qPDMAEMA}_{18})_8$  microcapsules to 500 kDa FITC-dextran after adding  $\text{K}_3\text{Co}(\text{CN})_6$ : (a) without  $\text{K}_3\text{Co}(\text{CN})_6$ , (b) 0.08 mM, (c) 0.8 mM, (d) 4 mM of  $\text{K}_3\text{Co}(\text{CN})_6$ . Scale bar is 5  $\mu\text{m}$ .

These changes in shell permeability can be understood considering well-known results for polyelectrolyte solutions.<sup>349</sup> For instance, it has been demonstrated that the presence of multivalent ions leads to attraction between planar polyelectrolyte brushes and similarly charged polyelectrolytes.<sup>350</sup> As known, adding multivalent salt to the solution of star polyelectrolytes causes collapse of the star conformation if the salt concentration exceeds a critical value and the collapsed state can re-expand if the salt concentration increases beyond a second critical value (reentrant condensation).<sup>351</sup> At very low ionic strength the arms of  $\text{qPDMAEMA}_{18}$  star polyelectrolytes are nearly stretched to full length, and after LbL assembly of PSS and  $\text{qPDMAEMA}_{18}$ ,  $\text{qPDMAEMA}_{18}$  could maintain the stretched conformation, since the interpenetration between layers happens to

a low extent. For star polyelectrolyte like qPDMAEMA<sub>18</sub>, the correlation with counterions has proven to be much stronger, so that the counterions are mostly localized within the shells which are composed of arms. The strong binding of polyelectrolyte with counterions is accompanied by a significant reduced osmotic activity of the counterions, thus creating high osmotic pressure within star polyelectrolytes, as a result, the arms of qPDMAEMA stars should be strongly stretched.

The conformation of star polyelectrolytes is largely controlled by the balance between osmotic pressure of the entrapped counterions and the arm elasticity. Upon the addition of K<sub>3</sub>Co(CN)<sub>6</sub>, the monovalent counterions Γ are replaced by Co(CN)<sub>6</sub><sup>3-</sup>. On average three Γ ions are replaced by one Co(CN)<sub>6</sub><sup>3-</sup>, with ion exchange process controlled by Donnan effect. Thus the osmotic pressure inside qPDMAEMA<sub>18</sub> is reduced by a factor of 3 and strong shrinking of the arm stretching and a collapse occurs. Previous study showed that star polyelectrolytes collect multivalent counterions from the surroundings until they become saturated, so that the collapse of star polyelectrolytes begins at quite low salt concentration.<sup>352</sup> In our system, we use relatively low concentration of qPDMAEMA<sub>18</sub> solution (0.2 mg/mL) to perform LbL assembly, and after the assembly process, the actual qPDMAEMA<sub>18</sub> concentration would be even lower. Therefore, very low concentration K<sub>3</sub>Co(CN)<sub>6</sub> should be enough to make qPDMAEMA<sub>18</sub> star polyelectrolyte to collapse effectively.

The interaction of qPDMAEMA<sub>18</sub> star polyelectrolytes within swollen shells is mediated by three factors: the electrostatic interactions, steric repulsion between arms, and the

entropic repulsion of counterions. It has been proven that entropic repulsion of the counterions is the dominant force between two star polyelectrolytes. During the collapse of qPDMAEMA<sub>18</sub> star polyelectrolytes upon adding Co(CN)<sub>6</sub><sup>3-</sup>, the steric stabilization effect also breaks down. The interaction between PSS and qPDMAEMA<sub>18</sub> decreases because Co(CN)<sub>6</sub><sup>3-</sup> compensates a great portion of positive charges on qPDMAEMA<sub>18</sub> arms. What's more, the contraction of qPDMAEMA<sub>18</sub> arms would decrease the number of attraction sites between PSS and qPDMAEMA<sub>18</sub>. On the other hand, due to the presence of Co(CN)<sub>6</sub><sup>3-</sup> ions between qPDMAEMA<sub>18</sub> stars, there is attraction force between the star polyelectrolytes. The concentration of counterions surrounding qPDMAEMA<sub>18</sub> star molecules also decreases heavily due to the replacement of I<sup>-</sup> ions with Co(CN)<sub>6</sub><sup>3-</sup> ions. Therefore, the entropic repulsion between qPDMAEMA<sub>18</sub> stars decreases, which also contributes to the attraction between stars with added K<sub>3</sub>Co(CN)<sub>6</sub>.

We suggest that the collapse of the arm chains and the attraction between qPDMAEMA<sub>18</sub> stars jointly contribute to the significant decrease in the permeability of (PSS/qPDMAEMA<sub>18</sub>)<sub>n</sub> shells with salt concentration changes. On the other hand, the pore size is largely determined by the space between arms of the qPDMAEMA<sub>18</sub> stars packed in shells (Figure 7.13). Upon addition of the K<sub>3</sub>Co(CN)<sub>6</sub> salt, the contraction of qPDMAEMA<sub>18</sub> stars significantly decreases the distance between the arms. At the same time, the increasing attractive forces between qPDMAEMA<sub>18</sub> stars make them migrate closer, thus the molecular packing become denser. As a result, the pore size as well as the overall size of the microcapsule decreases, which corresponds to the permeability

measurements. The small angle neutron scattering experiments are in progress to further elucidate this behavior.

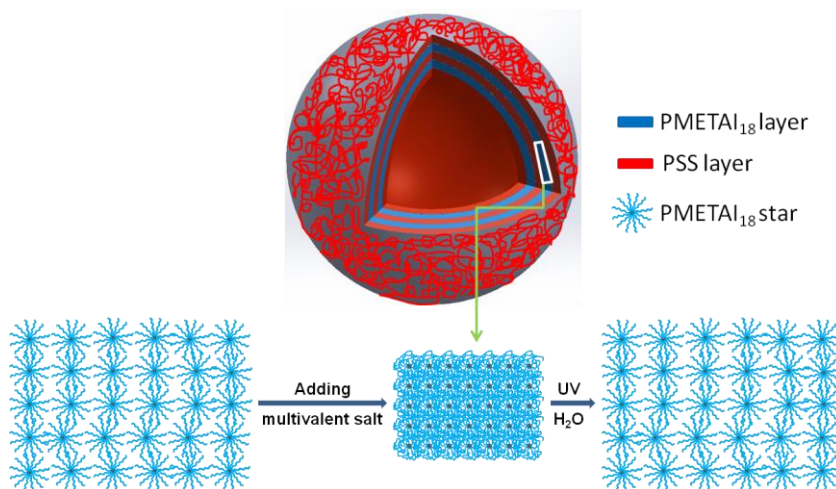


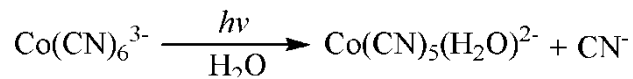
Figure 7.13. Responsive behavior of  $(\text{PSS}/\text{qPDMAEMA}_{18})_n$  microcapsules to multivalent salt and UV irradiation.

As suggested, the most contracted structure of star polyelectrolytes appears when the total charge of multivalent counterions neutralizes the polyelectrolyte charge. When the multivalent salt concentration increases beyond that point, the arms start to expand again. In contrast, in the presence of monovalent counterions, star polyelectrolytes exhibit a slow, monotonic decrease of radius of gyration with the increase of salt concentration. Arm re-expansion is linked to charge reversal, when the arms of  $\text{qPDMAEMA}_{18}$  stars are filled with  $\text{Co}(\text{CN})_6^{3-}$  ions, the repulsion between these ions induces the separation of arms. Therefore, at relatively high  $\text{K}_3\text{Co}(\text{CN})_6$  salt concentration when the  $\text{qPDMAEMA}_{18}$  stars re-expand, the space between arms of  $\text{qPDMAEMA}_{18}$  as well as the intermolecular distances increase, so that the shell permeability also increases. Thus, if external stimuli can affect the ion state inside shells, the permeability and thus loading-

unloading behavior of microcapsules can be tuned on-demand, this intriguing possibility is further discussed below.

#### 7.3.4 UV Triggered Release of (PSS/ qPDMAEMA)<sub>n</sub> Microcapsules

In our next effort, we took advantage of the simple and well known photochemical behavior of cyanide complex, Co(CN)<sub>6</sub><sup>3-</sup> ions can be converted into monovalent and divalent ions with UV irradiation according to the reaction:



This photoaquation reaction has a quantum yield of 0.31 at 25 °C independent of the wavelength of irradiation (254, 313 and 365 nm), the concentration of the complex, and the pH of the solution (2.0-7.5). It has also been demonstrated that the thermal reaction opposed to the photoaquation was not appreciable.<sup>353</sup> The photochemical reaction could complete in about 30 min under normal illumination condition. The decomposition of Co(CN)<sub>6</sub><sup>3-</sup> ions into Co(CN)<sub>5</sub><sup>2-</sup> and CN<sup>-</sup> results in the total number of counterions increasing dramatically, so that the osmotic pressure within qPDMAEMA<sub>18</sub> stars becomes much higher. Moreover, the entropic repulsion between counterions also increases at higher concentration, which also contributes to a stretched conformation of arms.

In order to explore this possibility to tune the state of LbL shells, the suspension of (PSS/qPDMAEMA<sub>18</sub>)<sub>n</sub> microcapsules was irradiated using a UVP B-100A high powered UV lamps (100 W) at a wavelength of 365 nm. The samples were placed in quartz cuvettes and then immersed in a cooled water bath, which was placed 7 cm away from

the lamp. First, we observed that  $(\text{PSS}/\text{qPDMAEMA}_{18})_8$  microcapsules are impermeable to 500kDa FITC-dextran after adding 0.8mM  $\text{K}_3\text{Co}(\text{CN})_6$  (Figure 7.14). However, after UV irradiation for 45 min, these microcapsules become permeable to 500kDa dextran again.

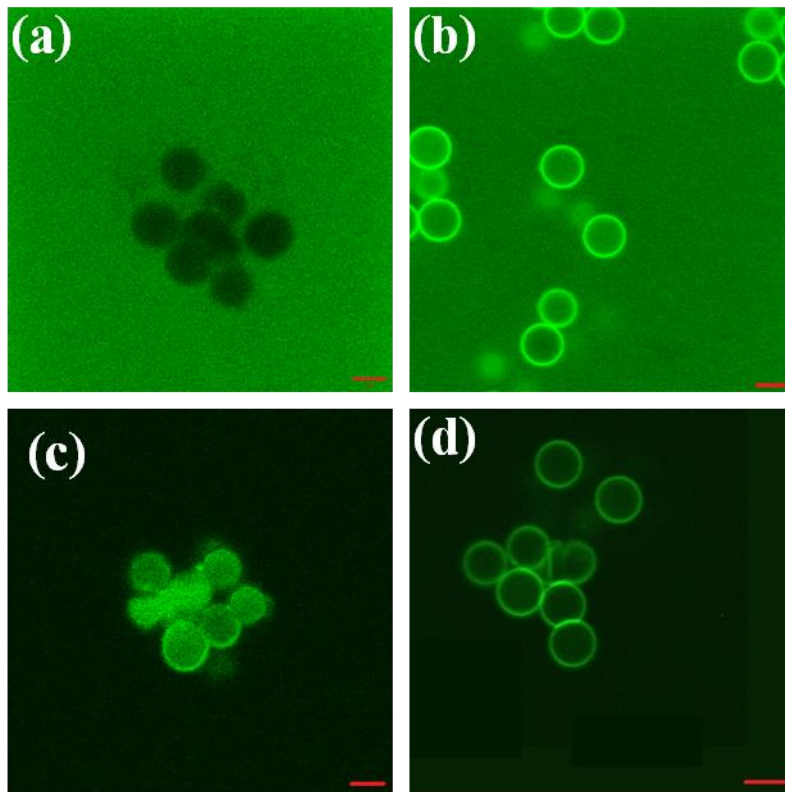


Figure 7.14. Permeability of  $(\text{PSS}/\text{qPDMAEMA}_{18})_8$  microcapsules to 500 kDa FITC-dextran, (a) after adding 0.8 mM  $\text{K}_3\text{Co}(\text{CN})_6$ , (b) add 0.8 mM  $\text{K}_3\text{Co}(\text{CN})_6$ , then irradiate by UV for 45 min, (c) encapsulation of 500 kDa FITC-dextran by adding 0.8 mM  $\text{K}_3\text{Co}(\text{CN})_6$ , (d) release of FITC-dextran by 45 min UV irradiation.

To further explore the role of the multivalent salt and UV irradiation on the permeability of  $(\text{PSS}/\text{qPDMAEMA}_{18})_n$  microcapsules, we also conducted loading-unloading test. For this test, 500kDa FITC-dextran was added to the solution of  $(\text{PSS}/\text{qPDMAEMA}_{18})_n$  microcapsules and it permeates quickly into microcapsules. Then  $\text{K}_3\text{Co}(\text{CN})_6$  was added

to the solution to reach a concentration of 0.8mM, so that the pores on the wall of capsules became effectively closed thus trapping the labeled dextran. Subsequently, FITC-dextran outside of the capsules was removed by several centrifugation and washing steps and replaced with pure water. Thus, encapsulation of 500kDa FITC-dextran was achieved in this way with fluorescent FITC-dextran encapsulated inside (PSS/qPDMAEMA<sub>18</sub>)<sub>8</sub> microcapsules as confirmed by confocal microscopy (Figure 7.14c).

On the other hand, the encapsulated FITC-dextran can be released by initiating pore opening with UV irradiation based on the mechanism discussed above (Figure 7.14d). After UV irradiation for 45 min, FITC-dextran encapsulated within the (PSS/qPDMAEMA<sub>18</sub>)<sub>8</sub> microcapsules was released, so that both the background and microcapsule interior are dark. Only the microcapsule shells remain fluorescent due to the residual FITC-dextran. In order to exclude the possibility of excessive photobleaching, we also conducted control experiment, which was shown in Figure S7.8. The fluorescence intensity inside the microcapsules is a direct evidence of the existence of the probe molecules. Before adding K<sub>3</sub>Co(CN)<sub>6</sub> to the suspension, the microcapsule interior is nearly as bright as the background, which shows that FITC-dextran can easily permeate into the microcapsules. After trivalent salt was added, pores on the microcapsule shells are largely closed, so that the microcapsule interior would still be bright due to encapsulated FITC-dextran and the background would be dark after removing surrounding dye molecules.

The encapsulation efficiency can be estimated by the ratio of the average fluorescence intensity of microcapsule interior before and after removing the labeled dextran from

exterior. This intensity comparison shows that around 84% of FITC-dextran was successfully encapsulated. This encapsulation and release cycle can be repeated with high efficiency multiple times by alternatively adding  $K_3Co(CN)_6$  salt and UV irradiation. The encapsulation efficiency as measured in the ratio of fluorescent intensities remains high and stable over multiple cycles of UV-irradiation followed by ion additions (Figure 7.15).

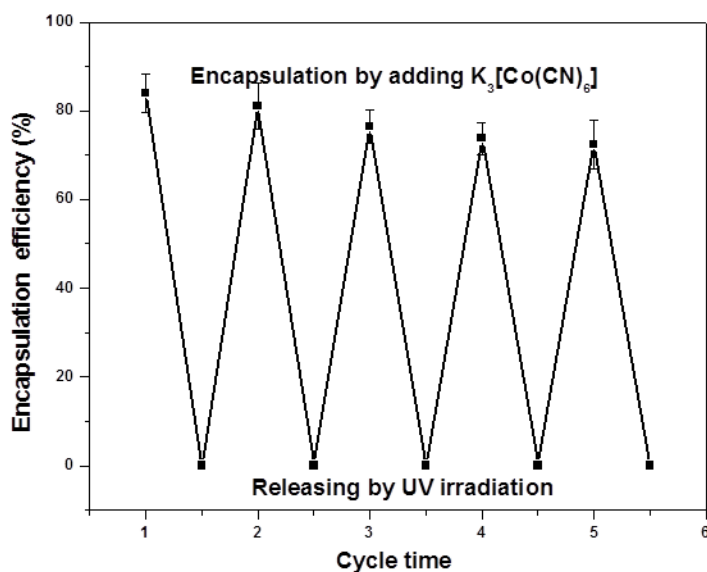


Figure 7.15. Encapsulation efficiency (defined by the ratio of average fluorescence intensity of microcapsule interior before and after removing surrounding dye) *versus* repeatable UV irradiation cycles.

The phenomenon demonstrated here can be compared to several existing approaches to remotely control shell permeability of LbL microcapsules with light. One of the popular approaches incorporated metal nanoparticles like gold or silver into shells which absorb the light energy, the heat produced by nanoparticles can be harvested to release encapsulated substances from microcapsules, which are shown to be viable and

applicable even for intracellular release. But at high nanoparticle content, the microcapsules are less stable and the responsiveness to light also decrease. Next, UV responsive polymer core-shell micelles were developed as nanocarriers, with the micelle core-forming hydrophobic block containing a photolabile chromophore as a pendant group.<sup>35</sup> Upon UV irradiation, the chemical bond breaks detaching the chromophore from the polymer and transforming the hydrophobic block into a hydrophilic block, which leads to the dissociation of polymer micelles. Compared to our approach, due to the small size of polymer micelles (around 15 nm), they have much lower loading capacity and their dissociation is irreversible. Another approach is utilizing macromolecules containing photoisomerizable azobenzene moieties.<sup>333</sup> These microcapsules can shrink and encapsulated fluorescently labeled polymers and the permeability decreased upon UV irradiation, however, the permeability change was found to be irreversible. Therefore, light-stimulated loading-unloading ability based upon internal ion state control suggested here is very different from previous mostly destructive approaches and provides much more efficient path for remote, reversible, cyclical tuning of shell permeability without drawbacks of most current approaches.

### **7.3.5 SANS Study on the Structural Changes of Microcapsules**

In order to characterize the structure of the thin shell microcapsules, confocal microscopy, AFM and TEM can be used. However, these techniques usually either only apply to samples in dry state or partially wetted state, which have significantly different structure as compared to that in solution. SANS, on the other hand, provides a powerful

and non-destructive way to elucidate the porous morphology of the microcapsules in solution directly.

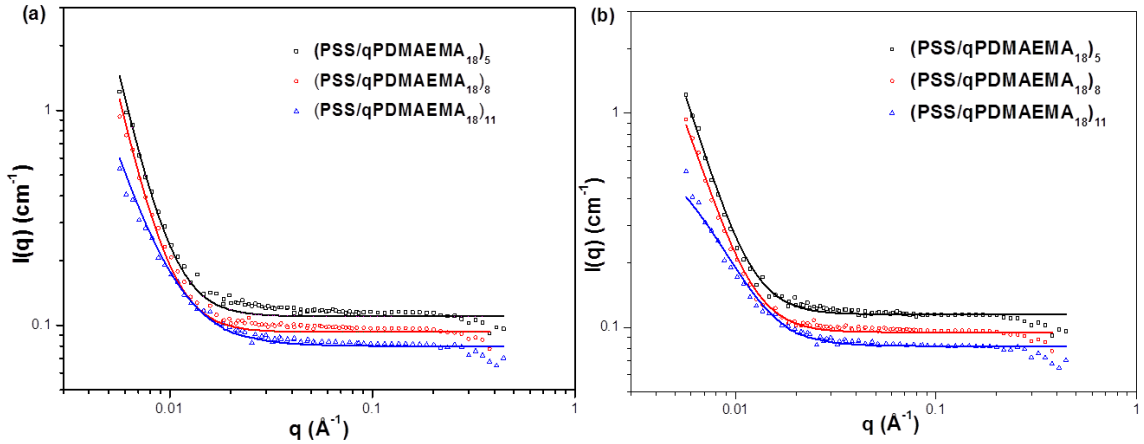


Figure 7.16. SANS data of PSS/qPDMAEMA<sub>18</sub> microcapsules with (square) 5 bilayers, (circle) 8 bilayers, and (triangle) 11 bilayers in D<sub>2</sub>O solution (at 25 °C) that have been fitted with a power law model (a, solid lines) to determine the evolution of the fractal dimension, and Debye-Anderson-Brumberger (DAB) model (b, solid lines) to obtain the correlation length.

SANS measurements were first conducted for PSS/qPDMAEMA<sub>18</sub> microcapsules with different number of bilayers (Figure 7.16). The  $q$  range of the scattering data in this experiment corresponds to a distance roughly from 1 nm to 100 nm, which actually covers several characteristic dimensions of the microcapsules including thickness of the shell, star polyelectrolyte size and the mesh size within the shell. However, considering the fact that the porous shell is filled with D<sub>2</sub>O, and the scattering contrast is highest between D<sub>2</sub>O and the hydrogenated polyelectrolyte matrix, while the contrast between the hydrogenated domain morphology is much smaller and can be neglected. Therefore, we suggest that the scattering in this region is likely dominated by the porous structure filled with D<sub>2</sub>O within the LbL shell.

Our initial attempt to fit the data utilized a shape-dependent model to describe the pores within the shell, with the shapes (spherical, ellipsoidal, cylindrical *etc.*), dimensions, and their polydispersity to be varied. However, no such model can provide satisfactory fitting of the entire  $q$  range. Therefore, the assumption of a porous shell with isolated and well-defined closed pores can be excluded from further consideration. Next, we suggest that the structure of the microcapsule shell can be more accurately described as randomized interconnected network.

Two shape-independent models which are suitable for weakly-contrasted inhomogeneities at multiple length scales were applied to the SANS data of PSS/qPDMAEMA<sub>18</sub> microcapsules with different number of bilayers. The first one to be used is a power law or Porod model, which corresponds to a probed range smaller than the scattering object, so that the scattering is related to the local structure.<sup>354</sup> The scattering intensity can be expressed as  $I(q)=A/q^n+B$ , where a power law exponent  $n$  between 3 and 4 characterizes rough interfaces, which is called surface fractal, and the surface fractal dimension  $D_f = 6 - n$ . A power law exponent between 2 and 3 is for “mass fractals” such as branched systems (gels) or networks,<sup>355</sup> the mass fractal dimension  $D_m = n$ . It can be seen that the power law model yields relatively good fitting for the scattering data over the entire  $q$  range for microcapsules with different number of bilayers (Figure 7.16a), and the fractal dimensions obtained are summarized in Table 7.2.

Table 7.2. SANS fitting results for from (PSS/qPDMAEMA<sub>18</sub>)<sub>n</sub> microcapsules using Power-law model and DAB model. The first index indicates the number of arms of the star and the second one the number of bilayers. The salt added is K<sub>3</sub>Co(CN)<sub>6</sub>.

Sample	Power-law model		DAB model
	power law exponent	fractal type	correlation length(nm)
(PSS/qPDMAEMA <sub>18</sub> ) <sub>5</sub>	3.98	surface	31.4
(PSS/qPDMAEMA <sub>18</sub> ) <sub>8</sub>	3.92	surface	26.7
(PSS/qPDMAEMA <sub>18</sub> ) <sub>8</sub> with salt	2.63	mass	13.5
(PSS/qPDMAEMA <sub>18</sub> ) <sub>11</sub>	2.84	mass	13.0
(PSS/qPDMAEMA <sub>18</sub> ) <sub>11</sub> with salt	2.12	mass	9.0

Importantly, the fitting results from PSS/qPDMAEMA<sub>18</sub> microcapsules with different number of bilayers have obvious differences. The 5 and 8 bilayer microcapsules have power law exponents of 3.98 and 3.92, which strongly suggests surface fractal morphology, in other words, a thin shell network of pores and with rough surface. Measurements from other techniques such as AFM confirm that the 5 and 8 bilayers microcapsules have thin porous shells and rough surfaces, with a thickness of 12.8 nm and 16.1 nm in the dry state, respectively. This result is consistent with SANS characterization of particles like microgels, where a power law exponent of 4 indicating smooth surfaces, and a power law exponent between 3 and 4 indicating a microporous system with rough surfaces.<sup>356</sup>

In contrast, the shells with 11 bilayers have a fractal dimension of 2.84, which suggests a mass fractal structure. The shell structure corresponds to a network-like porous morphology with network elements randomly oriented within the shell. This combination is likely indicative of a denser shell with major elements of high contrast

formed by the swollen hydrogenated polyelectrolyte matrix and the nanopores filled with deuterated water.

Such a transition from the surface fractal to the mass fractal structure with increasing shell thickness corresponds to general trends in morphological changes based on microscopic observations and expected for the growth of LbL structures.<sup>357</sup> The gradual filling of the initial two-dimensional thin shell by subsequent polymer layers results in the formation of more uniform films with diminishing through-pores and decreasing pore dimensions. The occurrence of such a reorganization is further supported by the results from confocal microscopy and AFM, which demonstrate a densification of the surface morphology and a consistent decrease in the permeability.

Another model to calculate the scattering from a randomly distributed, two-phase system, the Debye-Anderson-Brumberger (DAB) model, was used to fit the SANS data of the LbL microcapsules. The two-phase system is characterized by a single correlation length, which is a measure of the average spacing between regions of phase 1 and phase 2.<sup>358</sup> The model also assumes a smooth interface between the phases and hence exhibits Porod behavior at large  $q$ . The scattering intensity can be expressed as

$$I(q) = \frac{scale \cdot \xi^3}{(1 + (q\xi)^2)^2} + bck, \quad (7.1)$$

where  $\xi$  is the correlation length.<sup>359</sup> The DAB model fits the SANS data quite well over the entire  $q$ -range (Fig. 7.16b) and provides correlation lengths which can be interpreted as the characteristic dimensions of density inhomogeneities represented by pores. The results are shown in Table 7.2. The correlation length for PSS/qPDMAEMA<sub>18</sub>

microcapsules with 5, 8 and 11 bilayers are 31.4, 26.7 and 13.0 nm, respectively, which is in good agreement with the results estimated from permeability measurements.

As we discussed before, adding multivalent salt to the solution of qPDMAEMA star polyelectrolytes would induce the collapse of the arm chains. Taking advantage of this unique salt-responsive behavior, it is possible to achieve salt controlled permeability changes in the PSS/qPDMAEMA<sub>18</sub> microcapsules. To get direct evidence of the structure and mesh size changes of the microcapsules after adding the multivalent salt, SANS was performed on the microcapsule solution before and after the addition, as shown in Figure 7.17. The scattering intensity in the low  $q$  range significantly decreased after adding  $K_3Co(CN)_6$  salt, which indicates the characteristic dimension which related to the structure of the shell decreases.

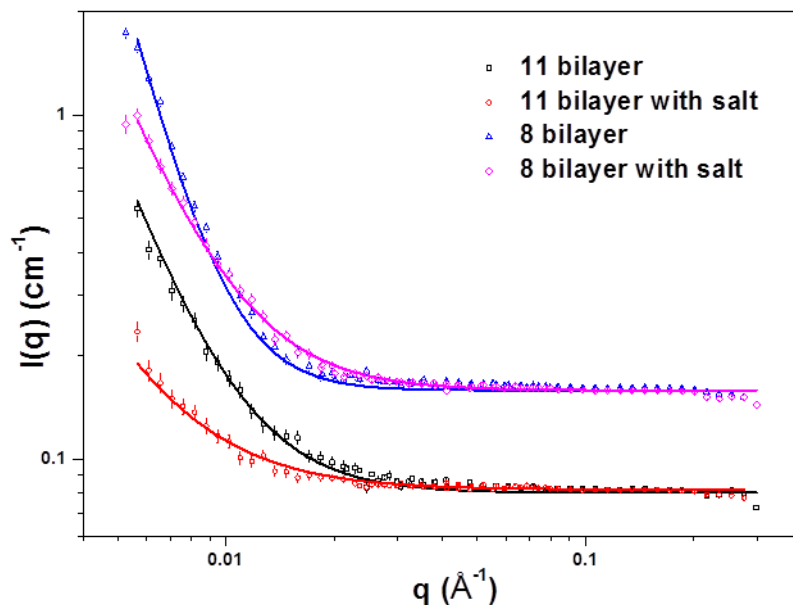


Figure. 7.17. SANS data of (PSS/qPDMAEMA<sub>18</sub>)<sub>8</sub> and (PSS/qPDMAEMA<sub>18</sub>)<sub>11</sub> microcapsules before and after adding 0.8 mM  $K_3Co(CN)_6$  (at 25 °C); solids lines are fitting by the power law model, the two curves for (PSS/qPDMAEMA<sub>18</sub>)<sub>8</sub> were shifted upward for clarity.

By fitting with the DAB model, the results in Table 7.2 show that after adding 0.8 mM trivalent salt, the correlation length  $\xi$  decreases from 26.7 to 13.5 nm for (PSS/qPDMAEMA<sub>18</sub>)<sub>8</sub> microcapsules, and from 13.0 to 9.0 nm for (PSS/qPDMAEMA<sub>18</sub>)<sub>11</sub> ones. Moreover, there is a surface- to mass-fractal transition upon adding salt for (PSS/qPDMAEMA<sub>18</sub>)<sub>8</sub> microcapsules, and the mass fractal dimension also significantly decreases for (PSS/qPDMAEMA<sub>18</sub>)<sub>11</sub> microcapsules. The decrease in fractal dimension is generally related to the increased aggregation and roughness in the local structure.<sup>360</sup> The results from SANS data analysis well supported the proposed mechanism of structural organization.

#### **7.4 Conclusions**

LbL films and microcapsules based on qPDMAEMA star polyelectrolytes were successfully assembled and explored as efficient cargo carriers with light-induced remote control of shell permeability, and capable of multiple and reversible loading-unloading behavior. This novel “soft” path in contrast to current mostly destructive approaches is based upon light-initiated ionic state transformation, which affects the porosity of shells composed of ion-sensitive star polyelectrolytes. The permeability of (PSS/qPDMAEMA<sub>18</sub>)<sub>n</sub> shells can be significantly reduced by adding a small amount of K<sub>3</sub>Co(CN)<sub>6</sub> salt to the suspension due to a collapse of qPDMAEMA stars, causing a dramatic reduction in the pore size. Then K<sub>3</sub>Co(CN)<sub>6</sub> salt can be decomposed into monovalent and divalent ions by UV irradiation, so that the permeability and dimension of (PSS/qPDMAEMA<sub>18</sub>)<sub>n</sub> microcapsules can be recovered. The responsive properties of

microcapsules also prove that star polyelectrolytes could retain their stimuli-responsive character after incorporating within LbL system, which is in accordance with previous reports.<sup>81-84</sup>

The light-induced changes in microcapsule permeability demonstrated here are completely reversible and can be used for light-mediated loading-unloading behavior of LbL microcapsules in contrast to current microcapsule-destructive approaches. SANS measurements give direct and strong evidences about the structural changes of the microcapsule shell in terms of fractal dimension and correlation length during ionic condition change and UV irradiation. The UV-responsive microcapsules composed of star polyelectrolytes offer a uniquely adaptive and tunable way of cargo delivery and unloading which could find applications in sustained release, controlled delivery, microreactors, and catalytic systems.

## Appendix: Supporting Information

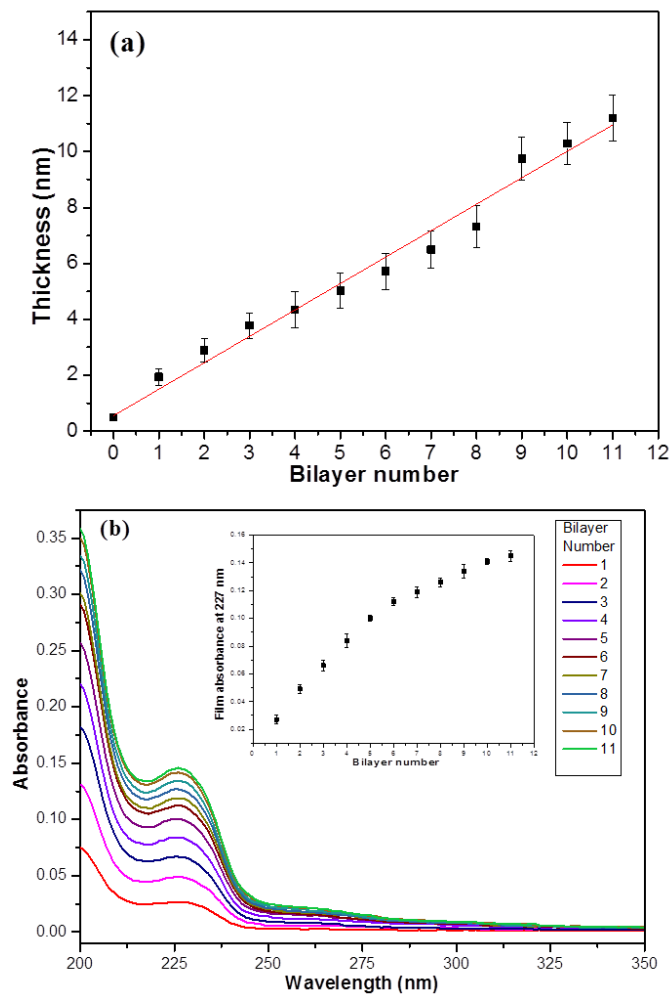


Figure S7.1. (a) Thickness of  $(\text{PSS}/\text{qPDMAEMA}_{5,6})_n$  films as a function of bilayer number as measured by ellipsometry. (b) UV-Vis spectra of  $(\text{PSS}/\text{qPDMAEMA}_{5,6})_n$  films with different number of layers assembled on quartz substrate. Inset shows the intensity increase of peak at 227 nm with bilayer number.

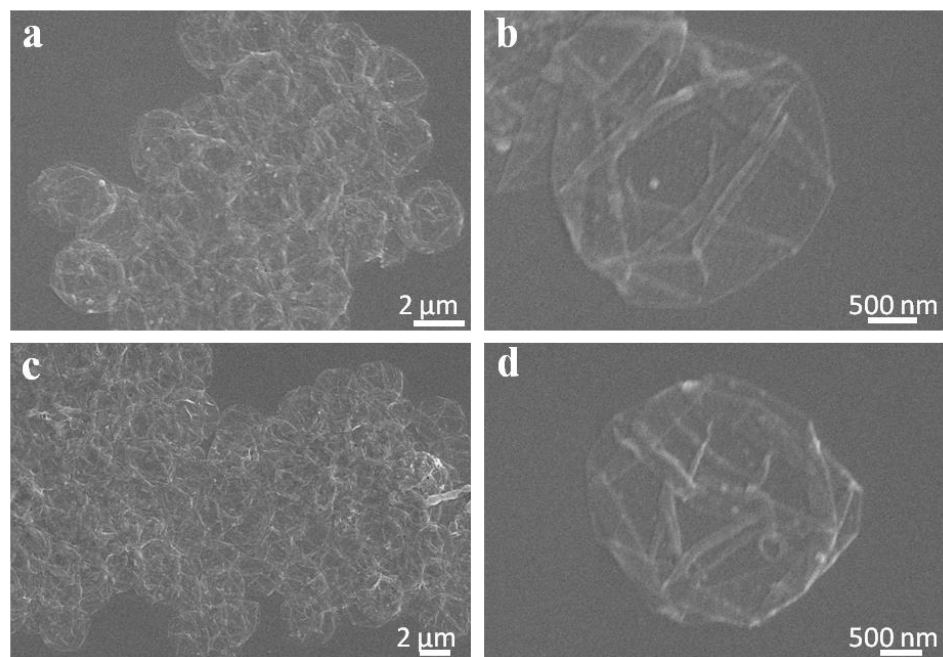


Figure S7.2. (a, b) SEM images of (PSS/qPDMAEMA<sub>18</sub>)<sub>5</sub> microcapsules, (c, d) SEM images of (PSS/qPDMAEMA<sub>18</sub>)<sub>8</sub> microcapsules.

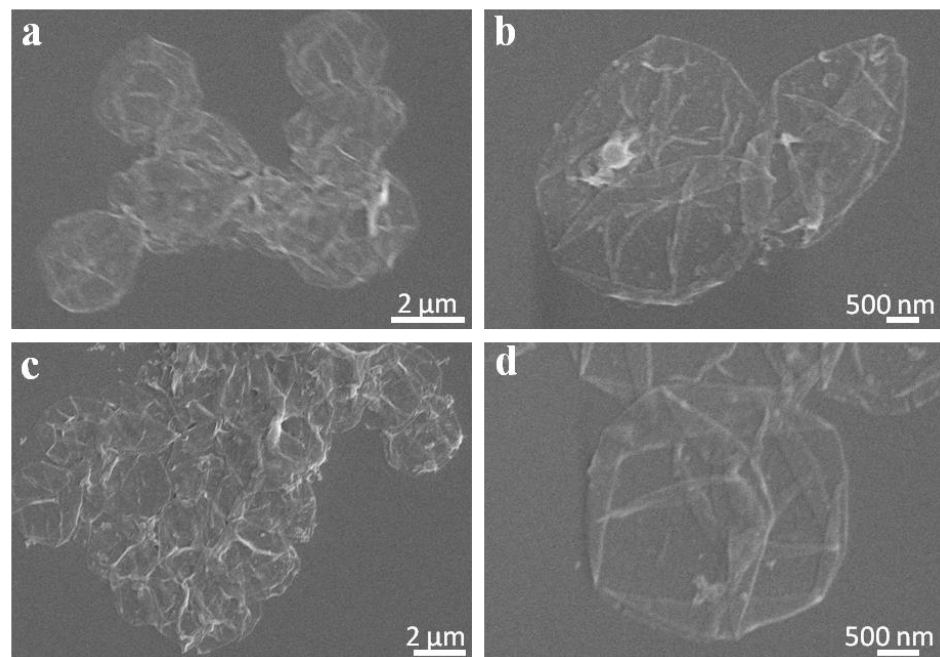


Figure S7.3. (a, b) SEM images of (PSS/qPDMAEMA<sub>5.6</sub>)<sub>5</sub> microcapsules, (c, d) SEM images of (PSS/qPDMAEMA<sub>5.6</sub>)<sub>8</sub> microcapsules.

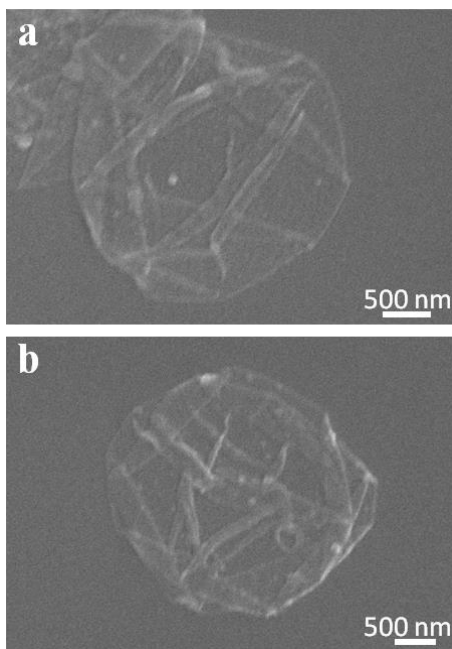


Figure S7.4. (a) SEM images of  $(\text{PSS}/\text{qPDMAEMA}_{18})_{11}$  microcapsules, (b) SEM images of  $(\text{PSS}/\text{qPDMAEMA}_{5,6})_{11}$  microcapsules.

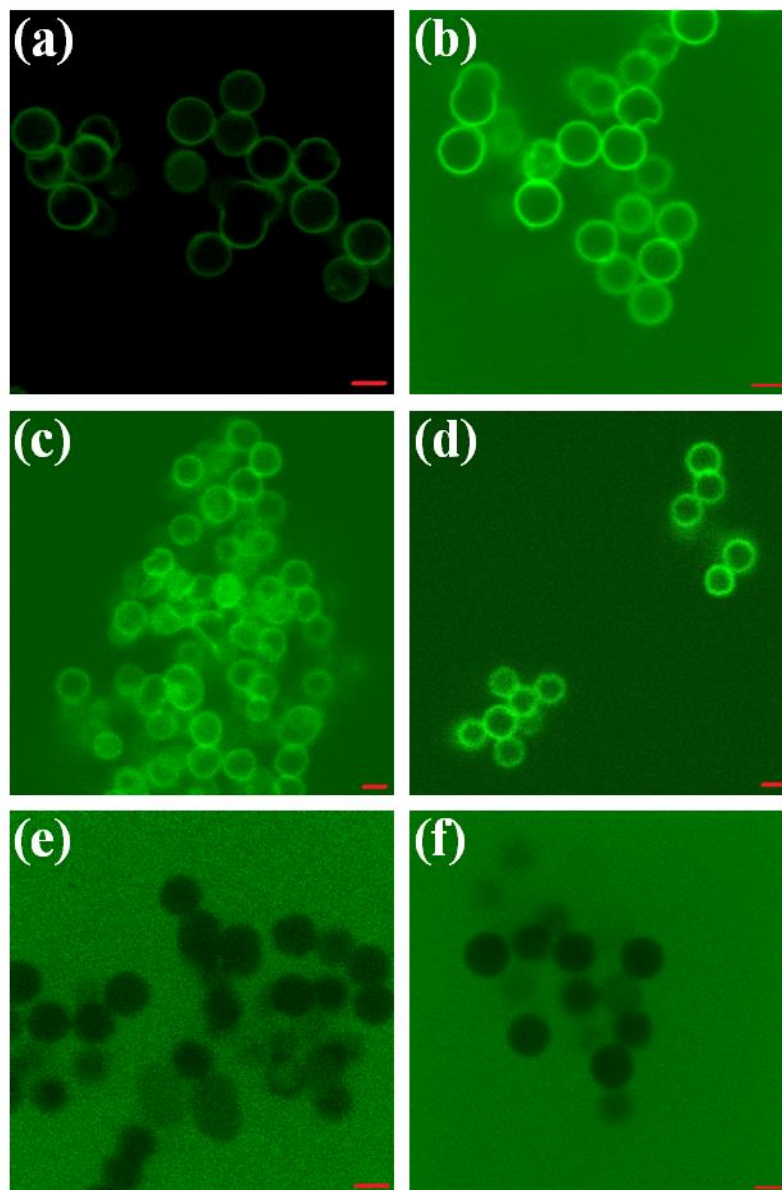


Figure S7.5. Confocal images of (PSS/qPDMAEMA<sub>18</sub>)<sub>5</sub> microcapsules exposed to FITC (a), and FITC-dextran solutions with Mw of 2000 kDa (b), 500 kDa (c), 70 kDa (d). After adding 0.8 mM K<sub>3</sub>Co(CN)<sub>6</sub>, (PSS/qPDMAEMA<sub>18</sub>)<sub>5</sub> microcapsules exposed FITC-dextran solutions with Mw of 500 kDa (e), 70 kDa (f). Scale bar is 2  $\mu$ m.

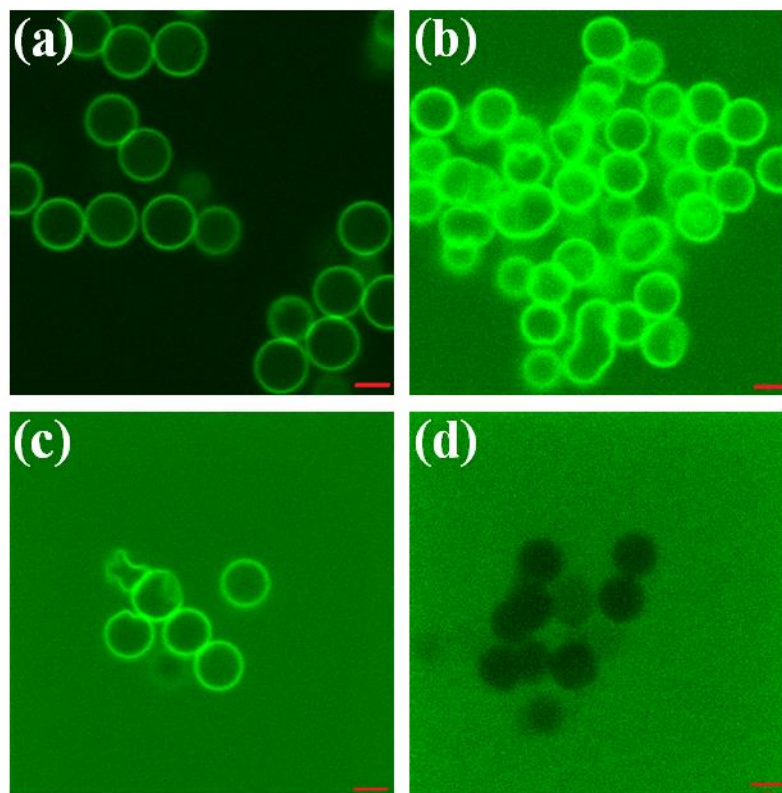


Figure S7.6. Confocal images of  $(\text{PSS}/\text{qPDMAEMA}_{18})_8$  microcapsules exposed to FITC (a), and FITC-dextran solutions with Mw of 2000 kDa (b), 70 kDa (c). After adding 0.8 mM  $\text{K}_3\text{Co}(\text{CN})_6$ ,  $(\text{PSS}/\text{qPDMAEMA}_{18})_8$  microcapsules exposed FITC-dextran solutions with Mw of 70 kDa (d). Scale bar is 2  $\mu\text{m}$ .

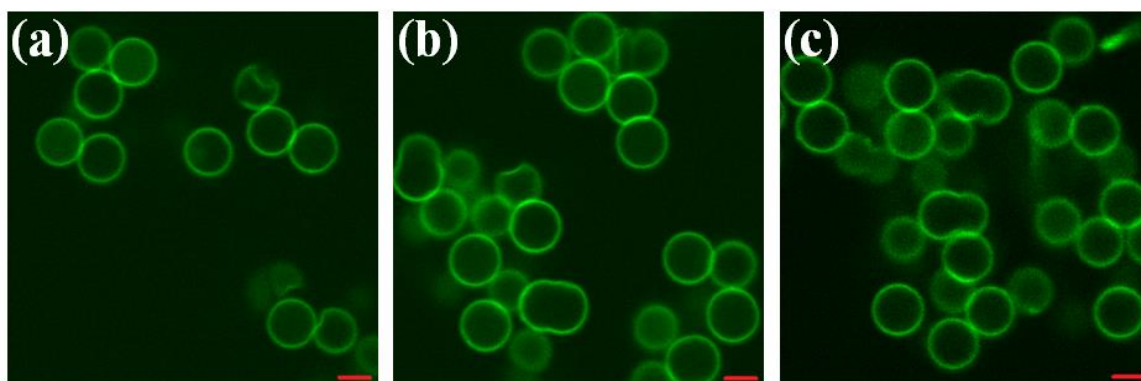


Figure S7.7. Confocal microscopy images of  $(\text{PSS}/\text{qPDMAEMA}_{5,6})_n$  microcapsules in aqueous solution with different number of layers, (a) 5 bilayers, (b) 8 bilayers, (c) 11 bilayers. Scale bar is 2  $\mu\text{m}$ .

### Controll experiments

We also conducted a negative control experiment to prove that the release of FITC-dextran was released from the microcapsule due to permeability changes rather than photobleaching. In which we prepared (PSS/PAH)<sub>5</sub> microcapsules with the same condition as (PSS/qPDMAEMA<sub>18</sub>)<sub>5</sub> microcapsules. FITC was used to label the microcapsule shell for clarity (Figure S7.8a), then the microcapsule suspension was irradiated by UV under the same condition for 45 min, it can be seen that no obvious change in the capsule was observed (Figure S7.8b). Moreover, FITC-dextran with molecular weight of 500 kDa can also permeate into (PSS/PAH)<sub>5</sub> microcapsules (Figure S7.8c), after UV irradiation under the same condition for 45 min, the fluorescence intensity inside the microcapsules as well as in the background has no noticeable change (Figure S7.8d). All these results clearly show that FITC and FITC-dextran can maintain their fluorescence property after 365 nm UV irradiation for 45 min under our experiment conditions, and the effect of photobleaching is negligible.

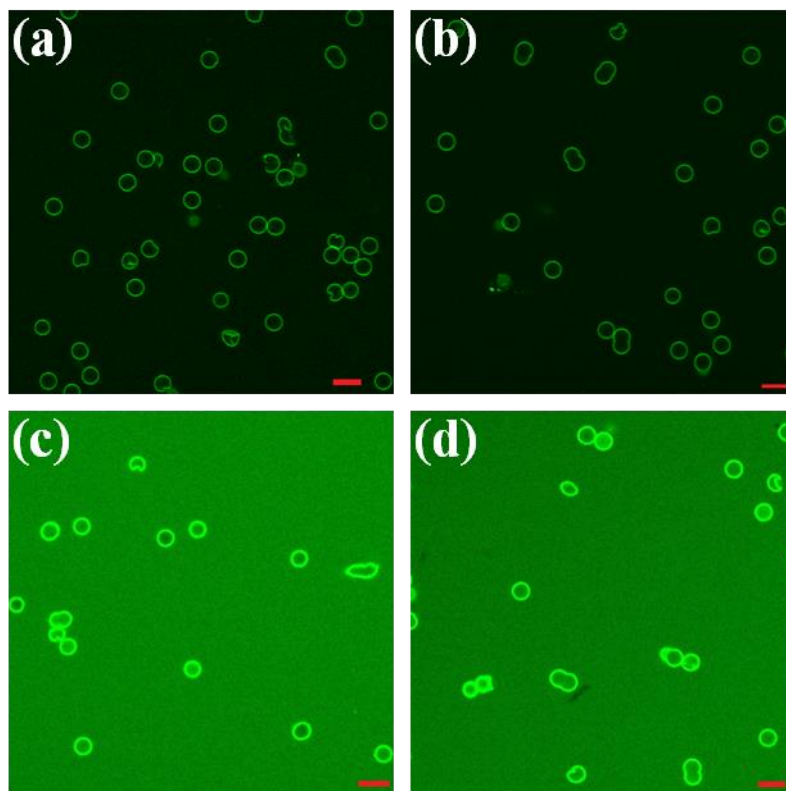


Figure S7.8. (PSS/PAH)<sub>5</sub> microcapsules with FITC labeled shell (a) before and (b) after 45 min UV irradiation. Confocal images of (PSS/PAH)<sub>5</sub> microcapsules exposed to 500 kDa FITC-dextran solution (c) before and (d) after 45 min UV irradiation.

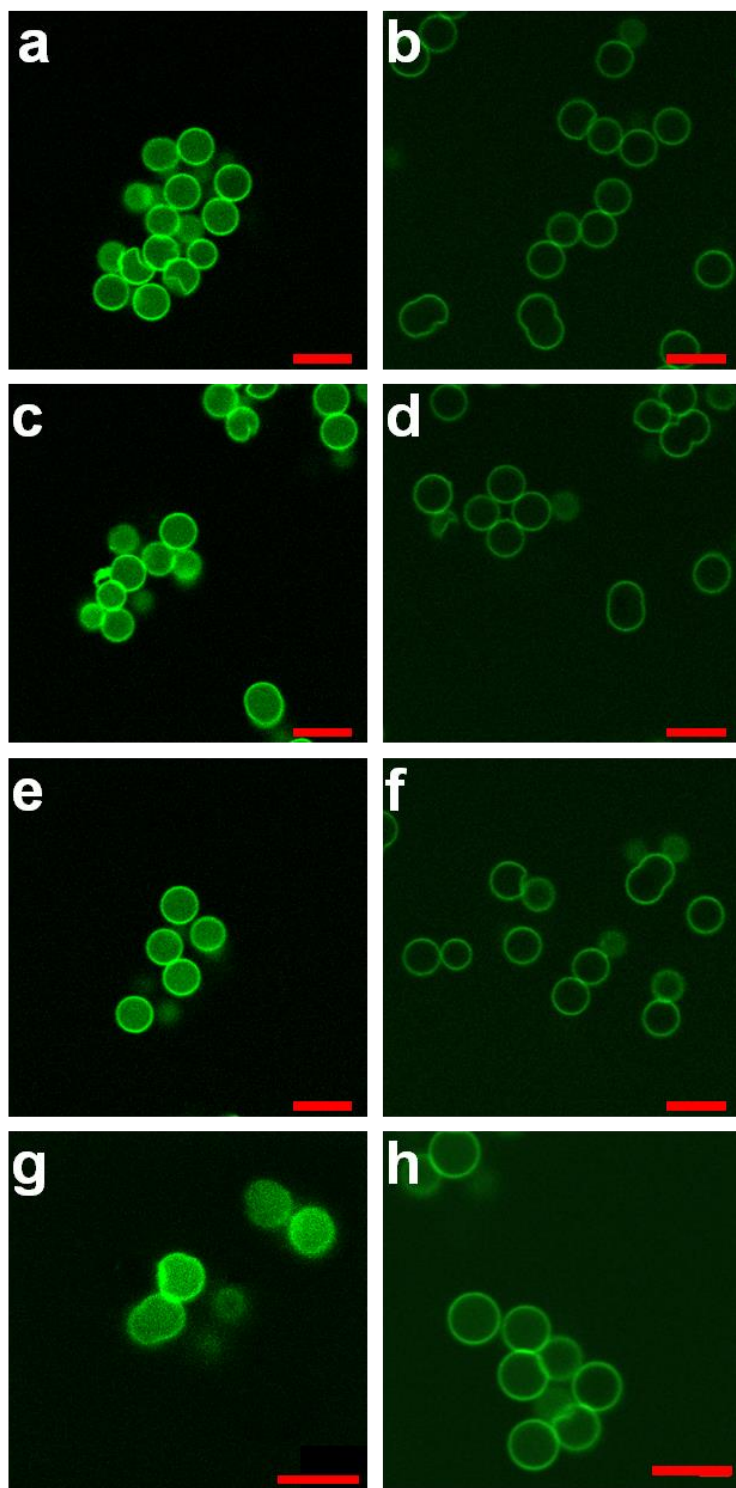


Figure S7.9. Confocal microscopy images of  $(\text{PSS}/\text{qPDMAEMA}_{18})_8$  microcapsules for five cycles of encapsulation and releasing by adding trivalent salt and UV irradiation. (a, b) second cycle, (c, d) third cycle, (e, f) fourth cycle, (g, h) fifth cycle. Scale bar is  $5\mu\text{m}$ .

### Morphology changes of the microcapsules with salt addition

During the drying process of the microcapsules with  $\text{K}_3\text{Co}(\text{CN})_6$ , the higher rigidity of their shell makes them very easily broken and causes them to form large pores on the surface, as shown in Figure S7.10. Moreover, the diameter of the microcapsules in the collapsed state on silicon wafer decrease to  $2.47\ \mu\text{m}$  on average. On the other hand, when the suspension of  $\text{PSS}/\text{qPDMAEMA}_{18}$  microcapsules was exposed to UV irradiation after adding  $\text{K}_3\text{Co}(\text{CN})_6$ , the trivalent ions decompose into monovalent and divalent ions, so that the  $\text{qPDMAEMA}_{18}$  star polyelectrolytes would resume their original stretched conformation and the overall size and permeability of the microcapsules was also recovered. Figure S7.10c is the AFM image of  $(\text{PSS}/\text{qPDMAEMA}_{18})_8$  microcapsules after drying, which were UV irradiated for 45 min in suspension after adding  $0.8\ \text{mM}\ \text{K}_3\text{Co}(\text{CN})_6$ , it can be seen that the capsules keep their integrity and the average diameter is  $3.51\ \mu\text{m}$ , which is similar with  $\text{PSS}/\text{qPDMAEMA}_{18}$  microcapsules without adding trivalent salt (Figure S7.10a).

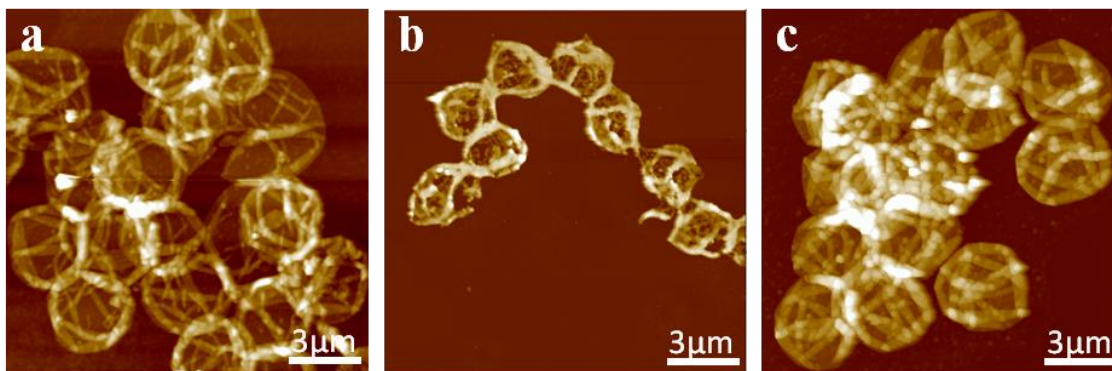


Figure S7.10. AFM images of  $(\text{PSS}/\text{qPDMAEMA}_{18})_8$  capsules before (a) and after (b) adding  $0.8\ \text{mM}\ \text{K}_3\text{Co}(\text{CN})_6$ , (c) UV irradiation for 45 min after adding  $\text{K}_3\text{Co}(\text{CN})_6$ . Z-scale is  $300\ \text{nm}$ .

## CHAPTER 8. MULTI-COMPARTMENTAL MICROCAPSULES WITH DUALCARRIER AND PROGRAMMABLE RELEASE CAPABILITIES

### 8.1 Introduction

Microcapsules have undergone rapid development in recent years due to their ease of fabrication, high loading capacity, versatility of structure and composition. Polymeric microcapsules have already found promising applications in drug delivery, tissue engineering, nanomedicine and self-healing.<sup>322</sup> However, most previous reported microcapsules have simple or homogenous structure, which can only delivery one type of cargo molecules in their interior. For some advanced application, it is desirable to have simultaneous delivery of several vectors or biomolecules, microcapsules with such capability are considered as next generation of carriers with more complex structures, or the so called multicompartmental microcapsules.<sup>324</sup>

The concept of multicompartmental microcapsules was introduced only several years ago, it is still a new filed and much more work needs to be done. One popular method to fabricate multicompartmental microcapsules is based on the assembly of porous microparticles, such as  $\text{CaCO}_3$ . For example, Skirtach et al.<sup>361</sup> showed that by coating  $\text{CaCO}_3$  microparticles with polyelectrolyte shell, and then absorbing smaller particles on the surface of large particles, or growing another  $\text{CaCO}_3$  shell on the coated microparticles, multicompartmental microcapsules can be generated after dissolving the core. But this method has the drawback of irregular shape, high polydispersity and low yield.

In this work, we presented a novel and unique way to fabrication multicompartamental microcapsules, by using complex star polymers with core-shell structure as main building blocks. The star polymers have a hydrophobic core and a dense thermal-responsive PNIPAM shell, therefore they can serve as nanocarriers for hydrophobic molecules, and at the same time, the PNIPAM shell enables their LbL assembly with another component, such as tannic acid used here, and another type of hydrophilic molecules can be encapsulated inside the microcapsules. By combining the pH and temperature dual responsive property, a programmable and sequential release of hydrophobic and hydrophilic molecules is successfully achieved.

## 8.2 Experimental section

**Materials** The  $\text{PS}_n(\text{P2VP-}b\text{-PAA})_n$  heteroarm star block terpolymers were synthesized via a one-pot/four-step sequential “living” anionic polymerization procedure (an extended “in-out” method), which was described in detail elsewhere.<sup>362</sup> Briefly, *sec*-BuLi was used as the initiator to prepare “living” PS chains in the first step, then the PS chains were used to polymerized a small quantity of DVB, resulting in a living star-shaped PS bearing active sites in the PDVB core. Then the “living” star polymers were used to initiate polymerization of 2VP, leading to a second generation of P2VP arms. Finally, *t*BA was polymerized from the end of each P2VP arms. The  $\text{PS}_n(\text{P2VP-}b\text{-PAA})_n$  terpolymers were obtained after acidic hydrolysis of the *Pt*BA blocks, detailed parameters about the star terpolymers is summarized in Table S1. In order to graft PNIPAM chains to the PAA blocks, PNIPAM-NH<sub>2</sub> chains with  $M_n$  of 5500 (purchased from Aldrich)

were grafted to the carboxylate groups of PAA in the presence of 1-Ethyl-3-(3-dimethylaminopropyl) carbodiimide (EDC). The detailed characterization of the final star-graft quarterpolymers (SG polymer)  $PS_n[P2VP-b-(PAA-g-PNIPAM)]_n$  can be found in<sup>249</sup> and some characteristics are summarized in Table 3.2.

Tannic acid ( $M_w = 1700$  Da) was purchased from Sigma-Aldrich. Silica particles with a diameter of  $4.0 \pm 0.2$   $\mu\text{m}$  and 10% dispersion in water were obtained from Polysciences. Hydrofluoric acid (48–51%) was purchased from BDH Aristar. Tris-HCl (1.0 M) was purchased from Rockland and was diluted to 0.01 M in ultrapure pure water with pH adjusted by HCl or NaOH for use.

***Encapsulation of Nile Red in SG polymers*** The SG polymers were dissolved in DI water with a concentration of 0.2 mg/mL, Nile Red was dissolved in methanol with a concentration of 0.5 mg/mL. 60  $\mu\text{L}$  Nile Red solution was added to 10 mL SG polymer solution dropwise with constant stirring for 1 h, then the solution was dialyzed against DI water for 24 h with repeated change of water to remove excess Nile Red molecules in the solution.

***Preparation of LbL microcapsules and films*** SG polymers with or without encapsulated Nile Red aqueous solution has a concentration of 0.2 mg/mL. Tannic acid was dissolved in 0.1 M NaCl solution with the concentration of 0.2 mg/mL, and the pH is adjusted to 5 with HCl and NaOH. The preparation of LbL  $(TA/SG)_n$  microcapsules is shown in Figure 8.4b: the bare, negatively charged silica particles with average diameter of 4.0  $\mu\text{m}$

were first incubated in 1.5 mL TA solution (0.2 mg/mL) for 15 min, followed by two centrifugation (3000 rpm for 2 min)/wash cycles. 1.5 mL of SG polymer solution was then added and 15 min was allowed for adsorption, also followed by two centrifugation/wash cycles. The adsorption steps were repeated until the desired number of layers was built on silica particles. Hollow microcapsules were finally obtained by dissolving silica cores in 4% HF solution for 2h, followed by dialysis in Nanopure water for 2 days with repeated change of water. The LbL films were prepared by dip-assisted LbL method: the silicon substrate was alternately immersed in TA and SG polymer solution for 15 min, followed by two times rinsing with 0.01 M Tris-HCl buffer (pH = 5).

## **8.3 Results and Discussion**

### **8.3.1 Properties of SG Polymers and the LbL Films**

The star-graft quarterpolymers  $PS_n[P2VP-b-(PAA-g-PNIPAM)]_n$  have two class of arms, one is shorter PS arm with degree of polymerization (DP) of 33, the other is longer P2VP-*b*-PAA block copolymer arm (DP of P2VP: ~130, DP of PAA: 69 or 119) with grafted PNIPAM (DP=48) chains on the PAA block (Figure 8.1a). The core regions of the SG polymer consist of hydrophobic PDVB core and PS chains, therefore, the SG polymers have the potential to encapsulate hydrophobic molecules in the core.

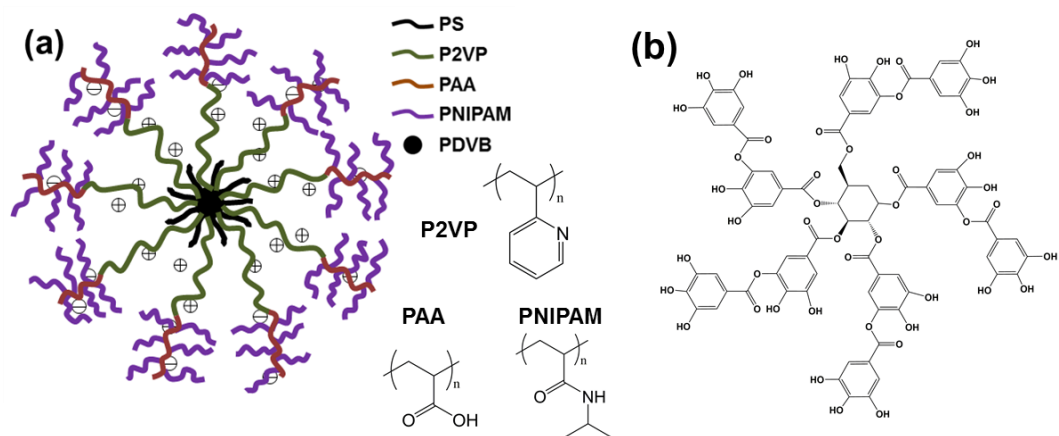


Figure 8.1. Chemical structure of the (a) SG polymers and (b) tannic acid.

The hydrophilic block copolymer arms consist of oppositely charged P2VP and PAA, which can interact with each other through electrostatic or hydrogen bonding depending on the pH condition. At acidic condition ( $\text{pH} < 4.2$ ), the P2VP blocks are highly protonated and positively charged; at the isoelectric region ( $4.2 < \text{pH} < 7.5$ ), the two blocks are both partially charged and mutually neutralized; at basic condition ( $\text{pH} > 7.5$ ), the PAA blocks are largely deprotonated and negatively charged.

Previous studies on the SG polymers have shown that upon heating their aqueous solutions, intermolecular hydrophobic association was observed above a critical temperature, which leads to the appearance of a gel phase at concentrated solutions. This phenomenon is also strongly dependent on pH, ionic strength, along with the number of arms and the PNIPAM grafting density.

Due to the presence of high density of PNIPAM chains on the shell, the SG polymers can be used to build multilayer structure via hydrogen bonding with another component. For

this purpose, we use tannic acid, a natural polyphenol, to interact with the SG polymers. To study the effect of number of arms and PNIPAM graft density on the layer-by-layer assembly process, we choose three star-graft quarterpolymers with the same chemical composition but different arm number or PNIPAM grafting density. Briefly, SG2 has 9 PS arms and 9 P2VP-*b*-(PAA-*g*-PNIPAM) arms, with 4.5 PNIPAM chains per PAA block on average; SG3 has the same number of arms, but 11.0 PNIPAM chains per PAA block; and SG4 has 22 PS arms and 22 P2VP-*b*-(PAA-*g*-PNIPAM) arms, with 4.0 PNIPAM chains per PAA block. The detailed information of star composition can be found in Table 3.2 and Table S5.1.

The  $pK_a$  value of TA is the range of 4.9 to 7.4,<sup>363</sup> therefore, at  $pH < 5$ , the TA mainly in the protonation form, and can form strong hydrogen bonding with the PNIPAM chains, therefore, the pH condition for the LbL assembly of SG polymers and TA was chosen to be 5. Figure 8.2 shows the film thickness increase as a function of bilayer number, it can be seen that all the three SG polymers can form strong LbL assembly with TA with consistent thickness increase, but the growth modes are quite different. The (TA/SG3) LbL film has a linear increase in film thickness, with an average bilayer thickness of 7.1 nm in dry state; while that of (TA/SG2) and (TA/SG4) LbL films has an exponential growth pattern, with an average bilayer thickness of 9.8 nm and 12.4 nm, respectively.

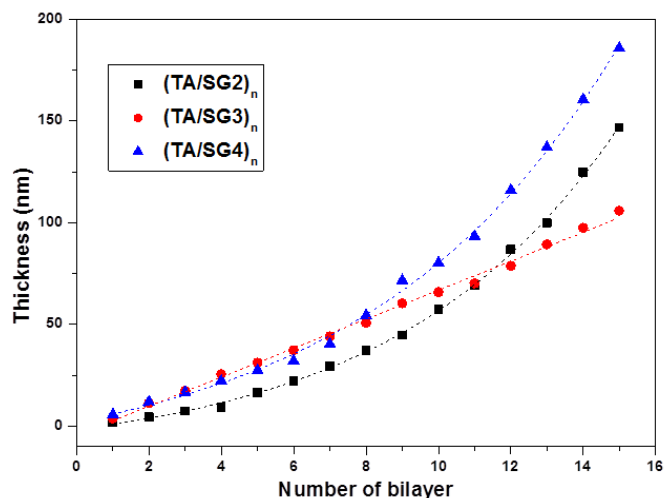


Figure 8.2. Thickness increase with the number of bilayers for  $(TA/SG)_n$  LbL thin films.

The surface morphology of the LbL thin films were characterized by AFM (Figure 8.3), it can be seen that  $(TA/SG2)$  and  $(TA/SG4)$  LbL films have nonuniform surface morphology with large aggregates on the surface, while the  $(TA/SG3)$  LbL film have much smoother surface. The root mean square (RMS) roughness of a  $1 \mu\text{m}^2$  area for  $(TA/SG2)$ ,  $(TA/SG3)$  and  $(TA/SG4)$  LbL films is 22.1 nm, 10.9 nm and 29.6 nm, respectively. Such morphological differences also explains the thickness growth pattern differences, the exponential growth of  $(TA/SG2)$  and  $(TA/SG4)$  LbL films can be attributed to sub-surface diffusion resulting in the increase of film surface roughness with the number of deposited layers.<sup>52</sup> From the higher magnification AFM images on the right column (Figure 8.3), it can be seen that the surface of the films have high density of granule structures, the size of which match with the size of individual SG polymer.

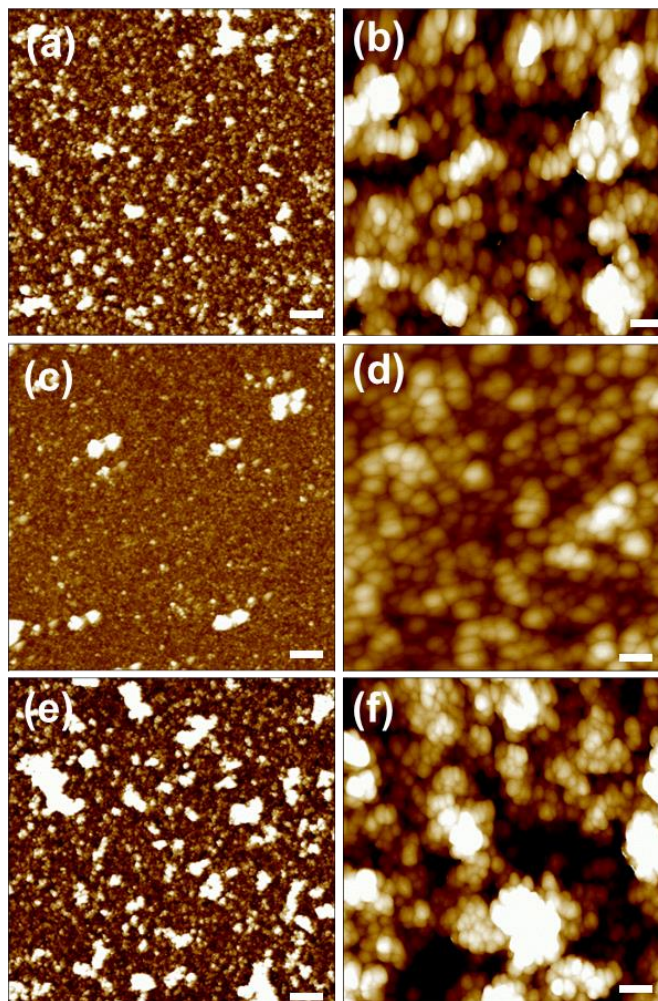


Figure 8.3. AFM images of the (a, b)  $(\text{TA}/\text{SG}2)_{15}$ , (c, d)  $(\text{TA}/\text{SG}2)_{15}$ , (e, f)  $(\text{TA}/\text{SG}2)_{15}$  LbL films, the scale bar is 1  $\mu\text{m}$  on the left column, and 100 nm on the right column; the Z range is 200 nm on the left column and 100 nm on the right column.

### 8.3.2 Morphology of the $(\text{TA}/\text{SG}3)$ LbL Microcapsules

The LbL assembly on a spherical substrate which results in hollow microcapsules after dissolving the core (Figure 8.4a), the pH condition is also chosen to be 5 for the LbL assembly, so that the overall SG polymer is close to neutral, with strong hydrogen bonding interaction between TA and SG polymers. Electrophoresis experiments were conducted to monitor the LbL growth of TA and SG polymer on silica microparticles

(Figure 8.4b). The zeta-potential of bare silica microparticles is -10.3 mV at pH 5 condition due to the ionized silanol groups. The surface charge shifts to between -2.4 mV to -7.7 mV when TA is the outmost layer, and only slightly negative charged ( $< -1.0$  mV) when the SG3 polymer is the outmost layers.

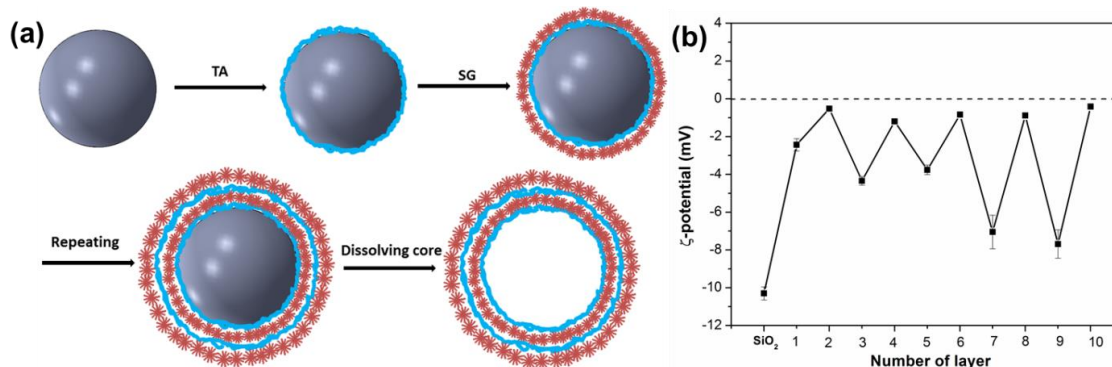


Figure 8.4. (a) Scheme of the LbL fabrication process of (TA/SG3) microcapsules, (b)  $\zeta$ -potential as a function of number of layers during LbL assembly on silica microparticles.

Usually for conventional electrostatic LbL assembly, there is a charge reversal between positive and negative during the deposition process. Our results indicate that the surface of the microparticles remain negatively charged in the whole process, which proves that hydrogen bonding is the main driving force for the assembly between TA and SG polymers.

AFM images of the (TA/SG3)<sub>6</sub> microcapsules are shown in Figure 8.5, the hollow microcapsules collapse after drying with formation of random wrinkles on the surface. From the higher magnification image (Figure 8.5b), it can be seen that the surface of the microcapsules also possesses a highly dense granular morphology, which corresponds to the 3D structure of individual SG polymers. Cross section analysis of the AFM images

gives the thickness of the (TA/SG3)<sub>6</sub> microcapsules, which is  $36.1 \pm 5.2$  nm, and matches very well with the thickness of 6 bilayer planar film (37.2 nm).

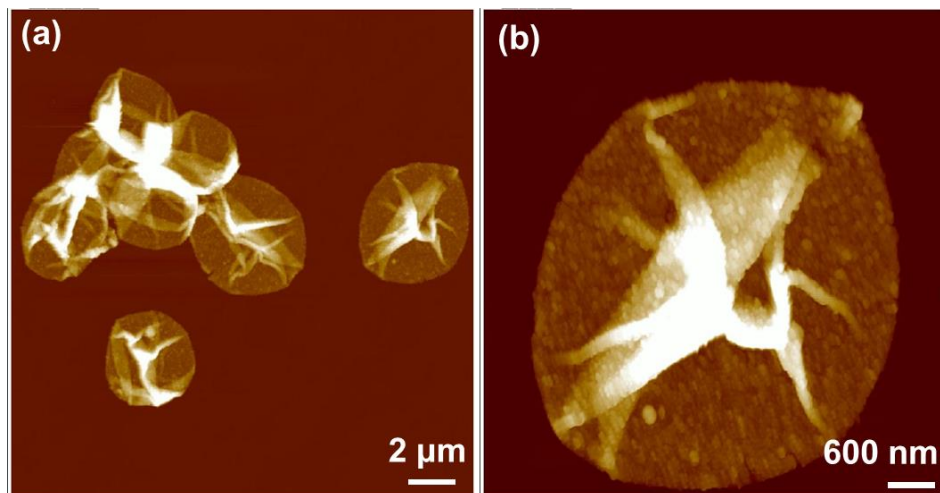


Figure 8.5. AFM images of (TA/SG3)<sub>6</sub> microcapsules after drying; Z range is 800 nm in (a) and 500 nm in (b).

SEM images of the (TA/SG3)<sub>6</sub> microcapsules are shown in Figure 8.6, from the higher magnification image it can be seen that the microcapsules have a porous surface structure even after drying. The surface is uniform with high density of granule structure, and no sign of irregular aggregates was found, which corresponds well with the surface morphology of the (TA/SG3) planar thin film.

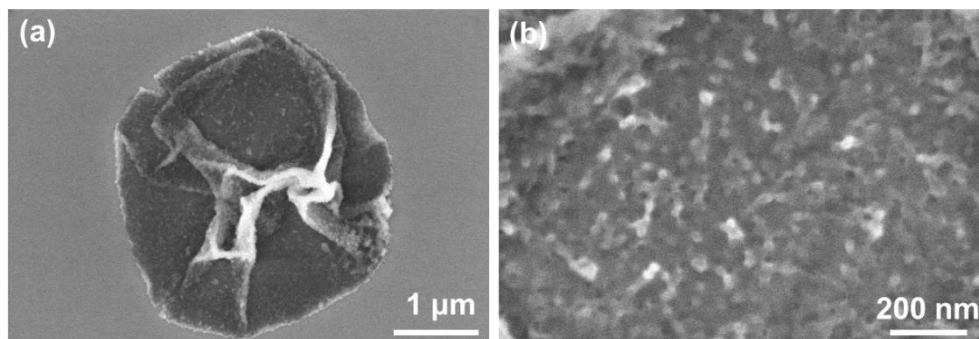


Figure 8.6. SEM images of (TA/SG3)<sub>6</sub> microcapsules at (a) low and (b) high magnification.

### 8.3.3 pH Controlled Permeability of Microcapsules

The SG polymers have strongly pH dependent conformation and size, and the hydrogen bonding between SG polymer and TA is also affected by pH, therefore, the structure and permeability of the (TA/SG3) microcapsules are expected to be pH responsive. To test the permeability of the microcapsules, fluorescein isothiocyanate (FITC) labeled dextran with various molecular weights as fluorescent probes. When the pore size of the microcapsules shell is larger than the size of the fluorescent probe, then the fluorescent intensity would be almost the same for the interior and exterior of the microcapsules, otherwise the interior would be dark and the background appears bright.

Figure 8.7 shows that permeability test of the (TA/SG3)<sub>6</sub> microcapsules at different pH conditions to 70 kDa and 150 kDa FITC-dextran. It can be seen that 70 kDa FITC-dextran can permeate inside the microcapsules at all three different pH conditions. For 150 kDa FITC-dextran, it can permeate inside the microcapsules at pH 3, and partially permeable at pH 5, and completely impermeable at pH 7 condition. The complete summary of the permeability test results is in Table 8.1. The results show that the permeability of the (TA/SG3)<sub>6</sub> microcapsules decreases with increasing pH. Considering the hydrodynamic diameter of 70 kDa FITC-dextran is 13.0 nm, and that of 150 kDa Dextran is around 20 nm,<sup>346</sup> so the average mesh size of the (TA/SG3)<sub>6</sub> microcapsules is in the range of 13 to 23 nm and highly dependent on pH.

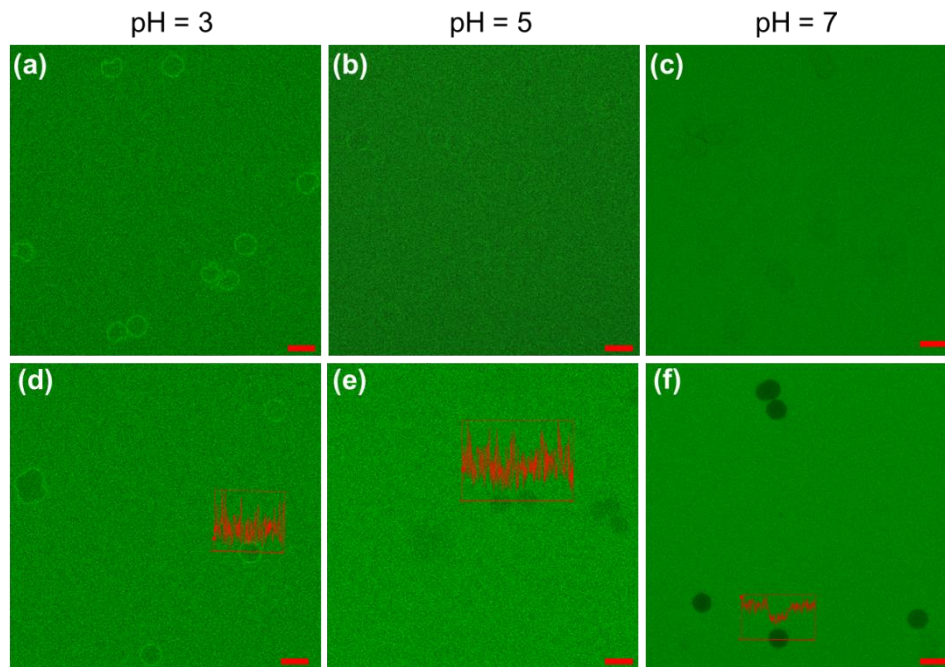


Figure 8.7. Permeability of  $(TA/SG3)_6$  microcapsules at different pH condition to 70K FITC-dextran (a, b, c) and 150 K FITC-dextran (d, e, f), the inserts are the representative fluorescent intensity profile over the microcapsule, the scale bar is 5  $\mu$ m.

Table 8.1. Permeability of  $(TA/SG3)_6$  microcapsules to FITC-dextran with various molecular weights at different pH conditions (“+”: permeable, “-” not permeable, “+/-” partially permeable).

Sample	pH	FITC-dextran 20kDa	FITC-dextran 70kDa	FITC-dextran 150kDa	FITC-dextran 250kDa	FITC-dextran 500kDa
$(TA/SG)_6$	3	+	+	+	-	-
$(TA/SG)_6$	5	+	+	+/-	-	-
$(TA/SG)_6$	7	+	+	-	-	-

The mechanism for the pH controlled permeability of the  $(TA/SG3)_6$  microcapsules is a combination of the conformational changes of the SG polymer and the hydrogen bonding interaction between TA and SG3. As shown in Figure 8.8, the SG3 polymer has a core-

shell structure, with P2VP block in the core region and PAA with graft PNIPAM chains in the shell region. At pH 3 condition, the P2VP blocks are highly charged and extended, the grafted PNIPAM chains can interact with PAA block via hydrogen bonding, so that the SG polymer have a collapsed arm end, which also interact with TA molecules to form multilayer structure. The fully extended inner block as well as the loose interaction between collapsed arm ends with TA gives the microcapsules relatively high permeability.

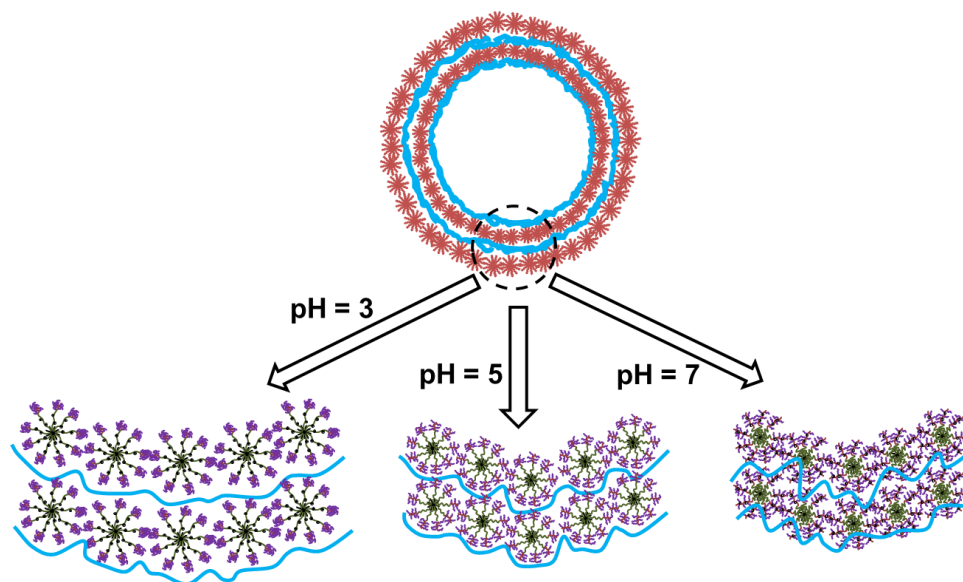


Figure 8.8. The structural changes of the  $(TA/SG3)_6$  microcapsules at different pH conditions, blue curve represents the TA layer.

When pH increases to 7, the inner P2VP blocks are neutral and hydrophobic, and tend to have collapse conformation; the PAA blocks are highly negatively charged and extended, so that the PNIPAM chains are well separated. As a result, the SG polymers have a condensed core region, and an extended shell region that can interact with TA *via* hydrogen bonding. Moreover, the neutral P2VP block and also interact with TA molecules through hydrogen bonding, so that there is more interpenetrating of TA

molecules with SG polymer in the shell. On the other hand, at pH 7 the TA molecules are partially deprotonated and charged, which weakens the hydrogen bonding between TA and SG polymers, leading to a more flexible membrane, and possible defects in the microcapsule shell are filled by the more dynamic chains and molecules. All the above mentioned factors contribute to the significant decrease in microcapsules permeability.

At pH 5 condition (the isoelectric region), both the PAA and P2VP blocks are partially charged, and they can interact with each other electrostatically. The overall size of the SG polymers as well as the extent their hydrogen bonding with TA is in between pH 3 and pH 7, so that the permeability of the (TA/SG3)<sub>6</sub> microcapsules is also in between. The overall average size of the microcapsules also decreases from 3.93 μm at pH 3 to 3.59 μm at pH 7.

It can be seen that the binding of the FITC-dextran to the microcapsule shell is also affected by the pH, at pH 3 the shell have higher fluorescence intensity than the background, which means the fluorescence molecules have strong affinity to the shell, while at pH 5 and 7 the shell have almost the same or even lower fluorescence intensity with the background. This phenomenon is mainly due to the electrostatic interaction between FITC-dextran and the SG polymers. FITC is negatively charged in the pH range used for our study. The charging state of the SG3 polymer depends on pH, and at pH 3 it is positively charged, while at pH 5 and pH 7 it is close to neutral or slightly negatively charged, as a result, the attraction between FITC-dextran and the SG polymers decreases with increasing pH.

### **8.3.4 Temperature Controlled Release of Nile Red from the Shell**

As mentioned in the earlier, the SG polymers have a core-shell structure, which can be used as nanocarriers by themselves. In this work, we choose a hydrophobic fluorescent molecule Nile Red as the model molecules, since the core region of the SG polymers are most composed of hydrophobic PS and PDVB, Nile Red would have strong affinity to the interior of the SG polymers.

The UV-Vis and fluorescence spectra of Nile Red in methanol and SG3 with encapsulated Nile Red were shown in Figure 8.9. It can be seen that the absorption peak of Nile red after encapsulated in SG3 is quite different from that of free molecules in methanol solution, because the absorption and emission maxima of Nile Red are strongly depend on the polarity of the environment. The absorption peak is at 553 nm in methanol, and after encapsulated in SG3 polymer, the main peak shifts to 496 nm, which roughly corresponds to the H-aggregate; and there is another shoulder peak at 635 nm, which corresponds to the J-aggregate of Nile Red.<sup>364</sup> The corresponding fluorescence emission spectra are shown in Figure 8.9b, the emission peak blue shifts from 660 nm for Nile Red in methanol to 604 nm when encapsulated in SG3 polymers.

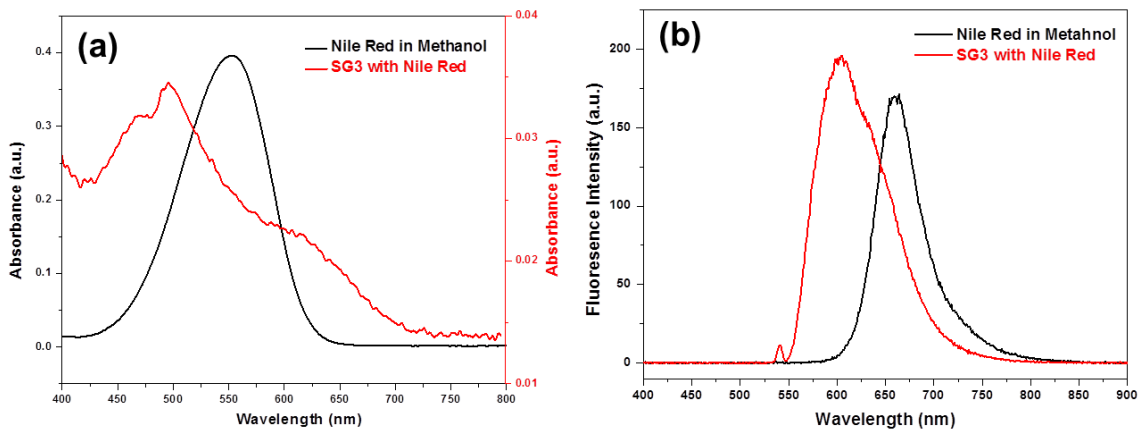


Figure 8.9. (a) UV-Vis spectra of Nile Red in methanol (black) and SG3 with encapsulated Nile Red (red), (b) fluorescence spectra of Nile Red in methanol (black) and SG3 with encapsulated Nile Red (red).

SG polymers with encapsulated Nile Red were used to prepare LbL microcapsules with TA following the same procedure. Figure 8.10a shows the CLSM images of  $(TA/SG3)_6$  microcapsules with encapsulated Nile Red in the shell, it can be seen that the shell are strongly red fluorescent due to the presence of Nile Red. When the microcapsule suspension is heated to 45 °C for a short time, the encapsulated Nile Red on the shell is completely released and the microcapsules remain robust and intact, as shown in Figure 8.10b, c.

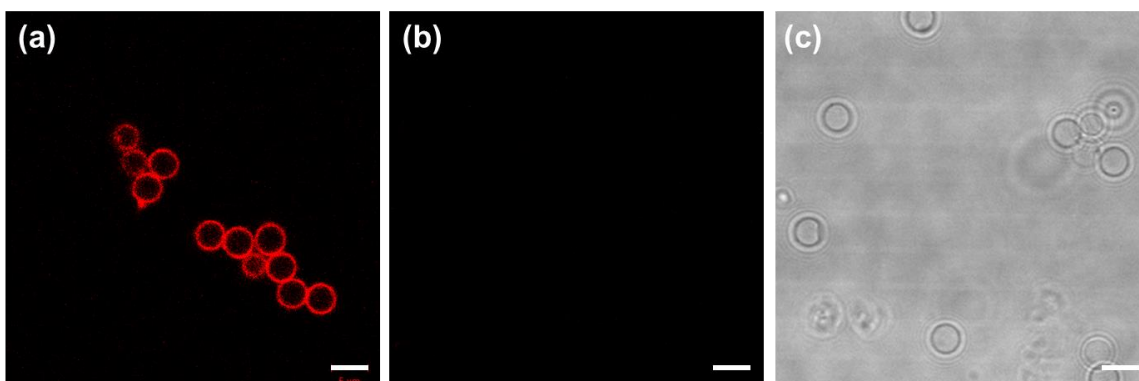


Figure 8.10. (a) CLSM images of  $(TA/SG3)_6$  microcapsules with encapsulated Nile Red in the shell, (b) CLSM images of the same sample after heating to 45 °C for 15 min, (c) transmission mode image of the same area with b. Scale bar is 5  $\mu$ m.

The temperature induced release of Nile Red from the SG3 polymers results from the combinational effects of thermal motion and change in hydrophobicity of the polymer chains. When the temperature increases to 45 °C, the mobility of Nile Red molecules is significant higher than that at room temperature. On the other hand, with temperature increase, the PNIPAM chains transform from hydrophilic to hydrophobic, so that the shell region of the SG3 polymers is largely hydrophobic, which can attract the Nile Red to move from the core region to the shell region, and diffuse out of the shell eventually.

### **8.3.5 Programmable Encapsulation and Release Induced by pH and Temperature**

Taking advantage of the pH and thermal dual responsive properties, as well as the encapsulation capability of the SG3 polymers themselves, the (TA/SG3)<sub>6</sub> microcapsules have the potential to be multicompartmental responsive carrier for two different types of target molecules. This can be achieved by pre-encapsulation of Nile Red in the shell, and then post-encapsulate FITC-dextran inside the microcapsules.

Firstly, Nile Red was encapsulated in the SG3 polymers through hydrophobic interaction, the SG3 polymers were then used to fabricate LbL microcapsules, so that Nile Red was encapsulated in the shell of the microcapsules. Secondly, by utilizing the pH-controlled permeability of the prepared (TA/SG3)<sub>6</sub> microcapsules (Figure S8.2), FITC-dextran ( $M_w$  of 70 kDa) can permeate inside the microcapsules at pH 5, and switching the pH to 7 can encapsulate the FITC-dextran inside the microcapsules due to the decrease in permeability of the shell.

The results are shown in Figure 8.11a, the double channel CLSM image shows that the microcapsules successfully encapsulate green FITC-dextran inside, and the red Nile Red only present on the shell of the microcapsules (the shell is orangish due to the presence of small amount of FITC-dextran close to the shell region). From the separate red channel (Figure 8.11b) and green channel (Figure 8.11c), it is easier to see the multicompartental nature of the microcapsules: SG3 polymers serve as nanocarriers in the shell, and the overall microcapsules can also encapsulate larger molecules inside the hollow interior.

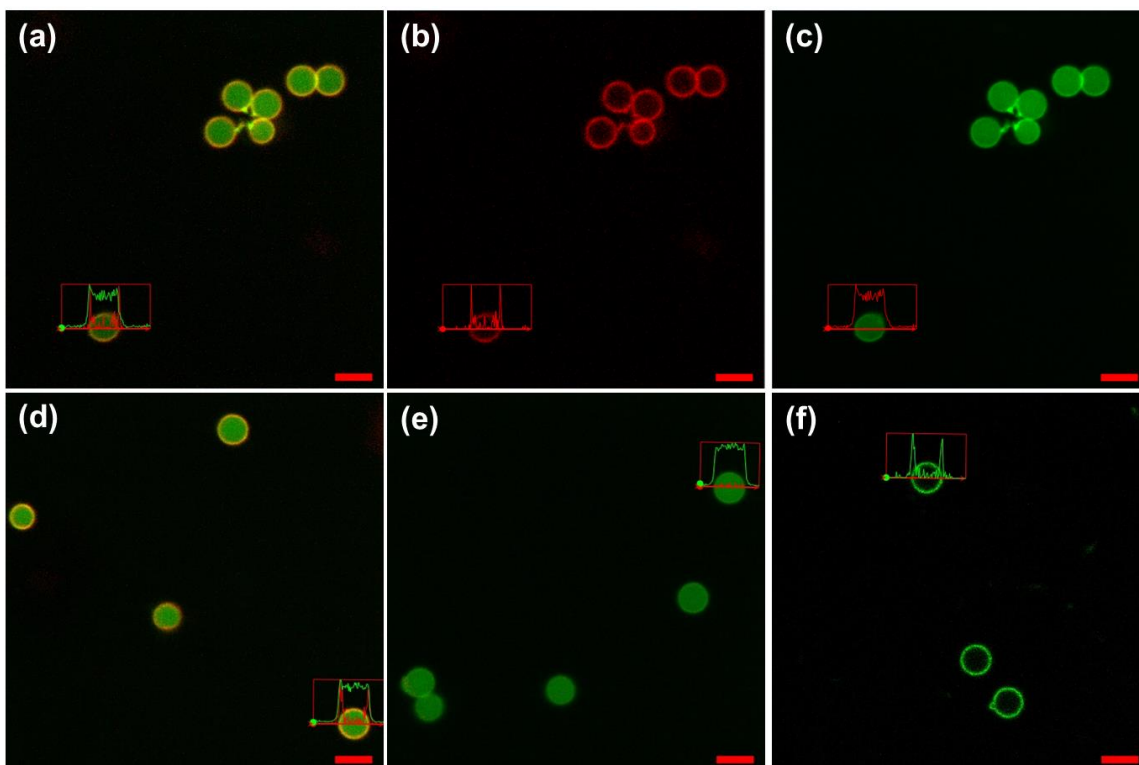


Figure 8.11. (a) CLSM images of the  $(TA/SG3)_6$  microcapsules with encapsulated Nile Red in the shell and FITC-dextran inside the microcapsules, (b) red channel and (c) green channel of the same area in the same sample. (d)  $(TA/SG3)_6$  microcapsules with encapsulated Nile Red and FITC-dextran, (e) release of Nile Red by increasing temperature, (f) subsequent release of FITC-dextran by decrease pH from 7 to 5. The inserts are the representative fluorescent intensity profile over the microcapsule. Scale bar is 5  $\mu\text{m}$ .

Sequential or programmable release of the encapsulated target molecules can be achieved based on the multiple responsive properties of the (TA/SG3)<sub>6</sub> microcapsules. Firstly, as discussed in the previous section, temperature increase is able to selectively release the Nile Red molecules encapsulated within the shell, and the FITC-dextran remain encapsulated inside the microcapsules without any loss, as shown in Figure 8.11e. Afterwards, decreasing the microcapsule suspension pH from 7 to 5 induces the increase in permeability of the shell, so that the FITC-dextran in the interior of the microcapsules can be readily released (Figure 8.11f). The whole programmable encapsulation and release process is schematically shown in Figure 8.12.

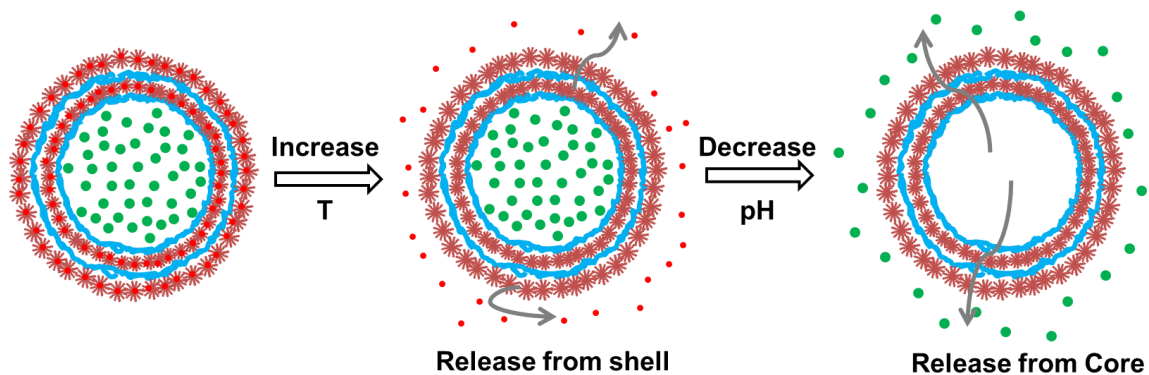


Figure 8.12. Schematic illustration of the programmable encapsulation and release of Nile Red and FITC-dextran from the shell and core region, triggered by temperature and pH change, respectively.

#### 8.4 Conclusions

Multicompartmental microcapsules were successfully prepared based on stat-graft quarterpolymers, the SG polymers have a core-shell structure which enables the encapsulation of hydrophobic molecules in the core region. The fabricated microcapsules have the capability to encapsulated two different types of target molecules simultaneously: hydrophobic molecules in the shell, and another kind of hydrophilic

molecules in the interior of the microcapsules. Temperature and pH can be used to release the encapsulated molecules in a programmable and controllable way: heating induces the release of Nile Red, and pH decrease induces the subsequent release of FITC-dextran. The smart multicompartmental microcapsules have promising applications in drug delivery, self-healing materials as well as microreactors.

## Appendix: Supporting Information

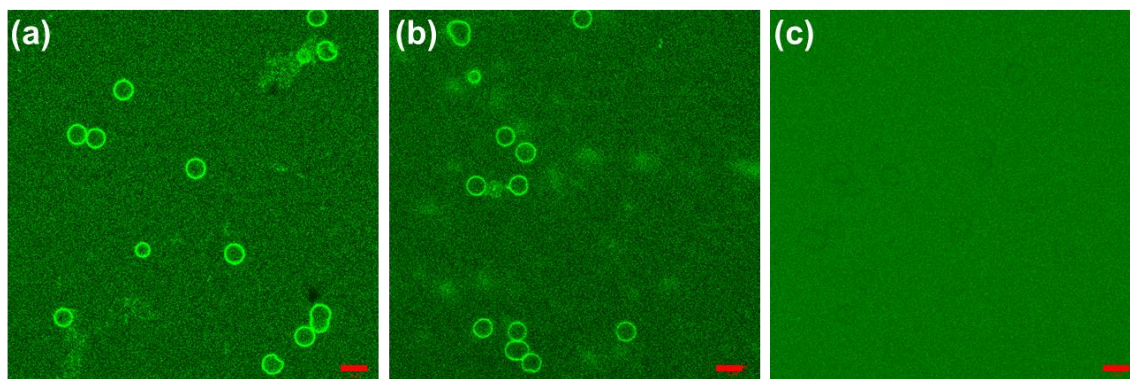


Figure S8.1. CLSM images of (TA/SG3)<sub>6</sub> microcapsules at (a) pH 3, (b) pH 5 and (c) pH 7 conditions, and the solution are colored due to FITC addition.

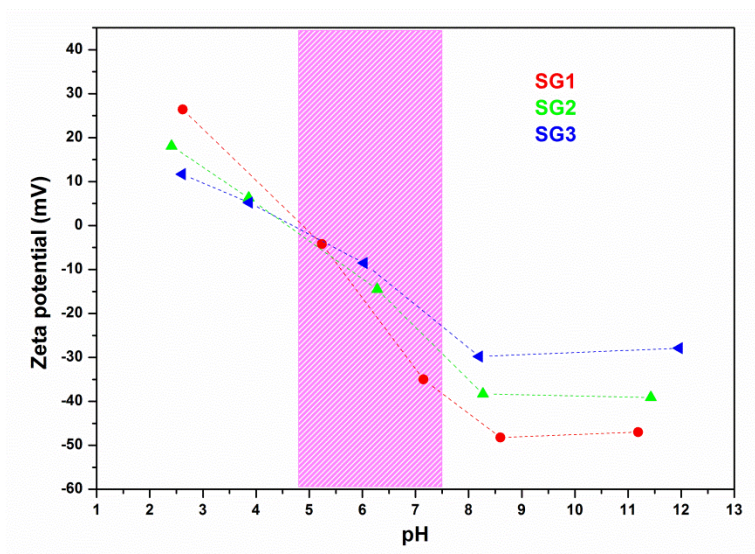


Figure S8.2. Zeta potential of SG polymers at different pH conditions, the shaded area indicates the isoelectric region.

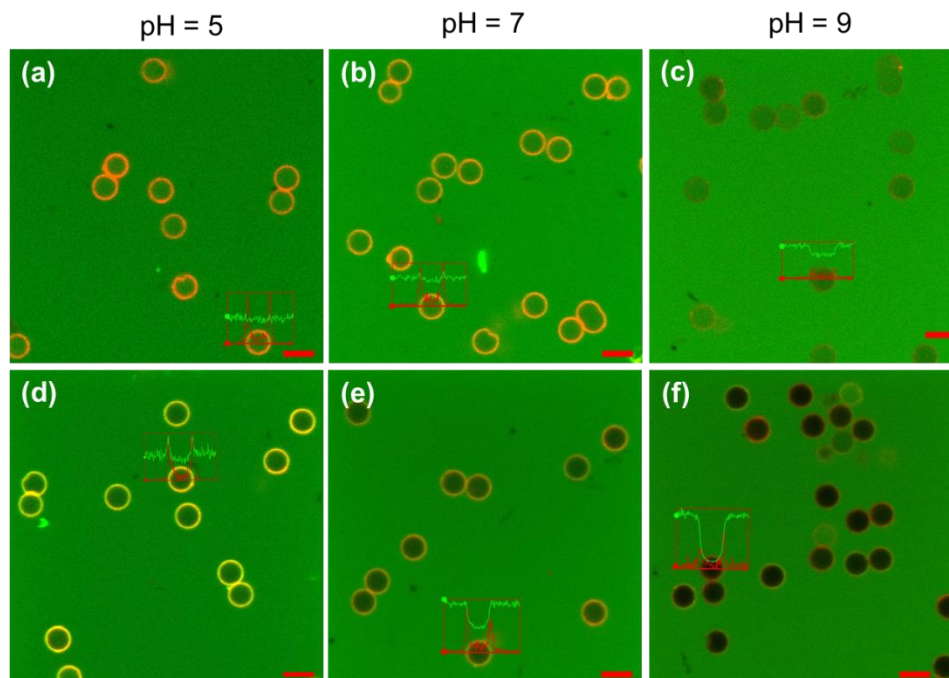


Figure S8.3. Permeability of  $(\text{TA}/\text{SG3-NR})_6$  microcapsules at different pH condition to 20K FITC-dextran (a, b, c) and 70 K FITC-dextran (d, e, f), the inserts are the representative fluorescent intensity profile over the microcapsule, the scale bar is 5  $\mu\text{m}$ .

## CHAPTER 9. POLYMERSOME BASED MULTI-COMPARTMENTAL MICROCAPSULES

### 9.1 Introduction

Polymeric microcapsules have attracted intensive attention in recent years due to their promising applications in various fields including drug delivery, tissue engineering, nanomedicine, and self-healing materials. The fabrication of polymeric microcapsules is usually based on self or directed assembly of polymers, two representative examples include polyelectrolyte multilayer microcapsules and microemulsion based microcapsules,<sup>141</sup> the former class is based on the electrostatic interaction between cationic and anionic polyelectrolytes, and the latter class relies on the assembly of amphiphilic polymers at oil/water interface. These microcapsules usually have simple and homogenous structure and can only encapsulate one type of cargo molecules.

On the other hand, for some advanced applications, it is important to be able to deliver several different types of molecules at the same time. To this purpose, traditional microcapsules are not enough, and it is desirable to develop the next generation microcapsules with hierarchical multicompartmental structures which can encapsulate and release different molecules simultaneously.

Despite the superior properties and promising application of multicompartmental microcapsules, their fabrication is quite challenging, and only a few successful attempts have been reported so far.<sup>361</sup> For instance, hollow microcapsules with shell constructed from a cationic/zwitterionic pairs of pH-responsive block copolymer micelles have been

prepared, it was shown that the core/shell structure of the micelles remains intact after LbL assembly,<sup>365</sup> but the loading capacity of the micelles is quite low due to its small size and low stability. In another example, hydroxy-functionalized polymersomes were used as Pickering emulsifiers for the stabilization of emulsions, which has a similar structure to microcapsules,<sup>366</sup> but the polymersomes are not stable at the interface and additional cross-linking between them is required.

In this work, we utilized a novel way to fabricate polymersomes and assemble them into multilayered microcapsules with hierarchical structure. Taking advantage of the electrostatic interaction between a cationic miktoarm star polyelectrolyte and a linear anionic polyelectrolyte, robust polymersomes with interpolyelectrolyte complex wall and PEO brushes can be prepared. The polymersomes are used as the main component to fabricate microcapsules with tannic acid (TA) *via* hydrogen bonding using layer-by-layer (LbL) assembly. The multicompartamental microcapsules have the capability to encapsulate and deliver two different types of target molecules simultaneously: one type of molecules can be encapsulated inside the polymersomes, and another type of molecules can be encapsulated in the hollow core region of the microcapsules. The hydrogen bonding between TA and polymersomes can be affected by pH, and the structure of the polymersomes themselves strongly depends on ionic strength, therefore, a combination of pH and ionic condition changes enable us to achieve controllable and programmable release of two different types of encapsulated molecules.

## 9.2 Experimental section

### Materials

The miktoarm star polymer consisting of one poly-(ethylene oxide) (PEO) and on average 4.1 shorter poly(dimethylaminoethyl methacrylate) (PDMAEMA) or their quaternized salt (qPDMAEMA) arms. The polymer was synthesized by atom transfer radical polymerization (ATRP) of a PEO and dipentaerythritol-based macroinitiator, aiming for five PDMAEMA grafts. The pendant amino groups of miktoarm star PEO-PDMAEMA<sub>4.1</sub> were quaternized with methyl iodide, leading to PEO-qPDMAEMA<sub>4.1</sub> star polymers. The completeness of quaternization was verified by elemental analysis. The synthesis and detailed characterization are explained in a previous publication,<sup>135</sup> the overall formula was determined to PEO<sub>113</sub>-(qPDMAEMA<sub>60</sub>)<sub>4.1</sub>, indicating the number-average degree of polymerization for the PEO arm is 113, and 60 for one qPDMAEMA arm. The miktoarm star polymer was labeled with rhodamine B during synthesis (feed ratio of DMAEMA to rhodamine B: 1277: 1)

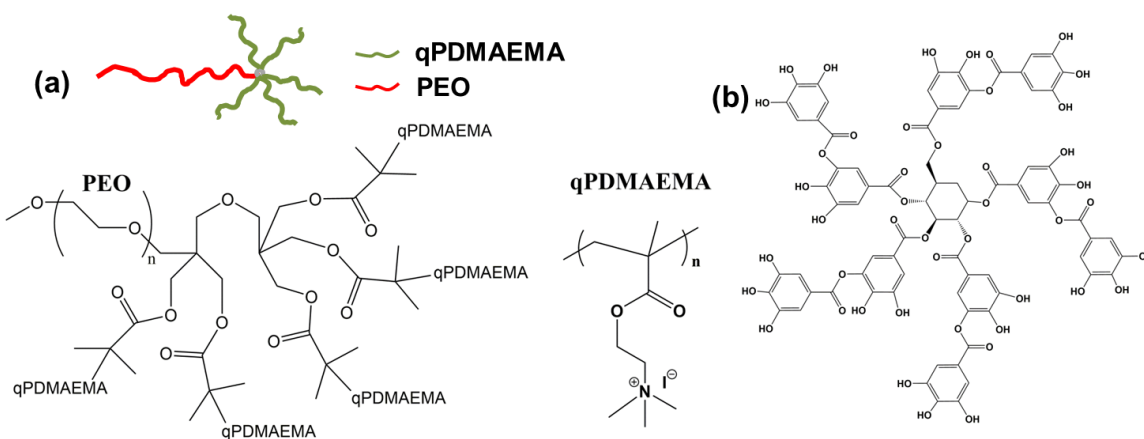


Figure 9.1. Chemical structures of (a) PEO<sub>113</sub>-(qPDMAEMA<sub>60</sub>)<sub>4.1</sub> miktoarm star polymer and (b) tannic acid.

Tannic acid ( $M_w = 1700$  Da) was purchased from Sigma-Aldrich. Silica particles with a diameter of  $4.0 \pm 0.2$   $\mu\text{m}$  and 10% dispersion in water were obtained from Polysciences. Hydrofluoric acid (48–51%) was purchased from BDH Aristar. Tris-HCl (1.0 M) was purchased from Rockland and was diluted to 0.01 M in ultrapure pure water with pH adjusted by HCl or NaOH for use.

### ***Fabrication of polymersome***

SG polymers were dissolved in DI water with a concentration of 0.2 mg/mL, Nile Red was dissolved in methanol with a concentration of 0.5 mg/mL. 60  $\mu\text{L}$  Nile Red solution was added to 10 mL SG polymer solution dropwise with constant stirring for 1 h, then the solution was dialyzed against DI water for 24 h with repeated change of water to remove excess Nile Red molecules in the solution.

***Preparation of LbL microcapsules and films*** The prepared polymersomes have a solid content of around 0.3 mg/mL, tannic acid was dissolved in 0.1 M NaCl solution with the concentration of 0.3 mg/mL, and the pH is adjusted to 5 with HCl and NaOH. The preparation of LbL (TA/polymerosome)<sub>n</sub> microcapsules is shown in Figure 9.2b: the bare, negatively charged silica particles with average diameter of 4.0  $\mu\text{m}$  were first incubated in 1.5 mL TA solution (0.2 mg/mL) for 15 min, followed by two centrifugation (3000 rpm for 2 min)/wash cycles. 1.5 mL of polymerosome solution was then added and 15 min was allowed for adsorption, also followed by two centrifugation/wash cycles. The adsorption steps were repeated until the desired number of layers was built on silica particles. Hollow microcapsules were finally obtained by dissolving silica cores in 4%

HF solution for 2h, followed by dialysis in Nanopure water for 2 days with repeated change of water. The LbL films were prepared by dip-assisted LbL method: the silicon substrate was alternately immersed in TA and polymersome solution for 15 min, followed by two times rinsing with 0.01 M Tris-HCl buffer (pH = 5).

## **9.3 Results and Discussion**

### **9.3.1 Polymersome Formation via Electrostatic Interaction**

Previous study by us showed that mixing a bis-hydrophilic, cationic miktoarm star polymer with a linear polyanion leads to the formation of unilamellar polymersomes, which consist of an interpolyelectrolyte complex (IPEC) wall sandwiched between poly(ethylene oxide) brushes, as shown in Figure 9.2a. The star-based vesicles have some advantages like ease of preparation, and expected biocompatibility (stealth character of PEO, mutual shielding of the charges of the polyelectrolyte components), so that they are suitable for applications in diverse biomedical fields as nanocontainers and nanocarriers due to their rather small size. The miktoarm star we use is  $\text{PEO}_{113}\text{-}(\text{qPDMAEMA}_{60})_{4,1}$ , the anionic polyelectrolyte used to interact with the miktoarm stars is PSS.

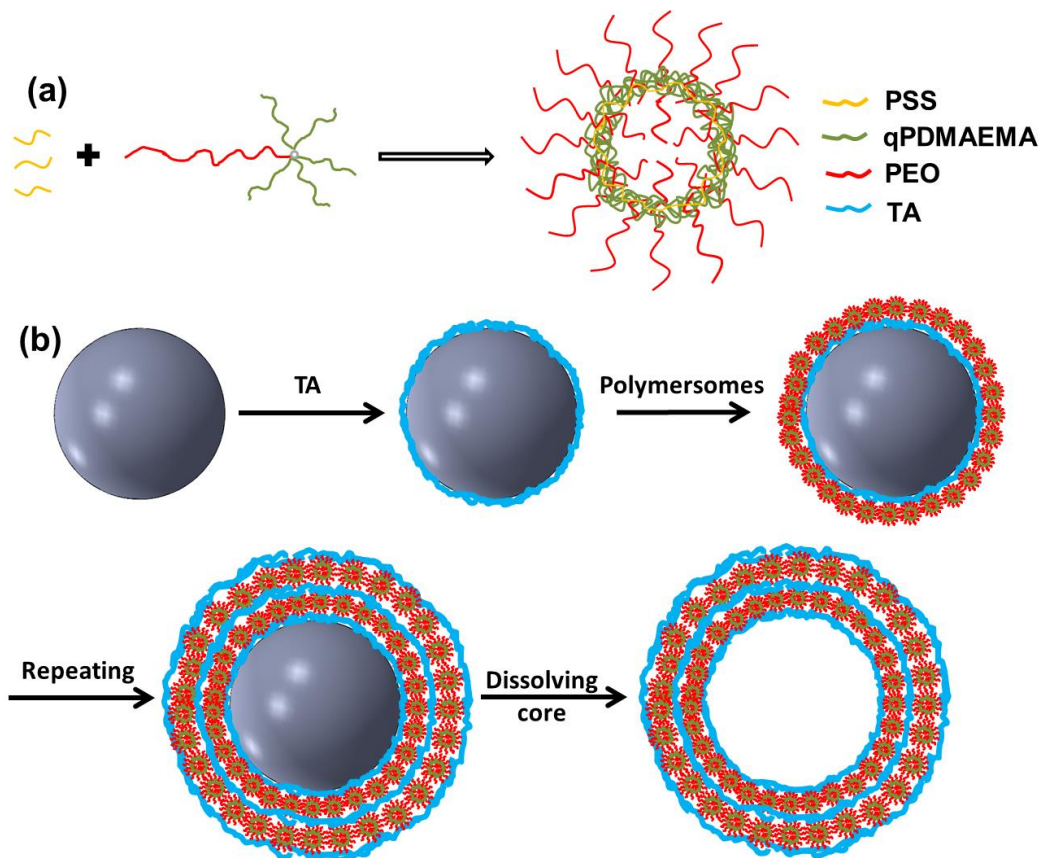


Figure 9.2. (a) Formation of polymersomes by mixing cationic miktoarm stars and anionic linear polyelectrolytes. (b) Scheme of the LbL fabrication process of (TA/polymersome) microcapsules.

The vesicles are very stable in solution and DLS measurements show that the hydrodynamic radius of the polymersomes is around 90 nm (Figure 9.3b). Cryo-TEM image clearly shows the vesicular structure of the formed polymersome, with average size between 60-70 nm, and the thickness of the wall can be estimated as 13-15 nm. AFM images of the polymersomes in dry state are shown in Figure 9.4, the average height in dry state is around 12.4 nm.

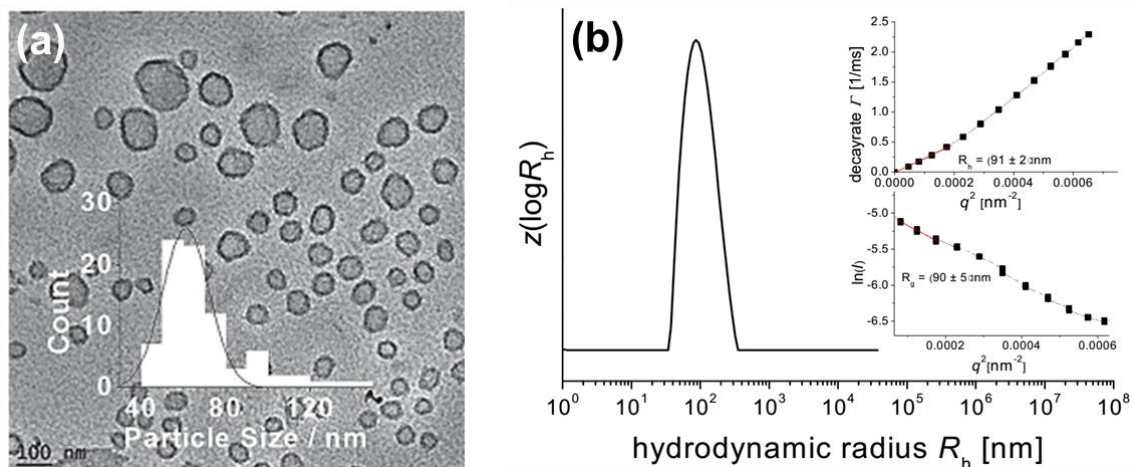


Figure 9.3. (a) Cryo-TEM image of the polymersomes with the particle diameter histogram, (b) Intensity-weighted size distribution as obtained by DLS (CONTIN; 60°;  $\lambda = 633$  nm); insets: extraction of the average hydrodynamic radius  $R_h$  (decay rate  $\Gamma$ , obtained by cumulant analysis, against squared length of scattering vector  $q$ ) and the radius of gyration  $R_g$  (Guinier plot).<sup>155</sup>

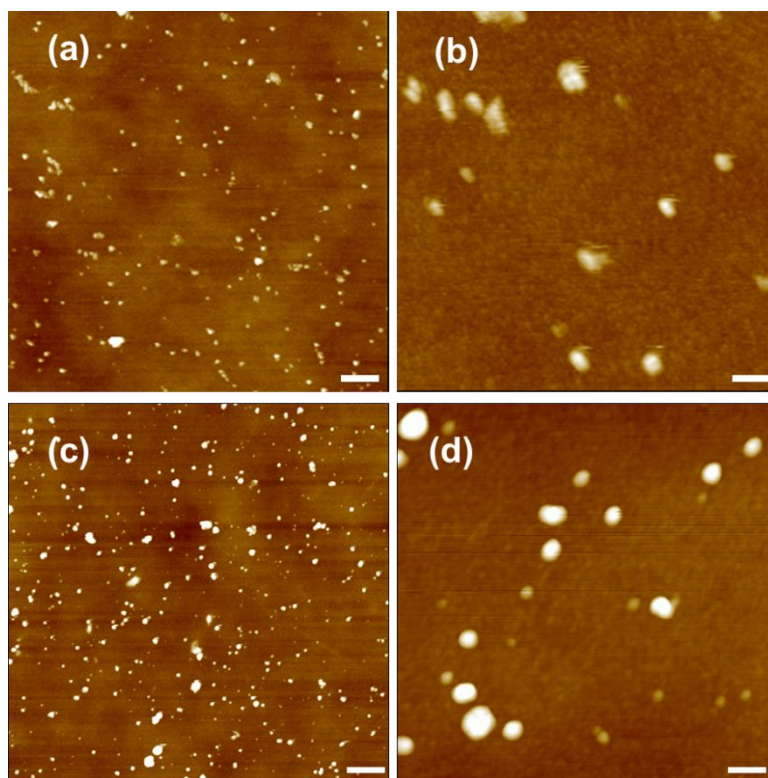


Figure 9.4. AFM images of the polymersomes (a, b), and polymersomes with encapsulated Rhodamine b (c, d) in dry state. Z range is 40 nm, and scale bar is 500 nm (a, c), and 100 nm (b, d).

### 9.3.2 Encapsulation of Rhodamine B Inside the Polymersomes

The polymersomes have a hollow core-shell structure, which enables the incorporation of target molecules inside the core region during their formation. To this purpose, we used rhodamine B as a model molecule, which was added to the solution during the formation of polymersomes, and the excess molecules were removed by dialysis afterwards. The UV-Vis spectra of the polymersomes before and after rhodamine B incorporation are shown in Figure 9.5a, the miktoarm star polymers are rhodamine B labeled during synthesis, so the pristine polymersomes show an absorption peak at 568 nm. After rhodamine B incorporation, the characteristic peak intensity increases significantly, and the peak position blue shifts to 555 nm. The fluorescence spectra of the polymersomes are shown in Figure 9.5b, it can be seen that the pristine polymersomes have a emission peak at 588 nm, and the ones with rhodamine B inside have a peak position of 579 nm, with the intensity increases by 17 times.

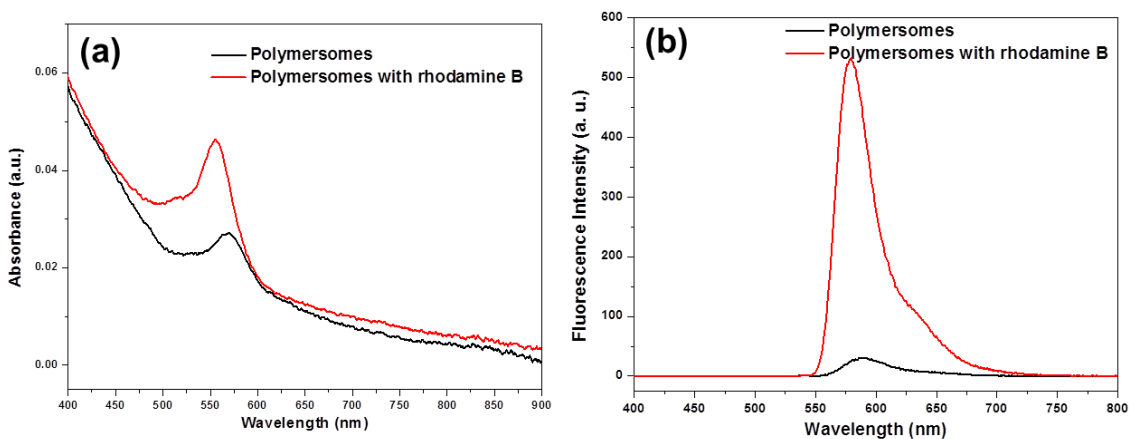


Figure 9.5. UV-Vis (a) and fluorescence (b) spectra of the polymersomes before and after rhodamine B incorporation.

The morphology of the polymersomes before and after rhodamine B incorporation is also studied by AFM (Figure 9.4), average height of the pristine polymersomes in dry state is

12.4 nm, and after rhodamine B incorporation the height increases to 18.2 nm, which is another strong evidence that target molecules can be successfully encapsulated inside the polymersomes during the preparation step.

### 9.3.3 LbL Assembly of Polymersomes and TA

The polymersomes have PEO brushes on the shell, which enables them to interact with another component through hydrogen bonding, thus LbL assembly can be achieved at optimized conditions. In this study, we use tannic acid to interact with the polymersomes to form multilayered structures. The LbL assembly was conducted at planar substrate at first, the increase in thickness of the LbL film with number of bilayers is shown in Figure 9.6a, it can be seen that the thickness growth follows a linear mode, which is indication of the strong interaction between TA and polymersomes.

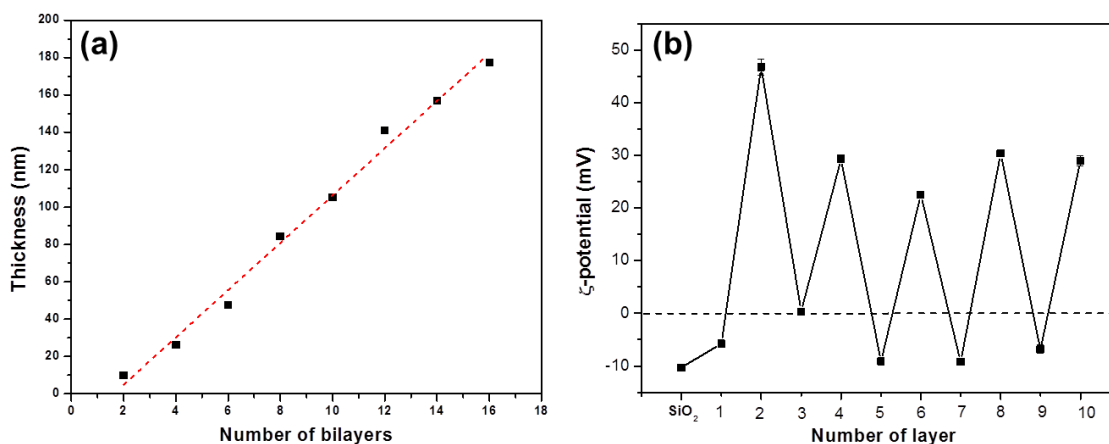


Figure 9.6. (a) Thickness increase with the number of bilayers for (TA/polymersome)<sub>n</sub> LbL thin films, (b)  $\zeta$ -potential as a function of number of layers during LbL assembly on silica microparticles.

The morphology of the (TA/polymersome) LbL film is shown in Figure 9.7a and 9.7b, it can be seen that the film have high roughness with high density of granule structure, the

size of which matches well with individual polymersome. The polymersome loaded multilayer thin films have the potential to be functional multicompartmental coatings.

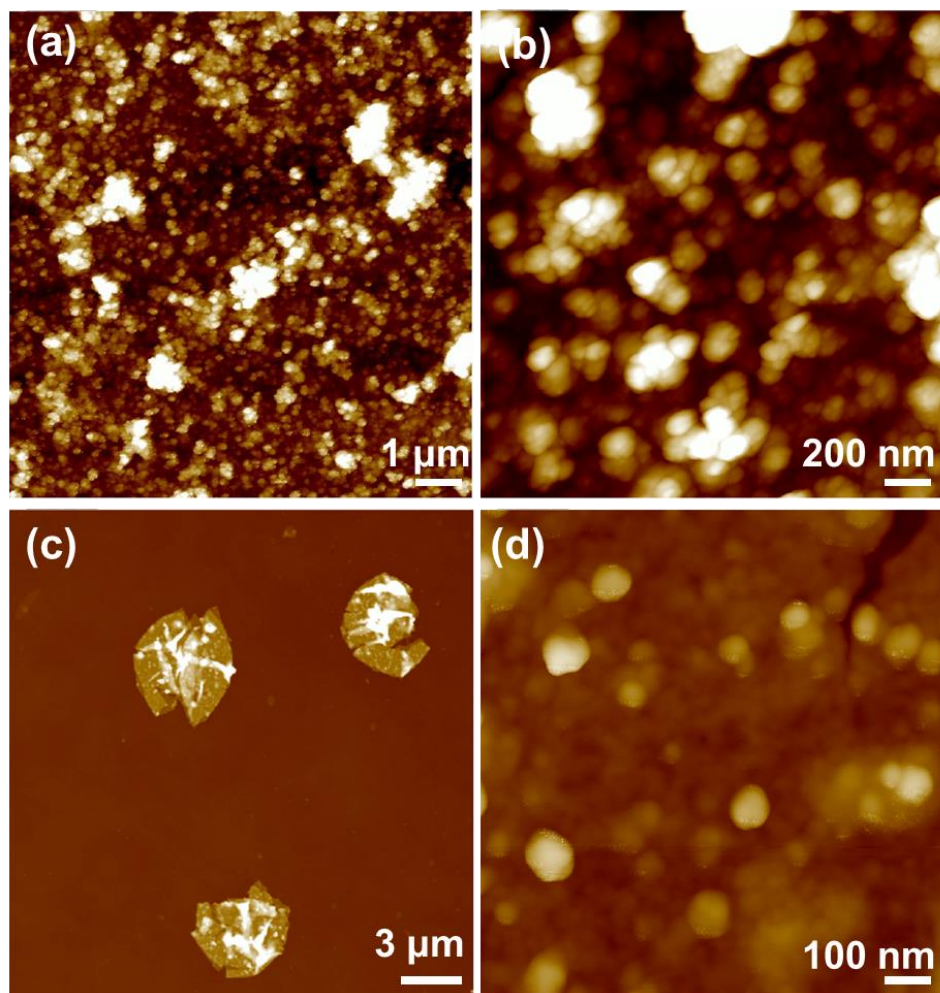


Figure 9.7. AFM images of the (a, b)  $(\text{TA}/\text{polymersome})_{16}$  LbL films, (c, d)  $(\text{TA}/\text{polymersome})_5$  LbL microcapsules. Z range is 300 nm (a, c) and 150 nm (b, d).

#### 9.3.4 $(\text{TA}/\text{polymersome})$ LbL Microcapsules

The LbL assembly of TA and polymersomes can also be conducted on a spherical substrate: silica microparticles, and after dissolving the core, hollow microcapsules can be produced. The LbL assembly process on silica microparticles was monitored by zeta

potential measurements, as shown in Figure 9.6b. The zeta-potential of bare silica microparticles is -10.3 mV at pH 5 condition due to the ionized silanol groups. The  $pK_a$  value of TA is the range of 4.9 to 7.4,<sup>363</sup> therefore, at pH 5 TA is mainly in the protonation form, and when TA is the outmost layer, the microparticles have slightly negative charge ( $< -10.0$  mV). The zeta potential for pristine polymersome is close to zero (+5.5 mV), as expected from the charge compensation between cationic qPDMAEMA and anionic PSS. However, after incorporation of rhodamine B, which is a positively charged molecules inside the polymersomes, they are overall positively charged, the zeta potential is around 30.0 mV when the polymersomes are in the outmost layer.

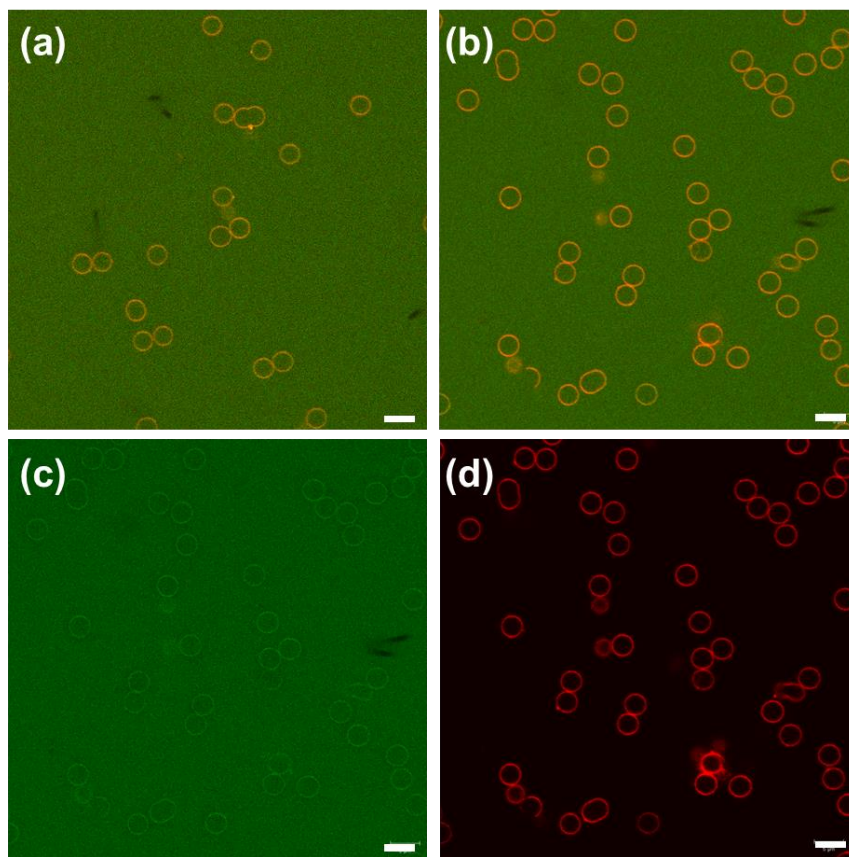


Figure 9.8. CLSM images of the  $(TA/polymersome)_5$  (a) and  $(TA/polymersome)_8$  (b) microcapsules, (c, d) green and red channel of the same sample as in b. Scale bar is 5  $\mu m$ .

The CLSM images of the prepared hollow microcapsules are shown in Figure 9.8, in this study we prepared microcapsules with two different number of layers: 5 and 8. It can be seen that the (TA/polymersome)<sub>n</sub> microcapsules are uniform and robust in solution. The microcapsule suspension is colored by adding FITC, so the background is green, and the microcapsule shell is orangish due to the intrinsic red fluorescence from the rhodamine B molecules on the qPDMAEMA chains and the absorbed green fluorescence FITC molecules on the shell. The separated green and red channels are shown in Figure 9.8c, d, which clearly demonstrates our hypothesis.

The morphology of the (TA/polymersome)<sub>5</sub> microcapsules is shown in AFM images (Figure 9.7c,d), it can be seen that after drying the microcapsules tend to collapse on the substrate with random wrinkles on the surface. Higher magnification AFM image shows that the shell of the microcapsules also has high density of granular structures, which probably corresponds to individual polymersome. The average thickness of the 5 bilayer (TA/polymersome) microcapsules is 23.6 nm, which is obviously lower than that of 5 bilayer thin film (36.8 nm), the main reason is that the polymersomes have higher degree of deformation when absorbed on a curved substrate, and the amount of absorption for each layer is also possibly lower.

### **9.3.5 Response to External Conditions and Multicompartmental Capability**

The main driving force for the interaction between the TA and polymersome layers is hydrogen bonding (between hydroxyl groups on TA and PEO on polymersome shell),

and the protonation and deprotonation equilibrium of TA depends on pH, so that the structure and permeability of the microcapsules are also expected to be pH responsive. The CLSM images of the (TA/polymersome)<sub>6</sub> microcapsules at different pH conditions are shown in Figure 9.9, from which it can be seen that the permeability of the microcapsules strongly depends on pH.

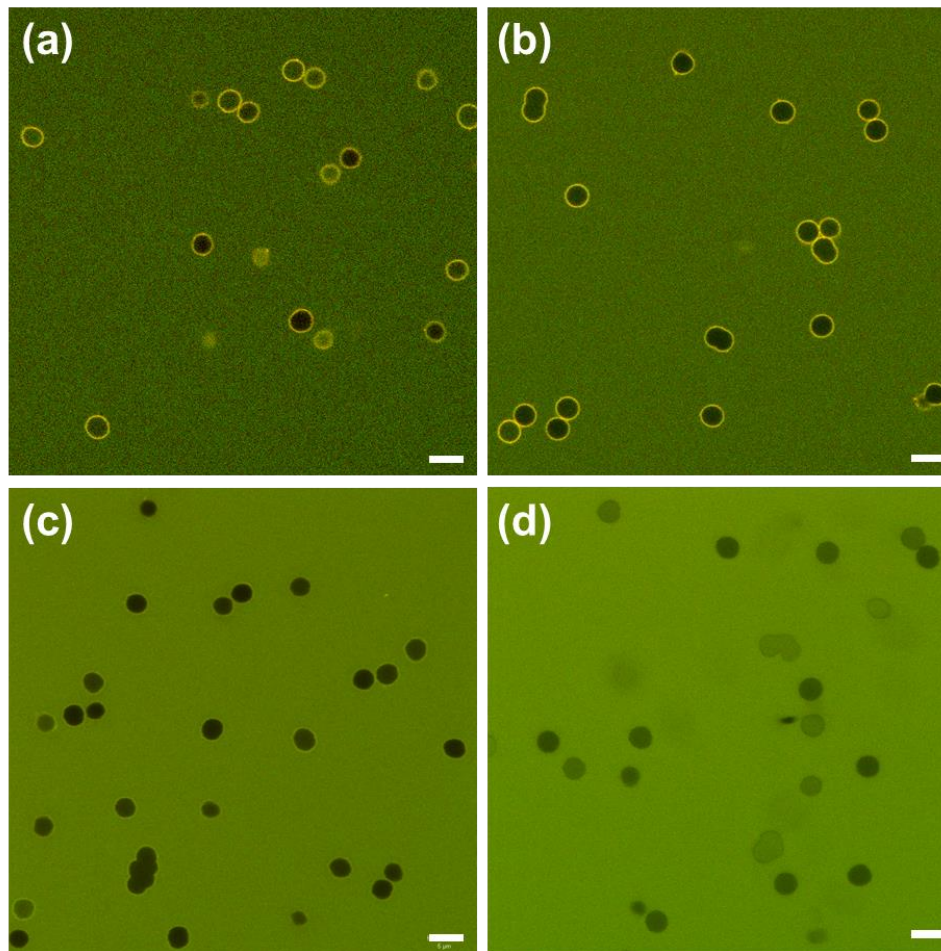


Figure 9.9. Permeability of (TA/polymersome)<sub>5</sub> microcapsules at different pH conditions to 70K FITC-dextran, the scale bar is 5  $\mu\text{m}$ .

To test the permeability of the microcapsules, fluorescein isothiocyanate (FITC) labeled dextran with various molecular weights as fluorescent probes. When the pore size of the microcapsules shell is larger than the size of the fluorescent probe, then the fluorescent

intensity would be almost the same for the interior and exterior of the microcapsules, otherwise the interior would be dark and the background appears bright. At pH 3, the microcapsules are partially permeable to 70 kDa FITC-dextran, and at pH 5 and pH 7, the microcapsules are completely impermeable to the FITC-dextran molecules, or the permeability of the microcapsule decreases. When pH further increases to 9, the microcapsules become partially permeable again, which means the permeability of the microcapsule increases to a higher level.

Table 9.1. Permeability of (TA/polymersome)<sub>5</sub> microcapsules to FITC-dextran with various molecular weights at different pH conditions (“+”: permeable, “-” not permeable, “+/-” partially permeable).

Sample	pH	FITC-dextran 20kDa	FITC-dextran 70kDa	FITC-dextran 150kDa	FITC-dextran 250kDa
(TA/Vesi) <sub>5</sub>	3	+	+/-	-	-
	5	+	-	-	-
	7	+	-	-	-
	9	+	+/-	-	-

As mentioned above, the protonation and deprotonation equilibrium of TA depends on pH, and at low pH (3, for instance) the TA molecules are almost in fully protonated state, the hydrogen bonding between TA and the polymersomes is very strong. When pH increases to between 5 and 7, the percentage of deprotonated hydroxyl groups on TA increases, as a result, the hydrogen bonding between TA and polymersome decreases, leading to a more flexible membrane, and possible defects in the microcapsule shell are filled by the more dynamic chains and molecules. When pH further increases to basic

condition (9, for instance), the hydrogen bonding between TA and polymersome significantly decreases, and some of the microcapsules are partially broken or decomposed, so that FITC-dextran molecules can permeate inside again.

Moreover, the driving force for the formation of polymersome is the electrostatic interaction between anionic PSS and cationic qPDMAEMA chains on the miktoarm stars, and it is well known that ionic strength has significant effect on the electrostatic interaction due to charge screening effect of ions. The ionic condition can be used as another important tool to regulate the structure and permeability of the  $(\text{TA/polymerosome})_n$  microcapsules, which will be within the scope of future work.

On the other hand, the shell of the microcapsules is composed of high density of polymerosomes, and as we demonstrated before, the polymerosomes themselves are able to serve as nanocontainers and nanocarriers, therefore, the  $(\text{TA/polymerosome})_n$  microcapsules have the potential to be multicompartamental carriers with one type of molecules encapsulated in the polymerosomes on the shell, and another type of molecules encapsulated in the hollow core region of the microcapsules.

To this purpose, we first encapsulated rhodamine B molecules inside the polymerosomes, and then used such polymerosomes as components to fabricate LbL microcapsules following the same procedure. The CLSM images of the prepared microcapsules with 5 and 8 bilayers are shown in Figure 9.10. It can be seen that the microcapsules have strong red fluorescence shell, and 8 bilayer shells are clearly more fluorescent than that of 5 bilayer, which are strong evidence that multicompartamental microcapsules with

rhodamine B encapsulated in the shell are successful prepared. The incorporation of another type of target molecules inside the microcapsules as well as the programmable release of the two types of molecules will be the focus of future work.

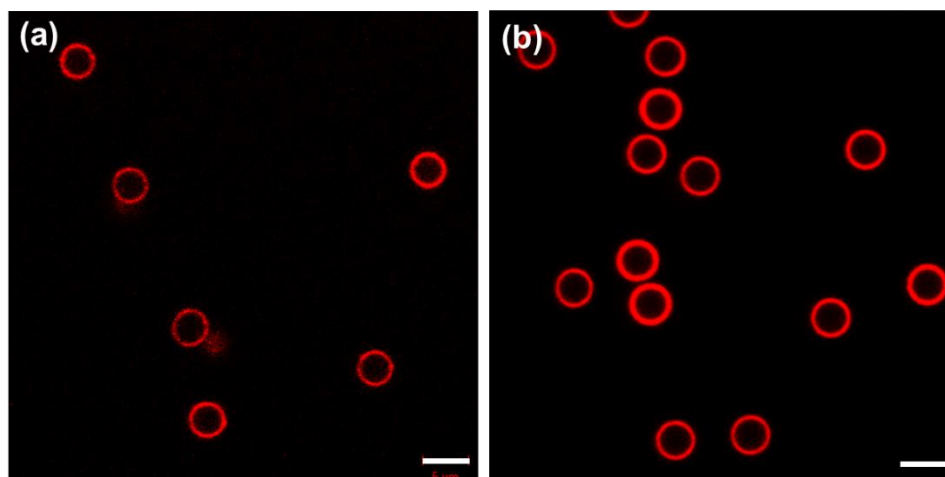


Figure 9.10. CLSM image so the multicompartamental  $(\text{TA}/\text{polymersome})_5$  and  $(\text{TA}/\text{polymersome})_5$  microcapsules with rhodamine B encapsulated within the polymersomes. Scale bar is  $5 \mu\text{m}$ .

#### 9.4 Conclusions

Responsive multicompartamental microcapsules were successfully fabricated with polymersomes as the major component. The polymersomes were prepared by electrostatic interaction driving complexation between a cationic miktoarm star polyelectrolyte and a linear anionic polyelectrolyte. The microcapsules prepared have multicompartamental structure with dual carrier ability, two type of target molecules can be encapsulated inside the polymersome and within the hollow core of the microcapsules, respectively. On the other hand, the structure of the polymersomes with IPEC wall can be disrupted by increasing the ionic strength, the hydrogen bonding between TA and

polymersomes is affected by pH condition. Therefore, the microcapsules are dual responsive to pH and ionic strength, which enables the programmable release of two types of cargo molecules encapsulated inside. The responsive multicompartmental microcapsules can find applications in drug delivery, self-healing materials, smart coatings and microreactors.

## **CHAPTER 10. GENREAL CONCLUSIONS AND BROAD IMPACT**

### **10.1 Summary of Major Results**

In the field of surface and interface assembly of polymers, most previous work focused on conventional linear polymers, while our work focuses on the properties and assembly of branched polymers, especially star-shaped polymers. The results achieved provide complimentary and valuable insight to this filed, especially on the significant role of polymer architecture on their behaviors and the properties of their assembled structures.

For the first time, star-shaped polymers with responsive properties were systematically studied at confined interfaces (air/water and air/solid interfaces). The conformational changes and molecular organization due to complex intra- and inter-molecular interaction between different blocks were investigated by using LB technique and high resolution AFM imaging.

We also successfully demonstrated that star polymers with complex architecture and chemical composition can be assembled into multilayered structures, the compact 3D structure of the star polymers enable them to behave both independently and collectively in the assembled structures. Moreover, the multiple functionalities and hierarchical internal structure of the star polymer based microstructures have significantly improved performance in certain aspects, such as multi-responses to external stimuli and multi-carrier capability, compared with traditional linear polymer based structures.

To be more specific, our studies in solution and interfaces cover a broad range of star polymer architectures, as well as their assemblies at different dimensions and states, such as those summarized below:

**Firstly**, we studied homo-arm star polymers, or star polymers with arms of a single chemical composition, including PDMAEMA and qPDMAEMA star polyelectrolytes, which are weak and strong cationic polyelectrolytes, respectively. PDMAEMA stars are pH and temperature dual responsive, their solution behaviors and LbL assembly are studied. The results showed that their conformational changes and aggregation induced by temperature are significantly different from their linear counterparts. Their responsive properties are well maintained after being assembled into LbL microcapsules, so that the pH and thermo dual responsive microcapsules are successfully demonstrated, especially the pH controlled permeability can be achieved within a very narrow range, which is superior to most previous reports.

The qPDMAEMA star polyelectrolytes have unique response to ionic condition, with the addition of a small amount of multivalent counterions, the stars are effectively collapsed, and can recover to extended chain conformation when the multivalent ions are decomposed by UV irradiation. Based on this unique property, we demonstrated a non-destructive, light initiated way to reversibly control the permeability of microcapsules, which has many advantages over conventional ways to achieve light-responsive properties, such as embedding toxic nanoparticles, or using azobenzene polymers.

**Secondly**, we investigated star block polymers, including triblock and quarterblock star polymers, with arms composed of PS, P2VP-b-PAA block copolymer or P2VP-PAA-g-PNIPAM graft-copolymer arms. These star block polymers are amphiphilic and have intriguing responsive behaviors and assembly at air/water interface. Due to the pH responsiveness of PAA and P2VP, thermo-responsiveness of PNIPAM chains, the conformation and aggregation are strongly depend on the spatial distribution of the arms and intramolecular interactions between different blocks, which can be controlled by the external conditions, including pH, temperature, ionic strength and surface pressure. The combination of chemical confinement (by covalently linking different blocks into a single core) and physical confinement (air/water interface with controlled intermolecular spacing) enables the precise control of interactions between polymer chains with different properties, and elucidation of the role of each blocks in the overall structure of complex polymers.

Based upon the chemical inhomogeneity and core-shell structure of the star block polymers, we suggest that they can serve as nanocarriers for hydrophobic molecules in the core region. After assembling them in a LbL fashion, the microcapsules have hierarchical and multicompartmental structure, which allow the encapsulation and release of multiple molecules simultaneously.

**Lastly**, miktoarm star polymers with one PEO arm and several polyelectrolyte arms were studied in terms of their ability to form novel nanostructures. By mixing the cationic miktoarm star polyelectrolyte and a linear anionic polyelectrolyte, polymersomes with

interpolyelectrolyte complex wall and PEO corona can be successfully prepared *via* electrostatic interaction. The polymersomes are further used as major component to build multicompartmental microcapsules with dual carrier ability. Moreover, pH and ionic strength can be used to induce the programmable release of two types of cargo molecules independently. The asymmetric structure of miktoarm star polymers plays a significant role in their complexation with linear polymers, such complexation is usually not possible for symmetric star polymer with large number of arms.

From a different perspective, the work presented in this dissertation can also be summarized based on the molecular assembly at different dimensions and states, as described below:

**Firstly**, at the solution state, we used SANS to demonstrate that the unique star architecture enables star polyelectrolytes to have non-uniform, micelle-like structure when they are partially charged. For star polyelectrolytes with temperature responsive properties, their aggregation or phase separation upon changes in temperature can be dramatically different from that of linear polyelectrolytes due to the spatial confinement of the arm chains.

Upon increasing the temperature, the PDMAEMA star polyelectrolytes first experience a dramatic contraction in the loose shell region while the core size remains almost unchanged, and then start to form intermolecular aggregates within narrow temperature range, while linear PDMAEMA polyelectrolytes show conventional macrophase

separation with increasing temperature under the same conditions. This result provides deep insight to the effect of polymer architecture on their phase behavior and responsive properties, and gives strong support to some recent simulation and theoretical studies on branched polyelectrolytes.<sup>367</sup>

**Secondly**, for 2D assembly, we studied the detailed conformational changes and responsive properties of amphiphilic star polymers at air/water interface in a molecular level by using Langmuir-Blodgett technique. As we observed, the surface active star polymers usually show 2D or quasi-3D structure at the air/water interface and after transferring to solid surfaces, with local rearrangement of the arm chains upon external condition changes including compression and expansion, which is usually more stable and have more diverse structures at air/water interface than linear amphiphiles.

Moreover, the amphiphilic star block polymers have complex structure and multiple responsive properties, for instance, pH responsive PAA and P2VP blocks, thermo-responsive PNIPAM blocks. As a result, their conformation and aggregation are strongly depend on the intramolecular interactions between different blocks and spatial distribution of the arms, which can be controlled by the external conditions, including pH, temperature, ionic strength and surface pressure.

On the other hand, the behavior of the polymers at air/water interface is quite different than those in bulk solution state in some cases. For instance, the PNIPAM chains have a hydrophilic to hydrophobic transition upon increasing temperature, the chains tend to go

from water subphase to air/water interface, resulting in an increase in molecular size at the interface, rather than conventional coil to globule transition in aqueous solution.

The study of branched polymers assembly at air/water interface has broad impact in several areas. For instance, it serves as a model system to study the adsorption of polymers on a solid substrate, which is an important process for many applications such as surface coating, tribology and biofouling. Moreover, the uniform ultrathin monolayer deposited from air/water interface is in analogy to self-assembled monolayers and polymer brushes, expect that the anchoring force to the substrate is usually physical interaction such as electrostatic attraction rather than covalent linking. The branched polymer monolayer can find applications in lithography, sensing and microfluidics.

**Thirdly**, for 3D assembly by using LbL technique, we successfully demonstrated that star polymers can be used as the main component to fabricate multilayered microstructures such as microcapsules. Due to the abundant functional groups as well as the multi-responsive properties, star polymer based microcapsules are more robust and have more complex stimuli-responsive behaviors than conventional microcapsules.

As we found, for the robust microcapsules based on PDMAEMA star polyelectrolytes, they are multi-responsive to pH, temperature and ionic strength. For instance, with increasing pH, the permeability of microcapsules decreases, and the transition from “open” to “close” state for target molecules can be achieved within a narrow pH range (from pH 7 to 8), which has not been achieved in most previous reports. On the other

hand, the overall size and permeability of the (PSS/PDMAEMA<sub>18</sub>) microcapsules decrease with increasing temperature, thus allowing reversibly loading and unloading the microcapsules with high efficiency.

In another example, a non-destructive way to achieve remote, reversible, light-controlled tunable permeability of ultrathin shell microcapsule is demonstrated in our study. The microcapsules are based on LbL assembly of qPDMAEMA star polyelectrolyte, and their permeability can be dramatically altered by photo-induced transformation of the trivalent counterions into a mixture of mono- and divalent ions by UV irradiation. The reversible contraction of qPDMAEMA star polyelectrolyte arms and the compaction of star polyelectrolytes in the presence of multivalent counterions are considered to be the main reason for the tunable permeability.

The conformational changes and organization of star polyelectrolytes within confined multilayer structure are the main driving forces for the responsiveness to external stimuli. The magnitude of changes in permeability for the star polyelectrolytes based microcapsules are usually much larger than conventional ones based on linear polymers, which enables encapsulation and release with higher efficiency. The multi-responsive microcapsules represent a novel category of smart microstructures as compared to traditional microcapsules with “one-dimensional” response to a single stimulus, and they also have the potential to mimic the complex responsive microstructures found in nature.

The characteristic porous morphology of the thin shell microcapsules based on star polymers was investigated by SANS, which gives direct and high resolution information of the porous LbL shell, in complementary to indirect measurements such as permeability test. For instance, with the increase of shell thickness, the microcapsules undergo a change of fractal dimension: the thinner shell has a surface fractal structure with rough interface, while the thicker shell generally has a mass fractal structure of 3D random network. The correlation length in the porous shell, which is directly related to the mesh size, also changes concurrently with variations of surrounding environment (pH, temperature, or ionic condition). The results from SANS measurements match well with other characterization techniques such as AFM and permeability test, which strongly supports our proposed mechanism for structural changes of the microcapsules at different conditions.

**Finally**, multicompartamental 3D microstructures can be fabricated based on star polymers and their assembled structures, because the star polymers themselves can act as nanocontainers for target molecules. Therefore, multiple stages and programmable encapsulation and release of target molecules can be achieved, which is an important development in the field of controlled release.

In the first example, star-graft quarterpolymers  $PS_n[P2VP-b-(PAA-g-PNIPAM)]_n$  with a core-shell structure act as nanocarriers to encapsulate hydrophobic molecules in their core region. The SG polymers were further assembled into LbL microcapsules, due to the pH dependent conformation and size of the stars at different pH conditions, as well as

the thermal-responsive PNIPAM shell, the structure and permeability of the microcapsules can be tuned by pH and temperature, so that a programmable and sequential release of hydrophobic and hydrophilic molecules is successfully achieved.

In the second example, taking advantage of the electrostatic interaction between a cationic miktoarm star polyelectrolyte and a linear anionic polyelectrolyte, robust polymersomes with interpolyelectrolyte complex wall and PEO brushes can be prepared. The polymersomes are used as the main component to fabricate microcapsules with tannic acid (TA) *via* hydrogen bonding using LbL assembly. The multicompartamental microcapsules have the capability to encapsulate and deliver two different types of target molecules simultaneously: one type of molecules can be encapsulated inside the polymersomes, and another type of molecules can be encapsulated in the hollow core region of the microcapsules. The hydrogen bonding between TA and polymersomes can be affected by pH, and the structure of the polymersomes themselves strongly depends on ionic strength, therefore, a combination of pH and ionic condition changes enable us to achieve controllable and programmable release of two different types of encapsulated molecules in a step-wise fashion.

The directed stepwise assembly of complex star polymers in a fine controlled way to fabricate responsive and functional microstructures is a critical step for their materials science development, and greatly expands the potential applications of star polymers. It also provides new perspective to the structure-property study and assembly of biomacromolecules, since many biomacromolecules such as polysaccharides and

polypeptide can also have branched architecture, which is important for their biological functions.

## **10.2 Proposed Future Work and Applications**

We propose several suggestions in terms of future directions for this field, as described below:

The branched polymer can be co-assembled with inorganic component, such as nanoparticles, or atomically thin 2D materials such as graphene, to fabricate functional nanocomposites. Because the low extent of entanglement and aggregation of branched polymers, they are expected to be able to form better ordered composite structures with inorganic materials.

On the other hand, the branched polymers can be used as nanoreactors, controlled and programmable reactions are possible based on their assembled structures. For instance, multicompartmental microcapsules can be fabricated based on branched polymers, with enzyme molecules encapsulated inside the branched polymers on the shell, and biological molecules encapsulated within the microcapsules. Upon release of the enzyme, corresponding biological reactions can happen within the microcapsules.

Moreover, in our work, we successfully demonstrated the programmable encapsulate and release of two different types of cargo molecules based on multicompartmental microcapsules as a proof of concept. It can be further extended to multistage (more than

two) encapsulation and delivery of cargo molecules, which is very important for some biomedical applications.

The branched polymers are essentially 3D soft nanoparticles, so amphiphilic branched polymers can be used to stabilize Pickering emulsion, and most previous research on Pickering emulsion is focused on solid inorganic and organic nanoparticles. Moreover, since the amphiphilic star block copolymers have stimuli-responsive properties, the responsive Pickering emulsion based on them can be particularly useful in oil recovery, catalyst recovery and cosmetics.

Finally, in recent years an emerging novel class of polyelectrolytes, so-called poly(ionic liquid)s, have attracted much attention. These macromolecules are usually synthesized by the polymerization of common ionic liquids.<sup>368</sup> Poly(ionic liquid)s combine unique properties of monomeric ionic liquids with properties of macromolecules, they are very attractive for a variety of applications including as ion-conductive media for solar cells and photoluminescent devices,<sup>369</sup> as building blocks for biomaterials, chemical nanocatalysts,<sup>370</sup> nanoreactors,<sup>371</sup> and antifouling agents, and many other uses.<sup>372,373</sup> The same principle and assembly techniques demonstrated in this work can be readily used to fabricate functional structures from poly(ionic liquid)s.

The work presented in this dissertation has been summarized in the following major publications:

[1] **Xu, W.**; Ledin, P. A.; Shevchenko, V. V.; Tsukruk, V. V. Architecture, Assembly, and Emerging Applications of Branched Functional Polyelectrolytes and Poly(ionic liquids). *ACS Appl. Mater. Interfaces* **2015**, *7*, 12570-12596.

[2] **Xu, W.**; Malak, S. T.; Plamper, F. A.; Synatschke, C. V.; Müller, A. H.; Melnichenko, Y. B.; Heller, W. T.; Tsukruk, V. V. Structural Study of Star Polyelectrolytes and Their Porous Multilayer Assembly in Solution. In *Physics of Liquid Matter: Modern Problems*, Springer Proceedings in Physics, **2015**, 299-315.

[3] **Xu, W.**; Ledin, P. A.; Iatridi, Z.; Tsitsilianis, C.; Tsukruk, V. V. Multi-Responsive Star-Graft Quarterpolymer Monolayers. *Macromolecules* **2015**, *48*, 3344-3353.

[4] **Xu, W.**; Ledin, P. A.; Plamper, F. A.; Synatschke, C. V.; Müller, A. H.; Tsukruk, V. V. Multiresponsive Microcapsules Based on Multilayer Assembly of Star Polyelectrolytes. *Macromolecules* **2014**, *47*, 7858-7868.

[5] **Xu, W.**; Choi, I.; Plamper, F. A.; Synatschke, C. V.; Müller, A. H.; Melnichenko, Y. B.; Tsukruk, V. V. Thermo-Induced Limited Aggregation of Responsive Star Polyelectrolytes. *Macromolecules* **2014**, *47*, 2112-2121.

[6] **Xu, W.**; Choi, I.; Plamper, F. A.; Synatschke, C. V.; Müller, A. H.; Tsukruk, V. V. Nondestructive Light-Initiated Tuning of Layer -by-Layer Microcapsule Permeability. *ACS Nano* **2013**, *7*, 598-613.

[7] Choi, I.; Malak, S. T.; **Xu, W.**; Heller, W. T.; Tsitsilianis, C.; Tsukruk, V. V. Multicompartmental Microcapsules from Star Copolymer Micelles. *Macromolecules* **2013**, *46*, 1425-1436.

The following publications are related to the work in this dissertation:

[8] Ledin, P. A.; **Xu, W.**; Friscourt, F.; Boons, G.; Tsukruk, V. V. Branched Polyhedral Oligomeric Silsesquioxane Nanoparticles Prepared via Strain-Promoted 1,3-Dipolar Cycloadditions. *Langmuir*. **2015**, *31*, 8146-8155.

[9] Steinschulte, A. A.; **Xu, W.**; Draber, F.; Hebbeker, P.; Jung, A.; Bogdanovski, D.; Schneider, S.; Tsukruk, V. V.; Plamper, F. A. Interface-Enforced Complexation between Copolymer Blocks. *Soft Matter* **2015**, *11*, 3559-3565.

[10] Ledin, P. A.; Tkachenko, I. M.; **Xu, W.**; Choi, I.; Shevchenko, V. V.; Tsukruk, V. V. Star-Shaped Molecules with Polyhedral Oligomeric Silsesquioxane Core and Azobenzene Dye Arms. *Langmuir* **2014**, *30*, 8856-8865.

[11] Choi, I.; Kulkarni, D. D.; **Xu, W.**; Tsitsilianis, C.; Tsukruk, V. V. Star Polymer Unimicelles on Graphene Oxide Flakes. *Langmuir* **2013**, *29*, 9761-9769.

### Conference presentations related to this dissertation:

- [1] Assembly of Branched Polymers into Responsive 2D and 3D Microstructures. *251th National ACS Meeting*, San Diego, CA, Spring 2016 (*Submitted*). **Nominated to Excellence in Graduate Polymer Research Symposium.**
- [2] Multi-Compartmental Microcapsules with Dual Carrier and Programmable Release Capabilities. *251th National ACS Meeting*, San Diego, CA, Spring 2016 (*Submitted*).
- [3] Responsive Star Polymers at Surfaces and Interfaces. Institute of Physical Chemistry, RWTH Aachen University, Aachen, Germany. May 2015 (Oral).
- [4] Interfacial Behavior and Assembly of Multi-Responsive Star Graft Copolymers. *249th National ACS Meeting*, Denver, CO, Spring 2015 (Oral).
- [5] SANS Study on the Phase Behaviors of Responsive Star Polyelectrolytes. *249th National ACS Meeting*, Denver, CO, Spring 2015 (Oral).
- [6] Star Polyelectrolytes Based Microcapsules with Multi-Responsiveness to Ionic Strength, pH and Temperature. *249th National ACS Meeting*, Denver, CO, Spring 2015 (Oral).
- [7] Molecular structure and assembly of responsive star polyelectrolytes studied by SANS. Structure and Dynamics of Confined and Interfacial Fluids Workshop, ORNL, July 2014. (Oral)
- [8] Nondestructive Light-Initiated Tuning of Layer -by-Layer Microcapsule Permeability. *246th National ACS Meeting*, Indianapolis, IN, Fall 2013. **Selected as a finalist for AkzoNobel Student Award in Applied Polymer Science.**
- [9] Multicompartmental Microcapsules from Star Copolymer Micelles. *246th National ACS Meeting*, Indianapolis, IN, Fall 2013 (Oral).
- [10] Layer-by-Layer Microcapsule Permeability Tuning by a Nondestructive Light-Initiated Method. *Layer-by-Layer Assemblies: Science and Technology*, Hoboken, NJ, June 2014 (Poster).
- [11] pH- and temperature- dual responsive LbL microcapsules based on star polyelectrolytes. *Layer-by-Layer Assemblies: Science and Technology*, Hoboken, NJ, June 2014 (Poster).
- [12] Unimolecular Star Copolymer Micelles based multilayer microcapsules. *Layer-by-Layer Assemblies: Science and Technology*, Hoboken, NJ, June 2014 (Poster).
- [13] Star-Shaped Molecules with Polyhedral Oligomeric Silsesquioxane Core. *1st Annual GTPN Poster Competition*, Georgia Tech, Nov. 2014 (Poster).
- [14] Nondestructive Light-Initiated Tuning of Layer-by-Layer Microcapsule Permeability. *Georgia Tech Research & Innovation Conference*, Atlanta, GA, Feb. 2013 (Poster).

## REFERENCES

- 
- [1] Newkome, G. R.; Moorefield, C. N.; Vogtle, F., *Dendritic Molecules*, VCH Verlagsgesellschaft mbH.: Weinheim; New York; Basel; Cambridge; Tokyo. **1996**.
- [2] Hay, G.; MacKay, M. E.; Hawker, C. J. *J. Polym. Sci.* **2001**, *39*, 1766-1777.
- [3] Zhao, J.; Swinnen, A.; Assche, G. V.; Mancha, J.; Vanderzande, D.; Van Mele, B. *J. Phys. Chem. B* **2009**, *113*, 1587-1591.
- [4] Savenije, T. J.; Kroeze, J. E.; Yang, X.; Loos, J. *Thin Solid Films* **2006**, *2*, 511-512.
- [5] Jing, C.; Xu, X.; Zhang, X.; Liu, Z.; Chu, J. *J. Phys. D: Appl. Phys.* **2009**, *42*, 075402.
- [6] Percec, V.; Ahn, C. -H.; Ungar, G.; Yeardley, D. J. P.; Möller, M.; Sheiko, S. S. *Nature* **1998**, *391*, 161-64.
- [7] Khanna, K.; Varshney, S.; Kakkar, A. *Polym. Chem.* **2010**, *1*, 1171-1185.
- [8] Dobrynin, A. V.; Rubinstein, M. *Prog. Polym. Sci.* **2005**, *30*, 1049-1118.
- [9] Colby, R. H. *Rheol. Acta* **2010**, *49*, 425-442.
- [10]. Wignall, G. D.; Melnichenko, Y. B. *Rep. Prog. Phys.* **2005**, *68*, 1761-1810.
- [11] Szilagy, I.; Trefalt, G.; Tiraferri, A.; Maroni, P.; Borkovec, M. *Soft Matter* **2014**, *10*, 2479-2502.
- [12] Iatridi, Z.; Tsitsilianis, C. *Polymers* **2011**, *3*, 1911-1933.
- [13] Zhou, Y.; Huang, W.; Liu, J.; Zhu, X.; Yan, D. *Adv. Mater.* **2010**, *22*, 4567-4590.
- [14] Mintzer, M. A.; Grinstaff, M. W. *Chem. Soc. Rev.* **2011**, *40*, 173-190.
- [15] Walter, M. V.; Malkoch, M. *Chem. Soc. Rev.* **2012**, *41*, 4593-4609.
- [16] Rosen, B.; Wilson, C.; Wilson, D.; Peterca, M.; Imam, M.; Percec, V. *Chem. Rev.* **2009**, *109*, 6275-6540.
- [17] Lin, X.; He, Q.; Li, J. *Chem. Soc. Rev.* **2012**, *41*, 3584-3593.
- [18] Khandare, J.; Calderón, M.; Dagia, N. M.; Haag, R. *Chem. Soc. Rev.* **2012**, *41*, 2824-2848.
- [19] Zhou, Y.; Huang, W.; Liu, J.; Zhu, X.; Yan, D. *Adv. Mater.* **2010**, *22*, 4567-4590.
- [20] Plamper, F. A.; Reinicke, S.; Elomaa, M.; Schmalz, H.; Tenhu, H. *Macromolecules* **2010**, *43*, 2190-2203.
- [21] Peleshanko, S.; Tsukruk, V. V. *Prog. Polym. Sci.* **2008**, *33*, 523-580.
- [22] Jaeger, W.; Bohrisch, J.; Laschewsky, A. *Prog. Pol. Sci.* **2010**, *35*, 511-577.
- [23] Pergushov, D. V.; Babin, I. A.; Zezin, A. B.; Muller, A. H. E. *Polym. Int.* **2013**, *62*, 13-21.
- [24] Peleshanko, S.; Tsukruk, V. V. *J. Polym. Sci., Part B: Polym. Phys.* **2012**, *50*, 83-100.
- [25] Roovers, J. In *Encyclopedia of Polymer Science and Engineering*; Kroschwitz, J. I., Ed.; Wiley-Interscience: New York, 1985; Vol. 2, pp 478-499.
- [26] Mishra, M. K.; Kobayashi, S. Eds. *Star and Hyperbranched Polymers*; Marcel Dekker: New York, 1999; Vol. 53.

- 
- [27] Khokhlov, A. R.; Starodubtzev, S. G.; Vasilevskaya, V. V. Conformational Transitions in Polymer Gels: Theory and Experiment. In *Responsive Gels: Volume Transitions I*; Dušek, K. Ed.; Springer Berlin Heidelberg, 1993, 123-171.
- [28] Sheiko, S. S.; Prokhorova, S. A.; Beers, K. L.; Matyjaszewski, K.; Potemkin, I. I.; Khokhlov, A. R.; Möller, M. *Macromolecules* **2001**, *34*, 8354-8360.
- [29] Borisov, O. V.; Polotsky, A. A.; Rud, O. V.; Zhulina, E. B.; Leermakers, F. A. M.; Birshtein, T. M. *Soft matter* **2014**, *10*, 2093-2101.
- [30] Birshtein, T. M.; Zhulina, E. B. *Polymer* **1984**, *25*, 1453-1461.
- [31] Boudou, T.; Crouzier, T.; Ren, K.; Blin, G.; Picart, C. *Adv. Mater.* **2010**, *22*, 441-467.
- [32] Borue, V. Y.; Erukhimovich, I. Y. *Macromolecules* **1988**, *21*, 3240-3249.
- [33] Bokias, G.; Vasilevskaya, V. V.; Iliopoulos, I.; Hourdet, D.; Khokhlov, A. R. *Macromolecules* **2000**, *33*, 9757-9763.
- [34] Verso, F. L.; Likos, C. N.; Reatto, L. *Prog. Colloid Polym. Sci.* **2006**, *133*, 78-87.
- [35] Mei, Y.; Lauterbach, K.; Hoffmann, M.; Borisov, O. V.; Ballauff, M.; Jusufi, A. *Phys. Rev. Lett.* **2006**, *97*, 158301-158304.
- [36] Plamper, F. A.; Walther, A.; Müller, A. H.; Ballauff, M. *Nano Lett.* **2007**, *7*, 167-171.
- [37] Borisov, O. V.; Zhulina, E. B.; Leermakers, F. A. M.; Ballauff, M.; Müller, A. H. E. *Adv. Polym. Sci.* **2011**, *241*, 1-55.
- [38] Košovan, P.; Kuldová, J.; Limpouchová, Z.; Procházka, K.; Zhulina, E. B.; Borisov, O. V. *Soft Matter* **2010**, *6*, 1872-1874.
- [39] Ballauff, M.; Likos, C. N. *Angew. Chem. Int. Ed.* **2004**, *43*, 2998-3020.
- [40] Ramzi, A.; Scherrenberg, R.; Joosten, J.; Lemstra, P.; Mortensen, K. *Macromolecules* **2002**, *35*, 827-833.
- [41] Blaak, R.; Likos, C. N. *J. Phys.: Condens. Matter* **2012**, *24*, 322101.
- [42] Lee, H.; Larson, R. G. *Molecules* **2009**, *14*, 423-438.
- [43] Dobrynin, A. V. *Curr. Opin. Colloid Interface Sci.* **2008**, *13*, 376-388.
- [44] Borkovec, M.; Papastavrou, G. *Curr. Opin. Colloid Interface Sci.* **2008**, *13*, 429-437.
- [45] Abu-Lail, N. I.; Camesano, T. A. *Biomacromolecules* **2003**, *4*, 1000-1012.
- [46] Jessel, N.; Oulad-Abdelghani, M.; Meyer, F.; Lavalle, P.; Haikel, Y.; Schaaf, P.; Voegel, J. C. *Proc. Natl. Acad. Sci. U.S.A.* **2006**, *103*, 8618-8621.
- [47] Genson, K. L.; Hoffman, J.; Teng, J.; Zubarev, E. R.; Vaknin, D.; Tsukruk, V. V. *Langmuir* **2004**, *20*, 9044-9052.
- [48] Luzinov, I.; Minko, S.; Tsukruk, V. V. *Prog. Polym. Sci.* **2004**, *29*, 635-698.
- [49] Holzmüller, J.; Genson, K. L.; Park, Y.; Yoo, Y.-S.; Park, M.-H.; Lee, M.; Tsukruk, V. V. *Langmuir* **2005**, *21*, 6392-6398.
- [50] Borges, J.; Mano, J. F. *Chem. Rev.* **2014**, *114*, 8883-8942.
- [51] Boehm, I.; Ritter, H. *Macromol. Chem. Phys.* **2011**, *212*, 1080-1085.
- [52] Choi, I.; Suntivich, R.; Plamper, F. A.; Synatschke, C. V.; Müller, A. H. E.; Tsukruk, V. V. *J. Am. Chem. Soc.* **2011**, *133*, 9592-9606.

- 
- [53] Koper, G. J.; Borkovec, M. *Polymer* **2010**, *51*, 5649-5662.
- [54] Ariga, K.; Ji, Q.; Mori, T.; Naito, M.; Yamauchi, Y.; Abe, H.; Hill, J. P. *Chem. Soc. Rev.* **2013**, *42*, 6322-6345.
- [55] Ariga, K.; Yamauchi, Y.; Rydzek, G.; Ji, Q.; Yonamine, Y.; Wu, K. C. W.; Hill, J. P. *Chem. Lett.* **2014**, *43*, 36-68.
- [56] Ariga, K.; Kawakami, K.; Ebara, M.; Kotsuchibashi, Y.; Ji, Q.; Hill, J. P. *New J. Chem.* **2014**, *38*, 5149-5163.
- [57] Yu, T.; Wang, W.; Chen, J.; Zeng, Y.; Li, Y.; Yang, G.; Li, Y. *J. Phys. Chem. C* **2012**, *116*, 10516-10521.
- [58] Xu, Y.; Plamper, F.; Ballauff, M.; Müller, A. H. Polyelectrolyte Stars and Cylindrical Brushes. In *Complex Macromolecular Systems II*; Springer Berlin Heidelberg, 2010; pp 1-38.
- [59] Verduzco, R.; Li, X.; Pesek, S. L.; Stein, G. E. *Chem. Soc. Rev.* **2015**, *44*, 2405-2420.
- [60] Li, Z.; Ma, J.; Cheng, C.; Zhang, K.; Wooley, K. L. *Macromolecules* **2010**, *43*, 1182-1184.
- [61] Li, Z.; Ma, J.; Lee, N. S.; Wooley, K. L. *J. Am. Chem. Soc.* **2011**, *133*, 1228-1231.
- [62] Khelfallah, N.; Gunari, N.; Fischer, K.; Gkogkas, G.; Hadjichristidis, N.; Schmidt, M. *Macromol. Rapid Commun.* **2005**, *26*, 1693-1697.
- [63] Zheng, Z.; Daniel, A.; Yu, W.; Weber, B.; Ling, J.; Müller, A. H. E. *Chem. Mater.* **2013**, *25*, 4585-4594.
- [64] Larin, S. V.; Pergushov, D. V.; Xu, Y.; Darinskii, A. A.; Zezin, A. B.; Müller, A. H.; Borisov, O. V. *Soft Matter* **2009**, *5*, 4938-4943.
- [65] Shovskiy, A.; Varga, I.; Makuška, R.; Claesson, P. M. *Langmuir* **2012**, *28*, 6618-6631.
- [66] Sheiko, S. S.; Sumerlin, B. S.; Matyjaszewski, K. *Prog. Polym. Sci.* **2008**, *33*, 759-785.
- [67] Raguzin, I.; Stoychev, G.; Stamm, M.; Ionov, L. *Soft Matter* **2013**, *9*, 359-364.
- [68] Xu, Y.; Borisov, O. V.; Ballauff, M.; Müller, A. H. *Langmuir* **2010**, *26*, 6919-6926.
- [69] Störkle, D.; Duschner, S.; Heimann, N.; Maskos, M.; Schmidt, M. *Macromolecules* **2007**, *40*, 7998-8006.
- [70] Ruthard, C.; Maskos, M.; Kolb, U.; Gröhn, F. *Macromolecules* **2009**, *42*, 830-840.
- [71] Ruthard, C.; Maskos, M.; Yildiz, H.; Gröhn, F. *Macromol. Rapid Commun.* **2011**, *32*, 523-527.
- [72] Gunari, N.; Cong, Y.; Zhang, B.; Fischer, K.; Janshoff, A.; Schmidt, M. *Macromol. Rapid Commun.* **2008**, *29*, 821-825.
- [73] Cong, Y.; Gunari, N.; Zhang, B.; Janshoff, A.; Schmidt, M. *Langmuir* **2009**, *25*, 6392-6397.
- [74] Gao, H. *Macromol. Rapid Commun.* **2012**, *33*, 722-734.
- [75] Julthongpiput, D.; Lin, Y. Teng, J.; Zubarev, E. R.; Vladimir, V. V. *J. Am. Chem. Soc.* **2003**, *125*, 15912-15921.

- 
- [76] Gorodyska, G.; Kiriya, A.; Minko, S.; Tsitsilianis, C.; Stamm, M. *Nano Lett.* **2003**, *3*, 365-368.
- [77] Peleshanko, S.; Gunawidjaja, R.; Jeong, J.; Shevchenko, V. V.; Tsukruk, V. V. *Langmuir* **2004**, *20*, 9423-9427.
- [78] Genson, K. L.; Hoffman, J.; Teng, J.; Zubarev, E. R.; Vaknin, D.; Tsukruk, V. V. *Langmuir* **2004**, *20*, 9044-9052.
- [79] Gunawidjaja, R.; Peleshanko, S.; Tsukruk, V. V. *Macromolecules* **2005**, *38*, 8765-8774.
- [80] Hu, H.; Liu, G. *Macromolecules* **2014**, *47*, 5096-5103.
- [81] Vamvakaki, M.; Patrickios, C. S.; Lindner, P.; Gradzielski, M. *Langmuir* **2007**, *23*, 10433-10437.
- [82] Iatridi, Z.; Tsitsilianis, C. *Chem. Comm.* **2011**, *47*, 5560-5562.
- [83] Iatridi, Z.; Tsitsilianis, C. *Soft Matter* **2013**, *9*, 185-193.
- [84] Choi, I.; Gunawidjaja, R.; Suntivich, R.; Tsitsilianis, C.; Tsukruk, V. V. *Macromolecules* **2010**, *43*, 6818-6828.
- [85] Choi, I.; Kulkarni, D. D.; Xu, W.; Tsitsilianis, C.; Tsukruk, V. V. *Langmuir* **2013**, *29*, 9761-9769.
- [86] Kodiyath, R.; Choi, I.; Patterson, B.; Tsitsilianis, C.; Tsukruk, V. V. *Polymer* **2013**, *54*, 1150-1159.
- [87] Xu, W.; Ledin, P. A.; Iatridi, Z.; Tsitsilianis, C.; Tsukruk, V. V. *Macromolecules* **2015**, *48*, 3344-3353.
- [88] Sheiko, S. S.; Zhou, J.; Arnold, J.; Neugebauer, D.; Matyjaszewski, K.; Tsitsilianis, C.; Tsukruk, V. V.; Dobrynin, A. V.; Rubinstein, M. *Nat. Mater.* **2013**, *12*, 735-740.
- [89] Xu, W.; Ledin, P. A.; Plamper, F. A.; Synatschke, C. V.; Müller, A. H.; Tsukruk, V. V. Multiresponsive *Macromolecules* **2014**, *47*, 7858-7868.
- [90] Kim, B.; Gao, H.; Argun, A. A.; Matyjaszewski, K.; Hammond, P. T. *Macromolecules* **2009**, *42*, 368-375.
- [91] Connal, L. A.; Vestberg, R.; Hawker, C. J.; Qiao, G. G. *Adv. Funct. Mater.* **2008**, *18*, 3706-3714.
- [92] Gao, C.; Yan, D. *Prog. Polym. Sci.* **2004**, *29*, 183-275.
- [93] Yates, C. R.; Hayes, W. *Eur. Polym. J.* **2004**, *40*, 1257-1281.
- [94] Ornatska, M.; Peleshanko, S.; Genson, K. L.; Rybak, B.; Bergman, K. N.; Tsukruk, V. V. *J. Am. Chem. Soc.* **2004**, *126*, 9675-9684.
- [95] Rybak, B. M.; Ornatska, M.; Bergman, K. N.; Genson, K. L.; Tsukruk, V. V. *Langmuir* **2006**, *22*, 1027-1037.
- [96] Shen, Y.; Kuang, M.; Shen, Z.; Nieberle, J.; Duan, H.; Frey, H. *Angew. Chem. Int. Ed.* **2008**, *47*, 2227-2230.
- [97] Chen, M. L.; Chen, M. L.; Chen, X. W.; Wang, J. H. *Macromol. Biosci.* **2010**, *10*, 906-915.

- 
- [98] Canilho, N.; Scholl, M.; Klok, H. A.; Mezzenga, R. *Macromolecules* **2007**, *40*, 8374-8383.
- [99] Hoven, C. V.; Garcia, A.; Bazan, G. C.; Nguyen, T. Q. *Adv. Mater.* **2008**, *20*, 3793-3810.
- [100] Feng, G.; Liang, J.; Liu, B. *Macromol. Rapid Commun.* **2013**, *34*, 705-715.
- [101] Pu, K. Y.; Li, K.; Shi, J.; Liu, B. *Chem. Mater.* **2009**, *21*, 3816-3822.
- [102] Shi, H.; Xiujie, C.; Liu, S.; Xu, H.; An, Z.; Ouyang, L.; Tu, Z.; Zhao, Q.; Fan, Q.; Wang, L.; Huang, W. *ACS Appl. Mater. Interfaces* **2013**, *5*, 4562-4568.
- [103] Bao, B.; Yuwen, L.; Zhan, X.; Wang, L. *J. Polym. Sci., Part A: Polym. Chem.* **2010**, *48*, 3431-3439.
- [104] Taranekar, P.; Qiao, Q.; Jiang, H.; Ghiviriga, I.; Schanze, K. S.; Reynolds, J. R. *J. Am. Chem. Soc.* **2007**, *129*, 8958-8959.
- [105] Giupponi, G.; Buzzza, D. M. A.; Adolf, D. B. *Macromolecules* **2007**, *40*, 5959-5965.
- [106] Zhang, S.; Sun, H.; Hughes, A.D.; Draghici, B.; Lejnieks, J.; Leowanawat, P.; Bertin, A.; De Leon, L.O.; Kulikov, O.V.; Chen, Y.; Pochan, D.J.; Heiney, P.A.; Percec, V. *ACS Nano* **2014**, *4*, 1554-1565.
- [107] Lyulin, S. V.; Vattulainen, I.; Gurtovenko, A. A. *Macromolecules* **2008**, *41*, 4961-4968.
- [108] Welch, P.; Muthukumar, M. *Macromolecules* **2000**, *33*, 6159-6167.
- [109] Esfand, R.; Tomalia, D. A. *Drug Discovery Today* **2001**, *6*, 427-436.
- [110] Tsukruk, V. V. *Adv. Mater.* **1998**, *10*, 253-257.
- [111] Tsukruk, V. V.; Rinderspacher, F.; Bliznyuk, V. N. *Langmuir* **1997**, *13*, 2171-2176.
- [112] Bliznyuk, V. N.; Rinderspacher, F.; Tsukruk, V. V. *Polymer* **1998**, *39*, 5249-5252.
- [113] Lee, C. C.; MacKay, J. A.; Fréchet, J. M.; Szoka, F. C. *Nat. Biotechnol.* **2005**, *23*, 1517-1526.
- [114] Lin, W.; Galletto, P.; Borkovec, M. *Langmuir* **2004**, *20*, 7465-7473.
- [115] Pericet-Camara, R.; Papastavrou, G.; Borkovec, M. *Langmuir* **2004**, *20*, 3264-3270.
- [116] Khopade, A. J.; Caruso, F. *Nano Lett.* **2002**, *2*, 415-418.
- [117] Khopade, A. J.; Caruso, F. *Biomacromolecules* **2002**, *3*, 1154-1162.
- [118] Khopade, A. J.; Caruso, F. *Langmuir* **2002**, *18*, 7669-7676.
- [119] Khopade, A. J.; Caruso, F. *Langmuir* **2003**, *19*, 6219-6225.
- [120] Kim, B. S.; Lebedeva, O. V.; Kim, D. H.; Caminade, A. M.; Majoral, J. P.; Knoll, W.; Vinogradova, O. I. *Langmuir* **2005**, *21*, 7200-7206.
- [121] Kim, B. S.; Lebedeva, O. V.; Koynov, K.; Gong, H.; Caminade, A. M.; Majoral, J. P.; Vinogradova, O. I. *Macromolecules* **2006**, *39*, 5479-5483.
- [122] Liu, Z.; Wang, X.; Wu, H.; Li, C. *J. Colloid Interface Sci.* **2005**, *287*, 604-611.
- [123] He, J. A.; Valluzzi, R.; Yang, K.; Dolukhanyan, T.; Sung, C.; Kumar, J.; Tripathy, S. K.; Samuelson, L.; Balogh, L.; Tomalia, D. A. *Chem. Mater.* **1999**, *11*, 3268-3274.
- [124] Niu, Y.; Yeung, L. K.; Crooks, R. M. *J. Am. Chem. Soc.* **2001**, *123*, 6840-6846.
- [125] Kim, B. Y.; Bruening, M. L. *Langmuir* **2003**, *19*, 94-99.

- 
- [126] Fu, Y.; Bai, S.; Cui, S.; Qiu, D.; Wang, Z.; Zhang, X. *Macromolecules* **2002**, *35*, 9451-9458.
- [127] Tsukruk, V. V.; Rinderspacher, F.; Bliznyuk, V. N. *Langmuir* **1997**, *13*, 2171-2176.
- [128] Pang, X.; Zhao, L.; Han, W.; Xin, X.; Lin, Z. *Nat. Nanotech.* **2013**, *8*, 426-431.
- [129] Drachuk, I.; Calabrese, R.; Harbaugh, S.; Kelley-Loughnane, N.; Kaplan, D. L.; Stone, M.; Tsukruk, V. V. *ACS Nano*, **2015**, *9*, 1219-1235.
- [130] Popescu, M. T.; Tasis, D.; Tsitsilianis, C. *ACS Macro Lett.* **2014**, *3*, 981-984.
- [131] Ding, D.; Wang, G.; Liu, J.; Li, K.; Pu, K. Y.; Hu, Y.; Ng, J. C. Y.; Tang, B. Z.; Liu, B. *Small* **2012**, *8*, 3523-3530.
- [132] Plamper, F. A.; Schmalz, A.; Penott-Chang, E.; Drechsler, M.; Jusufi, A.; Ballauff, M.; Müller, A. H. E. *Macromolecules* **2007**, *40*, 5689-5697.
- [133] Tsitsilianis, C.; Voulgaris, D. *Macromol. Chem. Phys.* **1997**, *198*, 997-1007.
- [134] Stavrouli, N.; Kyriazis, A.; Tsitsilianis, C. *Macromol. Chem. Phys.* **2008**, *209*, 2241-2247.
- [135] Plamper, F. A.; Murtomäki, L.; Walther, A.; Kontturi, K.; Tenhu, H. *Macromolecules* **2009**, *42*, 7254-7257.
- [136] Sheller, N. B.; Petrash, S.; Foster, M. D.; Tsukruk, V. V. *Langmuir* **1998**, *14*, 4535-4544.
- [137] Larson, K.; Vaknin, D.; Villavicencio, O.; McGrath, D. V.; Tsukruk, V. V. *J. Phys. Chem. B* **2002**, *106*, 7246-7251.
- [138] Ulman, A. *An Introduction to Ultrathin Organic Films: From LB to Self-Assembly*; Academic Press: Boston, MA, 1991.
- [139] Markutsya, S.; Jiang, C.; Pikus, Y.; Tsukruk, V. V. *Adv. Funct. Mater.* **2005**, *15*, 771-780.
- [140] Xiang, Y.; Lu, S.; Jiang, S. P. *Chem. Soc. Rev.* **2012**, *41*, 7291-7321.
- [141] Johnston, A. P. R.; Cortez, C.; Angelatos, A. S.; Caruso, F. *Curr. Opin. Colloid Interface Sci.* **2006**, *11*, 203-209.
- [142] Cheng, G.; Melnichenko, Y. B.; Wignall, G. D.; Hua, F. J.; Hong, K.; Mays, J. W. *Macromolecules* **2008**, *41*, 9831-9836.
- [143] McConney, M. E.; Singamaneni, S.; Tsukruk, V. V. *Polym. Rev.* **2010**, *50*, 235-286.
- [144] Tsukruk, V. V.; Singamaneni, S. *Scanning Probe Microscopy of Soft Matter: Fundamentals and Practices*, Wiley-VCH, Weinheim, **2012**.
- [145] Elsner, N.; Dubreuil F.; Fery, A. *Phys. Rev. E: Stat., Nonlinear, Soft Matter Phys.* **2004**, *69*, 031802-031807.
- [146] Schuh, C.; Santer, S.; Prucker, O.; Rühle, J. *Adv. Mater.* **2009**, *21*, 1-5.
- [147] Ramzi, A.; Scherrenberg, R.; Joosten, J.; Lemstra, P.; Mortensen, K. *Macromolecules* **2002**, *35*, 827-833.
- [148] Liu, X.; Cheng, F.; Liu, H.; Chen, Y. *Soft Matter* **2008**, *4*, 1991-1994.
- [149] Peleshanko, S.; Gunawidjaja, R.; Petrash, S.; Tsukruk, V. V. *Macromolecules* **2006**, *39*, 4756-4766.

- 
- [150] Jusufi, A.; Likos, C. N. *Rev. Mod. Phys.* **2009**, *81*, 1753-1772.
- [151] Steinschulte, A.; Schulte, B.; Drude, N.; Erberich, M.; Herbert, C.; Okuda, J.; Möller, M.; Plamper, F. A. *Polym. Chem.* **2013**, *4*, 3885-3895
- [152] Gunawidjaja, R.; Peleshanko, S.; Tsukruk, V. V. *Macromolecules* **2005**, *38*, 8765-8774.
- [153] Gunawidjaja, R.; Peleshanko, S.; Genson, K. L.; Tsitsilianis, C.; Tsukruk, V. V. *Langmuir* **2006**, *22*, 6168-6176.
- [154] Stuart, M. C.; Huck, W.; Genzer, J.; Müller, M.; Ober, C.; Stamm, M.; Sukhorukov, G.; Szleifer, I.; Tsukruk, V. V.; Urban, M.; Winnik, F.; Zauscher, S.; Luzinov, I.; Minko, S. *Nat. Mater.* **2010**, *9*, 101-113.
- [155] Plamper, F. A.; Gelissen, A. P.; Timper, J.; Wolf, A.; Zezin, A. B.; Richtering, W.; Tenhu, H.; Simon, U.; Mayer, J.; Borisov, O. V.; Pergushov, D. V. *Macromol. Rapid Commun.* **2013**, *34*, 855-860
- [156] Dobrynin, A. V.; Rubinstein, M. *Prog. Polym. Sci.* **2005**, *30*, 1049-1118.
- [157] Boudou, T.; Crouzier, T.; Ren, K.; Blin, G.; Picart, C. *Adv. Mater.* **2010**, *22*, 441-467.
- [158] Kanai, S.; Muthukumar, M. *J. Chem. Phys.* **2007**, *127*, 244908.
- [159] Muthukumar, M.; Hua, J.; Kundagrami, A. *J. Chem. Phys.* **2010**, *132*, 084901.
- [160] Verso, F. L.; Likos, C. N.; Reatto, L. *Progr. Colloid. Polym. Sci.* **2006**, *133*, 78-87.
- [161] Borue, V. Y.; Erukhimovich, I. Y. *Macromolecules* **1988**, *21*, 3240-3249.
- [162] Prabhu, V. M.; Muthukumar, M.; Wignall, G. D.; Melnichenko, Y. B. *J. Chem. Phys.* **2003**, *119*, 4085-4098.
- [163] Bokias, G.; Vasilevskaya, V. V.; Iliopoulos, I.; Hourdet, D.; Khokhlov, A. R. *Macromolecules* **2000**, *33*, 9757-9763.
- [164] Korobko, A. V.; Jesse, W.; Egelhaaf, S. U.; Lapp, A.; van der Maarel, J. R. C. *Phys. Rev. Lett.* **2004**, *93*, 177801.
- [165] Adelsberger, J.; Grillo, I.; Kulkarni, A.; Sharp, M.; Bivigou-Koumba, A. M.; Laschewsky, A.; Muller-Buschbaum, P.; Papadakis, C. M. *Soft Matter* **2013**, *9*, 1685-1699.
- [166] Xu, W.; Choi, I.; Plamper, F. A.; Synatschke, C. V.; A. H. E. Müller, Tsukruk, V. V. *ACS Nano* **2013**, *7*, 598-613.
- [167] Choi, I.; Malak, S. T.; Xu, W.; Heller, W. T.; Tsitsilianis, C.; Tsukruk, V. V. *Macromolecules* **2013**, *46*, 1425-1436.
- [168] Schallon, A.; Synatschke, C. V.; Jérôme, V.; Müller, A. H. E.; Freitag, R. *Biomacromolecules* **2012**, *13*, 3463-3474.
- [169] Luzinov, I.; Minko, S.; Tsukruk, V. V. *Prog. Polym. Sci.* **2004**, *29*, 635-698.
- [170] Griffiths, P. C.; Alexander, C.; Nilmini, R.; Pennadam, S. S.; King, S. M.; Heenan, R. K. *Biomacromolecules* **2008**, *9*, 1170-1178.
- [171] Shibayama, M.; Tanaka, T.; Han, C. C. *J. Chem. Phys.* **1992**, *97*, 6829-6841.

- 
- [172] Stieger, M.; Richtering, W.; Pedersen, J. S.; Lindner, P. *J. Chem. Phys.* **2004**, *120*, 6197-6206.
- [173] Ramzi, A.; Rijcken, C. J.; Veldhuis, T. F.; Schwahn, D.; Hennink, W. E.; van Nostrum, C. F. *J. Phys. Chem. B* **2008**, *112*, 784-792.
- [174] He, L.; Cheng, G.; Melnichenko, Y. B. *Phys. Rev. Lett.* **2012**, *109*, 067801.
- [175] Lambeth, R. H.; Ramakrishnan, S.; Mueller, R.; Poziemski, J. P.; Miguel, G. S.; Markoski, L. J.; Zukoski, C. F.; Moore, J. S. *Langmuir* **2006**, *22*, 6352-6360.
- [176] Plamper, F. A.; Ruppel, M.; Schmalz, A.; Borisov, O.; Ballauff, M.; Mueller, A. H. E. *Macromolecules* **2007**, *40*, 8361-8366.
- [177] Rathgeber, S.; Gast, A. P.; Hedrick, J. L. *Appl. Phys. A: Mater. Sci. Process.* **2002**, *74*, s396-s398.
- [178] Guinier, A.; Fournet, G. *Small-Angle Scattering of X-Rays*; John Wiley and Sons, New York, 1955.
- [179] Hansen, J. P.; Hayter, J. B. *Mol. Phys.* **1982**, *46*, 651-656.
- [180] Richter, D.; Jucknischke, O.; Willner, L.; Fetiers, L. J.; Lin, M.; Huang, J. S.; J. Roovers, J.; Toporovski, C.; Zhou, L. L. *Journal de Physique IV* **1993**, *3*, 3-12.
- [181] Likos, C. N.; Lowen, H.; Poppe, A.; Willner, L.; Roovers, J.; Cubitt, B.; Richter, D. *Phys. Rev. E: Stat., Nonlinear, Soft Matter Phys.* **1998**, *58*, 6299-6307.
- [182] Mildner, D.; Hall, P. *J. Phys. D: Appl. Phys.* **1986**, *19*, 1535-1545.
- [183] Crawford, M.K.; Smallew, R.J.; Cogen, G.; Hogan, B.; Wood, B.; Kumar, S.K.; Melnichenko, Y.B.; He, L.; Guise, W.; Hammouoda, B. *Phys. Rev. Lett.* **2013**, *110*, 196001.
- [184] Debye, P.; Anderson, H. R.; Brumberger, H. *J. Appl. Phys.* **1957**, *28*, 679-683.
- [185] De Gennes, P. G. *Scaling concepts in polymer physics*; Cornell university press: New York, 1979.
- [186] Hammouoda, B.; Ho, D.; Kline, S. *Macromolecules* **2002**, *35*, 8578-8585.
- [187] Moore, P. B. *J. Appl. Cryst.* **1980**, *13*, 168-175.
- [188] Daoud, M.; Cotton, J. P. *Journal de Physique* **1982**, *43*, 531-538.
- [189] Dozier, W. D.; Huang, J. S.; Fetters, L. J. *Macromolecules* **1991**, *24*, 2810-2814.
- [190] Borisov, O. V.; Zhulina, E. B.; Leermakers, F. A. M.; Ballauff, M.; Müller, A. H. E. *Adv. Polym. Sci.* **2011**, *241*, 1-55.
- [191] Kjøniksen, A. L.; Zhu, K.; Behrens, M. A.; Pedersen, J. S.; Nyström, B. *J. Chem. Phys. B* **2011**, *115*, 2125-2139.
- [192] Hedden, R. C.; Bauer, B. J. *Macromolecules* **2003**, *36*, 1829-1835.
- [193] Hammouoda, B. *Macromol. Theory Simul.* **2012**, *21*, 372-381.
- [194] Yun, S. I.; Lai, K.; Briber, R. M.; Teertstra, S. J.; Gauthier, M.; Bauer, B. J. *Macromolecules* **2008**, *41*, 175-183.
- [195] Rathgeber, S.; Monkenbusch, M.; Kreitschmann, M.; Urban, V.; Brulet, A. *J. Chem. Phys.* **2002**, *117*, 4047-4062.
- [196] Yun, S. I.; Briber, R. M.; Kee, R. A.; Gauthier, M. *Polymer* **2003**, *44*, 6579-6587.

- 
- [197] Sperling, L. H. *Introduction to Physical Polymer Science*; John Wiley & Sons, Inc., Hoboken, New Jersey, 2006.
- [198] Rud, O. V.; Mercurieva, A. A.; Leermakers, F. A. M.; Birshtein, T. M. *Macromolecules* **2012**, *45*, 2145–2160.
- [199] An, S. W.; Su, T. J.; Thomas, R. K.; Baines, F. L.; Billingham, N. C.; Armes, S. P.; Penfold, J. J. *Phys. Chem. B* **1998**, *102*, 387-393.
- [200] Wang, D.; Moses, D.; Bazan, G. C.; Heeger, A. J.; Lal, J. J. *Macromol. Sci., Part A: Pure Appl. Chem.* **2001**, *38*, 1175-1189.
- [201] Hsu, H.; Paul, W.; Binder, K. *J. Chem. Phys.* **2012**, *137*, 174902.
- [202] Plamper, F. *Star shaped polyelectrolytes*. University of Bayreuth, Bayreuth, **2007**.
- [203] Khalatur, P. G.; Khokhlov, A. R.; Mologin, D. A.; Reineker, P. *J Chem. Phys.* **2003**, *119*, 1232-1247.
- [204] Stradner, A.; Sedgwick, H.; Cardinaux, F.; Poon, W. C.; Egelhaaf, S. U.; Schurtenberger, P. *Nature* **2004**, *432*, 492-495.
- [205] Mai, Y.; Eisenberg, A. *Chem. Soc. Rev.* **2012**, *41*, 5969–5985.
- [206] Andreeva, A. S.; Philippova, O. E.; Khokhlov, A. R.; Islamov, A. K.; Kuklin, A. I. *Langmuir* **2005**, *21*, 1216-1222.
- [207] Ermi, B. D.; Amis, E. J. *Macromolecules* **1998**, *31*, 7378-7384.
- [208] Micka, U.; Holm, C.; Kremer, K. *Langmuir* **1999**, *15*, 4033-4044.
- [209] Micka, U.; Kremer, K. *Europhys. Lett.* **2000**, *49*, 189–195.
- [210] Huisman, S.; Blaak, R.; Likos, C. N. *Macromolecules* **2009**, *42*, 2806-2816.
- [211] Košován, P.; Kuldová, J.; Limpouchová, Z.; Procházka, K.; Zhulina, E. B.; Borisov, O. V. *Soft Matter* **2010**, *6*, 1872-1874.
- [212] Winkler, R. G.; Gold, M.; Reineker, P. *Phys. Rev. Lett.* **1998**, *80*, 3731-3734.
- [213] Guinier, A.; Fournet, G. *Small-Angle Scattering of X-Rays*; John Wiley and Sons, New York, 1955.
- [214] Hansen, J. P.; Hayter, J. B. *Mol. Phys.* **1982**, *46*, 651-656.
- [215] Mildner, D.; Hall, P. *J. Phys. D: Appl. Phys.* **1986**, *19*, 1535-1545.
- [216] Benoit, H. *J. Polym. Sci.* **1953**, *11*, 507-510.
- [217] Laurati, M.; Stellbrink, J.; Lund, R.; Willner, L.; Zaccarelli, E.; Richter, D. *Phys. Rev. E* **2007**, *76*, 041503.
- [218] Willner, L.; Jucknischke, O.; Richter, D.; Roovers, J.; Zhou, L. L.; Toporowski, P. M.; Fetters, L. J.; Huang, J. S.; Lin, M. Y.; Hadjichristidis, N. *Macromolecules* **1994**, *27*, 3821-3829.
- [219] Yun, S. I.; Lai, K.; Briber, R. M.; Teertstra, S. J.; Gauthier, M.; Bauer, B. J. *Macromolecules* **2008**, *41*, 175-183.
- [220] Jensen, G. V.; Shi, Q.; Hernansanz, M. J.; Oliveira, C. L. P.; Deen, G. R.; Almdal, K.; Pedersen, J. S. *J. Appl. Cryst.* **2011**, *44*, 473–482.
- [221] De Gennes, P. G. *Scaling concepts in polymer physics*; Cornell university press: New York, 1979.

- 
- [222] Debye, P.; Anderson, H. R.; Brumberger, H. *J. Appl. Phys.* **1957**, *28*, 679-683.
- [223] Hammouda, B. *J. Appl. Cryst.* **2010**, *43*, 716-719.
- [224] Park, J.; Jang, S.; Kon Kim, J. *J. Polym. Sci., Part B: Polym. Phys.* **2015**, *53*, 1-21.
- [225] Xu, W.; Choi, I.; Plamper, F. A.; Synatschke, C. V.; Muller, A. H.; Melnichenko, Y. B.; Tsukruk, V. V. *Macromolecules* **2014**, *47*, 2112-2121.
- [226] Iatridi, Z.; Tsitsilianis, C. *Polymers* **2011**, *3*, 1911-1933.
- [227] Steinschulte, A. A.; Xu, W.; Draber, F.; Hebbeker, P.; Jung, A.; Bogdanovski, D.; Schneider, S.; Tsukruk, V. V.; Plamper, F. A. *Soft Matter* **2015**, *11*, 3559-3565.
- [228] Ariga, K.; Yamauchi, Y.; Mori, T.; Hill, J. P. *Adv. Mater.* **2013**, *25*, 6477-6512.
- [229] Aoki, H.; Takahashi, T.; Ito, S. *Polym. J.* **2011**, *43*, 218-221.
- [230] Peleshanko, S.; Anderson, K. D.; Goodman, M.; Determan, M. D.; Mallapragada, S. K.; Tsukruk, V. V. *Langmuir* **2007**, *23*, 25-30.
- [231] Genson, K. L.; Holzmueller, J.; Jiang, C.; Xu, J.; Gibson, J. D.; Zubarev, E. R.; Tsukruk, V. V. *Langmuir* **2006**, *22*, 7011-7015.
- [232] D'Souza M. M.; Manga, M. S.; Hunter, T. N.; Cayre, O. J.; Biggs, S. *Langmuir*, **2012**, *28*, 5085-5092.
- [233] Njikang, G. N.; Cao, L.; Gauthier, M. *Langmuir* **2008**, *24*, 12919-12927.
- [234] Logan, J. L.; Masse, P.; Dorvel, B.; Skolnik, A. M.; Sheiko, S. S.; Francis, R.; Taton, D.; Gnanou, Y.; Duran, R. S. *Langmuir* **2005**, *21*, 3424-3431.
- [235] Logan, J. L.; Masse, P.; Gnanou, Y.; Taton, D.; Duran, R. S. *Langmuir* **2005**, *21*, 7380-7389.
- [236] Xu, H.; Erhardt, R.; Abetz, V.; Müller, A. H.; Goedel, W. A. *Langmuir* **2001**, *17*, 6787-6793.
- [237] Peleshanko, S.; Jeong, J.; Gunawidjaja, R.; Tsukruk, V. V. *Macromolecules* **2004**, *37*, 6511-6522.
- [238] Gunawidjaja, R.; Peleshanko, S.; Genson, K. L.; Tsitsilianis, C.; Tsukruk, V. V. *Langmuir* **2006**, *22*, 6168-6176.
- [239] Genson, K. L.; Hoffman, J.; Teng, J.; Zubarev, E. R.; Vaknin, D.; Tsukruk, V. V. *Langmuir* **2004**, *20*, 9044-9052.
- [240] Choi, I.; Gunawidjaja, R.; Suntivich, R.; Tsitsilianis, C.; Tsukruk, V. V. *Macromolecules* **2010**, *43*, 6818-6828.
- [241] Wei, H.; Cheng, S. X.; Zhang, X. Z.; Zhuo, R. X. *Prog. Polym. Sci.* **2009**, *34*, 893-910.
- [242] Lencina, M. M. S.; Iatridi, Z.; Villar M. A.; Tsitsilianis, C. *Eur. Polym. J.* **2014**, *61*, 33-44.
- [243] Tokarev, I.; Minko, S. *Soft Matter* **2009**, *5*, 511-524.
- [244] Sukhishvili, S. A. *Curr. Opin. Colloid Interface Sci.* **2005**, *10*, 37-44.
- [245] Vogel, N.; Fernández-López, C.; Pérez-Juste, J.; Liz-Marzán, L. M.; Landfester, K.; Weiss, C. K. *Langmuir* **2012**, *28*, 8985-8993.
- [246] Liu, G.; Yang, S.; Zhang, G. *J. Phys. Chem. B* **2007**, *111*, 3633-3639.

- 
- [247] Matmour, R.; Joncheray, T. J.; Gnanou, Y.; Duran, R. S. *Langmuir* **2007**, *23*, 649-658.
- [248] Iatridi, Z.; Roiter, Y.; Stavrouli, N.; Minko, S.; Tsitsilianis, C. *Polym. Chem.* **2011**, *2*, 2037-2044.
- [249] Iatridi, Z.; Lencina, M-M-S.; Tsitsilianis, C. *Polym. Chem.* **2015**, *6*, 3942-3955.
- [250] Iatridi, Z.; Tsitsilianis, C. *Chem. Commun.* **2011**, *47*, 5560-5562.
- [251] Kodiyath, R.; Choi, I.; Patterson, B.; Tsitsilianis, C.; Tsukruk, V. V. *Polymer* **2013**, *54*, 1150-1159.
- [252] Reitzel, N.; Greve, D. R.; Kjaer, K.; Howes, P. B.; Jayaraman, M.; Savoy, S.; McCullough, R. D.; McDevitt, J. T.; Bjørnholm, T. *J. Am. Chem. Soc.* **2000**, *122*, 5788-5800.
- [253] Sorokin, A. V.; Bai, M.; Ducharme, S.; Poulsen, M. *J. Appl. Phys.* **2002**, *92*, 5977-5981.
- [254] Koutsopoulou, E.; Tsitsilianis, C. *Macromol. Chem. Phys.* **2004**, *205*, 2116-2123.
- [255] Genson, K. L.; Hoffman, J.; Teng, J.; Zubarev, E. R.; Vaknin, D.; Tsukruk, V. V. *Langmuir* **2004**, *20*, 9044-9052.
- [256] Zhai, X.; Peleshanko, S.; Klimenko, N. S.; Genson, K. L.; Vaknin, D.; Vortman, M. Y.; Shevchenko, V. V.; Tsukruk, V. V. *Macromolecules* **2003**, *36*, 3101-3110.
- [257] Chung, B.; Choi, M.; Ree, M.; Jung, J. C.; Zin, W. C.; Chang, T. *Macromolecules* **2006**, *39*, 684-689.
- [258] Ulman, A. *An Introduction to Ultrathin Organic Films: From Langmuir--Blodgett to Self-Assembly*, Academic press, Boston, 1991.
- [259] Joncheray, T. J.; Bernard, S. A.; Matmour, R.; Lepoittevin, B.; El-Khoury, R. J.; Taton, D.; Gnanou, Y.; Duran, R. S. *Langmuir* **2007**, *23*, 2531-2538.
- [260] Wu, C.; Wang, X. *Phys. Rev. Lett.* **1998**, *80*, 4092-4094.
- [261] Gorodyska, G.; Kiriy, A.; Minko, S.; Tsitsilianis, C.; Stamm, M. *Nano Lett.* **2003**, *3*, 365-368.
- [262] Borisov, O. V.; Zhulina, E. B.; Leermakers, F. A. M.; Ballauff, M.; Müller, A. H. E. *Adv. Polym. Sci.* **2011**, *241*, 1-55.
- [263] Roiter, Y.; Minko, S. *J. Am. Chem. Soc.* **2005**, *127*, 15688-15689.
- [264] Luzinov, I.; Minko, S.; Tsukruk, V. V. *Soft Matter* **2008**, *4*, 714-725.
- [265] Santer, S.; Kopyshchev, A.; Donges, J.; Yang, H. K.; Ruhe, J. *Adv. Mater.* **2006**, *18*, 2359-2362.
- [266] Hendrikson, G. R.; Lyon, L. A. *Soft Matter* **2009**, *5*, 29-35.
- [267] Synatschke, C. V.; Nomoto, T.; Cabral, H.; Förtsch, M.; Toh, K.; Matsumoto, Y.; Miyazaki, K.; Hanisch, A.; Schacher, F. H.; Kishimura, A.; Nishiyama, N.; Müller, A. H. E.; Kataoka, K. *ACS Nano* **2014**, *8*, 1161-1172.
- [268] Steinschulte, A.; Schulte, B.; Rütten, S.; Eckert, T.; Okuda, J.; Möller, M.; Schneider, S.; Borisov, O. V.; Plamper, F. A. *Phys. Chem. Chem. Phys.* **2014**, *16*, 4917-4932.

- 
- [269] Lu, Y.; Mei, Y.; Drechsler, M.; Ballauff, M. *Angew. Chem. Int. Ed.* **2006**, *45*, 813-816.
- [270] Plamper, F. A.; Gelissen, A. P.; Timper, J.; Wolf, A.; Zezin, A. B.; Richtering, W.; Tenhu, H.; Simon, U.; Mayer, J.; Borisov, O. V.; Pergushov, D. V. *Macromol. Rapid Commun.* **2013**, *34*, 855-860.
- [271] Chia, K.; Rubner, M. F.; Cohen, R. E. *Langmuir* **2009**, *25*, 14044-14052.
- [272] Ionov, L. *Adv. Funct. Mater.* **2013**, *23*, 4555-4570.
- [273] Drachuk, I.; Shchepelina, O.; Lisunova, M.; Harbaugh, S.; Kelley-Loughnane, N.; Stone, M.; Tsukruk, V. V. *ACS Nano* **2012**, *6*, 4266-4278.
- [274] Fakhrullin, R. F.; Lvov, Y. M. *ACS Nano* **2012**, *6*, 4557-4564.
- [275] Wang, Y.; Hosta-Rigau, L.; Lomas, H.; Caruso, F. *Phys. Chem. Chem. Phys.* **2011**, *13*, 4782-4801.
- [276] De Cock, L. J.; De Koker, S.; De Geest, B. G.; Grooten, J.; Vervaet, C.; Remon, J. P.; Sukhorukov, G. B.; Antipina, M. N. *Angew. Chem., Int. Ed.* **2010**, *49*, 6954-6973.
- [277] Ariga, K.; Hill, J. P.; Ji, Q. *Phys. Chem. Chem. Phys.* **2007**, *9*, 2319-2340.
- [278] Fery, A.; Tsukruk, V. V. In *Multilayer thinfilms: sequential assembly of nanocomposite materials*, 2nd ed.; Decher, G., Schlenoff, J., Eds.; Wiley-VCH: Weinheim, Germany 2012; Vol. 1.
- [279] Jiang, C.; Tsukruk, V. V. *Adv. Mater.* **2006**, *18*, 829-840.
- [280] De Geest, B. G.; Sanders, N. N.; Sukhorukov, G. B.; Demeester, J.; De Smedt, S. C. *Chem. Soc. Rev.* **2007**, *36*, 636-649.
- [281] Sukhishvili, S. A. *Curr. Opin. Colloid Interface Sci.* **2005**, *10*, 37-44.
- [282] Ye, C.; Shchepelina, O.; Calabrese, R.; Drachuk, I.; Kaplan, D. L.; Tsukruk, V. V. *Biomacromolecules* **2011**, *12*, 4319-4325.
- [283] Yi, Q.; Wen, D.; Sukhorukov, G. B. *Langmuir* **2012**, *28*, 10822-10829.
- [284] Hoy, O.; Zdyrko, B.; Lupitskyy, R.; Sheparovych, R.; Aulich, D.; Wang, J.; Bittrich, E.; Eichhorn, K.; Uhlmann, P.; Hinrichs, K.; Müller, M.; Stamm, M.; Minko, S.; Luzinov, I. *Adv. Funct. Mater.* **2010**, *20*, 2240-2247.
- [285] Dong, W. F.; Ferri, J. K.; Adalsteinsson, T.; Schönhoff, M.; Sukhorukov, G. B.; Möhwald, H. *Chem. Mater.* **2005**, *17*, 2603-2611.
- [286] Bedard, M. F.; De Geest, B. G.; Skirtach, A. G.; Möhwald, H.; Sukhorukov, G. B. *Adv. Colloid Interface Sci.* **2010**, *158*, 2-14.
- [287] Lu, Z. H.; Prouty, M. D.; Guo, Z. H.; Golub, V. O.; Kumar, C.; Lvov, Y. M. *Langmuir* **2005**, *21*, 2042-2050.
- [288] Plamper, F. A. *Adv. Polym. Sci.* **2015**, *266*, 125-212
- [289] Zahn, R.; Voros, J.; Zambelli, T. *Curr. Opin. Colloid Interface Sci.* **2010**, *15*, 427-434.
- [290] Skirtach, A. G.; De Geest, B. G.; Mamedov, A.; Antipov, A. A.; Kotov, N. A.; Sukhorukov, G. B. *J. Mater. Chem.* **2007**, *17*, 1050-1054.
- [291] Xu, L.; Zhu, Z.; Sukhishvili, S. *Langmuir*, **2011**, *27*, 409-415.

- 
- [292] Bedard, M. F.; Munoz-Javier, A.; Mueller, R.; del Pino, P.; Fery, A.; Parak, W. J.; Skirtach, A. G.; Sukhorukov, G. B. *Soft Matter* **2009**, *5*, 148-155.
- [293] Kozlovskaya, V.; Kharlampieva, E.; Drachuk, I.; Cheng, D.; Tsukruk, V. V. *Soft Matter* **2010**, *6*, 3596-3608.
- [294] Kuroki, H.; Tokarev, I.; Nykypanchuk, D.; Zhulina, E.; Minko, S. *Adv. Funct. Mater.* **2013**, *23*, 4593-4600.
- [295] Kowalczyk, A.; Trzcinska, R.; Trzebicka, B.; Dworak, A.; Müller, A. H. E.; Tsvetanov, C. B. *Prog. Polym. Sci.* **2014**, *39*, 43-86.
- [296] Yang, W. C.; Xie, R.; Pang, X. Q.; Ju, X. J.; Chu, L. Y. *J. Membr. Sci.* **2008**, *321*, 324-330.
- [297] Wang, Z.; Feng, Z.; Gao, C. *Chem. Mater.* **2008**, *20*, 4194-4199.
- [298] Berger, S.; Zhang, H.; Pich, A. *Adv. Funct. Mater.* **2009**, *19*, 554-559.
- [299] Gao, H.; Matyjaszewski, K. *Prog. Polym. Sci.* **2009**, *34*, 317-392.
- [300] Jia, P. T.; Argun, A. A.; Xu, J. W.; Xiong, S. X.; Ma, J.; Hammond, P. T.; Lu, X. H. *Chem. Mater.* **2010**, *22*, 6085-6091.
- [301] Kim, B. S.; Gao, H. F.; Argun, A. A.; Matyjaszewski, K.; Hammond, P. T. *Macromolecules* **2009**, *42*, 368-375.
- [302] Majewski, A. P.; Stahlschmidt, U.; Jérôme, V.; Freitag, R.; Müller, A. H. E.; Schmalz, H. *Biomacromolecules* **2013**, *14*, 3081-3090.
- [303] Déjugnat, C.; Sukhorukov, G. B. *Langmuir* **2004**, *20*, 7265-7269.
- [304] Tong, W.; Gao, C.; Möhwald, H. *Macromolecules* **2006**, *39*, 335-340.
- [305] Lvov, Y.; Antipov, A. A.; Mamedov, A.; Möhwald, H.; Sukhorukov, G. B. *Nano Lett.* **2001**, *1*, 125-128.
- [306] Gelissen, A. P. H.; Schmid, A. J.; Plamper, F. A.; Pergushov, D. V.; Richtering, W. *Polymer* **2014**, *55*, 1991-1999.
- [307] Yuan, W.; Lv, Y.; Zeng, M.; Fu, B. M. *Microvasc. Res.* **2009**, *77*, 166-173.
- [308] Lavalle, P.; Gergely, C. F.; Cuisinier, J. G.; Decher, G.; Schaaf, P.; Voegel, J. C.; Picart, C. *Macromolecules* **2002**, *35*, 4458-4465.
- [309] Picart, C.; Lavalle, P.; Hubert, P.; Cuisinier, F. J. G.; Decher, G.; Schaaf, P.; Voegel, J. C. *Langmuir* **2001**, *17*, 7414-7424.
- [310] Burke, S. E.; Barrett, C. J. *Macromolecules* **2004**, *37*, 5375-5384.
- [311] Chung, A. J.; Rubner, M. F. *Langmuir* **2002**, *18*, 1176-1183.
- [312] Arslan, H.; Pfaff, A.; Lu, Y.; Stepánek, P.; Müller, A. H. E. *Macromol. Biosci.* **2014**, *14*, 81-91.
- [313] Thavanesan, T.; Herbert, C.; Plamper, F. A. *Langmuir* **2014**, *30*, 5609-5619.
- [314] Yuan, W.; Zou, H.; Guo, W.; Wang, A.; Ren, J. *J. Mater. Chem.* **2012**, *22*, 24783-24791.
- [315] Leporatti, S.; Gao, C.; Voigt, A.; Donath, E.; Möhwald, H. *Eur. Phys. J. E.* **2001**, *5*, 13-20.

- 
- [316] Gao, C.; Leporatti, S.; Moya, S.; Donath, E.; Möhwald, H. *Chem. Eur. J.* **2003**, *9*, 915-920.
- [317] Bergström, M.; Pedersen, J. S.; Schurtenberger, P.; Egelhaaf, S. U. *J. Phys. Chem. B* **1999**, *103*, 9888-9897.
- [318] Nallet, F.; Laversanne, R.; Roux, D. *J Phys II* **1993**, *3*, 487-502.
- [319] Dimitrov, I.; Trzebicka, B.; Müller, A. H. E.; Dworak, A.; Tsvetanov, C. B. *Prog. Polym. Sci.* **2007**, *32*, 1275-1343.
- [320] Wang, Y.; Hosta-Rigau, L.; Lomas, H.; Caruso, F. *Phys. Chem. Chem. Phys.* **2011**, *13*, 4782-4801.
- [321] Zhuk, A.; Mirza, R.; Sukhishvili, S. *ACS Nano* **2011**, *5*, 8790-8799.
- [322] Pavluchina, S.; Sukhishvili, S. *Adv. Drug Del. Rev.* **2011**, *63*, 822-836.
- [323] Johnston, A. P. R.; Such, G. K.; Ng, S. L.; Caruso, F. *Curr. Opin. Colloid Interface Sci.* **2011**, *16*, 171-181.
- [324] De Geest, B. G.; Sanders, N. N.; Sukhorukov, G. B.; Demeester, J.; De Smedt, S. C. *Chem. Soc. Rev.* **2007**, *36*, 636-649.
- [325] Wang, A.; Cui, Y.; Li, J.; van Hest, J. C. M. *Adv. Funct. Mater.* **2012**, *22*, 2673-2681.
- [326] Antipov, A. A.; Sukhorukov, G. B.; Leporatti, S.; Radtchenko, I. L.; Donath, E.; Möhwald, H. *Colloids Surf., A* **2002**, *198*, 535-541.
- [327] Yi, Q.; Wen, D.; Sukhorukov, G. B. *Langmuir* **2012**, *28*, 10822-10829.
- [328] Lu, Z. H.; Prouty, M. D.; Guo, Z. H.; Golub, V. O.; Kumar C.; Lvov, Y. M. *Langmuir* **2005**, *21*, 2042-2050.
- [329] Bedard, M. F.; De Geest, B. G.; Skirtach, A. G.; Mohwald, H.; Sukhorukov, G. B. *Adv. Colloid Interface Sci.* **2010**, *158*, 2-14.
- [330] Skirtach, A. G.; Karageorgiev, P.; Bedard, M. F.; Sukhorukov, G. B.; Mohwald, H. *J. Am. Chem. Soc.* **2008**, *130*, 11572-11573.
- [331] Kim, J.; Lim, H.; Hwang, Y. K.; Woo, H.; Kim, J. W.; Char, K. *Langmuir* **2012**, *28*, 11899-11905.
- [332] Bedard, M. F.; Sadasivan, S.; Sukhorukov, G. B.; Skirtach, A. *J. Mater. Chem.* **2009**, *19*, 2226-2233.
- [333] Bedard, M.; Skirtach, A. G.; Sukhorukov, G. B. *Macromol. Rapid Commun.* **2007**, *28*, 1517-1521.
- [334] Antipina, M. N.; Sukhorukov, G. B. *Adv. Drug Delivery Rev.* **2011**, *63*, 716-729.
- [335] Tsitsilianis, C. *Soft Matter* **2010**, *6*, 2372-2388.
- [336] Gao, H.; Matyjaszewski, K. *Prog. Polym. Sci.* **2009**, *34*, 317-350.
- [337] Borisov, O. V.; Zhulina, E. B.; Leermakers, F. A. M.; Ballauff, M.; Müller, A. H. E. *Adv. Polym. Sci.* **2011**, *241*, 1-55.
- [338] Khopade, A. J.; Caruso, F. *Biomacromolecules* **2002**, *3*, 1154-1162.
- [339] Feng, C. L.; Caminade, A. M.; Majoral, J. P.; Gu, J.; Zhu, S.; Su, H.; Hu, X.; Zhang, D. *Analyst* **2010**, *135*, 2939-2944.

- 
- [340] Kim, B. S.; Lebedeva, O. V.; Koynov, K.; Gong, H.; Caminade, A. M.; Majoral, J. P.; Vinogradova, O. I. *Macromolecules* **2006**, *39*, 5479-5483.
- [341] Addison, T.; Cayre, O. J.; Biggs, S.; Armes, S. P.; York, D. *Langmuir* **2010**, *26*, 6281-6286.
- [342] Sheller, N. B.; Petrash, S.; Foster, M. D.; Tsukruk, V. V. *Langmuir* **1998**, *14*, 4535-4544
- [343] Hübsch, E.; Ball, V.; Senger, B.; Decher, G.; Voegel, J.; Schaaf, P. *Langmuir* **2004**, *20*, 1980-1985.
- [344] Feng, Z.; Wang, Z.; Gao, C.; Shen, J. *Adv. Mater.* **2007**, *19*, 3687-3691.
- [345] Cavalieri, F.; Postma, A.; Lee, L.; Caruso, F. *ACS Nano* **2009**, *3*, 234-240.
- [346] Armstrong, J. K.; Wenby, R. B.; Meiselman, H. J.; Fisher, T. C. *Biophys. J.* **2004**, *87*, 4259-4270.
- [347] Shchepelina, O.; Drachuk, I.; Gupta, M. K.; Lin, J.; Tsukruk, V. V. *Adv. Mater.* **2011**, *23*, 4655-4660.
- [348] Roiter, Y.; Trotsenko, O.; Tokarev, V.; Minko, S. *J. Am. Chem. Soc.* **2010**, *132*, 13660-13662.
- [349] Trotsenko, O.; Roiter, Y.; Minko, S. *Langmuir* **2012**, *28*, 6037-6044.
- [350] Ishikubo, A.; Mays, J.; Tirrell, M. *Ind. Eng. Chem. Res.* **2008**, *47*, 6426-6433.
- [351] Nguyen, T. T.; Rouzina, I.; Shklovskii, B. I. *J. Chem. Phys.* **2000**, *112*, 2562-2568.
- [352] Mei, Y.; Lauterbach, K.; Hoffmann, M.; Borisov, O. V.; Ballauff, M.; Jusufi, A. *Phys. Rev. Lett.* **2006**, *97*, 158301-158304.
- [353] Moggi, L.; Bolletta, F.; Balzani V.; Scandola, F. *J. Inorg. Nucl. Chem.* **1966**, *28*, 2589-2597.
- [354].Freltoft, T.; Kjems, J. K.; Sinha, S. K. *Phys. Rev. B* **1986**, *33*, 269-275.
- [355].Schmidt, P. W. *J. Appl. Cryst.* **1991**, *24*, 414-435.
- [356] Kratz, K.; Hellweg, T.; Eimer, W. *Polymer* **2001**, *42*, 6631-6639
- [357].Tsukruk, V. V.; Bliznyuk, V. N.; Visser, D. W.; Campbell, A. L.; Bunning, T.; Adams, W. W. *Macromolecules* **1997**, *30*, 6615-6625.
- [358].Debye, P.; Bueche, A. M. *J. Appl. Phys.* **1949**, *20*, 518-525.
- [359].Debye, P.; Anderson, R.; Brumberger, H. *J. Appl. Phys.* **1957**, *28*, 679-683.
- [360].Roldán-Vargas, S.; Barnadas-Rodríguez, R.; Martín-Molina, A.; Quesada-Pérez, M.; Estelrich, J.; Callejas-Fernández, J. *Phys. Rev. E* **2008**, *78*, 010902.
- [361] Delcea, M.; Yashchenok, A.; Videnova, K.; Kreft, O.; Möhwald, H.; Skirtach, A. G. *Macromol. Biosci.* **2010**, *10*, 465-474.
- [362] Iatridi, Z.; Roiter, Y.; Stavrouli, N.; Minko, S.; Tsitsilianis, C. *Polym. Chem.* **2011**, *2*, 2037-2044.
- [363] Lin, D.; Liu, N.; Yang, K.; Zhu, L.; Xu, Y.; Xing, B. *Carbon* **2009**, *47*, 2875-2882.
- [364] Kurniasih, I. N.; Liang, H.; Kumar, S.; Mohr, A.; Sharma, S. K.; Rabe, J. P.; Haag, R. *J. Mater. Chem. B.* **2013**, *1*, 3569-3577.

- 
- [365] Addison, T.; Cayre, O. J.; Biggs, S.; Armes, S. P.; York, D. *Langmuir* **2010**, *26*, 6281–6286.
- [366] Thompson, K. L.; Chambon, P.; Verber, R.; Armes, S. P. *J. Am. Chem. Soc.* **2012**, *134*, 12450-12453.
- [367] Polotsky, A. A.; Zhulina, E. B.; Birshstein, T. M.; Borisov, O. V. *Soft Matter* **2012**, *8*, 9446-9459.
- [368] Yuan, J. Y.; Mecerreyes, D.; Antonietti, M. *Prog. Pol. Sci.* **2013**, *38*, 1009-1036.
- [369] Stathatos, E.; Jovanovski, V.; Orel, B.; Jerman, I.; Lianos, P. *J. Phys. Chem. C* **2007**, *111*, 6528-6532.
- [370] Wang, Y.; Luo, J.; Liu, Z. *J. Organomet. Chem.* **2013**, *739*, 1-5.
- [371] Hallett, J. P.; Welton, T. *Chem. Rev.* **2011**, *111*, 3508-3576.
- [372] Greaves, T. L.; Drummond, C. J. *Chem. Rev.* **2008**, *108*, 206-237.
- [373] Le Bideau, J.; Viau, L.; Vioux, A. *Chem. Soc. Rev.* **2011**, *40*, 907-925.

---

## VITA

### Weinan Xu

Weinan Xu was born and raised in Henan province, China. From 2007 to 2011, he studied at Donghua University (Shanghai, China), and earned a bachelor degree in Polymer Science and Engineering. Since Aug. 2011, he works in the Surface Engineering and Molecular Assemblies (SEMA) Laboratory under the supervision of Prof. Vladimir Tsukruk (<http://polysurf.mse.gatech.edu/>). His current work focuses on the interfacial assembly of branched polymers, especially star shaped polymers with responsive properties, into functional microstructures including thin film, polymersomes, microemulsions, and microcapsules; with potential applications in smart coating, drug carrier and microreactors.